



Faculty of Science
Department of Physics

Modelling three-dimensional nanoparticle transformations based on quantitative transmission electron microscopy

Modellering van driedimensionale transformaties van nanodeeltjes op
basis van kwantitatieve transmissie-elektronenmicroscopie

Thesis submitted for the degree of Doctor of Science at the University of Antwerp
to be defended by:

Ece Arslan Irmak

Supervisors:

Prof. Dr. Sandra Van Aert

Prof. Dr. Sara Bals

Antwerp 2022

Doctoral committee

Chairman

Prof. Dr. Milorad Milosevic, University of Antwerp - Belgium

Supervisor

Prof. Dr. Sandra Van Aert, University of Antwerp - Belgium

Prof. Dr. Sara Bals, University of Antwerp - Belgium

Members

Prof. Dr. Erik Neyts, University of Antwerp - Belgium

Assoc. Prof. Dr. Ir. Marijn van Huis, Utrecht University – The Netherlands

Asst. Prof. Dr. Lewys Jones, Trinity College Dublin - Ireland

Contact information

Ece Arslan Irmak

University of Antwerp – Department of Physics

EMAT – Electron Microscopy for Materials Science

Groenenborgerlaan 171

2020 Antwerp

Belgium

ece.arslanirmak@uantwerpen.be

Contents

Chapter 1. Introduction	1
1.1. Nanotechnology and nanomaterials.....	2
1.2. Transmission electron microscopy	5
1.3. Electron tomography.....	8
1.4. Quantitative electron microscopy	11
1.5. 3D structure of nanoparticles under realistic conditions	13
1.6. Thesis motivation and outline.....	15
Chapter 2. Quantitative 3D characterization from 2D STEM images	19
2.1. Physics of image formation in ADF STEM.....	20
2.1.1. Electron-probe formation	20
2.1.2. Electron-specimen interaction.....	22
2.1.3. Multislice simulations	23
2.1.4. Intensity integration over the detector.....	26
2.2. Model-based statistical parameter estimation for ADF STEM images	28
2.3. Atomistic simulations	35
2.4. Conclusion	42
Appendix A: Interpretation of ICL.....	43
Appendix B: Validation of EAM potential for Au and Pt systems.....	46
Chapter 3. 3D atomic structure of supported Au nanoparticles at high temperature.....	49
3.1. Introduction.....	50
3.2. Methods	51
3.2.1. ADF STEM image acquisition.....	51
3.2.2. ADF STEM image restoration and registration	51
3.2.3. Normalization of ADF STEM images.....	53
3.2.4. Multislice simulations to create library values.....	54
3.2.5. Combined simulation and statistics-based atom counting	55
3.3. 3D equilibrium structure of supported Au NPs as a function of temperature	56
3.4. Non-equilibrium transformations of supported Au NPs at high temperature.....	60
3.5. Conclusion	63
Chapter 4. 3D atomic structure of supported metallic nanoparticles: a combination of atom counting and a local minima search algorithm.....	65

4.1. Introduction	66
4.2. Experimental details	67
4.3. Details of MD simulations and particle-support interaction	68
4.4. Atom counting for NPs at high temperatures	69
4.4.1. Accuracy of the atom counting approach evaluated on simulated images	69
4.4.2. Counting the number of atoms from experimental images	71
4.5. 3D reconstruction based on atom counting results	73
4.5.1. Validation of the method on the simulated image	73
4.5.2. Experimental results	76
4.6. Comparison to other approaches	77
4.7. Conclusion	81
 Chapter 5. Unravelling Pt-driven morphological transformations in Au@Pt nanorods upon heating	83
5.1. Introduction	84
5.2. Synthesis and 3D characterization of Au@Pt NRs	85
5.3. Thermal stability of Au@Pt NRs	87
5.4. MD simulations	88
5.4.1. MD simulations by using experimental morphology	88
5.4.2. Thermodynamic behavior of Au-Pt NPs	91
5.4.3. The effect of Pt surface morphology on thermal stability of NRs	93
5.5. Discussion and conclusion	99
 Chapter 6. 3D atomic-scale dynamics of laser light induced restructuring of nanoparticles unraveled by electron tomography and molecular dynamics simulations	101
6.1. Introduction	102
6.2. Synthesis and femtosecond laser excitation	103
6.3. 2D STEM characterization	103
6.4. 3D characterization by electron tomography	105
6.5. MD simulations for femtosecond laser excitation of NRs	107
6.5.1. Modelling heating regime of a femtosecond laser pulse	108
6.5.2. MD simulations by using model-like inputs	110
6.5.3. MD simulations based on the experimentally determined morphology	114
6.6. Discussion	117
6.7. Conclusion	120

Chapter 7. General conclusion & Outlook.....	125
7.1. General conclusion	126
7.2. Outlook	127
7.2.1. 3D characterization of different types of nanomaterials	127
7.2.2. 3D operando studies	129
7.2.3. Combination of operando studies and atomistic simulations.....	130
References.....	131
List of scientific contributions.....	159
Summary.....	161
Samenvatting.....	165
Acknowledgements	169

List of abbreviations

Acronyms	Descriptions
1D	One-dimensional
2D	Two-dimensional
3D	Three-dimensional
ABF	Annular bright field
ADF	Annular dark field
AR	Aspect ratio
BCC	Body-centered cubic
BF	Bright field
CBED	Convergent beam electron diffraction pattern
CCD	Charge-coupled device
CN	Coordination number
CNN	Convolutional neural network
CPU	Central processor unit
DWF	Debye-Waller factor
EAM	Embedded atom model
EDX	Energy-dispersive X-ray
EELS	Electron energy loss spectrometry
FCC	Face-centered cubic
FWHM	Full width at half maximum
GPU	Graphical processor unit
HAADF	High-angle annular dark field
HCP	Hexagonal close packed
iDPC	Integrated differential phase-contrast
ICL	Integrated classification likelihood
LJ	Lennard-Jones
LSPR	Localized surface plasmon resonance
MC	Monte Carlo
MD	Molecular dynamics
NP	Nanoparticle
NPT	Fixed number of atoms N , fixed pressure P , fixed temperature T
NR	Nanorod
NVT	Fixed number of atoms N , fixed volume V , fixed temperature T
PTM	Polyhedral template matching
RMSD	Root mean square displacement

SCS	Scattering cross section
SIRT	Simultaneous iterative reconstruction technique
SNR	Signal-to-noise ratio
STEM	Scanning transmission electron microscopy
TDS	Thermal diffuse scattering
TEM	Transmission electron microscopy

Units	Descriptions
--------------	---------------------

Å	Angstrom
°C	Celsius
cm	Centimeter
eV	Electronvolt
fs	Femtosecond
g	Gram
kV	Kilovolt
K	Kelvin
m	Meter
µm	Micrometer
mm	Millimeter
mrad	Milliradian
nm	Nanometer
ns	Nanosecond
pA	Picoampere
ps	Picosecond
s	Second

Element symbols	Descriptions
------------------------	---------------------

Ag	Silver
Au	Gold
In	Indium
N	Nitrogen
O	Oxygen
P	Phosphorus
Pt	Platinum
Si	Silicon
Sr	Strontium
Ti	Titanium

Chapter 1. Introduction

This chapter introduces the background and theoretical fundamentals for the research comprising this thesis. The goal of this thesis is to present robust approaches to capture the three-dimensional atomic scale transformations observed in metallic nanoparticles under application-relevant conditions. This chapter starts with a short introduction to nanomaterials and relevance of transmission electron microscopy for their investigation. The chapter continues with the basic principles and different imaging modes of transmission electron microscopy. Next, developments in the three-dimensional characterization of nanomaterials from two-dimensional transmission electron microscopy images are given. Within this purpose, the principles of three-dimensional characterization by electron tomography and quantitative electron microscopy under both static and application-relevant conditions are summarized. Finally, the motivation and outline of this thesis are presented.

1.1. Nanotechnology and nanomaterials

Nanotechnology is a multidisciplinary field that comprises the development, controlling, and use of materials at the nanometer (nm) scale which corresponds to a billionth of a meter (m). Nanomaterials are materials which have at least one dimension smaller than 100 nm. When three dimensions are confined to the nanometer scale, these materials are referred to as nanoparticles (NPs).¹ To get a perspective of the scale of 1 nm, a length scale of the nanomaterials range in comparison to the diameter of a human hair and some daily life objects is presented in Figure 1.1.

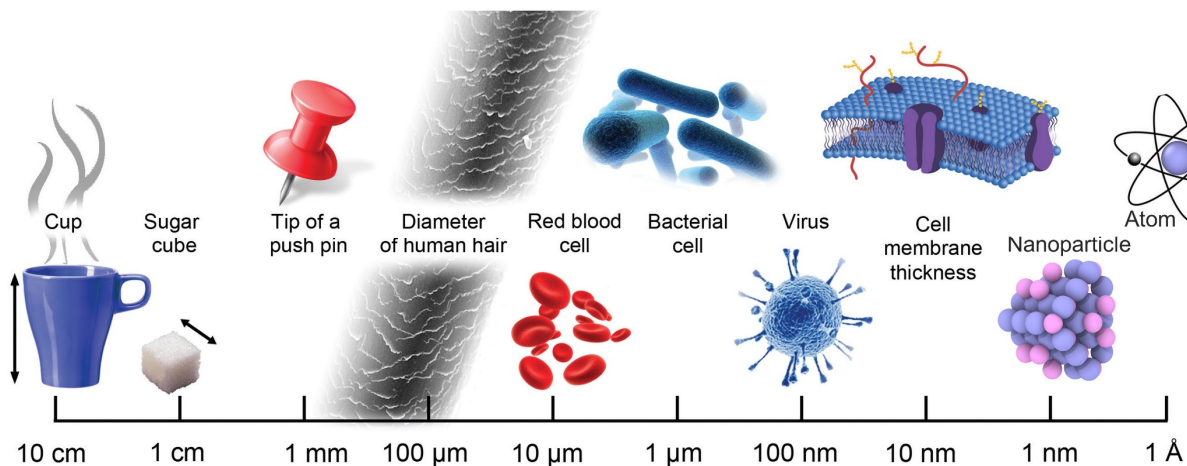


Figure 1.1 Sequence of images showing the various levels of length scale. Adapted from ref².

Nanomaterials are of great interest since they exhibit unique physical and chemical properties that cannot be observed for macroscopic systems. As the size of a material is confined to the nanoscale, the ratio of the surface area compared to its volume, the so-called surface-to-volume ratio, increases. Consequently, surface atoms start to control the properties of these nanomaterials.^{1,3} For example, bulk gold (Au) is considered as an inert material because Au often does not react with chemicals present in the atmosphere, which makes it so valuable. However, Au particles smaller than 5 nm are effective catalysts since their surface atoms present chemically active sites for catalytic reactions.⁴ The large surface-to-volume ratio also plays a key role in the thermal stability and mechanical properties of the nanomaterials.¹ It is important to note these properties are strongly linked to the shapes and sizes of NPs since varying shapes or sizes will produce distinct surface-to-volume ratios. Furthermore, as another example, the size confinement in metal NPs causes strong interaction with light due to localized surface plasmon resonances (LSPRs), which are collective oscillations of conduction electrons. An LSPR leads to efficient light absorption and scattering at specific wavelengths. The sensitivity of LSPRs to the size, shape, or composition of the NPs enables one to achieve unique and tunable optical properties, which cannot be achieved by bulk materials. Moreover, the intensive light absorption may cause heat generation within and around the metal NPs, which is known as the photothermal effect. Converting the absorbed light into heat by the photothermal effect turns the NPs into localized nano-heat sources.^{4,5}

It is interesting to note that the special properties of nanomaterials have been exploited long before one could observe them. One of the famous examples is the Lycurgus cup manufactured by Romans in the 4th century (Figure 1.2).^{4,6} The color of the cup changes in certain lighting conditions. An analysis in 1990⁷ showed that the different colors of the cup stem from the silver (Ag) and Au alloy NPs dispersed in the glass. When the cup is illuminated outside, it appears green (Figure 1.2a) due to the diffusion of light. However, when it is illuminated inside, it shines red-purple (Figure 1.2b) because of the absorption of light by the metal NPs, originating from LSPRs. Using NPs to obtain different colors of glasses is commonly seen in the late medieval church windows, as well. It was also found that a glittering effect on the surface of medieval pots was obtained by the dispersion of alloyed NPs into the decorative glaze during the 9th century in Mesopotamia.^{4,8} In addition to decorative purposes, nanomaterials were also used to improve the mechanical properties of materials in history. For example, Damascus steel swords, manufactured during the 17th century in ancient India, are known for their extraordinary toughness and sharp cutting edges. An electron microscopy study in 2009⁹ surprisingly revealed that the steel blades contain cementite nanowires and carbon nanotubes which certainly enhanced the mechanical properties of the sword. These historical objects were, of course, the results of hundreds of years' empirical optimization by artisans and blacksmiths who would not know the scientific origin of the properties of these nanomaterials.

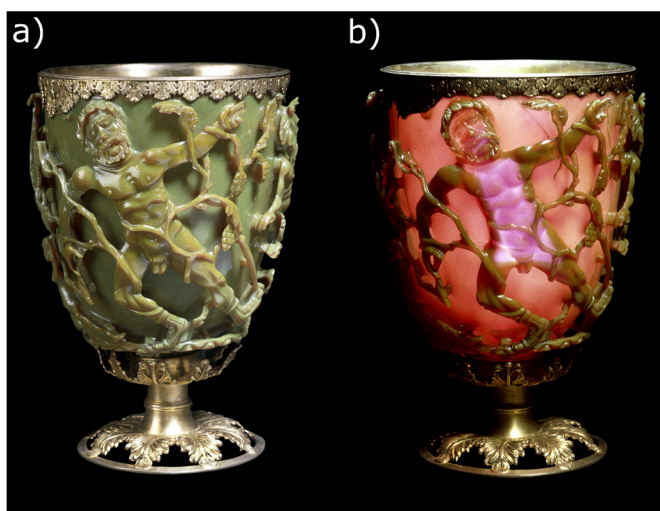


Figure 1.2 The Lycurgus Cup from the 4th century a) illuminated from the outside b) illuminated from the inside. The images are obtained from the free image service of the British museum.

Broad scientific attention to materials at the nanoscale was first drawn by a talk of the Nobel laureate Richard Feynman titled “There’s Plenty of Room at the Bottom” in 1959, where he discussed the possibility of creating new devices and materials by direct manipulation of atoms. Although he did not use the term “nanotechnology” during his speech, Feynman raised the hope to make things smaller, lighter or work better than is possible with conventional materials.¹⁰ The term nanotechnology was first used in 1974 by Norio Taniguchi to refer to the precise and accurate tolerances required for machining and finishing materials.¹ In the following years, various approaches to the synthesis were established, opening the possibility to create peculiar, highly

tunable and controllable structures, which are not possible to obtain using conventional chemical synthesis.^{1,11}

Nowadays, nanomaterials have become a part of our daily life, even though people are not always aware of it. For example, nanoparticles are used in food packaging,¹² scratch-resistant and anti-reflection coatings,¹³ sport goods,¹⁴ and sunscreen.¹⁵ One of the most common applications of nanostructures may correspond to rechargeable batteries which power most of the portable electronics around us, such as wireless headphones, smartphones, laptops, and electronic toys. Due to their large size and weight, conventional batteries were one of the limiting factors against the miniaturization of portable devices. To achieve high-performance and light-weight batteries, the tunable physicochemical properties of nanomaterials have provided great advancements in terms of increasing energy density, cycle life, stability, and minimizing size.^{16–18} Nanotechnology is also expected to play a crucial role in solving many problems that our society is facing, such as reducing the emission of greenhouse gases and finding effective treatments for cancer. Researchers have already demonstrated that nanosensors are able to detect pollutants,^{19,20} the large surface area of a nanocatalyst can speed up the transformation of harmful vapors from cars and industrial plants into harmless gases,^{21–23} and tunable optical properties of quantum dots (confined semiconductors to nanoscale) can enhance the efficiency of renewable solar cells.^{24–26} Furthermore, recent advancements in nanomedicine have shown that the unique photothermal and optical properties of Au NPs are promising to be used in improved, targeted, and even personalized hyperthermia cancer treatment and drug delivery.^{27–29}

It is known that the functional properties of these materials are directly linked to their size, morphology, structure, and composition. If one is able to measure the positions of the atoms, their chemical nature, and the bonding between them, it becomes possible to predict the physicochemical properties of the nanomaterials. In this manner, the development of novel nanostructures can be triggered. For example, recent studies showed that the appearance of crystalline defects, such as twinings or stacking faults, affects the optical properties of Au and Ag NPs.^{30,31} Also, it has been observed that the atomic arrangements at the surface strongly influence the activity of platinum (Pt) NPs for some specific catalytic reactions, such as carbon monoxide oxidation in hydrogen fuel cells.^{32–34} The rational design of nanomaterials with desired functional properties therefore strongly depends on the availability of three-dimensional (3D) structural characterization techniques.

Different characterization techniques to investigate materials at the nanometer scale are available and some of them can even provide 3D structural information. However, scanning probe techniques such as scanning electron microscopy, scanning tunneling microscopy, and atomic force microscopy only provide surface or near-surface information.^{35–37} Classical X-ray or neutron diffraction provides structural information, albeit averaged over an ensemble instead of local. Transmission Electron Microscopy (TEM) is, in comparison to all other characterization techniques, probably the most suitable and versatile tool to extract 3D structural information since it can provide atomically resolved images, which are sensitive to the local 3D structure of the investigated sample. Moreover, radiation damage on the investigated sample is lower in TEM

compared to X-rays.³⁸ This is because electrons in TEM are charged in comparison to X-rays, amplifying the interaction with the atoms of the structure. An additional advantage therefore is that TEM observations are not only sensitive to the atomic structure but also contain information on the atom type and ionization state of the atoms.^{39,40}

1.2. Transmission electron microscopy

Historically, TEM was developed to overcome the limitations of visible light microscopes, which have widespread use for inspecting the microstructure of various organisms and inanimate objects. The main limitation of a visible light microscope is that its resolution is only to the order of 200 nm, which is imposed by the relatively large wavelength of optical light (400-700 nm).⁴¹ This length scale corresponds to thousands of atoms and is not sufficient for studying nanomaterials. To overcome the limitation of visible light microscopes, TEM was first developed by Max Knoll and Ernst Ruska in the 1930s.⁴² The main idea of TEM comes from the wave-particle duality of electrons. The wave-particle duality states that electrons can be described not only as particles but also waves with a wavelength proportional to their momentum. Therefore, the wavelength of electrons in TEM can be manipulated by applying different accelerating voltages, achieving potentially much smaller wavelengths than visible light.⁴³

With the development of TEM, the wavelength was no longer the main limiting factor against the visualization of atomic arrangements in nanomaterials. For example, electrons accelerated by a voltage of 300 kilovolts (kV) yield a wavelength of about 0.02 Angstrom (\AA). However, when Richard Feynman asked “Is there no way to make the electron microscope more powerful?” in his famous 1959 talk, the practically attainable resolution was only about 10 \AA which was inadequate to be able to see matter on the atomic scale. This discrepancy was mainly due to the fact that the optical systems used to manipulate the electrons in a TEM are affected by severe imperfections. Ever since, a lot of effort has been made to increase the image resolution in TEM by reducing the aberrations of the electromagnetic lenses with the introduction of aberration correctors, improving instrument stability and the brightness of the field-emission guns. Today, most of the advanced electron microscopes can achieve a resolution of around 0.5 \AA , which is orders of magnitude better than the state-of-art in 1959. These achievements have allowed TEM to visualize the structure of nanomaterials down to the atomic scale.⁴⁴⁻⁴⁷

Two main modes of operation are commonly used in TEM: conventional TEM (CTEM) and scanning TEM (STEM). Figure 1.3 outlines simplified schemes of CTEM and STEM. In CTEM (Figure 1.3a), electrons are obtained from an electron source, such as a tungsten filament, by heating the material and simultaneously applying a strong electric field. In this manner, the electrons are accelerated to the desired wavelength with the applied voltage typically ranging from 60 to 300 kV. The beam of electrons created in this manner enters the condenser system consisting of a series of electromagnetic lenses, which focus the beam onto the sample. The high energy of the incident electrons enables the electrons to propagate through the specimen and interact with the positive electrostatic potential of the atoms. The complex electron wave function that leaves the specimen is called the “exit wave”.⁴⁸ A set of objective apertures and electromagnetic lenses create

a virtual image of the exit wave, which is further magnified by the projector lenses. Since these lenses are not perfect, the exit wave is distorted by lens aberrations such as spherical aberration, defocus, and chromatic aberration while propagating to the image plane. Finally, electron counts are recorded in the detector plane by a CCD camera.^{43,49} CTEM is a coherent imaging technique. Coherency is a wave property and refers to a phase relationship of different electron beams. The coherent images suffer from a phase problem where contrast reversals may appear depending on the aberrations of the objective lenses, thickness, and orientation of the specimen.^{43,50} Therefore, a direct image interpretation in terms of structural information can be complicated. Moreover, although the exit wave function contains structural information, the phase information is lost upon the detection of the image intensity by a CCD camera. Therefore, for the structural interpretation of the investigated sample, the phase should be reconstructed, for example, using focal series reconstruction, off-axis holography, or using a phase plate.^{51–54}

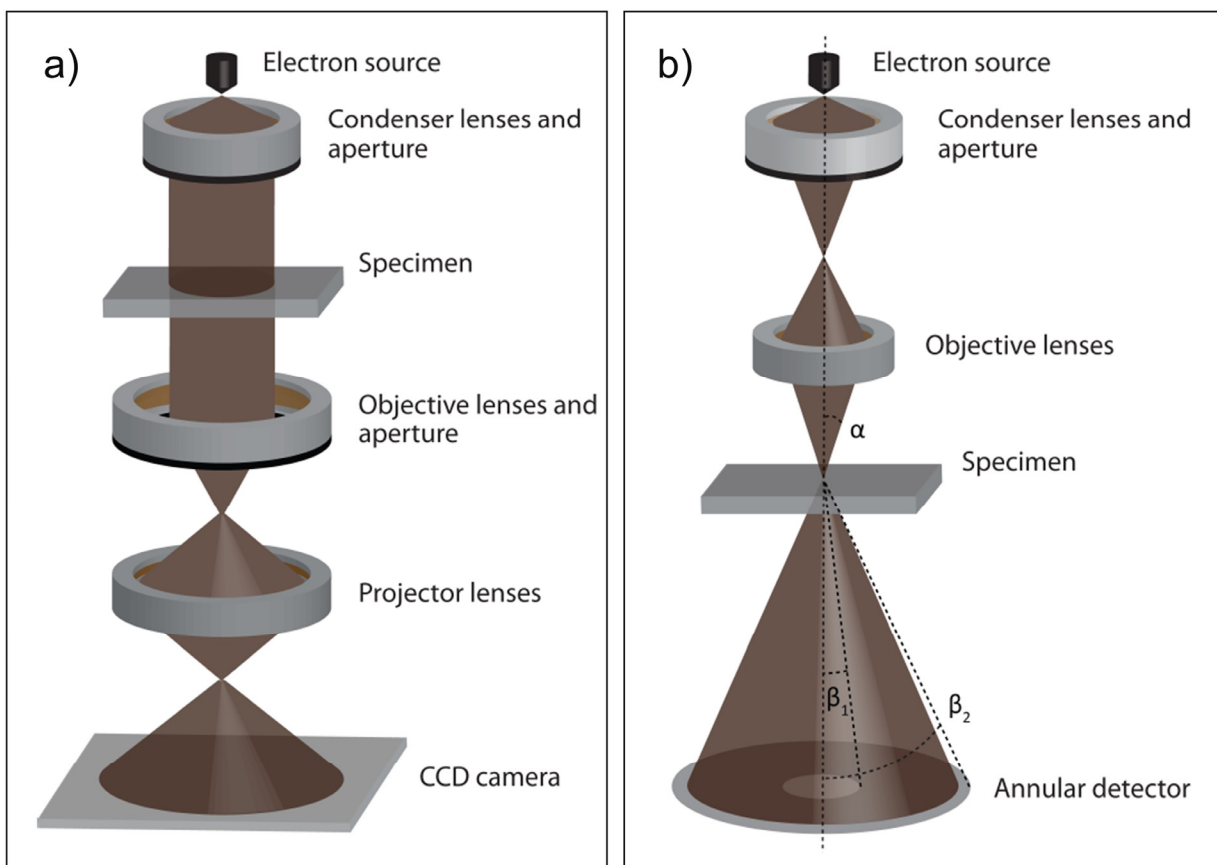


Figure 1.3 Simplified schematic representations of two different operational modes used in TEM: (a) CTEM and (b) STEM. The figure is adapted from ref⁵⁵.

Differently from CTEM, where the electron beam is parallel, in STEM (Figure 1.3b), the electron beam is focused into an atomic scale probe which is used to scan the specimen point-by-point. The spatial resolution of an STEM image is mainly controlled by the size of the illuminating probe: the smaller the probe, the better resolution of STEM images. The lens system before the sample hence aims to provide enough demagnification of the finite-sized electron source.^{50,56–58} Next, for each

probe position, electrons propagate through and interact with the specimen. The scattered electrons from the specimen as a function of probe position are collected on a detector. In STEM, a variety of signals can be recorded by using different detector geometries or collection angle ranges (β_1 and β_2 in Figure 1.3b).

The transmitted electrons that leave the sample at angles smaller than the probe convergence angle ($\beta_1 = 0$ and $\beta_2 \leq \alpha$) form so-called the bright-field (BF) STEM image on a disk-shaped BF detector located in the optical axis (Figure 1.4a). Due to the principle of reciprocity, which states that the electron beam path in an electron microscope remains the same if their direction is reversed, a small BF detector located on the optical axis corresponds to the illuminating source geometry in CTEM. Therefore, a coherent CTEM image is formed with a BF STEM detector.^{50,56,59} It should be noted that although both images are equivalent, the signal-to-noise ratio (SNR) may differ for the same incident electron dose, because, compared to CTEM, a BF detector collects only a very small fraction of all scattered electrons.^{57,60}

Transmitted electrons that are collected by an annular detector lying within a BF disk but without using its central part ($\beta_1 > 0$ and $\beta_2 \leq \alpha$) form an annular BF (ABF) STEM image. As an example, an ABF image of a sample is shown in Figure 1.4b. The recorded image consists of atomic columns with black contrast on a white background.⁶¹ Although ABF STEM images still include coherent details, they suffer from contrast reversals less than CTEM or BF STEM. Hence, these images are more easily interpretable in terms of the structure of the sample.

The coherency of the scattered electrons is related to their scattering angle and as this angle becomes larger, the degree of coherency becomes less apparent. If the inner collection angle β_1 of an annular detector is larger than the probe semi-convergence angle α , an annular dark field (ADF) STEM image is obtained.^{43,62,63} For low-angle ADF (LAADF) STEM, the inner angle of the detector is slightly larger as compared to the probe semi-convergence angle. This setup gives rise to images of bright atomic columns on a dark background (Figure 1.4c). The signal obtained in LAADF STEM imaging mode can be considered as a mixture of coherent and incoherent electron scattering.⁵⁸ When the inner collection angle β_1 of an annular detector is about three times larger than the probe convergence angle α and the outer angle β_2 is several hundred milliradians (mrad), the STEM imaging is often called high-angle ADF (HAADF) STEM (see Figure 1.4d). HAADF STEM is one of the most commonly used STEM imaging modes. Only the electrons scattered to high-angles contribute to the HAADF STEM image contrast and these images provide almost a perfect approximation to incoherent imaging.⁵⁷ Such incoherent imaging is important in three main aspects. First, in contrast to coherent imaging modes, incoherent images have no phase or contrast reversal problem. Second, the primary interaction mechanism between the electron and the specimen is Rutherford scattering for high scattering angles. Since the probability of Rutherford scattering is proportional to the atomic number of nuclei Z^n ($1.6 < n < 2$), these images exhibit elemental sensitivity. Third, total scattered intensity scales with the total number of atoms in the sample. As a result, the incoherent imaging mode is suitable for both qualitative and quantitative structural analysis, as discussed in the following sections.^{43,50,56-58}

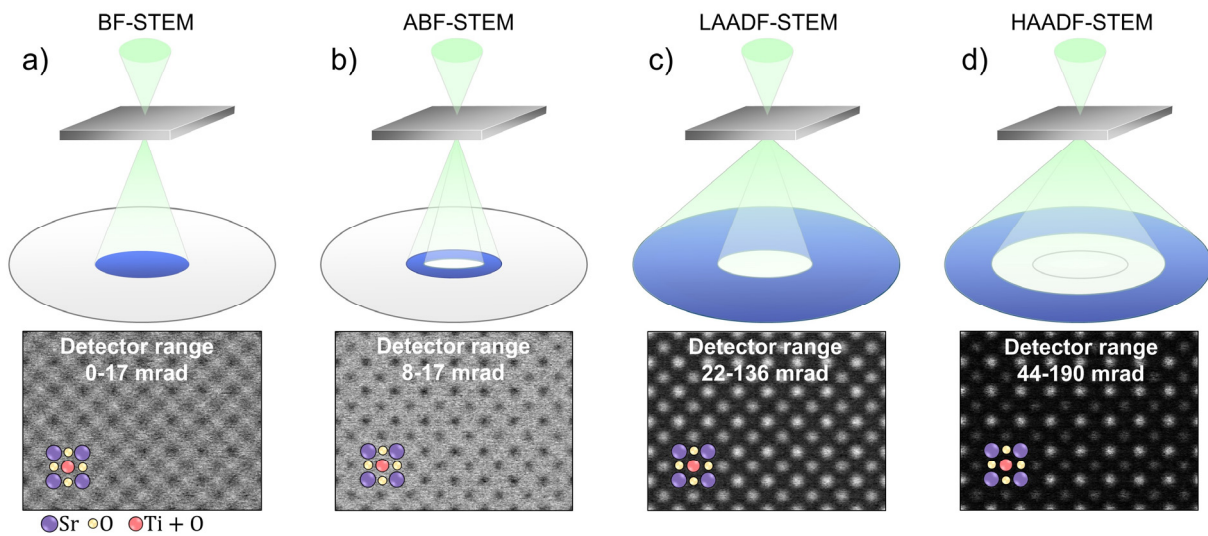


Figure 1.4 Schematic illustration of STEM imaging modes using different angular ranges of an annular detector. In the first row, the green regions represent electron optics, the gray boxes represent the sample, and the blue oval regions represent collection angles of annular STEM detectors. The second row demonstrates simulated STEM images of a SrTiO_3 structure corresponding to each imaging mode. a) BF STEM imaging. b) ABF STEM imaging. c) LAADF STEM imaging. d) HAADF STEM imaging. The simulated STEM images are obtained by using MULTEM software.⁶⁴

Another advantage of STEM imaging is the option to simultaneously acquire STEM and spectral signals, such as energy dispersive X-rays (EDX) and electron energy loss spectrometry (EELS). The high energy of the incident electrons may excite atoms in a specimen, which will emit X-rays when falling back to their ground states. Since the energy of an emitted X-ray is directly related to the electron shell structure of an atom, the recorded signal can be used for chemical mapping.^{65,66} Measurement of EELS is an analysis of the energy distribution of electrons. The electrons which have lost energy through the interaction with the specimen while travelling in it can be dispersed using a magnetic prism. The resulting EELS spectrum can provide numerous information about the chemical and electronic structure of a specimen, including its bonding, valence state, and free-electron density.^{43,67}

The modes of operations used in TEM, CTEM and STEM, differ in the kind of information they can provide about the object of interest and in the required experimental parameters. For example, the main advantage of CTEM is that it avoids the time-consuming scanning process, which reduces acquisition time, scanning image distortions, and possible damage effects induced by the electron beam. On the other hand, in STEM, a wider range of useful signals is available, making this technique indispensable for many studies to interpret quantitative structural information of nanomaterials.

1.3. Electron tomography

TEM is one of the most efficient and versatile tools not only for the structural characterization of nanomaterials down to the atomic scale but also for investigating their chemical and electronic

properties.^{44–47} However, TEM images are only two-dimensional (2D) projections of 3D (nano)-objects. The interpretation of a 3D structure based on only 2D projections may lead to an incomplete understanding. Different techniques to retrieve the 3D atomic structure have been suggested in the field of electron microscopy. The most known and powerful technique for the 3D characterization of nanomaterials is electron tomography.^{68–71}

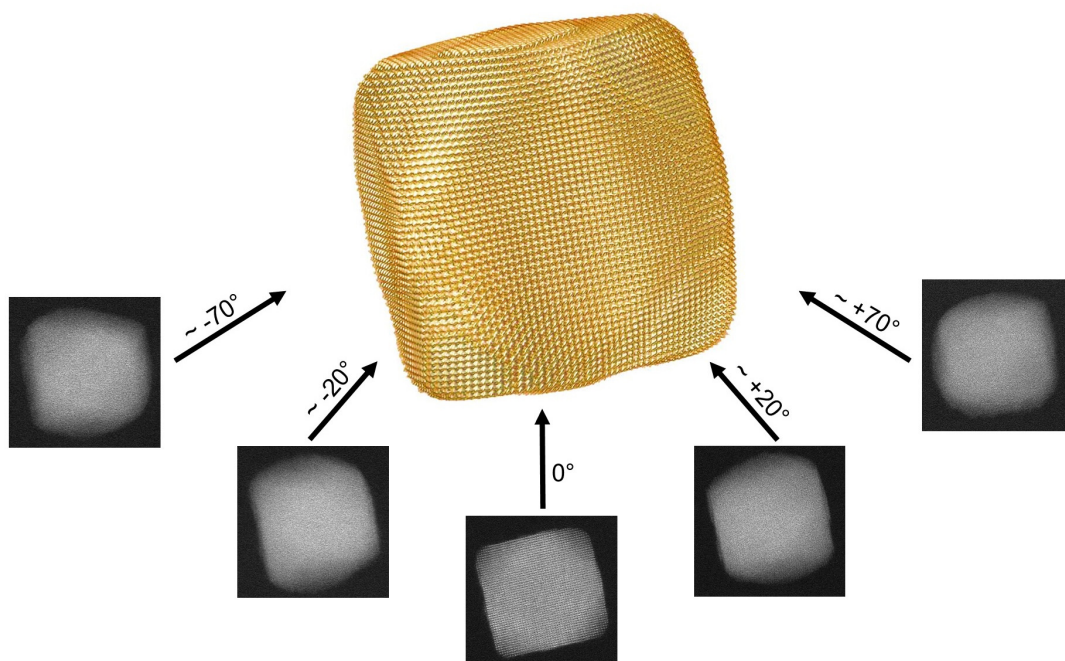


Figure 1.5 Schematic illustration of high resolution electron tomography applied to a Pt NP. A HAADF STEM tilt series was acquired by Prof. Dr. Thomas Altantzis. For the reconstruction of the Pt NP, the recently developed reconstruction algorithm, by Dr. Ivan Lobato at EMAT, was used.

Electron tomography is conceptually similar to X-ray tomography, e.g. in radiology, which is widely used in healthcare for 3D imaging of a human body. In radiography, a patient is illuminated by X-rays at different angles and the rays passing through the patient are collected as 2D projection images by a dedicated detector. From the 2D projection tilt series acquired at different angles, the 3D internal structure of the patient is obtained. In the same manner, electron tomography allows for investigating the 3D structure of NPs (Figure 1.5). Over the years, different electron microscopy techniques such as BF TEM, HAADF STEM, electron holography, EDX, and energy-filtered TEM have been extended to 3D.^{71–75}

Acquisition of tilt series

To perform a 3D reconstruction by electron tomography, a series of 2D projection images of a NP is acquired at different tilt angles. An important requirement, which 2D projection images need to fulfill for a suitable 3D reconstruction, is that the recorded intensities represent a monotonic function of a sum or integral of the property of interest (for example, density or thickness) within the investigated particle. This requirement is known as the “projection requirement”.⁷² Therefore, certain TEM modes are more appropriate than others depending on the nature of the sample to be

investigated and the information to be extracted. For example, in CTEM, the intensities are sensitive to the orientation of the sample with respect to the electron beam. This often violates the monotonic relation between the intensity in the projected images and the thickness of the sample under study.⁷⁶ To fulfill the projection requirement for the 3D reconstruction of crystalline NPs by electron tomography, (HA)ADF STEM is mostly considered as an ideal imaging mode due to the monotonic relation between the recorded signal and the thickness of the sample. EELS and EDX STEM also fulfill the projection requirement since these signals have incoherent nature.⁵⁷

For an optimal reconstruction, the ideal tilt range is $\pm 90^\circ$ with small tilt increments. In contrast to X-ray tomography, where a full tilt range of 360° can be achieved, TEM instruments have restricted physical space between the pole pieces of the objective lens.⁷⁶ By using dedicated sample holders for electron tomography, a typical tilt range of $\pm 75\text{-}80^\circ$ can be achieved with tilt increments between 1° and 3° . The limited tilt range leads to a gap of missing information and will result in artifacts in the final 3D reconstruction which is typically called the “missing wedge”.⁷² The development of a dedicated on-axis tomography holder has enabled researchers to acquire images over a full tilt range of $\pm 90^\circ$ using a needle-shaped sample prepared by focused ion beam milling which avoids missing wedge artifact.⁷⁷ However, the sample preparation to obtain needle-shaped samples is only possible for specific sample types.

Electron tomography reconstruction

Once a tilt series is collected, images are aligned with respect to a common tilt axis by cross-correlation, which is important to eliminate relative shifts in the successive images. The aligned 2D projection images are used as input for a reconstruction algorithm to retrieve the 3D morphology and interior structure of a NP.

There are different reconstruction algorithms to perform a 3D reconstruction, each with different advantages and limitations. One of the most popular reconstruction algorithms for electron tomography is the simultaneous iterative reconstruction technique (SIRT).^{78,79} This approach treats the 3D reconstruction algorithm as an optimization problem. It finds an optimum solution by minimizing the sum of squared differences between the input data and the estimated reconstruction in an iterative way. At each step of the iteration of the SIRT algorithm, a difference between the projections of the currently estimated reconstruction and projection tilt series is found. This difference is then backprojected onto the reconstruction to reduce the mismatch. Backprojection smears out the projected intensities across the 3D volume.⁸⁰ As expected, the quality of the final reconstructed 3D volume depends on the number of iterations applied during the SIRT algorithm. On the other hand, since projection and backprojection operations need to be computed at each iteration, applying SIRT may require large computational power, especially for a sufficiently large number of iterations. Even if computer power is available, increasing the number of iterations does not always improve the reconstruction, especially in the presence of noise in the input data. In this case, the SIRT algorithm may not converge to the optimal solution; instead, a larger number of iterations may result in a lower resolution in the reconstructed volume due to the overfitting of the noise during the iterations.⁸⁰

Recently, Dr. Ivan Lobato at EMAT proposed a new approach where SIRT is combined with an error reduction algorithm.⁸¹ This approach starts with the correction of imperfections, e.g. Poisson noise, scanning distortions or drift, in a tilt series by a convolutional neural network (CNN) and rigid and non-rigid registration.^{82,83} Afterwards, SIRT is applied with constraints in real and Fourier space. This approach allows high-quality 3D reconstruction with diminished artifacts, i.e. missing wedge (Figure 1.5).

Electron tomography is a powerful method to retrieve the 3D atomic structure of NPs. However, there are some technical limitations for a successful 3D reconstruction by electron tomography. The required time to acquire electron tomography tilt series is one of the main limitations of electron tomography. Even under ideal conditions, approximately one or several hours are required to collect a tilt series for a single NP. Therefore, the sample needs to be stable under the illumination of the electron beam. This is challenging when one wants to investigate very small or electron beam-sensitive NPs since reshaping or degradation may occur in NPs during the acquisition of tomography tilt series. Therefore, retrieving the 3D atomic structure information from a few viewing directions or even from a single image is very promising to shorten the acquisition time, to prevent beam damage, and to avoid practical issues concerned with controlled tilting of NPs.

1.4. Quantitative electron microscopy

To retrieve the 3D structure of NPs from limited (S)TEM images, quantitative interpretations of images are essential. For quantitative analysis, a high-resolution (S)TEM image is considered as a data plane where unknown structural information, such as positions of the atoms, thickness and types of atoms, can be extracted with high accuracy and precision.

Quantitative electron microscopy can be performed by comparing the experimental image intensities with image simulations or by using statistical, model-based techniques. When experimental image intensities are directly compared to image simulations, accurate knowledge of microscope parameters, such as detector sensitivity and lens aberrations, are crucial.^{84,85} Furthermore, image intensities from the experimental electron microscopy image should first be put on an absolute scale. In TEM, quantification through comparison with image simulations can be hampered by the Stobbs factor, which is a scaling problem between the simulated and experimental image contrast.⁸⁶ Alternatively to the comparison with image simulations, the exit wave can be used to quantify the atomic structure from TEM images after the phase reconstruction.

For ADF STEM, neither the scaling problem between simulations and experimental images nor the phase problem exists as it is an incoherent imaging technique. Moreover, due to its sensitivity to the thickness and atomic number, high-resolution ADF STEM images provide a robust approach for quantitative structural characterization of nanomaterials from limited data. For this purpose, a model-based method was introduced at EMAT for ADF STEM images.⁸⁷ The starting point is the availability of a parametric model that describes the expectations of the experimental measurements. When the atomic columns are aligned with the incoming electron beam, image intensities in high-resolution ADF STEM images are peaked at projected atomic column positions. These directions are commonly called “zone axis”. The image intensities, viewed along a major

zone axis, can be modelled as a superposition of Gaussian functions. Then, the unknown structure parameters are estimated by fitting this model to the experimental images using a criterion of goodness of fit, quantifying the similarity between the experimental images and the model. It has been shown that unknown structure parameters can be measured with high accuracy and precision from 2D ADF STEM experimental images using statistical parameter estimation theory. This enables one to retrieve local structural information of a NP, e.g. lattice parameter, identify structural changes, characterization of interfaces or strain measurements.^{61,88–90}

In addition to column position measurements, statistical parameter estimation theory can quantify image intensities revealing information about the specimen thickness and composition. Using the empirical model-based approach, the total scattered intensity corresponding to each atomic column, i.e. the so-called “scattering cross section”, can be obtained. The scattering cross sections quantify the total intensity of electrons scattered towards the annular detector from atomic columns and can be estimated by the volume under fitted Gaussian peaks. Alternatively, the scattering cross sections can be obtained by integrating the intensities in Voronoi cells around the atomic column positions.⁹¹ The scattering cross sections can then be used to determine the composition of nanomaterials,^{87,92–94} and to count the number of atoms in each atomic column of monoatomic^{95–98} and mixed columns.^{99,100} As compared to peak intensities, the scattering cross sections are robust to sample mistilt or microscope aberrations, such as defocus, astigmatism or source size broadening. Furthermore, it increases monotonically with respect to thickness, which makes it suitable as a measure for quantification.^{101,102}

The atom counting results for each atomic column of high-resolution ADF STEM images can then be used to build a 3D reconstruction of a NP. Van Aert et al. showed that retrieval of 3D atomic structures of crystalline nanomaterials is possible by discrete tomography, which combines atom counting results obtained from only a few zone axis orientations. As it can be seen from Figure 1.6, a 3D model of a Ag cluster embedded in an aluminum matrix at an atomic level can be obtained by using the output of the atom counting results from two high-resolution images.¹⁰³ Since ADF images are also sensitive to composition, the same approach has been used to characterize the atomic configuration of a core-shell semiconductor nanocrystal.¹⁰⁴ Shortly after, different methodologies were proposed for 3D reconstructions with atomic resolution using a limited number of projection images.^{99,105,106}

Moreover, using atom counting results as an input of atomistic simulations showed that one could describe the 3D structure of a nanomaterial even from a single STEM image. Indeed, by combining statistical parameter estimation theory and *ab initio* calculations, the 3D dynamics of ultrasmall germanium clusters at room temperature and in a vacuum could be followed.¹⁰⁷ Although *ab initio* calculations give sufficiently reliable results, it requires high computational efforts for systems having more than a few tens of atoms. Therefore, for the 3D characterization of larger NPs from (HA)ADF images acquired along a single viewing direction, the atom counting method has been combined with a computationally more efficient atomistic simulation, such as Monte Carlo or molecular dynamics simulations. In this approach, a starting 3D configuration is obtained by positioning the atoms on a perfect crystal grid symmetrically arranged around a central plane. Then,

the potential energy of the starting 3D configuration is minimized by Monte Carlo or molecular dynamics simulations. For example, atom counting results were combined with a Monte Carlo-based approach to retrieve the 3D structure of beam-sensitive lead selenide nanocrystals or to investigate the damage mechanism of Pt NPs under the electron beam.^{108,109} To observe 3D restructuring of Au nanodumbbell after heating to high temperatures, atom counting results were used as an input for molecular dynamics simulations.¹¹⁰

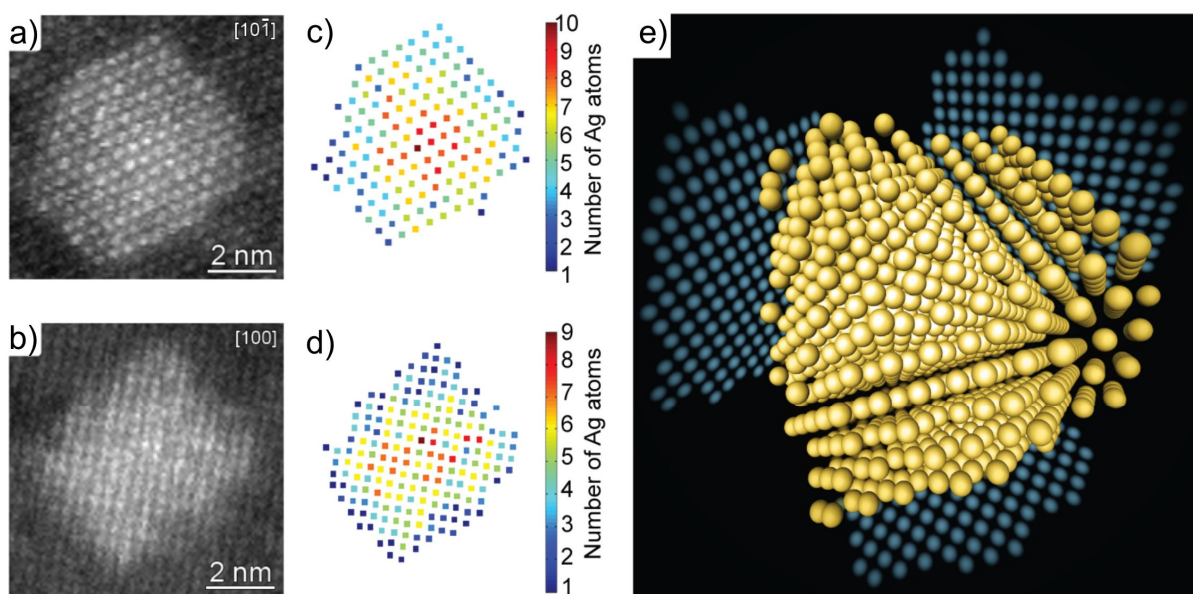


Figure 1.6 HAADF STEM images of an Ag nanocluster embedded in an aluminum matrix in (a) [101] and (b) [100] direction. c, d) Estimated number of Ag atoms per atomic column from the HAADF STEM images of different viewing directions. e) 3D reconstruction of the Ag nanocluster retrieved by combining the counting results shown in (c,d). The figure is adapted from ref¹⁰³.

1.5. 3D structure of nanoparticles under realistic conditions

Most of the conventional (S)TEM measurements are performed under static conditions, at room temperature and in ultrahigh vacuum conditions. However, it is known that the morphology and structure of nanomaterials are highly sensitive to the conditions for relevant applications and any small change in the local structure of nanomaterials at higher temperatures or pressures may significantly modify their performance. Therefore, 3D characterization under static conditions is often inadequate to predict the structure-dependent properties of nanomaterials when being exposed to various environments. Visualizing transformations of the nanomaterials under the conditions for relevant applications, therefore, has crucial importance to design and control their functionalities for a broad range of applications, such as catalysis or plasmonics.⁷⁶ For the characterization of irreversible transformations, a NP can be exposed to such stimuli outside the microscope. The change in structure and morphology of the NP can be measured afterwards by *ex situ* TEM analysis.^{30,76,111–113} This approach is essential when environmental triggers are challenging to introduce inside TEM, such as laser excitation which is required for many applications of metallic NPs, including photocatalysis, drug delivery, biosensing and optical

recording. However, *ex situ* studies cannot provide direct visualization of ongoing transformations. Therefore, to observe dynamics in NPs under working conditions, such as higher temperatures or pressures, *in situ* characterization is indispensable.

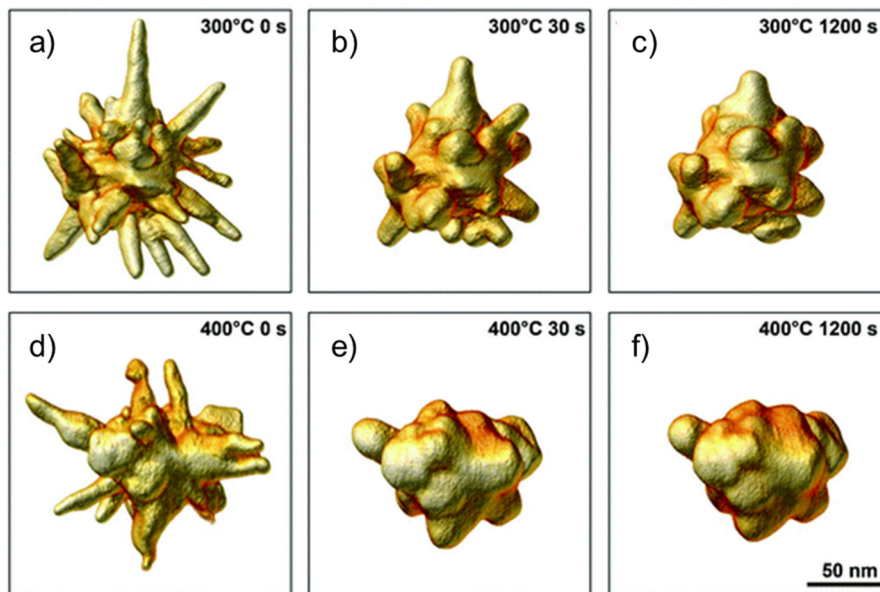


Figure 1.7 3D morphological changes of Au nanostars during heating at 300 and 400 °C. The figure is adapted from ref¹¹⁴.

Essentially two different technologies exist to perform the measurements under the relevant conditions, such as high temperatures or pressures. A so-called “Environmental TEM” (ETEM) is a dedicated TEM in which a differential pumping system separates the increased pressure in the sample area from the high vacuum regions surrounding the sample. Another possibility is the use of dedicated *in situ* holders. Currently, a wide variety of holders is available, ranging from the application of strain and heat to electric biasing.^{115–118} Furthermore, different environments such as liquids and gasses can be created in a TEM using environmental cells. While *in situ* atomic-resolution (S)TEM analysis provides great opportunities to directly observe dynamic changes in nanomaterials with atomic resolution, most of these investigations have been performed by using 2D TEM techniques and extending them to 3D *in situ* TEM is far from straightforward.

As mentioned before, rapid structural or morphological transformations can be observed in electron beam sensitive or small NPs when they are illuminated by the electron beam. Since NPs have higher relative content of the surface atoms than their bulk counterparts, the rapid reshaping events even become more likely in response to application-relevant conditions, such as high temperatures and a gaseous environment. Therefore, it becomes highly challenging to perform 3D *in situ* characterization of a NP by conventional electron tomography because of the long acquisition time required to collect a tilt series. To overcome this limitation, fast HAADF STEM tomography has been recently developed which allows to decrease the acquisition time of tomography series to around 5–6 minutes.^{119,120} It has been shown that by combining fast HAADF STEM tomography with a Micro-ElectroMechanical Systems heating holder (Wildfire, DENSSolutions), which is able

to tilt over a range of $\pm 80^\circ$, enables measuring the 3D transformations in morphology and composition of NPs as a function of temperature.^{119,121} For example, as it is shown in Figure 1.7, reshaping of Au nanostars at high temperatures was captured by the fast electron tomography approach. Although these experiments are already state-of-art, unfortunately, fast tomography is not always applicable. First, the current achievable spatial resolution by fast tomography is limited to the nanometer regime. Second, these experiments can only be carried out in a stop-and-go manner, where heating cycles are interrupted to acquire tomography tilt series. Finally, the tilting range of most gas cell holders does not allow one to perform fast electron tomography experiments based on continuous tilt series.

Therefore, to accurately describe the 3D structure of these materials at the atomic scale and capture the reversible or irreversible transformations under working conditions, it is often needed to estimate 3D models from (HA)ADF STEM images acquired along a single viewing direction. To that end, the combination of the atom counting approach with molecular dynamics simulations has been extended to measure the transformations of the 3D structure of a Pt NP under the flow of a selected gas.⁸¹ As it can be seen from Figure 1.8, reversible morphological changes and surface restructuring of a Pt NP could be investigated quantitatively by using (HA)ADF images acquired from a single viewing direction. These results indicate the great potential of the technique for the studies where tilting of the holder to large angles is impossible. Since the data acquisition is much faster in comparison to electron tomography, this approach enables one to capture dynamical changes in the 3D structure of nanomaterials during *in situ* experiments providing critical information to understand their structure-property relationship.

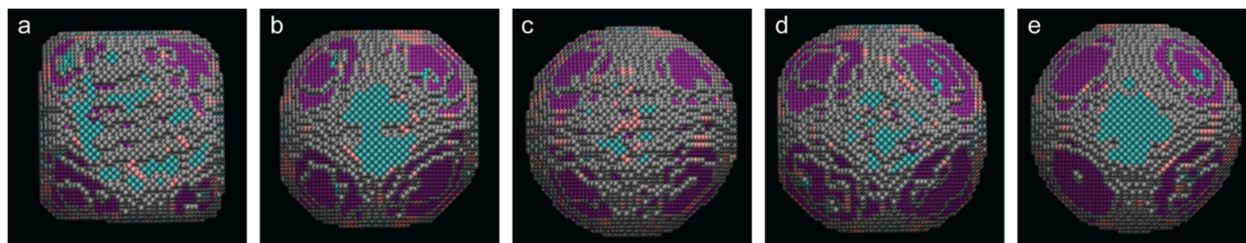


Figure 1.8 3D structure of a Pt NP in vacuum (a) and in repeating different gaseous environments at 300 °C: (b, d) in 5% H₂ in Ar; (c, e) in O₂. The atoms are colored, according to the type of facet: blue = {100}, pink = {110}, purple = {111}, gray = higher index. Reprinted from ref⁸¹.

1.6. Thesis motivation and outline

Nanotechnology has shaped our society tremendously over the past few decades with usages in our everyday lives, ranging from the food industry to medicine. The developments in nanotechnology are furthermore expected to play a crucial role in solving many problems that our society is facing, such as reducing the emission of greenhouse gases and finding effective cancer treatments. For further developments in nanotechnology and improvements of the existing nanotechnology, it is of utmost importance to understand and control the properties of the underlying nanomaterials.

Among the variety of promising nanomaterials, metal NPs are of great interest in many applications, such as (bio)sensing, (photo)catalysis, optical data storage and hypothermic cancer treatment, since these particles exhibit superior catalytic, optical and photothermal properties, which cannot be observed in macroscopic systems. The unique physical and chemical properties of the metallic NPs are linked to their positions of the atoms and even small changes in the local structure of a given nanostructure may significantly affect its performance for a specific application. However, due to the high surface-to-volume ratio, atom positions can dynamically change in nanostructures in response to changes in their environment, possibly leading to morphological and compositional modifications. Such environmental changes can be elevated temperatures, or intense light illumination, which are likely to occur in actual applications. Therefore, in order to gain control over the structure-dependent properties and performance of metal NPs, an atomic-scale understanding of the structure and possible reshaping under realistic conditions is of crucial importance. Unravelling such environmentally-induced atomic rearrangements is not straightforward. Even with state-of-the-art high-resolution TEM, novel workflows and analysis concepts are needed to accurately interpret measurements performed in realistic environments. This thesis aims to present robust approaches to do so by linking the experimental observations and theoretical calculations to capture the 3D atomic-scale transformations observed in metallic NPs when they are exposed to application-relevant conditions.

In the first part of my thesis, I focus on the 3D atomically resolved structural characterization of metallic NPs lying on an oxide support at high temperatures. Oxides are common supports during catalytic reactions and it is hence important to understand the behavior of the complete oxide-metal NP system during catalytic reactions at elevated temperatures. Although *in situ* (S)TEM experiments provide useful information to analyze NP changes down to the atomic scale under elevated temperatures, these investigations are often performed by using 2D (S)TEM techniques. However, for complex nanostructures, the analysis needs to be extended to 3D, which is far from straightforward. HAADF-STEM tomography has been developed to overcome the limitations and extend the investigation to 3D, but the long acquisition time required to collect a tilt series limits this technique when one wants to observe 3D dynamic changes with atomic resolution. Therefore, the ability to capture 3D atomic information from single projection images, which can be taken at much faster speeds compared to electron tomography, is crucial to investigate *in situ* structural transformations.

For this purpose, ADF STEM imaging mode provides a valuable tool for quantitative structural investigation of nanomaterials from single 2D images due to its thickness and mass sensitivity. For quantitative analysis, an ADF STEM image is considered as a 2D array of pixels where the relative variation of pixel intensity values is proportional to the total number of atoms. By applying advanced statistical approaches to these images, the number of atoms can be retrieved, i.e. so-called atom counting, with high accuracy and precision. The outcome can then be used to build a 3D starting model for energy minimization by atomistic simulations. The concepts of quantitative 3D characterization based on 2D ADF STEM images are introduced in Chapter 2. For this purpose, the main principles of ADF STEM image formation, image simulations, statistical parameter estimation theory and atomistic simulations are explained.

Prior to the research presented in this thesis, the approach for the 3D characterization of NPs from single ADF STEM images was only applied to symmetrical particles along the electron beam direction in the electron microscope by ignoring particle-support interaction. However, this approach cannot be directly applied to the case of the oxide-supported metal NPs at elevated temperatures. The reason is that increased thermal displacements of atoms and particle-support interactions should also be taken into account as they influence the morphology of the particle. Moreover, it is expected that supported metallic nanoparticles at elevated temperatures may significantly deviate from their ground state configuration, which is difficult to determine using purely computational energy minimization approaches. Therefore, in this part (Chapter 3 and Chapter 4), I optimize several critical steps in the methodology and propose a refined approach to accurately measure the positions of atoms in supported NPs from ADF STEM images acquired along a single zone axis orientation during *in situ* heating experiments.

In Chapter 3, I focus on the post-processing of the STEM images and the combined simulation and statistics-based atom counting approach for reliable quantification of 2D ADF STEM images acquired during *in situ* heating experiments. By combining the atom counting results with molecular dynamics structural relaxation by including particle-support interaction, I investigate the shape and surface facets evolution of supported Au NPs as a function of time, temperature, and size.

In Chapter 4, a novel methodology is presented to overcome the limitations of energy minimization approaches for the 3D reconstruction of a given particle based on atom counting results. For this purpose, atom counting is combined with a local minima search algorithm by taking the particle-support interaction and temperature into account. Validation is performed on both simulated and experimental Au NPs. Moreover, to test its performance, the outcome of the proposed approach is compared with to the previously used methods in literature.

Despite the progress in the field of *in situ* STEM, atomic-scale transformations cannot be captured by experimental techniques alone. This is for example the case when *in situ* STEM experiments do not provide the necessary time or spatial resolution or when the specific environmental trigger cannot be applied *in situ* in the electron microscope. In the second part of the thesis, corresponding to Chapter 5 and Chapter 6, I show that this limitation can be overcome by combining atomistic simulations with experimental techniques. I demonstrate that, in this manner, it becomes possible to extract missing atomic-scale dynamics of NPs in response to environmental stimuli. Such understanding is expected to contribute toward controlling the desired structure-dependent functional properties of metallic NPs for many applications, including biomedicine, sensing, data storage, and catalysis.

In Chapter 5, I investigate the thermal stability of Au@Pt bimetallic NPs, which is observed by *in situ* electron tomography experiments. Since these experiments are carried out in a stop-and-go manner, to monitor the ongoing transformations during the heating of Au@Pt NPs, experimentally determined 3D reconstructions are used as realistic input models in molecular dynamics simulations. In this manner, the influence of the detailed morphology of the Pt-shell on the thermal stability of Au@Pt NPs is investigated.

Next to *in situ* processes, in Chapter 6, the atomic scale structural transformations of a mesoporous silica-coated Au NP upon femtosecond-laser excitation are investigated. Due to the ultrafast time scales of pulsed laser excitation, these transformations cannot be monitored by *in situ* electron tomography experiments. Therefore, tomography tilt series of a mesoporous silica-coated Au NP are acquired before and after femtosecond laser excitation (*ex situ*). To mimic the laser experiments in molecular dynamics simulations, the heating regime of a femtosecond laser pulse is modelled considering the shape-dependent absorbed laser pulse energy and heat resistance at the surface due to the possible presence of a coating or surrounding medium. Using the measured 3D atomic structure of a mesoporous silica-coated Au NR resulting from *ex situ* electron tomography in molecular dynamics simulations, the complex atomistic rearrangements, causing shape deformations and defect generation, are unraveled.

At the end of this thesis, in Chapter 7, a general conclusion is drawn and future perspectives are discussed.

Chapter 2. Quantitative 3D characterization from 2D STEM images

The aberration-corrected STEM is capable of reaching atomic resolution. However, a solely qualitative interpretation of 2D electron microscopy images does not completely represent the 3D structure of nanomaterials. It has been shown that the combination of statistical parameter estimation theory and atomistic simulations can be used for the 3D atomic scale characterization of NPs from 2D STEM images when electron tomography experiments are not applicable. In this chapter, the concepts of quantitative 3D characterization based on 2D ADF STEM images are introduced.

In the first section of this chapter, the physics behind image formation in STEM is briefly explained from a theoretical point of view. Also, image simulations are addressed. The aim of this section is not to cover the full theory of image formation but rather to introduce the main concepts that are addressed throughout the thesis. Herein I specifically focus on the ADF STEM imaging mode, which is a valuable tool to extract quantitative structural and chemical information of a nanomaterial. In the second section, the basic principles of statistical parameter estimation theory for ADF STEM images are explained. Also, the main steps of counting the number of atoms from ADF STEM projection images of crystalline structures are demonstrated for a simulated system. In the last section, the basic principles of atomistic simulations, such as the Monte Carlo approach and molecular dynamics simulations, are given. Moreover, the main steps to retrieve the 3D model of a NP from atom counting results are shown.

2.1. Physics of image formation in ADF STEM

In STEM, a set of electromagnetic lenses focuses the electron beam to form a small spot, or probe, onto a specimen that is scanned across the specimen surface (Figure 2.1a). The electrons scattered to high angles with respect to the optical axis, larger than the incident beam semi-convergence angle α , are recorded as a function of the probe position and form ADF STEM image.^{57,58} This section starts with the STEM electron-probe formation which is followed by a quantum mechanical description of the interaction between the incident electron wave and the specimen. Due to the beam energies in electron microscopy, typically 60-300 kV, the electrons behave in a relativistic way. Although a full relativistic treatment of electron optics¹²² is far from straightforward to work with, studies^{123–126} showed that the non-relativistic Schrödinger equation with the relativistically corrected electron mass and wavelength provides an accurate description for the electron-specimen interaction in the typical energy ranges used in the electron microscope.^{122,127–129} Next, the multislice method, one of the most popular and accurate solutions for the Schrödinger equation, is described. Finally, the integration of the intensity over the ADF STEM detector is explained.

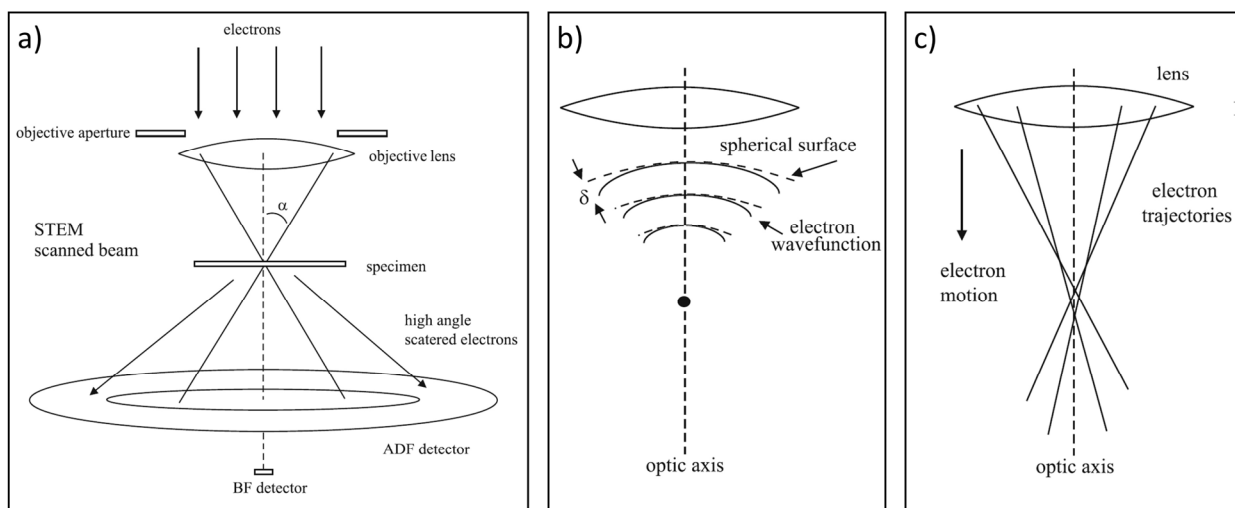


Figure 2.1 a) Simplified model of a STEM. The effect of spherical aberration on the incident electron wave function (b) and electron trajectories (c). The figure is adapted with permission from ref¹²³. Copyright 2022 Springer Nature.

2.1.1. Electron-probe formation

The lenses in the STEM optical system aim to provide enough demagnification of the electron source to form the smallest and most intense probe possible onto a specimen hence improving the resolution of STEM images. Ideally, a lens forms a spherical wave converging to a single point, as shown in Figure 2.1a. However, the aberrations of electromagnetic lenses cause a deviation in the electron wave function from an ideal spherical incoming wave (Figure 2.1b).^{57,58,123} Hence, the aberration wave function should be determined to measure the wave function of the focused probe.

50,130

For electromagnetic lenses, the most prominent type of aberration is spherical aberration. Since the magnetic field is stronger for the electrons away from the optic axis, off-axis electrons deflect more strongly than what is required to focus them.¹²³ As a result, spherical aberration causes a phase error (δ in Figure 2.1b) in the electron wave function and a deviation in the electron trajectory (Figure 2.1c).¹²³ Depending on the order of the geometric aberration, spherical aberration can be defined as the third-order spherical aberration ($C_{3,0}$) or the fifth-order spherical aberration ($C_{5,0}$) where the phase error is proportional to the fourth or sixth power of the convergence semi-angle α .¹²³

Defocusing the lens $C_{1,0}$ also causes a deviation of the electron trajectory and phase error in the electron wave function, which is proportional to the second power of the convergence semi-angle α . Scherzer¹³¹ found that the spherical aberration can be partially compensated by an optimum defocus value, the so-called ‘‘Scherzer defocus’’. The Scherzer defocus value is calculated as a function of the relativistic wavelength λ of the incident electron beam and the third-order spherical aberration $C_{3,0}$ of the magnetic lenses:^{123,131}

$$C_{1,0} = -\sqrt{1.5\lambda C_{3,0}} \quad . \quad (2.1)$$

Considering aberrations up to the fifth order $C_{5,0}$, the aberration wave function can be written as:^{123,124}

$$\chi(\alpha) = \frac{2\pi}{\lambda} \delta = \frac{2\pi}{\lambda} \left(\frac{1}{2} C_{1,0} \alpha^2 + \frac{1}{4} C_{3,0} \alpha^4 + \frac{1}{6} C_{5,0} \alpha^6 \right) \quad . \quad (2.2)$$

Since the convergence semi-angle α is related to the spatial frequency in the Fourier transform of the image plane (k), the aberration wave function $\chi(\alpha)$ can also be expressed as a function of k :

$$\chi(k) = \frac{2\pi}{\lambda} \left(\frac{1}{2} C_{1,0} \lambda^2 k^2 + \frac{1}{4} C_{3,0} \lambda^4 k^4 + \frac{1}{6} C_{5,0} \lambda^6 k^6 \right) \quad . \quad (2.3)$$

The third-order spherical aberration $C_{3,0}$ mainly limits the resolution of the non-corrected electron microscopes.¹²³ In aberration-corrected instruments, the fifth-order spherical aberration $C_{5,0}$ becomes important since the third-order spherical aberration $C_{3,0}$ can be controlled and reduced to near zero by coupling non-rotationally symmetric multipole lenses which produce negative spherical aberration to balance the positive spherical aberration of rotationally symmetric round lenses.¹²⁴ It should be noted that the other aberrations, such as astigmatism or coma can be included in Equation 2.2 and Equation 2.3.^{87,132}

To limit the influence of aberrations, an objective aperture (Figure 2.1a) is used, allowing the beams to pass up to the maximum aperture angle and eliminating the remaining off-axis electron waves. As a result, the aberrated electron probe wave function on the plane of the specimen is calculated by an integration over the objective aperture:^{57,123}

$$\psi_0(\mathbf{x}, \mathbf{x}_p) = A_p \int_0^{k_{max}} \exp[-i\chi(\mathbf{k}) - 2i\pi\mathbf{k} \cdot (\mathbf{x} - \mathbf{x}_p)] d^2\mathbf{k} \quad , \quad (2.4)$$

where $\mathbf{x} = (x, y)$ is the 2D Cartesian coordinates, $\mathbf{x}_p = (x_p, y_p)$ is the electron probe position and \mathbf{k} is a 2D wave vector in the spatial frequency domain. The maximum spatial frequency k_{max} is obtained by dividing the maximum angle in the objective aperture α_{max} by the electron wavelength λ , and A_p is a normalization constant chosen to yield: ¹²³

$$\int |\psi_0(\mathbf{x}, \mathbf{x}_p)|^2 d^2x = 1 \quad . \quad (2.5)$$

2.1.2. Electron-specimen interaction

As the electron probe ψ_0 passes through the specimen, the electron wave interacts with the electrostatic potential of the specimen. For high-angle scattering, the electrostatic potential of the specimen is commonly computed by linear superposition of the electrostatic potentials of nuclei in the specimen. ^{64,123,133} Since the electrons travel fast and the electron-specimen interaction occurs in an extremely short time, the electron-specimen interaction can be described by the time-independent Schrödinger equation. The time-independent Schrödinger equation for the full wave function $\psi_f(x, y, z)$ as a function of spatial coordinates (x, y, z) , where z -axis corresponds to the direction of electron beam propagation, in the electrostatic potential $V(x, y, z)$ of the specimen is: ¹²³

$$-\frac{\hbar^2}{2m} \Delta \psi_f(x, y, z) - eV(x, y, z) \psi_f(x, y, z) = E \psi_f(x, y, z) \quad , \quad (2.6)$$

where $\hbar = h/2\pi$ is Planck's constant h divided by 2π , m is the relativistic mass of an electron, $e = |e|$ denotes the magnitude of the charge of the electron, E represents the total kinetic energy of the electron, and Δ represents the 3D Laplacian operator:

$$\Delta = \left[\frac{\partial^2}{\partial x^2} + \frac{\partial^2}{\partial y^2} + \frac{\partial^2}{\partial z^2} \right] \quad . \quad (2.7)$$

For high-angle scattering, only elastic processes are considered, so the total kinetic energy E remains constant: ¹²³

$$E = \frac{h^2}{2m\lambda^2} \quad . \quad (2.8)$$

In electron microscopes, operated with typical acceleration voltages of 60-300 kV, the energy of the incident electrons is large compared to the additional energy that the electrons gain and/or lose inside the specimen. Therefore, the specimen causes a relatively minor perturbation on the motion of electrons and the electrons propagate predominantly in the forward z -direction, parallel to the optical axis. This means that the full wave function $\psi_f(x, y, z)$ can be represented as a modulated plane wave: ¹²³

$$\psi_f(x, y, z) = \psi(x, y, z) \exp\left(\frac{2\pi iz}{\lambda}\right) . \quad (2.9)$$

Hereby, the full wave function $\psi_f(x, y, z)$ has been written as a product of plane wave travelling in the z -direction and the portion of the wave function $\psi(x, y, z)$ that varies slowly with position z . Since the portion of the wave function $\psi(x, y, z)$ changes slowly in the z -direction, it is reasonable to ignore its second derivative with respect to the z -axis. This approximation is known as the paraxial approximation of the Schrödinger equation.¹²³ Consequently, the Schrödinger equation for fast electrons travelling along the z -direction can be written as a first order differential equation:^{64,123}

$$\frac{\partial \psi(x, y, z)}{\partial z} = \left[\frac{i\lambda}{4\pi} \Delta_{xy} + i\sigma V(x, y, z) \right] \psi(x, y, z) , \quad (2.10)$$

where Δ_{xy} represents the 2D Laplacian operator, and $\sigma = \frac{2\pi me\lambda}{h^2}$ is the parameter that describes interaction between the specimen and incident electrons. To determine the electron wave function after the interaction with the specimen, the differential Equation 2.10 needs to be solved. Different methods under certain approximations have been proposed in the literature.^{58,62,123} One of the solutions for this equation is provided by the multislice method.^{64,123,134–138}

2.1.3. Multislice simulations

The multislice method is one of the most suitable and efficient approaches to solve the non-relativistic Schrödinger equation given by Equation 2.10. For this method, the 3D specimen potential is divided into many slices along the electron beam propagation direction. The slices should be thin enough to be considered as a weak phase object which modifies only the phase of the incident wave. The electron beam alternately transmits through a slice and propagates to the next slice. In each slice, a transmission function is calculated and multiplied with the electron wave function. These succeeding steps continue until the electron wave function reaches the exit plane of the specimen.^{123,134}

In the multislice method, the wave function after interaction with a thin slice of the specimen between z and $z + dz$ can be written as:^{123,124}

$$\psi(x, y, z + dz) = \exp\left[\int_z^{z+dz} \left(\frac{i\lambda}{4\pi} \Delta_{xy} + i\sigma V(x, y, z') \right) dz' \right] \psi(x, y, z) , \quad (2.11)$$

where dz denotes the slice thickness. Equation 2.11 can be simplified by making use of a Taylor expansion and factorization:^{56,123,124}

$$\psi(x, y, z + dz) = \exp\left(\frac{i\lambda dz}{4\pi} \Delta_{xy}\right) t(x, y, z) \psi(x, y, z) + \mathcal{Q}(dz^2) . \quad (2.12)$$

Hereby, $\mathcal{Q}(dz^2)$ denotes the higher-order terms in Taylor expansion and $t(x, y, z)$ is the specimen transmission function which is equal to the phase change of the electron wave while passing

through the specimen between z and $z + dz$:

$$t(x, y, z) = \exp[i\sigma v_z(x, y, z)] \quad , \quad (2.13)$$

where $v_z(x, y, z)$ represents the projected potential of the specimen between z and $z + dz$:⁶⁴

$$v_z(x, y, z) = \int_z^{z+dz} V(x, y, z') dz' \quad . \quad (2.14)$$

For an easier interpretation of the first exponential term in Equation 2.12, a 2D Fourier transform (FT) can be performed:^{123,124}

$$\begin{aligned} FT \left[\exp \left(\frac{i\lambda dz}{4\pi} \Delta_{xy} \right) \right] FT[t(x, y, z) \psi(x, y, z)] \\ = P(k_x, k_y, dz) FT[t(x, y, z) \psi(x, y, z)] \end{aligned} \quad (2.15)$$

with

$$P(k_x, k_y, dz) = \exp[-i\pi\lambda dz(k_x^2 + k_y^2)] \quad . \quad (2.16)$$

Hereby, $P(k_x, k_y, dz)$ is the propagator function for a distance dz . Since a multiplication in Fourier space converts to a convolution in real space, the electron wave function after the interaction with a slice of thickness dz becomes:^{123,139}

$$\psi(x, y, z + dz) = p(x, y, dz) \otimes [t(x, y, z)\psi(x, y, z)] + \mathcal{Q}(dz^2) \quad , \quad (2.17)$$

where, $p(x, y, dz)$ is the propagator function in real space and \otimes represents a 2D convolution (in x and y). When the slices have the same small thickness of dz , a compact form of the wave function after interaction with a slice can be written as:⁵⁶

$$\psi_{n+1}(\mathbf{x}) = p_n(\mathbf{x}, dz) \otimes [t_n(\mathbf{x})\psi_n(\mathbf{x})] + \mathcal{Q}(dz^2) \quad . \quad (2.18)$$

Hereby, $\mathbf{x} = (x, y)$ is the 2D Cartesian coordinates and subscript n represents the slice number at a depth of $z = ndz$. An overview of the multislice simulation is illustrated in Figure 2.2. For a given probe position $\mathbf{x}_p = (x_p, y_p)$, the initial wave function is the incident probe wave function $\psi_0(\mathbf{x}, \mathbf{x}_p)$. The propagator and transmission functions for each slice are labeled as $p_n(\mathbf{x}, dz)$ and $t_n(\mathbf{x})$, respectively. The electron wave function exits from the specimen for a given probe position is denoted by $\psi_e(\mathbf{x}, \mathbf{x}_p)$.

In standard multislice simulations, the specimen is treated as being static and rigid, with the atoms located at their ideal positions. However, in realistic systems, atoms are in constant vibration due to thermal excitation. The thermal vibrations become pronounced especially at higher temperatures, e.g., during *in situ* heating experiments. These atomic vibrations produce a low-intensity, diffuse background, which is called thermal diffuse scattering (TDS).^{58,123,140,141} For high-angle scattering in ADF STEM imaging mode, the TDS signals play an important role. Based

on a rigorous quantum mechanical phonon excitation theory, it has been demonstrated that the frozen phonon model can be considered as the most accurate approximation to include TDS in the multislice simulations.^{64,142–145}

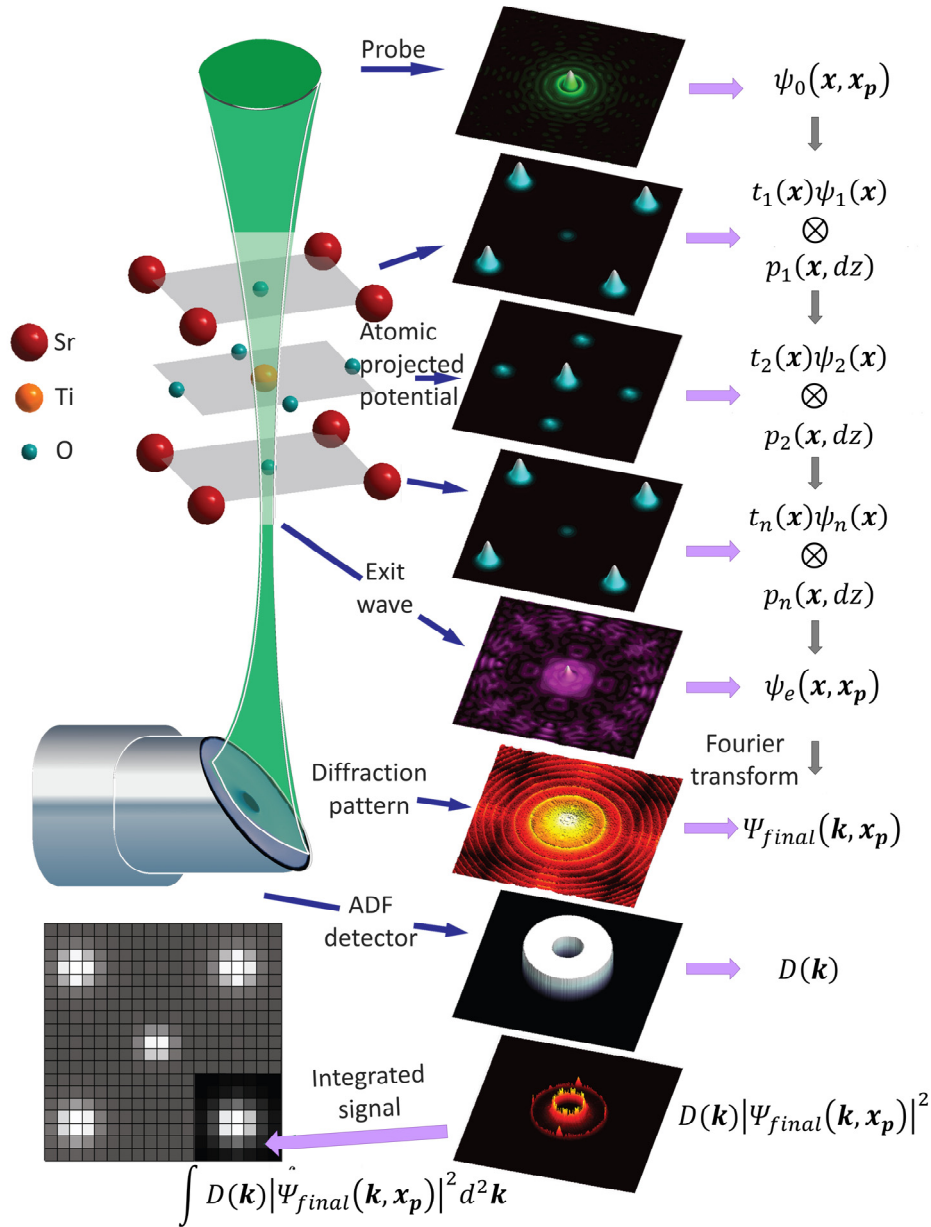


Figure 2.2 Schematic overview of an ADF STEM image simulation for a SrTiO₃ unit cell by multislice method. The figure is adapted from ref¹⁴⁶.

The frozen phonon model is based on the idea that the interaction time between the incident electrons and the specimen is much shorter than the vibration period of an atom. In addition, the current in the microscope is small enough such that the time between two successive incident electrons passing through the specimen is long compared to the oscillation period of the thermal vibration of phonons in the specimen. Therefore, each electron “sees” a different snapshot of the specimen where atoms are frozen at their displaced positions. The resulting image intensity is

calculated by averaging the intensities obtained from different configurations where each atom is displaced according to a root mean square displacement (RMSD) value. The RMSDs of atoms can be calculated by molecular dynamics, the approximated Einstein model, or by using Debye-Waller Factor (DWF).^{141,147–149} In this thesis, RMSDs of atoms are obtained using Equation 2.19 based on the parameterized DWF (Equation 2.20) measured from phonon densities of states.^{150,151}

$$RMSD = \sqrt{\frac{DWF}{8\pi^2}} \quad (2.19)$$

$$DWF = a_0 + a_1T + a_2T^2 + a_3T^3 + a_4T^4 \quad (2.20)$$

Hereby, the constants a_0 , a_1 , a_2 , and a_4 are taken from the study of Cao et al.¹⁵⁰

2.1.4. Intensity integration over the detector

After the interaction with the specimen, the resulting electron exit wave function $\psi_e(\mathbf{x}, \mathbf{x}_p)$ propagates towards the ADF detector. Commercially available ADF STEM detectors consist of a scintillator. Electrons hitting the scintillator are converted into a photon cascade and the output is digitized by an analog to digital converter providing the varying contrast in the final image.^{152,153} Since the ADF STEM detector is placed in the diffraction plane, the final wave function can be represented by a Fourier transform of the exit wave function:^{123,154}

$$\Psi_{final}(\mathbf{k}, \mathbf{x}_p) = FT[\psi_e(\mathbf{x}, \mathbf{x}_p)] \quad (2.21)$$

The intensity of the final wave function $|\Psi_{final}(\mathbf{k}, \mathbf{x}_p)|^2$ versus scattering angle $\lambda\mathbf{k}$ is the convergent-beam electron diffraction (CBED) pattern.¹²⁴ To calculate the ADF STEM intensity $I(\mathbf{x}_p)$ of a given probe position $\mathbf{x}_p = (x_p, y_p)$, the CBED pattern is incoherently integrated over annular STEM detector:

$$I(\mathbf{x}_p) = \int D(k) |\Psi_{final}(\mathbf{k}, \mathbf{x}_p)|^2 d\mathbf{k} \quad (2.22)$$

where $D(\mathbf{k})$ is the detector function:

$$D(\mathbf{k}) = \begin{cases} 1, & k_{D_{min}} \leq |\mathbf{k}| \leq k_{D_{max}} \\ 0, & otherwise \end{cases} \quad (2.23)$$

Hereby, $\lambda k_{D_{min}}$ and $\lambda k_{D_{max}}$ are the inner and outer radii of the ADF STEM detector.¹²³

The calculated intensity for each probe position forms a pixel in the final 2D ADF STEM image, as shown in Figure 2.2. Each pixel intensity in an ADF STEM image is related to the amount of scattered electrons that reach the detector. Depending on the probability of the scattering event taking place, the image shows bright or dark pixels.

It should be noted that the detector function in Equation 2.23, assumes a perfect circular annular

detector with homogeneous sensitivity to all the scattered electrons. In real experiments, on the other hand, the experimental detector exhibits a non-uniform sensitivity which implies that the scattered electrons are amplified differently depending on the area of the detector that they reach. To reproduce the experimental observations accurately by multislice simulations, the non-uniform sensitivity of an ADF STEM detector needs to be taken into account.^{155,156} Including experimentally determined detector characteristics into the multislice simulations is explained in Section 3.2.

So far, the electron source is modelled as a point object. In practice, however, the electron gun emits radiation from a finite-size source leading to an incoherent blurring of the image contrast in STEM images. The effect of finite source size can be included by a convolution of the simulated image $I(\mathbf{x}_p)$ and the source size distribution $S(\mathbf{x}_p)$:^{50,57,58,157}

$$I_{final}(\mathbf{x}_p) = S(\mathbf{x}_p) \otimes I(\mathbf{x}_p) \quad . \quad (2.24)$$

Hereby, the source size distribution can be approximated as a normalized 2D Gaussian distribution:^{84,87,158}

$$S(\mathbf{x}_p) = \frac{1}{2\pi d_s^2} \exp\left(-\frac{\mathbf{x}_p^2}{2d_s^2}\right) \quad , \quad (2.25)$$

where d_s is a measure for the extension of the source image and its relationship with the full width at half maximum (FWHM) of the source distribution can be expressed as:

$$FWHM = 2\sqrt{2\ln 2}d_s \approx 2.35d_s \quad . \quad (2.26)$$

In this thesis, the MULTEM software, which has been developed by Dr. Ivan Lobato at EMAT, is used to simulate ADF STEM images with the multislice method employing the frozen phonon model.^{64,133} The frozen phonon model requires repeated multislice calculations for a large number of different phonon configurations of the specimen. Therefore, this process requires a long computational time. The MULTEM software is a powerful tool to perform accurate and fast multislice calculations by using a central processor unit (CPU) or a graphical processor unit (GPU) which provides a huge advantage in computing time. As an example, Ivan Lobato et al.¹³³ showed that single-thread calculations for CBED pattern simulations of a Si crystal took around 1000 seconds (s). While the computation time of the same calculations was decreased to 450 s by CPU multithreading simulations (four threads), it took only 40 s by using GPU in MULTEM software.

To accurately reproduce experimental observations, image simulations should be performed with carefully chosen experimental parameters such as the acceleration voltage (V_0), probe convergence semi-angle (α), the third and fifth-order spherical aberrations ($C_{3,0}$, $C_{5,0}$), and detector geometry as an input. In addition, simulation-specific parameters, such as a sufficient number of frozen phonon configurations, the thickness of a single slice, as well as simulation box size and pixel size, need to be defined carefully to enable reliable image simulations. The pixel size can be measured by dividing the simulation box size by the number of pixels corresponding to the number of scan

points of the probe. Fourier transforms performed during the multislice simulations are applied on a periodic array where an identical copy of the image appears on each side of the image.¹²³ Therefore, the right and left edges, as well as top and bottom edges, wrap and touch each other. To avoid wrap-around errors, the simulation box size should be sufficiently large, especially for a NP since one cannot use periodic boundary conditions. This setup can be accomplished by adding a border of vacuum around the specimen.^{123,159}

As an example, a simulated ADF STEM image of a Au nanowedge (Figure 2.3a,b) using the MULTEM software is shown in Figure 2.3c, where simulation parameters are tabulated in Table 2.1. From Figure 2.3c, it can be clearly seen that the intensity of an ADF STEM is proportional to the number of atoms located in the projected atomic column.

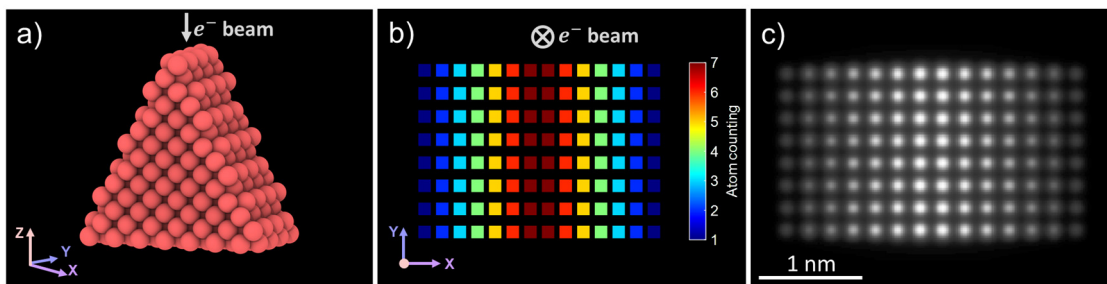


Figure 2.3 Simulated ADF STEM image of a Au nanowedge using MULTEM software. a) Input structure. b) Total number of atoms located in each atomic column of the input structure (a). c) Simulated ADF STEM image.

Table 2.1 Parameters used for the multislice simulations of the Au nanowedge, shown in Figure 2.3c.

Parameter	Symbol	Value
Acceleration voltage	V_0 (kV)	300
Defocus	$C_{1,0}$ (Å)	-83.001
3 rd order spherical aberration	$C_{3,0}$ (μm)	35.0
5 th order spherical aberration	$C_{5,0}$ (μm)	-
Convergence semi-angle	α (mrad)	21.788
Detector inner angle	(mrad)	46.0
Detector outer angle	(mrad)	215.0
Number of phonon configurations	-	15.0
Simulation box size	L_{xy} (Å)	50.0
RMSD	-	0.09
Pixel size	$\Delta x = \Delta y$ (Å)	0.09955
Number of pixels	$K \times L$	320x320
FWHM of the source size	FWHM (Å)	0.7

2.2. Model-based statistical parameter estimation for ADF STEM images

As it has been mentioned before, the physicochemical properties of nanostructures are controlled by their shape, size, and atomic arrangement. Therefore, the aim of the quantitative STEM analysis

is to measure the unknown structure parameters as accurately and precisely as possible from the high-resolution ADF STEM images.^{87,160,161} During this approach, an ADF STEM image is considered as a 2D data plane from which unknown structure parameters, such as the atomic positions, atomic displacements, atom types, and the number of atoms, can be estimated in a statistical way. For this purpose, the observed pixel values w_{kl} at position (x_k, y_l) of an STEM image having the dimensions of $K \times L$ pixels can be summarized in a vector:

$$\mathbf{w} = (w_{11}, w_{12}, \dots, w_{KL}) \quad . \quad (2.27)$$

Since a high-resolution STEM image is formed by counting electrons scattered to the detector, the pixel values are inevitably subject to Poisson noise, causing each observed image pixel value to be Poisson distributed.¹⁶² Due to the presence of noise, the intensities in a STEM image recorded under the same experimental conditions unavoidably fluctuate randomly around their expectation values. An effective way to describe this behavior is to model the observations as stochastic variables.^{96,163} The expectation value of the STEM image intensity w_{kl} at position (x_k, y_l) can then be described using a parametric imaging model given by the following expression:

$$\mathbb{E}[w_{kl}] = f_{kl}(\boldsymbol{\theta}) \quad , \quad (2.28)$$

where \mathbb{E} represents the mathematical expectation and $\boldsymbol{\theta}$ denotes unknown parameters of the parametric imaging model $f_{kl}(\boldsymbol{\theta})$. Hereby, the proposed parametric model should accurately describe the pixel values in the formed STEM images to extract reliable quantitative structure information. Physics-based models can describe image intensities in detail, i.e. including the imaging parameters, electron-specimen interaction, and TDS, as explained in Section 2.1. However, such simulations would require high computational power since an iterative optimization procedure estimates model parameters. Furthermore, the number of unknown parameters would be higher for such models since unknown microscope parameters should then be included in the parametric model. Thus, the optimization might end up in a local minimum if appropriate starting values for the unknown parameters are not available. To overcome this problem, a simplified, empirical incoherent imaging model describing the expectations of the pixel values of an ADF STEM image is preferred.^{87,96}

The image intensities in an ADF STEM image increase with an increasing atomic number Z and with increasing specimen thickness. Furthermore, for high-resolution STEM images, the image intensities of crystalline structures viewed along a major axis are sharply peaked at the atomic column positions.^{49,57,164} Therefore, the projected atomic columns viewed along a major zone axis can be modelled as a superposition of 2D Gaussian peaks on a constant background. Although this model does not fully describe the physics behind the image formation process, its validity for describing high-resolution ADF STEM images has been proven in previously reported studies.^{160,161} This model is also acceptable since the width of an atomic column is mainly determined by the finite source size, which is often approximated as normalized Gaussian.^{165,166} The expectation value of the image intensity at position (x_k, y_l) can then be described as:¹⁶⁷

$$f_{kl}(\boldsymbol{\theta}) = \zeta + \sum_{n=1}^N \eta_n \exp\left(-\frac{(x_k - \beta_{x_n})^2 + (y_l - \beta_{y_n})^2}{2\rho^2}\right) , \quad (2.29)$$

where ζ is a constant background, ρ is the width of the 2D Gaussian peaks, η_n is the height of the n^{th} Gaussian peak, β_{x_n} and β_{y_n} are the x- and y-coordinate of the n^{th} atomic column, and N is the total number of analyzed atom columns. The unknown parameters of the parametric imaging model of Equation 2.29 are given by the parameter vector:

$$\boldsymbol{\theta} = (\beta_{x_1}, \dots, \beta_{x_N}, \dots, \beta_{y_1}, \dots, \beta_{y_N}, \dots, \rho, \dots, \eta_1, \dots, \eta_N, \zeta)^T . \quad (2.30)$$

The unknown parameters of $\boldsymbol{\theta}$ are estimated by uniformly weighted least squares estimator defined by: ^{168,169}

$$\hat{\boldsymbol{\theta}} = \underset{\boldsymbol{t}}{\operatorname{argmin}} \sum_{k=1}^K \sum_{l=1}^L (w_{kl} - f_{kl}(\boldsymbol{t}))^2 . \quad (2.31)$$

The parameters are then estimated by minimizing the least-squares sum, which quantifies the similarities between the image and the model. This is performed using an iterative optimization algorithm, which is implemented in the StatSTEM software package. ⁹⁷ Hereby, good starting values are essential in order to avoid convergence to a local minimum during the model estimation procedure (Equation 2.31). Starting values for the projected atomic column positions (β_{x_n} and β_{y_n}) can be defined manually or from a peak finding routine that searches for local maxima in the images. ⁹⁷ Figure 2.4 visualizes the working principle of model-based parameter estimation in STEM, where the height, width, and position of a Gaussian peak in the model are adjusted to find the best match with an observed atomic column.

Statistical parameter estimation enables the determination of atomic column positions with high precision from ADF STEM images. As a result, local interatomic distances, strain at a particle-support interface, or crystalline defects can reliably be measured. ^{88–90,170,171} Furthermore, the statistical parameter estimation also provides a robust methodology to quantify the atomic column intensities. For ADF STEM, the volume under each Gaussian peak reflects the total intensity of scattered electrons from a single atomic column toward the ADF STEM detector. This is the so-called scattering cross sections (SCSs). ^{91,101,102} The SCS monotonically increases with increasing sample thickness and can therefore be used to estimate the number of atoms in a projected atomic column from an ADF STEM image. The advantage of using SCSs, instead of peak intensities, to quantify the number of atoms in a projected atomic column is their robustness to sample mistilt or microscope aberrations, such as defocus, astigmatism or source size broadening. The SCS of the n^{th} Gaussian peak can be calculated as follows: ⁸⁷

$$V_n = 2\pi\eta_n\rho^2 . \quad (2.32)$$

As an example, the procedure to count the number of atoms is demonstrated on the simulated ADF STEM image of the Au nanowedge shown in Figure 2.3c. Poisson-distributed image noise is also

added by $N_d \Delta x \Delta y w_{kl}$ ⁹⁷ with an incoming electron dose of $N_d = 10000 e^-/\text{\AA}^2$, the pixel area of $\Delta x \Delta y$, and the observed pixel values of w_{kl} . A noise realization of the simulated Au nanowedge is illustrated in Figure 2.5a and its parametric model is shown in Figure 2.5b, where fitted atomic column positions are indicated as red dots.

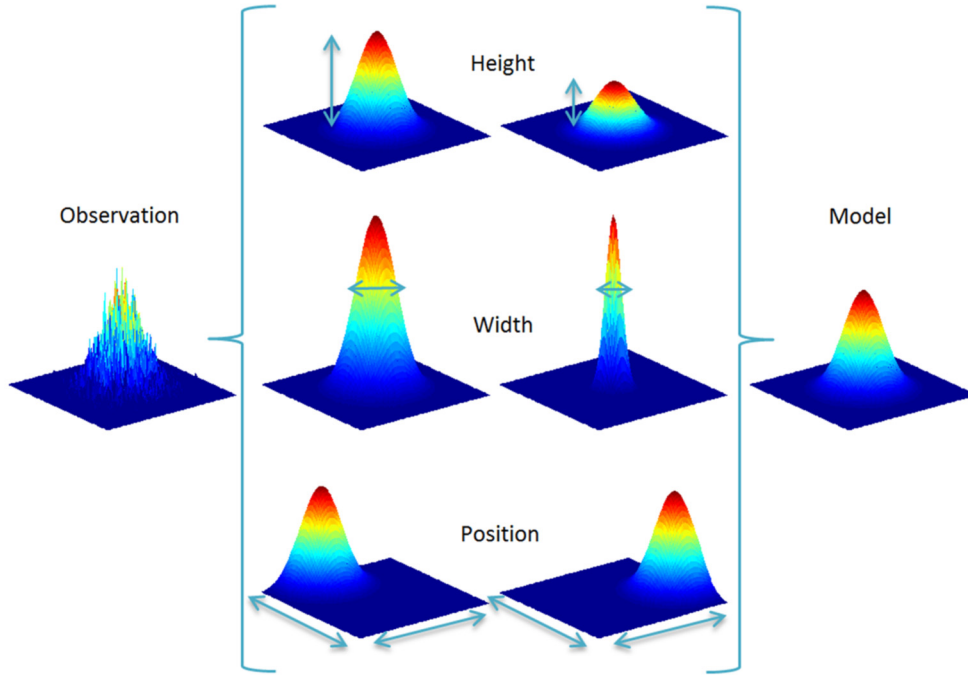


Figure 2.4 Visualization of modelling a Gaussian peak to an observed atomic column by adjusting the height, width and position. Reprinted from ref¹⁷².

The set of SCSs estimated from the fitted model is shown in Figure 2.5c. From the histogram of estimated SCSs in Figure 2.5c, the increase in SCSs with respect to thickness can be observed. Ideally, this histogram would consist of isolated components, where each component corresponds to a set of columns having the same number of atoms projected on top of each other. In practice, however, the peaks are often broadened because of different factors, such as a different vertical onset of columns of the same number of atoms, experimental detection noise, the influence of neighboring columns and relaxation at the boundaries. Therefore, the SCSs corresponding to atomic columns containing the same number of atoms g will not be identical but fluctuate around an average SCS, μ_g . This makes a visual interpretation of the components from the SCS histogram often impossible or highly subjective. To overcome this limitation, the distribution of SCSs can be modelled as a Gaussian distribution such that the SCSs in the histogram are regarded as independent statistical draws from a Gaussian mixture model. This model describes the probability that a specific SCS value is observed.^{103,168,173} The probability density function of the mixture model with G Gaussian components can parametrically be written as:

$$f_{mix}(V_n; \Psi_G) = \sum_{g=1}^G \pi_g \phi_g(V_n; \mu_g, \sigma) \quad . \quad (2.33)$$

Hereby, G is the number of atoms located in the thickest atomic column and V_n represents the stochastic variable for the n^{th} SCS. The symbol Ψ_G represents the vector containing all unknown parameters in the mixture model with G components:

$$\Psi_G = (\pi_1, \dots, \pi_{G-1}, \mu_1, \dots, \mu_G, \sigma)^T \quad . \quad (2.34)$$

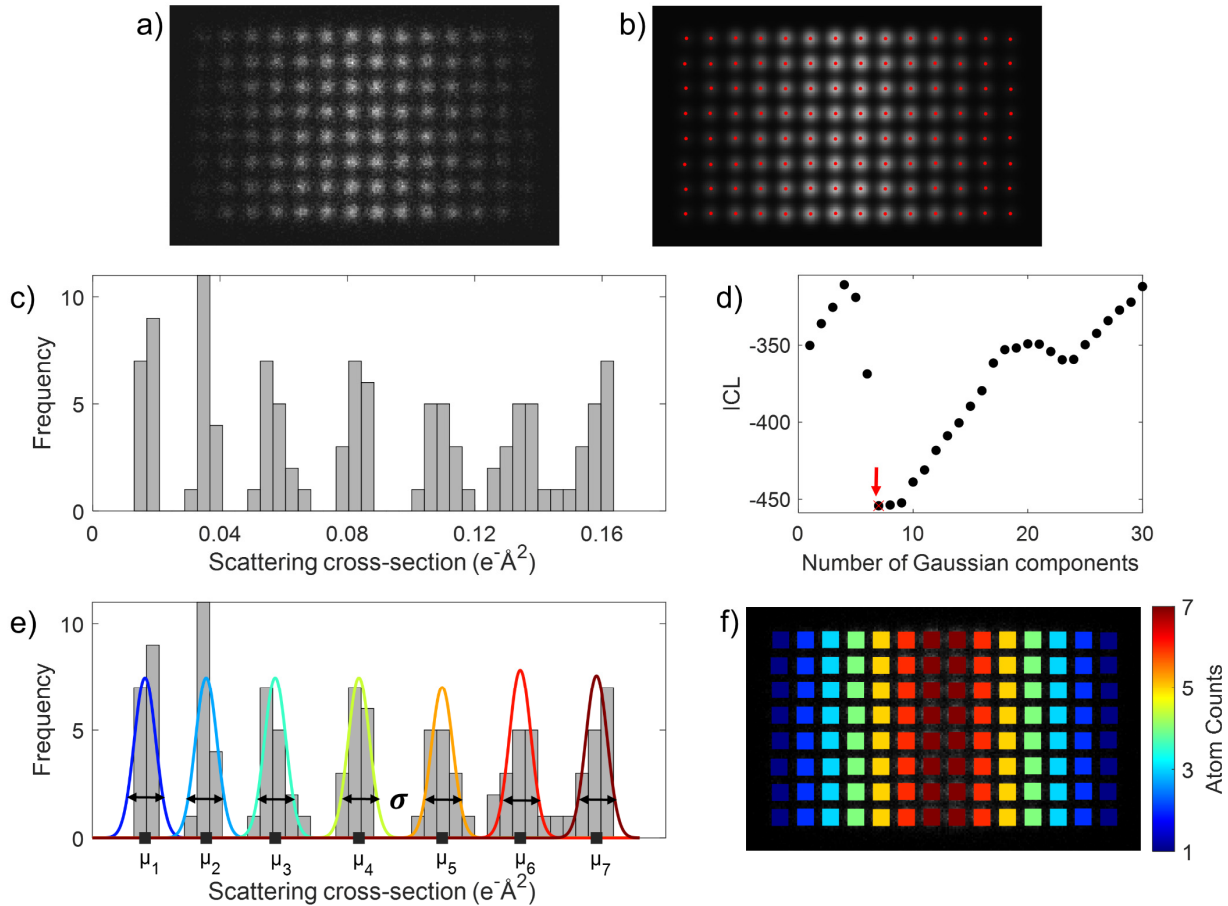


Figure 2.5 Summary of the statistics-based atom counting approach applied to a noise realization of the simulated image shown in Figure 2.3c. a) A noise realization for an incoming electron dose of $N_d = 10000 e^-/\text{\AA}^2$. b) The parametric model of the image shown in (a). Fitted atomic column positions are indicated as red dots. c) Histogram of the estimated SCSs from the model shown in (b). d) ICL criterion evaluated as a function of the number of Gaussian components. e) Gaussian mixture model with the estimated locations μ_g and width σ of the Gaussian components. The colored curves indicate the individual normal components. f) Estimated number of atoms in each atomic column.

The components $\phi_g(V_n; \mu_g, \sigma)$ of the mixture model are generated by set of atomic columns having the same number of atoms and they are modelled as homoscedastic normal components: ^{168,173}

$$\phi_g(V_n; \mu_g, \sigma) = \frac{1}{\sqrt{2\pi}\sigma} \exp\left(-\frac{(V_n - \mu_g)^2}{2\sigma^2}\right) \quad . \quad (2.35)$$

The mixing proportion of the g^{th} component, π_g , indicates the fraction of the columns having a

specific number of atoms, i.e. the weight of the g^{th} component in the Gaussian mixture model. Since the mixing proportions π_g sum up to unity, the G^{th} mixing proportion π_G is omitted in the parameter vector Ψ_G (Equation 2.34). Furthermore, μ_g denotes the location of the average SCS of g^{th} component in the mixture model. The width of the components σ describes the amount of fluctuation on the SCSs, corresponding to atomic columns with the same thickness, from the mean value μ_g .^{168,173}

In order to compute the parameters Ψ_G of the probability distribution of the estimated SCSs (V_n), the maximum likelihood estimator is used.^{96,174–177} Here, estimates are found by maximizing the log likelihood function of the unknown parameter vector Ψ_G for a given set of observed SCSs \hat{V}_n :

$$\log L(\Psi_G) = \sum_{n=1}^N \log \left(\sum_{g=1}^G \pi_g \phi_g(\hat{V}_n; \mu_g, \sigma) \right) . \quad (2.36)$$

To compute the maximum likelihood estimates of Ψ_G , an iterative procedure is applied using the expectation-maximization algorithm.¹⁷⁸ In this manner, a solution for the parameters Ψ_G can be obtained for a fixed number of G components. G is the number of atoms found in the thickest atomic column, which is often unknown and needs to be estimated as well. In order to identify the correct number of components G , the integrated classification likelihood (ICL) criterion is evaluated as a function of the number of components. Although many different information criteria exist, ICL outperforms other order selection criteria for atom counting.¹⁶⁸ The ICL criterion is expressed as follows:

$$ICL(G) = -2\log L(\hat{\Psi}_G) + 2EN(\hat{\tau}) + d\log N , \quad (2.37)$$

where $2\log L(\hat{\Psi}_G)$ is the likelihood term evaluated at the estimated parameters $\hat{\Psi}_G$ and $2EN(\hat{\tau}) + d\log N$ is a penalty term depending on the number of atomic columns N , the number of parameters d in the mixture model and the entropy term:

$$EN(\hat{\tau}) = - \sum_{g=1}^G \sum_{n=1}^N \tau_g(\hat{V}_n; \hat{\Psi}_G) \log \tau_g(\hat{V}_n; \hat{\Psi}_G) , \quad (2.38)$$

with $\tau_g(\hat{V}_n; \hat{\Psi}_G)$ the posterior probability that the estimated SCS \hat{V}_n of the n^{th} column belongs to the g^{th} component. The entropy term $EN(\hat{\tau})$ favors mixture models with well separated components, in order to estimate physically relevant Gaussian mixture models. The first term of ICL criterion (Equation 2.37), measuring the model fit, will decrease with increasing order, whereas the penalty term, measuring the complexity of the model, will increase with increasing order. Therefore, the ICL reaches a minimum value at the optimum solution.

The ICL criterion for the simulated Au nanowedge is shown in Figure 2.5d. Here, one searches for a local minimum and the red arrow indicates the selected local minimum at $G = 7$ components. This suggests that a particular column contains 1 up to a maximum of 7 Au atoms. Finally, by

assigning the measured SCSs to the corresponding number of atoms with the largest probability, the total number of atoms in each atomic column can be estimated. The histogram of estimated SCSs together with the underlying Gaussian mixture model and atom counting results are shown in Figure 2.5e and Figure 2.5f, respectively. It can be seen that this counting result is identical to the original input used for the MULTEM simulation shown in Figure 2.3b.

Using the statistical parameter estimation theory framework, atoms can be counted with single-atom sensitivity from high-resolution ADF STEM images.^{168,173} However, the precision of the counting results is limited by the overlap between the Gaussian components. To illustrate this effect on the atom counting results, Poisson-distributed noise was added to the simulated ADF STEM image of the Au nanowedge for lower electron doses, $N_d = 5000 e^-/\text{\AA}^2$, $N_d = 1500 e^-/\text{\AA}^2$ and $N_d = 1000 e^-/\text{\AA}^2$. The resultant images are shown in the first column of Figure 2.6 (Figure 2.6a,d,g). From the Gaussian mixture models in Figure 2.6b,e,h, it can be seen that the reduced electron dose resulted in more fluctuation of SCSs about their mean values and a larger overlap between the neighboring Gaussian components. The overlapped regions are indicated as dark gray in Figure 2.6e,h. In accordance with the literature,^{97,98,168,173} for a larger overlap, the probability that a wrong number of atoms is assigned to a particular column increases.¹⁷³ Although high precision in atom counting is observed in Figure 2.6c, where there is nearly no overlap between neighboring components (Figure 2.6b), the increased overlap between the components due to the limited electron dose causes a discrepancy between the estimated number of atoms per column (Figure 2.6f,i) and the original input shown in Figure 2.3b. In addition to the overlap between the Gaussian components, previously reported studies demonstrated that there should be a sufficiently large number of atomic columns for a reliable atom counting by statistical parameter estimation theory.^{98,173} Therefore, performing reliable atom counting can be challenging for very small NPs presenting a limited number of projected atomic columns, or for images exhibiting low SNR due to scanning distortions and a low electron dose.⁸¹

The true number of components often corresponds to a local minimum in the evaluation of the ICL but the presence of more than one minimum may complicate the analysis. For example, from Figure 2.6j, it can be seen that the shape of ICL is affected by different incoming electron doses and can show extra minima at different component numbers in addition to the correct component number at $G = 7$ (red arrows in Figure 2.6j). ICL may also equal-likely favor the mixture models having different component numbers (see Figure 2.5d for $G = 8$ and $G = 9$ components). More details regarding the interpretation of ICL are given in Appendix A. Moreover, depending on the nanostructure under study, it is possible that the first component does not correspond to one atom but to a higher number of atoms. In that case, an offset should be taken into account when assigning the number of atoms to atomic columns of the different components. However, finding the true number of components of the underlying distribution by using ICL and selecting the correct offset value can be highly subjective without prior knowledge about the shape and thickness of the experimentally imaged NP. To overcome these limitations, the outcome of statistics-based atom counting results can be validated with accurate multislice simulations. Therefore, in this thesis, the combination of simulation and statistics-based atom counting is used where the estimated SCSs from an experimental image are compared with SCSs obtained from multislice simulations.¹⁷³ In

Section 3.2, the procedure of combined simulation and statistics-based atom counting is explained in detail on an experimental system.

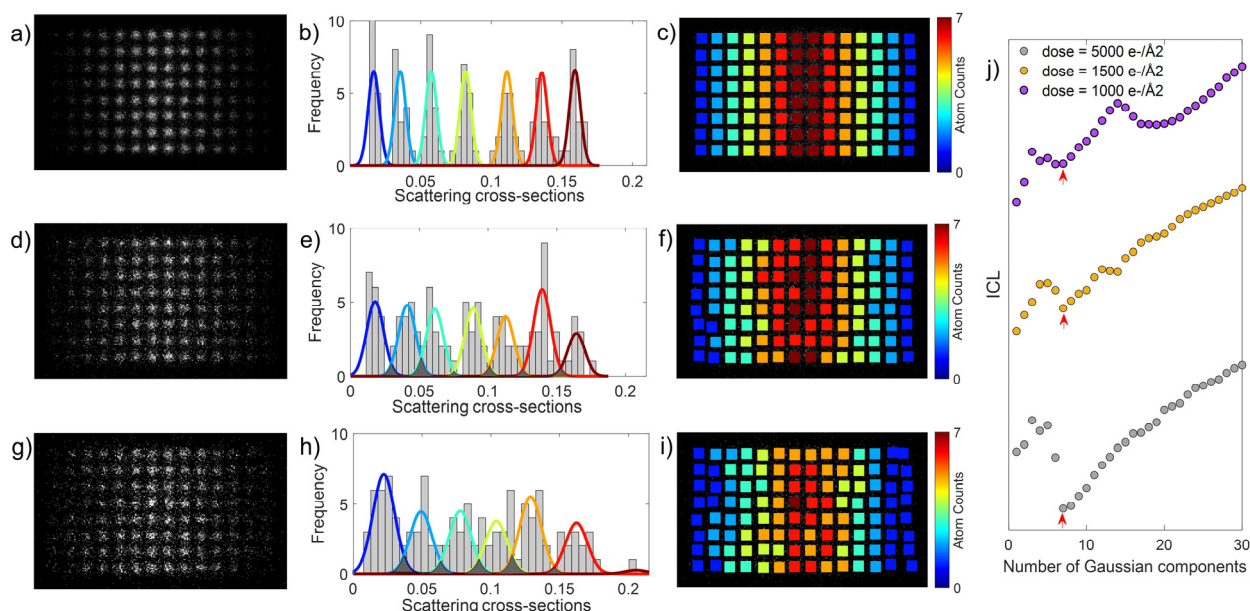


Figure 2.6 An example to show the effect of overlapped neighboring Gaussian components on the atom counting results. A noise realization (a) for an incoming electron dose of $N_d = 5000 e^-/\text{Å}^2$, the corresponding Gaussian mixture model (b) and resultant atom counting map (c). A noise realization (d) for an incoming electron dose of $N_d = 1500 e^-/\text{Å}^2$, the corresponding Gaussian mixture model (e) and resultant atom counting map (f). A noise realization (g) for an incoming electron dose of $N_d = 1000 e^-/\text{Å}^2$, the corresponding Gaussian mixture model (h) and resultant atom counting map (i). j) ICL as a function of number of components for different incident electron doses. The correct component number ($G = 7$) is indicated as a red arrow for each ICL.

2.3. Atomistic simulations

To reconstruct 3D models of the experimentally imaged NP based on atom counting results, two additional steps were performed in the previously reported studies: initialization of an appropriate starting model and structural relaxation of the starting model by the use of atomistic-based simulations, such as *ab initio* calculations, a Monte Carlo (MC) method or molecular dynamics (MD) simulations.^{81,107,109,110}

Ab initio calculations are based on atoms and electrons interacting with each other according to the laws of quantum mechanics. During such simulations, one solves the electronic Schrödinger equation given the positions of the nuclei and number of electrons. *Ab initio* calculations yield accurate results; however, the large number of quantum mechanical interactions makes the modelling of many-body systems computationally intensive. Although the developments in supercomputers and parallel programming allow increasing computational speed, investigating the dynamical behavior of systems having more than a few tens of atoms by quantum mechanical calculations is still highly challenging.

The MC method is a computationally more efficient approach compared to *ab initio* calculations. A standard MC method describes systems with a constant number of particles N , a constant volume V and a constant temperature T (NVT), which corresponds to canonical ensemble. The equilibrium average of some quantity $\langle B \rangle$, e.g. the potential energy, for systems in canonical ensemble can be given by: ¹⁷⁹

$$\langle B \rangle = \frac{\sum_{\alpha} e^{-\frac{E_{\alpha}}{k_B T}} B_{\alpha}}{\sum_{\alpha} e^{-\frac{E_{\alpha}}{k_B T}}} = \sum_{\alpha} B_{\alpha} \rho_{\alpha} \quad . \quad (2.39)$$

Hereby, k_B is the Boltzmann constant, and ρ_{α} is the probability of being in a possible configuration α :

$$\rho_{\alpha} = \frac{e^{-\frac{E_{\alpha}}{k_B T}}}{\sum_{\alpha} e^{-\frac{E_{\alpha}}{k_B T}}} = \frac{e^{-\frac{E_{\alpha}}{k_B T}}}{Q} \quad (2.40)$$

with Q is partition function:

$$Q = \sum_{\alpha} e^{-\frac{E_{\alpha}}{k_B T}} \quad . \quad (2.41)$$

From Equation 2.40, the relative probability between two states, such as the probability of an atomic configuration α with energy E_{α} relative to the probability of configuration β with energy E_{β} , can be calculated as follows:

$$\frac{\rho_{\alpha}}{\rho_{\beta}} = e^{-(E_{\alpha}-E_{\beta})/k_B T} \quad . \quad (2.42)$$

Since k_B and T are constant in MC, the relative probabilities of the two states does not vary with the partition function Q and depend only on the energy difference: if E_{α} is equal to or smaller than E_{β} , the relative probability ($\frac{\rho_{\alpha}}{\rho_{\beta}}$) is larger than 1; otherwise it becomes smaller than 1.

A simplified flowchart of MC algorithm for atomistic simulations is illustrated in Figure 2.7a. MC simulations start with random atomic displacements in an initial atomic model. Then, the energy corresponding to the new configuration with displaced atoms is calculated. The new configuration is accepted if the energy decreases. This process is repeated until either the energy of the system remains unchanged or a user-defined number of iterations is reached. It should be noted that MC method can be simply extended to other ensembles, e.g., isobaric-isothermal ensemble, associated with different thermodynamic constraints by modifying the partition function (Equation 2.41). ¹⁷⁹

During the MC method, all possible configurations should be explored. However, many of the configurations of a system may not be probable. For example, if two atoms in a candidate structure are very close to each other compared to their equilibrium positions, the resultant energy of that configuration will be large and the probability of being in that state will be vanishingly small. Moreover, the MC method considers only the configuration space and ignores the dynamical

behavior of a system.¹⁷⁹ Therefore, it is limited to the static properties of a system and often fails when one wants to investigate the physical atomic trajectories or dynamical behavior of a NP under certain conditions, such as structural and morphological evolution of a NP upon heating.¹⁸⁰

MD simulations, on the other hand, can generate the dynamic behavior of systems. MD simulations are based on the idea of classical mechanics, which is the study of the dynamical response of objects under applied forces.^{179,181} A simplified algorithm for MD simulations is shown in Figure 2.7b. Classical MD simulations start with a set of atomic positions. Next, these simulations progress in time by computing the force acting on each atom in a system and solving Newton's equation of motion to obtain the time evolution of the set of interacting atoms. Thermodynamic and statistical mechanics quantities, such as energy, temperature, pressure, are then measured from the obtained trajectory of the atoms.

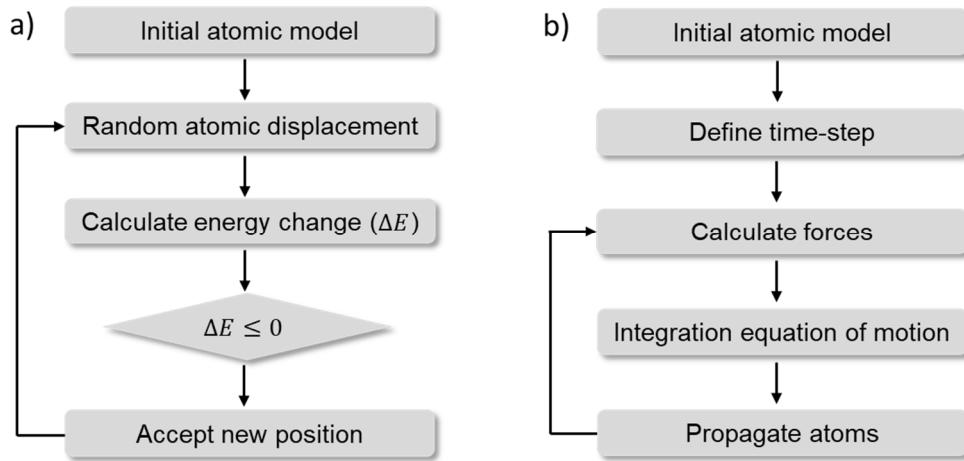


Figure 2.7 Simplified flowcharts of (a) MC algorithm and (b) MD simulations.

According to Newton's second law, the force F acting on a particle having mass m can be calculated as follows:

$$F = m\mathbf{a} = m \frac{d\mathbf{v}}{dt} = m \frac{d^2\mathbf{r}}{dt^2} , \quad (2.43)$$

where t is time, \mathbf{v} is velocity and \mathbf{a} is the time rate of position change ($d^2\mathbf{r}/dt^2$). From classical mechanics, the force acting a particle equals to the negative gradient of the potential energy with respect to the position of that particle. Hence, the force acting on an atom i is given by:¹⁷⁹

$$\mathbf{F}_i = -\nabla_i U(\mathbf{r}_1, \mathbf{r}_2, \dots, \mathbf{r}_N) . \quad (2.44)$$

Hereby, U denotes the potential energy of a system as a function of position of the atoms ($\mathbf{r}_i = x_i, y_i, z_i$) and the gradient is taken with respect to the coordinates of the atoms:

$$\nabla_i U(\mathbf{r}_1, \mathbf{r}_2, \dots, \mathbf{r}_N) = \frac{\partial U(\mathbf{r}_1, \mathbf{r}_2, \dots, \mathbf{r}_N)}{\partial x_i} + \frac{\partial U(\mathbf{r}_1, \mathbf{r}_2, \dots, \mathbf{r}_N)}{\partial y_i} + \frac{\partial U(\mathbf{r}_1, \mathbf{r}_2, \dots, \mathbf{r}_N)}{\partial z_i} . \quad (2.45)$$

By substituting Equation 2.44 into Equation 2.43, Newton's equation of motion for an atom i yields

to:

$$\frac{d^2\mathbf{r}}{dt^2} = \frac{1}{m_i} \mathbf{F}_i = \frac{1}{m_i} [-\nabla_i U(\mathbf{r}_1, \mathbf{r}_2, \dots, \mathbf{r}_N)] \quad . \quad (2.46)$$

From Equation 2.46, it can be interpreted that atoms tend to minimize the energy under a force. The forces needed to integrate the equations of motion (Equation 2.46) can be determined from *ab initio* calculations, the so-called “*ab initio* MD”. However, since *ab initio* calculations are computationally intensive for the simulations of many-body systems, in classical MD simulations, the system potential energy U as a function of atomic positions is often approximated by mathematical functions, which are known as force-fields or interatomic potentials or often just called as potentials.^{182,183}

One of the best known interatomic potentials is the Lennard-Jones (LJ) potential. LJ potential is a, so-called, pair potential that describes the potential energy U of a system from the interaction between individual pairs of atoms depending on the distance between the pairs. According to the LJ potential, the potential energy of a system, containing N number of atoms, is calculated as follows:¹⁸⁰

$$U = \frac{1}{2} \sum_{i=1}^N \sum_{j=1}^N \phi_{ij}(\mathbf{r}_i, \mathbf{r}_j) \quad (2.47)$$

with

$$\phi_{ij}(\mathbf{r}_i, \mathbf{r}_j) = 4\epsilon \left[\left(\frac{\sigma}{r_{ij}} \right)^{12} - \left(\frac{\sigma}{r_{ij}} \right)^6 \right] \quad \text{for } r_{ij} < r_c \quad . \quad (2.48)$$

Here, $\phi_{ij}(\mathbf{r}_i, \mathbf{r}_j)$ represents the interaction between the pairs of atoms i and j located at \mathbf{r}_i and \mathbf{r}_j with an interatomic distance $r_{ij} = |\mathbf{r}_i - \mathbf{r}_j|$. The first term in Equation 2.48 represents a short-range repulsion force, and the second term represents attraction between the interacting atoms within a defined cut-off distance r_c .¹⁷⁹ The parameters ϵ and σ are specific constants that are related to the types of interacting atoms. The parameter ϵ controls the strength of the interaction and the parameter σ defines the distance at which potential is zero. Typically, these parameters are chosen such that the estimated properties of a material under investigation by the LJ potential match a set of reference data obtained from either experimental observations or *ab initio* calculations.

The simplicity of the LJ potential provides a great advantage in the simulations of large systems. However, LJ potential considers atoms as neutral, point-like particles and does not represent the free-electrons in metals, which are of significant importance for reliable simulations of metallic systems.^{180,184} Therefore, the embedded atom method (EAM) has been developed. At about the same time, conceptually similar potentials having different functional forms were also developed, such as the glue model,¹⁸⁵ Finnis-Sinclair,¹⁸⁶ or Voter-Chen-type¹⁸⁷ potentials.

The EAM can be interpreted in the framework of density-functional theory. In this approach, the energy of a metallic system is described as the required energy to embed an atom into the local

electron density provided by the surrounding atoms. The energy contribution from two-body interactions is also included. In EAM, the total internal energy E_{tot} can be expressed as: ^{184,188}

$$U = \sum_i F_i(\rho_i) + \frac{1}{2} \sum_{i=1}^N \sum_{j=1}^N \phi_{ij}(r_{ij}) \quad (2.49)$$

and

$$\rho_i = \sum_{j \neq i} \rho_j(r_{ij}) \quad . \quad (2.50)$$

Hereby, $\phi(r_{ij})$ is the pair-wise potential term and $F_i(\rho_i)$ is the embedding energy required to place atom i in an electron density ρ_i . The latter can be defined as the sum of the electron density of individual surrounding atoms. Generally, these functions are generated by a numerical fitting procedure. A typical fitting procedure involves a set of reference atomic forces of many atomic configurations produced by first-principles calculations. ^{179,181,189,190} The optimum set of parameters of EAM (Equation 2.49) is determined by matching the prediction of EAM with the properties or forces supplied by reference first-principles calculations or experimental studies. Such potentials have been shown to be very successful in the modeling of the properties of metallic systems. ^{184,190–192} Therefore, in this thesis, the EAM is used for the MD simulations of metallic Au and Pt particles. The validity of EAM for the MD simulations of Au and Pt NPs performed in this thesis is discussed in Appendix B.

Once the forces acting on each atom have been calculated, the positions of these atoms are updated according to Newton's laws of motion (Equation 2.46). A number of methods have been developed for the numerical integration of Newton's equation of motion. ¹⁹³ A standard way is to discretize time t into the so-called "time steps δt " and then solve the equations of motion over those time intervals. By approximating the force \mathbf{F}_i acting on atom i and the acceleration \mathbf{a}_i as constant over the time interval δt , the position \mathbf{r}_i and velocity \mathbf{v}_i of atom i at time $t + \delta t$ can be evaluated from its position and computed force acting on it at time t : ¹⁸¹

$$\mathbf{r}_i(t + \delta t) = \mathbf{r}_i(t) + \mathbf{v}_i(t)\delta t + \frac{1}{2}\mathbf{a}_i(t)\delta t^2 \quad (2.51)$$

with

$$\mathbf{v}_i(t + \delta t) = \mathbf{v}_i(t) + \mathbf{a}_i(t)\delta t \quad , \quad (2.52)$$

and

$$\mathbf{a}_i(t) = \frac{d^2\mathbf{r}_i(t)}{dt^2} = \frac{1}{m_i}\mathbf{F}_i(t) \quad . \quad (2.53)$$

Hereby, $\mathbf{r}_i(t)$ is the position, and $\mathbf{v}_i(t)$ is velocity at time t . While this approach is straightforward, the solution of Equation 2.51 and 2.52 may not yield self-consistent results. ¹⁸¹ A better solution is provided by velocity Verlet algorithm where velocities at $t + \delta t$ are computed from the average of the accelerations at t and $t + \delta t$: ^{179,194}

$$\mathbf{v}_i(t + \delta t) = \mathbf{v}_i(t) + \frac{1}{2m_i} [\mathbf{F}_i(t) + \mathbf{F}_i(t + \delta t)] \delta t \quad . \quad (2.54)$$

The accuracy of velocity Verlet algorithm is related to the defined time step δt .¹⁹⁵ While large time steps allow simulations for larger time scales in reasonable computational time, the approximation of constant force over a large time interval δt leads to larger numerical errors in the calculations. The numerical errors can be reduced using smaller time steps. However, since the force acting on each atom is evaluated at each time step, using a too-small time step value may require high computational power.^{179,195} Therefore, defining an optimum time step δt is a matter of balance between accuracy and computational time. During the MD simulations presented in this thesis, a time step in femtosecond (fs) time scale is defined, i.e. 0.5-1 fs, for the resolution of the individual atomic vibrations.

Various ensembles can be applied to mimic different thermodynamic states during MD simulations. It is often desirable to study a system in a canonical ensemble (NVT) or at constant temperature T and pressure P in an isothermal-isobaric ensemble (NPT) to replicate a complementing experiment in a controlled environment. These thermostats and/or barostats are imposed by either rescaling the atom velocities or system pressure during the simulation via the Andersen and Berendsen methods or modifying the equations of motion with Nose-Hoover dynamics.¹⁹⁶ It has been shown that Nose-Hoover dynamics often outperform the other temperature control schemes and produce accurate canonical distribution.^{197,198} Thus, during the MD simulations presented in this thesis, Nose-Hoover thermostat was employed to control the temperature of the simulated systems.

For the MD simulations employing the Nose-Hoover thermostat in the NVT ensemble, an additional degree of freedom ζ is introduced into the equation of motion:¹⁹⁹

$$m_i \frac{d^2 \mathbf{r}}{dt^2} = \mathbf{F}_i - \zeta m_i \mathbf{v}_i \quad (2.55)$$

with

$$\frac{d\zeta(t)}{dt} = \frac{1}{Q} \left[\sum_{i=1}^N m_i \frac{\mathbf{v}_i^2}{2} - \frac{3N + 1}{2} k_B T \right] \quad . \quad (2.56)$$

Hereby, T denotes the target temperature and Q controls the relaxation of the dynamics of the friction $\zeta(t)$ which slows down or accelerates atoms until the target temperature is reached. The equations of motion of the Nose-Hoover thermostat can be implemented velocity Verlet algorithm by a similar modification.

During MD simulations, at each time step, the forces acting on atoms are calculated using interatomic potential. The position and velocity of each atom are then updated by solving the equation of motion with a defined ensemble. The iterative process is repeated until the overall simulation time is reached. The overall simulation time is defined according to system-specific purposes. Often, convergence of energy or a stationary behavior of the properties of interest, such

as temperature, pressure, RMSD of atoms, is considered as a criterion. Since complete trajectories of atoms are available, it is also possible to measure time-dependent variables and equilibrium thermodynamic properties of a simulated system. It should be noted that the calculated properties obtained from MD are not exactly the same as the real thermodynamic quantities of the materials due to error arising from the approximated interatomic potential functions, numerical solution of the equation of motion, and the size difference between the input model used in MD simulations and real systems.²⁰⁰

Considering the time scale of the MD simulations, which is in the nanosecond or microsecond range, and a proper time step, these calculations are repeated at around millions of times. Therefore, MD simulations are often performed on computer clusters or supercomputers using dozens or even hundreds of processors in parallel. Many different software packages have been developed to run MD in parallel. In this thesis, the Large-scale Atomic/Molecular Massively Parallel Simulator (LAMMPS) open source code is used to perform MD simulations.^{183,201}

MD simulations are a powerful approach to simulate both static properties and dynamic behaviors of solids, fluids and gases as well as their mixtures, solutions, alloys at the atomic scale.^{202–206} Moreover, it has been shown that combining MD simulations with atom counting results, estimated from ADF STEM images by statistical parameter estimation theory, allows one to determine the unknown 3D positions of atoms in a NP. In Figure 2.8, this procedure is summarized on an experimental ADF STEM image of a cubic Pt NP.

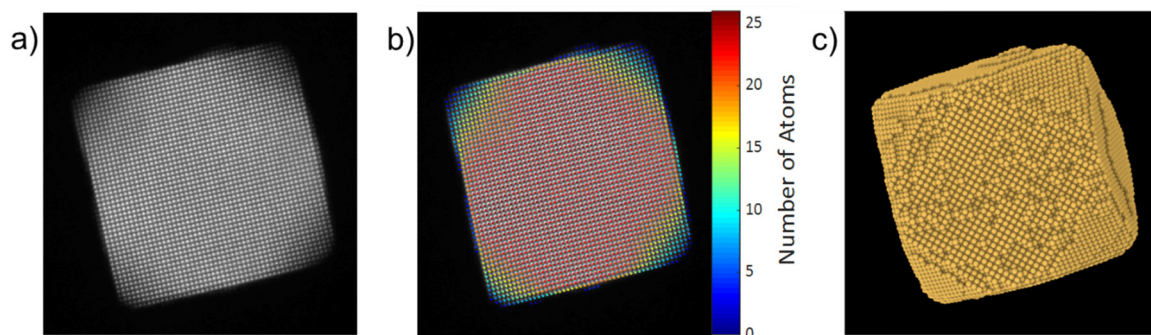


Figure 2.8 3D atomic reconstruction using a combination of atom counting and structural relaxation by MD simulations. (a) High resolution ADF STEM image. (b) Statistics-based atom counting. (c) Final 3D model of the Pt NP.

This procedure starts with creating an input model based on the atom counting results (Figure 2.8b). The fitted atomic column coordinates of the parametric model obtained by statistical parameter estimation, as explained in Section 2.2, were used as x and y coordinates of the starting input model. Along the z-direction, parallel to the beam direction, the estimated number of atoms in each atomic column were positioned symmetrically around a central plane using prior information about the [100] sample orientation and Pt face-centered cubic (FCC) crystal structure. The neighboring atoms along the beam direction were separated by fixed distances according to the lattice parameter of the projected crystalline structure. Next, structural relaxation by MD simulations was performed at

room temperature on the created starting model for 10 nanoseconds (ns) with *NVT* ensemble to determine the final 3D model, which is shown in Figure 2.8c.

To validate this approach, the outcome of this procedure was compared to a high-resolution 3D reconstruction obtained from electron tomography on the same Pt NP. Unlike the 3D reconstruction by electron tomography, the reconstruction using atom counting combined with MD simulations was based on a single projection image shown in Figure 2.8a. This high-resolution image was also part of a tomography series of the Pt NP. Tomographic reconstruction was retrieved by using the SIRT reconstruction algorithm developed by Dr. Ivan Lobato at EMAT.⁸¹ The reconstructed model by electron tomography is shown in Figure 2.9b. In Figure 2.9c,d, a comparison is shown between the two reconstruction methods. It can be seen that atom counts from both reconstructions are overlapped in Figure 2.9c,d, and an excellent visual match of the overall morphology of the Pt NP has been found. This shows a very good agreement with high-resolution electron tomography. However, it should be noted that this agreement can be possible only with the high accuracy of the estimated atom counts from ADF STEM image.

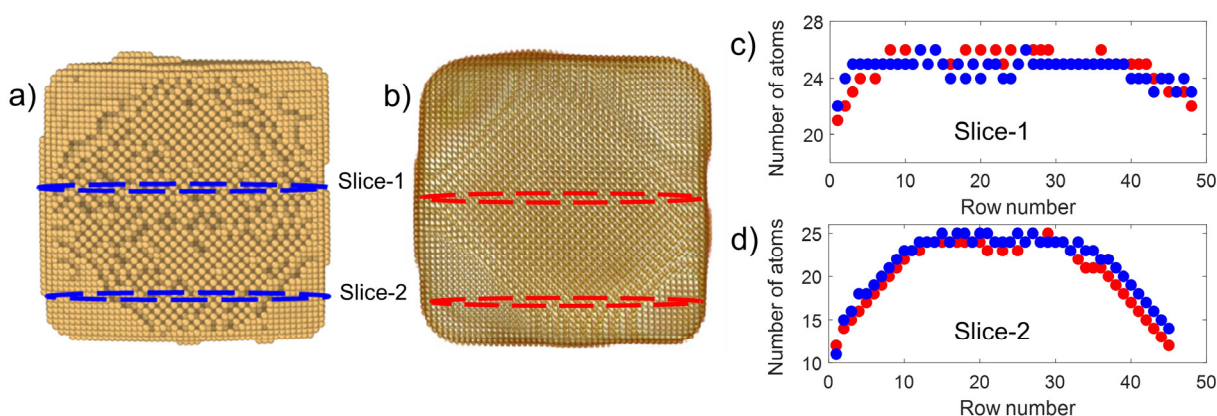


Figure 2.9 Comparison of 3D reconstructions by atom counting/relaxation and high-resolution electron tomography. a) Reconstruction based on the atom counting/relaxation approach. b) Reconstruction of a Pt NP using high-resolution tomography. c,d) Comparison of atom counts from slice-1 and slice-2.

2.4. Conclusion

In this chapter, the concepts that are used and extended in the remaining parts of this thesis have been introduced. First, an overview of the basic concepts of image formation for ADF STEM imaging mode was given. I also introduced multislice image simulations and highlighted some important aspects to consider when performing image simulations for quantitative analysis of STEM images. The Z-contrast and thickness dependence of ADF STEM images makes them suitable to extract quantitative structural information. Therefore, throughout this thesis, ADF STEM images are used to investigate 3D atomic structural information. In this thesis, I use the combined simulation and statistics-based atom counting approach, where the outcome of statistics-based atom counting results is validated with STEM image simulations to accurately and precisely quantify the atomic structure from ADF STEM images. Therefore, in this chapter, the principles of the quantitative STEM using statistical parameter estimation theory were described. This

framework enables one to accurately estimate the projected atomic column positions and the SCSs, which quantify the total intensity of electrons scattered towards the annular detector from a given atomic column. These SCSs are used to count the number of atoms in each atomic column with single-atom sensitivity as long as the ADF STEM image provides sufficiently high SNR. In this chapter, I also explained the basic principles of atomistic simulations, specifically focused on MD simulations. The 3D characterization of NPs by combining atom counting results and MD structural relaxations was also demonstrated. So far, this approach has been applied to free-standing particles roughly symmetrical along the electron beam. However, this methodology needs to be further evaluated for *in situ* experiments of metallic NPs lying on an oxide support as often used in catalysis. Within this perspective, each step of this method is optimized in Chapter 3 and Chapter 4.

Appendix A: Interpretation of ICL

To count the number of atoms located in the projected atomic columns, the distribution of measured SCSs is decomposed using a Gaussian mixture model, as explained in Section 2.2. The Gaussian mixture model describes the probability that a specific SCS value is observed, and the components of the model are defined as normal components with a constant width (Equation 2.35).¹⁶⁸ The component width describes the amount of fluctuation on the SCSs, corresponding to the atomic columns containing the same number of atoms, from the mean value. The component width and other parameters of the Gaussian mixture model (Equation 2.34) can be estimated using the maximum likelihood estimator for a fixed number of components G . To identify the correct number of components G in the Gaussian mixture model, the ICL criterion is evaluated as a function of the number of components.¹⁶⁸ The purpose of this section is to get more insight in the ICL criterion.

In the ICL criterion (Equation 2.37), the first term, $-2\log L(\hat{\Psi}_G)$, represents the log-likelihood function of the unknown parameter vector $\hat{\Psi}_G$ of Gaussian mixture model for a given set of measured SCSs. This term measures the goodness of model fit. As an example, Figure 2.10a shows a noise realization of the simulated Au nanowedge with an incoming electron dose of $N_d = 10000 e^-/\text{\AA}^2$ (the same system as in Figure 2.5). The estimated SCSs corresponding to all projected atomic columns are visualized in Figure 2.10b. The evaluation of the first term of ICL with respect to component number is presented in Figure 2.10c. It can be seen that the first term of ICL, $-2\log L(\hat{\Psi}_G)$, decreases, and so maximizes the likelihood function $L(\hat{\Psi}_G)$ of the parameter vector $(\hat{\Psi}_G)$ of the Gaussian mixture model, with an increasing component number. Since the Gaussian mixture model applies the same width for each component, the term represents log-likelihood function improves by adding extra components having a width as small as possible to decompose the measured SCSs into normal distributions with the largest probability. However, this may not correctly describe the true stochastic characteristics of the observations and degrade the model quality.

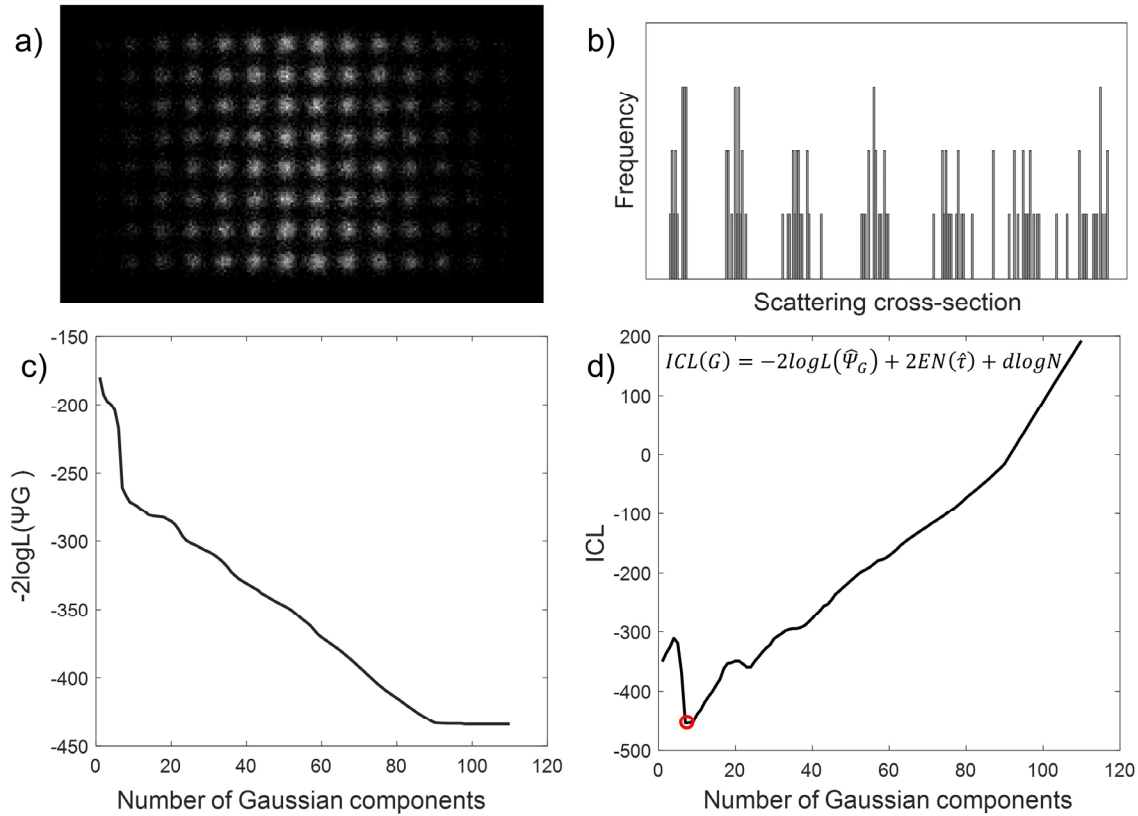


Figure 2.10 (a) A noise realization of the simulated Au nanowedge with an incoming electron dose of $N_d = 10000 e^-/\text{\AA}^2$. b) The measured SCSs corresponding to atomic columns shown in (a). c) The evaluation of the first term of ICL with respect to component number. d) The evaluation of ICL with respect to component number. The correct component number at $G = 7$ is indicated as a red circle.

The second term of the ICL (Equation 2.37) thus aims to balance the model fit and model quality by introducing a penalty term ($2EN(\hat{t}) + d\log N$). The penalty term is dependent on the number of atomic columns, the number of parameters in the mixture model, and the overlap between the neighboring Gaussian components. In this manner, ICL evaluates the statistical significance of an extra component in the model: ¹⁷³ while the first term decreases with an increasing number of components, the penalty term increases with increasing order. Eventually, the ICL reaches a minimum value at the correct component number, as shown in Figure 2.10d.

Here, it has been observed that ICL almost equal-likely favours the models with 8 and 9 components with the model corresponding to the true component number at 7. For better visualization, a magnified version of the ICL criterion evaluated as a function of the number of Gaussian components is presented in Figure 2.11a. The Gaussian mixture models and resultant atom counting maps for the selected component numbers at $G = 7$, $G = 8$ and $G = 9$ are shown in Figure 2.11b-d, respectively.

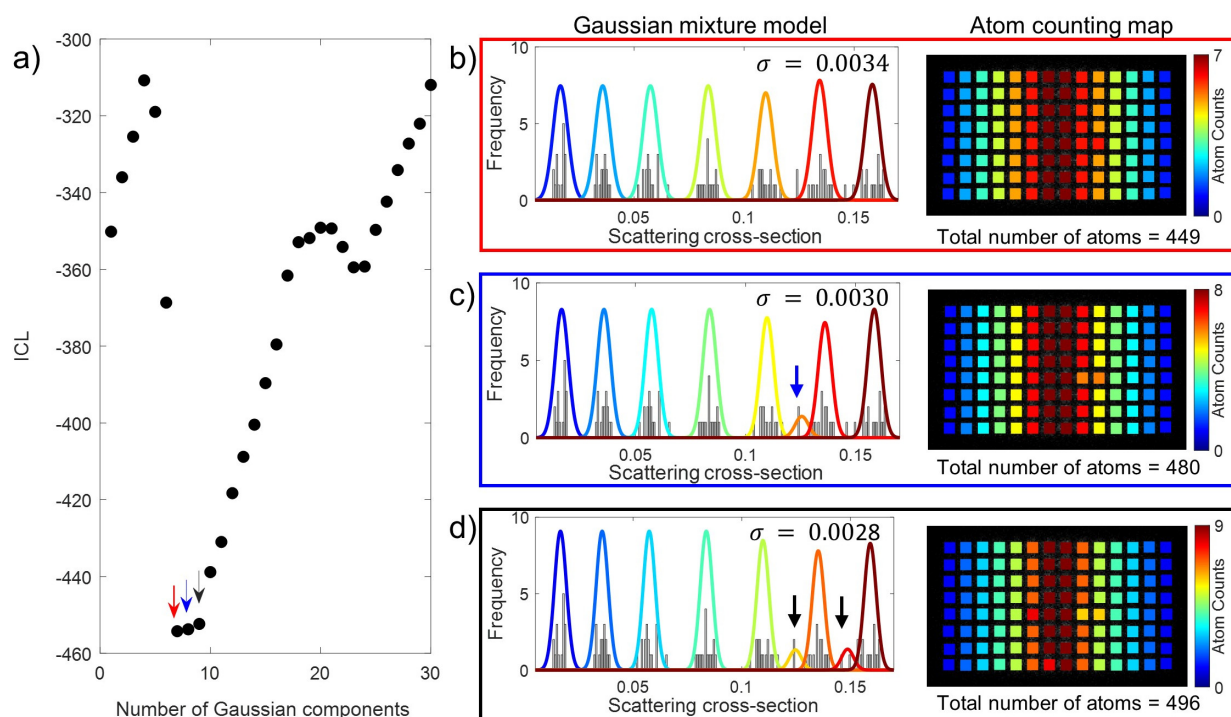


Figure 2.11 a) A magnified visualization of the ICL criterion which is shown in Figure 2.10d. (b-d) present Gaussian mixture models and atom counting maps for $G = 7$, $G = 8$ and $G = 9$ components as shown in (a) by purple, black and gray arrows. Extra components in the Gaussian mixture models are shown as blue and black arrows for the selected $G = 8$ and $G = 9$ number of components, respectively. The width of Gaussian components σ for each selected component number in (a) is indicated on each Gaussian mixture model in (c) and (d).

Observing very similar ICL values for the mixture models having 8 and 9 components with the corresponding value of the 7 components is related to the contribution of the first term of ICL. As explained above, the likelihood function $L(\hat{\Psi}_G)$ of the parameter vector $(\hat{\Psi}_G)$ of the Gaussian mixture model promotes assigning additional components having a smaller width to decompose the distribution of SCSs into homoscedastic components with the largest probability. However, the Poisson-like distributed SCSs corresponding to atomic columns containing the same number of atoms are not identical but fluctuate around an average SCS. Moreover, depending on the imaging parameters, the fluctuation in SCSs from their mean value often becomes larger for a thicker atomic column compared to the columns having a lower number of atoms.²⁰⁷ This results in an increase in the component width. Therefore, ICL favours the models with 8 and 9 components where extra components are added for larger SCSs. In this manner, the width of components is reduced (see Figure 2.11b-d) to attain the largest probability for a given SCS. The extra components added into the Gaussian mixture models are indicated as a blue arrow in Figure 2.11c for $G = 8$ components and indicated as black arrows in Figure 2.11d for $G = 9$ components.

It is important to note that, in this example (Figure 2.10 and Figure 2.11), Poisson noise was included that results in components with an increasing width for an increasing SCS value, since the variance of a Poisson distributed variable equals its expected value. However, the model with

homoscedastic components is applicable in experiments since many other contributions will affect the width of the components which are independent of the expected value of the SCSs, including the carbon support, different vertical onset of columns of the same number of atoms, intensity transfer between the columns, and the influence of neighbouring columns of different number of atoms.

Appendix B: Validation of EAM potential for Au and Pt systems

In this thesis, MD simulations were performed using EAM for Au¹⁹⁰ and Pt atoms.¹⁹² The lattice parameter is an important parameter for identifying crystal structure, phase identification, and physical properties. Therefore, the validity of EAM for the MD simulations of Au-Pt systems was first tested in terms of lattice parameters. The lattice parameters of Au and Pt were calculated based on the average energy per atom values corresponding to created FCC input structures having different lattice constants by employing EAM potentials. The calculations were performed with periodic boundary conditions. The change in energy with respect to the lattice parameter of Au and Pt FCC crystals is shown in Figure 2.12. The minimum value of each graph (black triangles in Figure 2.12) provides the lattice constant of Pt and Au, which are tabulated in Table 2.2 and Table 2.3, respectively.

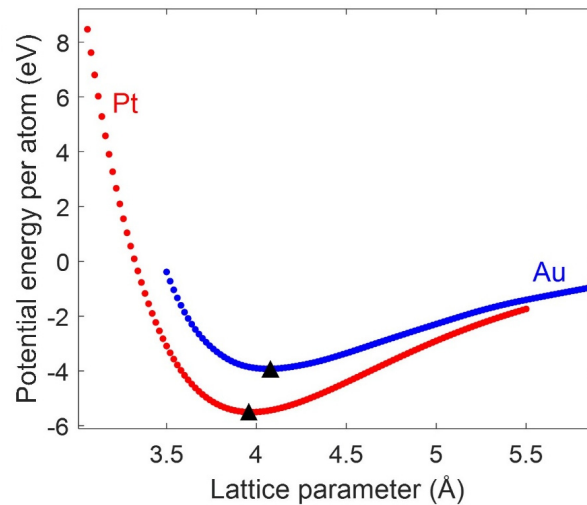


Figure 2.12 Potential energy change graphs of Au and Pt with respect to different lattice constants.

For nanostructured metals, the surface energy is an important descriptor that affects their shape and stability.^{208,209} Therefore, the surface energies of (100), (110), and (111) surfaces of Au and Pt were calculated by employing EAM. The surface energy of each facet can be calculated as:^{210,211}

$$\gamma = \frac{E_{slab} - NE_{bulk}}{2A} \quad , \quad (2.57)$$

where E_{slab} is energy of a slab composed of N layers, E_{bulk} is the energy of the bulk material per one layer and A is the area of the surface. The factor 2 results from the fact that the slab has two surfaces. For each slab, a layer of surface primitive cell having (111), (100) or (110) surface was

created perpendicular to the z-axis. Then, each system was extended along the x- and y-axis, and 4 layers were stacked along the z-axis followed by 10 Å thick vacuum, in accordance with the literature.^{210,211} To obtain E_{slab} , the positions of all atoms located in created each slab were relaxed by the conjugate gradient energy minimization method at 0 K with a force-stopping convergence criterion of 10^{-8} eV/Å. The calculated surface energies of (111) surface facet $\gamma_{(111)}$, (100) facet $\gamma_{(100)}$, and (110) facet, $\gamma_{(110)}$ are tabulated in Table 2.2 and Table 2.3.

According to Table 2.2, it can be seen that the predicted lattice parameter of Pt by EAM potential¹⁹² and corresponding energy per atom agree well with *ab initio* calculations. The calculated surface energies of Pt in this work are slightly lower than the reported values, but they present the same trend ($\gamma_{(111)} < \gamma_{(100)} < \gamma_{(110)}$) with the previously reported values.^{208,209,212} Therefore, it can be concluded that the EAM potential gives the structural parameters and surface energies comparable with *ab initio* calculations that show the reliability of EAM to model Pt inter-atomic interactions.

Table 2.2 Computed parameters of Pt obtained predicted by EAM potential.¹⁹²

Parameters	EAM ¹⁹²	<i>Ab initio</i>
Lattice properties		
a (Å)	3.98	3.92 ²¹³
E_0 (eV/atom)	-5.51	-5.77 ²¹³
Surface energies		
$\gamma_{(111)}$ (J/m ²)	1.30	1.34-1.98 ²¹⁴
$\gamma_{(100)}$ (J/m ²)	1.42	1.81-1.92 ²¹⁵⁻²¹⁷
$\gamma_{(110)}$ (J/m ²)	1.43	1.85-2.49 ^{215,216,218}

According to Table 2.3, it can be seen that the calculated lattice parameter of Au and the corresponding energy per atom value by using EAM¹⁹⁰ are in excellent agreement with previously published results which were obtained from *ab initio* calculations. Moreover, the predicted surface energies of Au for the (100), (110), and (111) surfaces are also in a reasonable agreement with the previously reported values. Here, the obtained values exhibit the same ordering $\gamma_{(111)} < \gamma_{(100)} < \gamma_{(110)}$ which demonstrates the stability of (111) facets compared to {100} and {110} surface.

In this thesis, the structural transformations of Au NPs upon heating and intense light illumination are also investigated. Therefore, in addition to the lattice properties and surface energies, employed EAM should accurately reproduce the stacking fault energy as well as FCC-HCP and FCC-BCC lattice energy differences of Au lattice. The reported parameters of Au obtained by using EAM potential, which is used to define the interaction between Au atoms in this thesis, are tabulated in Table 2.3. From Table 2.3, it can be seen that the EAM potential reproduces the stacking fault energy and structural energy differences in a reasonable agreement with the experimental information. Grochola et al.¹⁹⁰ stated that the slight error in FCC-HCP energy difference is due to

the fact that these reported values are room-temperature thermodynamically derived values. However, the overestimation of FCC-HCP energy, as in Table 2.3, is often preferred instead of an underestimation as it would make FCC more likely to be stable.

Table 2.3 Computed and previously reported parameters of Au predicted by EAM potential.

Parameters	EAM ¹⁹⁰	Experiment or <i>ab initio</i>
Lattice properties		
a (Å)	4.08	4.078 ²¹³
E_0 (eV/atom)	-3.92	-3.93 ²¹³
Surface energies		
$\gamma_{(111)}$ (j/m ²)	0.99	0.72–1.51 ^{210,214,219–221}
$\gamma_{(100)}$ (j/m ²)	1.08	0.87- 1.63 ^{210,219}
$\gamma_{(110)}$ (j/m ²)	1.22	0.91-1.70 ^{210,219}
Stacking fault energy (j/m ²)	0.043 ¹⁹⁰	0.032-0.055 ^{213,222}
Structural energy differences (ΔE)		
FCC – HCP (eV/atom)	0.009 ¹⁹⁰	0.003 ²¹³
FCC – BCC (eV/atom)	0.06 ¹⁹⁰	0.04 ²¹³

According to the calculated values in this section and previously reported results, the EAM potential, developed by Grochola et al. ¹⁹⁰, shows a satisfactory agreement to the experimental observations and *ab initio* calculations, in terms of lattice properties, surface energies, stacking fault energy, as well as FCC-HCP and FCC-BCC lattice energy differences. This potential has been successfully applied in the literature to investigate the stability of various nanorods with differing ratios of surface facets, ²²³ surface driven crystallization of icosahedral clusters, the instability of FCC structured NPs during vapor growth, ²²⁴ size and temperature-dependent aggregation of Au NPs, plastic deformation of Au nanocrystals, ²²⁵ dislocation nucleation and stacking fault formation in Au nanowires, ²²⁶ mechanical properties and coarsening of nanoporous Au. ²²⁷ Moreover, throughout this thesis, the outcome of MD simulations is compared with the experimental observations based on 2D (S)TEM images and 3D reconstructions by electron tomography. Very good agreement between the simulations, and the experimental observations confirms that the MD simulations employing EAM for Au ¹⁹⁰ and Pt atoms ¹⁹² can be used to model the atomistic processes.

Chapter 3. 3D atomic structure of supported Au nanoparticles at high temperature*

Au NPs deposited on CeO₂ are extensively used as thermal catalysts since the morphology of the NPs is expected to be stable at elevated temperatures. Although it is well known that the activity of Au NPs depends on their size and surface structure, their 3D structure at the atomic scale has not been completely characterized as a function of temperature. In this chapter, to overcome the limitations of conventional electron tomography, atom counting applied to aberration-corrected STEM images is combined with MD structural relaxation. In this manner, an atomic resolution 3D investigation of supported Au NPs is performed. The results presented in this chapter enable characterizing the 3D equilibrium structure of single NPs as a function of temperature. Moreover, the dynamic 3D structural evolution of the NPs at high temperatures, including surface layer jumping and crystalline transformations, is studied.

* This chapter is based on the following paper:

Liu, P.[†], [Arslan Irmak, E.](#)[†], De Backer, A., De wael, A., Lobato, I., Béch , A., Van Aert, S., Bals, S. Three-dimensional atomic structure of supported Au nanoparticles at high temperature. *Nanoscale* (2021) doi: 10.1039/D0NR08664A.

[†] Equal contribution to the published work.

My contribution consisted of implementing post-processing of STEM images, STEM detector characterization, applying combined simulation and the statistics-based atom counting method, designing and performing molecular dynamics simulations, as well as their analysis and discussion.

3.1. Introduction

Understanding the catalytic activity of CeO₂ supported Au NPs has been an intensive research topic for the last decades. Supported Au NPs smaller than 3–5 nm are highly effective catalysts in a wide range of catalytic reactions, e.g. CO oxidation and the water–gas shift reaction.^{33,34,206,228,229} It is generally recognized that the activity of Au NPs depends on their size and surface structure. For example, it has been observed that the presence of highly under-coordinated atoms or stepped facets at the surface promotes the adsorption of CO molecules or O₂ molecules.^{33,230,231} However, the general shape and surface facets of supported NPs are also highly dependent on environmental conditions, such as pressure and temperature.^{232–234} Quantitative investigations of the atomic configuration at the surface under relevant conditions are thus essential to reveal the active sites of the NPs.

To study these effects, *in situ* TEM has been used extensively. For example, it was shown that CeO₂ supported Au NPs yield a rounded morphology in an oxidative atmosphere, whereas they appear faceted in a reducing environment.²³⁵ A reversible dynamics for Au NPs under reactive environments^{116,117,235,236} was furthermore revealed, yielding crystalline transformations¹¹⁷ and surface atom diffusion.¹¹⁶ Phase transformations and morphological evolution of free-standing Au NPs have been extensively studied,²³² particularly at temperatures approaching the melting point of Au NPs.^{116,235} However, most of these observations are based on 2D information only, which is not sufficient to connect the entire 3D structure of the catalysts to their properties.

In this chapter, Au NPs deposited on CeO₂ are investigated. Supported Au NPs are used as thermal catalysts since it is expected that their morphology is stable at elevated temperatures. Experimentally imaging changes of the 3D atomic structure of catalytic NPs at high temperatures, including facet distribution and surface dynamics, is technically challenging but essential for design and control over the catalyst structure and performance. Although high-resolution electron tomography has been used to investigate the atomic structure of NPs in 3D, the combination with *in situ* measurements is far from straightforward because of several technical and more fundamental reasons, as explained in Section 1.5. Since catalysts can be in active or nonequilibrium states, conventional tomography approaches cannot be applied to investigate the fast changes that supported catalyst NPs undergo when being exposed to a relevant environment. Therefore, in this chapter, a 3D characterization method is applied based on counting the number of atoms in an atomic column from ADF STEM images and MD simulations to investigate the 3D atomic structure of supported Au NPs.^{81,110} This enables direct estimation of the 3D shapes of the NPs from the experimental observations.

As it has been shown in Section 2.2, the number of atoms in an atomic column of a NP can be counted with single-atom sensitivity from ADF STEM images provided that they yield a sufficiently large SNR.^{96,173} Therefore, Section 3.2 starts with ADF STEM image restoration and a registration performed to improve the SNR of the images. Also, in the same section, main steps of a combined simulation and statistics-based atom counting method are explained. In Section 3.3, the equilibrium morphology of CeO₂ supported Au NPs at different temperatures is investigated in

a quantitative manner. In Section 3.4, the dynamic 3D structure evolution of the NPs at high temperatures is characterized, including surface layer jumping and crystalline transformations.

3.2. Methods

3.2.1. ADF STEM image acquisition

Au NPs on a CeO₂ support were prepared by a physical sputtering coating method.¹¹⁶ Commercial CeO₂ powder (Sigma-Aldrich) was dispersed in ethanol and drop-casted on a DENSsolutions Nano-chip with a SiN membrane. Next, the chip was mounted in a DENSsolutions Wildfire double tilt holder and inserted into a Thermo Fisher Scientific Themis Z microscope. After heating at 500 °C in the vacuum of the microscope column for 1 h, Au NPs on CeO₂ was obtained for further *in situ* STEM experiments at 300 kV. The supported Au NPs were studied at 21 °C, 300 °C, 400 °C, 500 °C and in ultrahigh vacuum conditions. The image acquisition parameters of ADF STEM images are tabulated in Table 3.1. Sample preparation and the acquisition of ADF STEM experimental images were performed by Dr. Pei Liu.

Table 3.1 Image acquisition parameters.

Parameter	Figure 3.1, 3.4-3.6	Figure 3.7	Figure 3.8
Acceleration voltage (kV)	300	300	300
3 rd order spherical aberration (μm)	0.467	0.424	0.244
5 th order spherical aberration (μm)	19.8	-874	-
Convergence semi-angle (mrad)	30.0	30.4	21.4
Detector inner angle (mrad)	46.1	46.1	46.0
Detector outer angle (mrad)	198.6	198.6	215.0
Image size (pixels)	2048 x 2048	1024 x 1024	512 x 512
Beam current (pA)	50	50	50
Frame time (s)	2.52	0.629	2.00

3.2.2. ADF STEM image restoration and registration

A combination of different distortions can be observed in experimental ADF STEM images, such as sample drift, scan distortion or scan noise.^{81,82} These distortions depend on the instrument environment, scanning instabilities, scan-speed and electron dose.^{81,82} Indeed, Altantzis et al.⁸¹ showed that the distortions are likely related to particle rotation and become dominant with increasing acquisition time. Moreover, during *in situ* heating experiments, increased atomic movement due to thermal excitation or sample rotation while scanning may hamper reliable quantification.^{81,82,88,237} To overcome these limitations and to minimize the effect of particle rotation, multiple consecutive time frames were acquired with a low beam current of 50 pA. Recording multiple consecutive frames allows separating time-varying scanning distortions from sample information.⁸³ ADF STEM images of a supported Au NP at different temperatures are presented in Figure 3.1.

An in-house developed deep CNN was used to correct distortions. This approach is based on the use of a CNN that directly learns how to differentiate between distorted and undistorted ADF STEM images. By training the CNN, it implicitly learns to detect the presence of distortions and correct them, regardless of the level and combination of distortions present in the image. The CNN used in this thesis was trained using simulated ADF STEM images in the presence and absence of different types of distortions that can be expected for the experimental ADF STEM images. Training the CNN for the restoration of ADF STEM images was carried out by Dr. Ivan Lobato at EMAT and more details can be found in ref⁸¹.

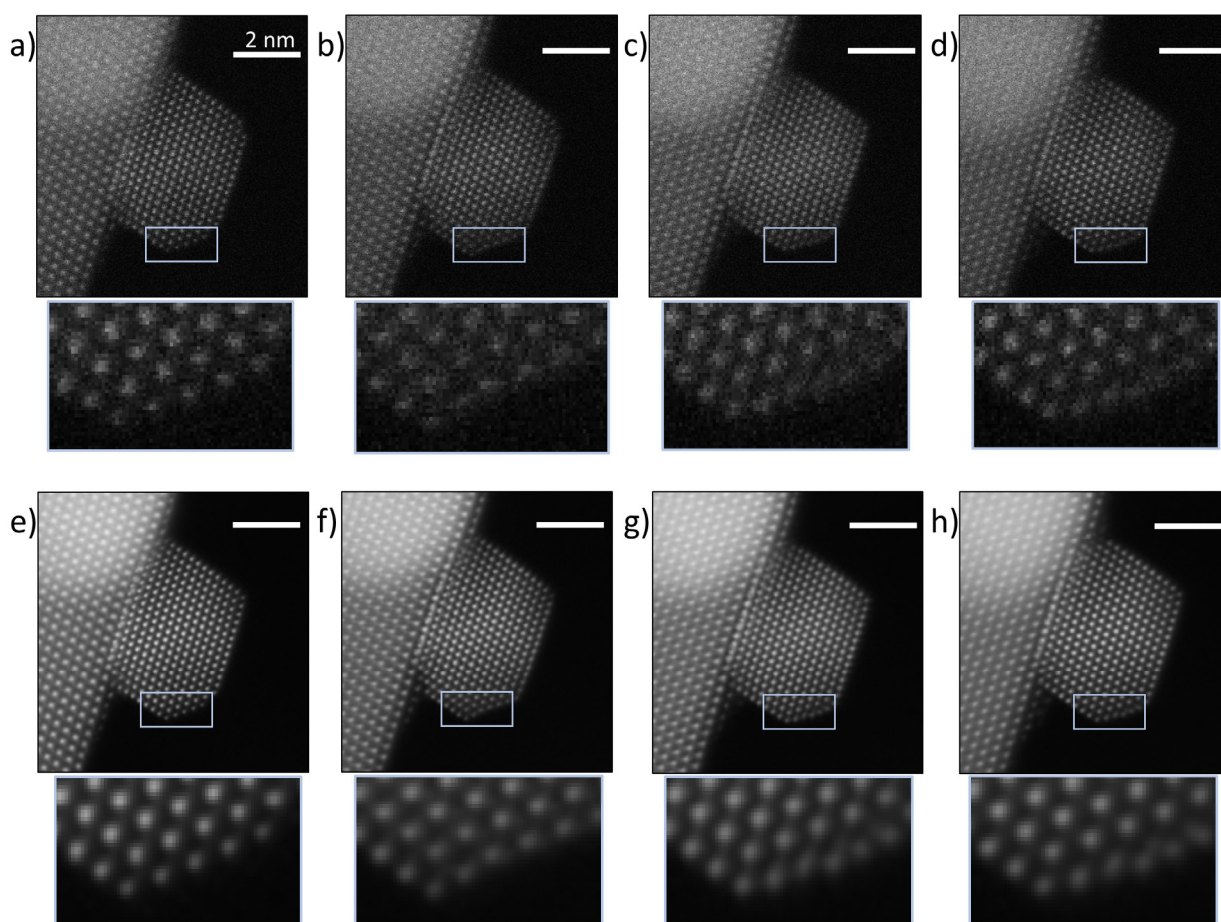


Figure 3.1 Original ADF STEM images of a supported Au NP at (a) room temperature, (b) 300 °C, (c) 400 °C, (d) 500 °C. Corrected and averaged images (based on ten consecutive frames) of the same Au NP at (e) room temperature, (f) 300 °C, (g) 400 °C, (h) 500 °C. Close-up images from the bottom part of the NP are given below each image.

Sample drift or rotation can be observed as a shearing of the known crystallographic angles and becomes more pronounced with slower scans. To correct sample drift or rotation, each time series of corrected images was then used as an input for an in-house developed rigid and non-rigid registration procedures.⁸³ In rigid registration, all points in the restored consecutive ADF STEM images are shifted with respect to each other by a single vector. Rigid registration assumes that the drift rate remains constant. However, the reported studies demonstrated that sample drift can occur

at different rates.^{83,238} In non-rigid image registration, different sub-regions of an image can therefore be shifted by different registration vectors. For non-rigid registration, the accelerated demons method^{83,239–241} has been implemented by Dr. Ivan Lobato in an iterative manner where differences between images are used to infer the direction of local motion.

Next, every series of individually corrected and registered ADF STEM images was averaged to increase SNR. Averaging of the restored and registered 2D images allowed clearly resolving projected atomic columns, especially at the surface region. The resulting corrected and averaged images of the supported Au NP at different temperatures are shown in the second row of Figure 3.1. It should be noted that to investigate the non-equilibrium transformations of supported Au NPs presented in Section 3.4, no averaging of consecutive corrected and registered images was performed.

3.2.3. Normalization of ADF STEM images

Image intensities in the simulated ADF STEM images are expressed in fractions of the incident electron dose. In order to compare the experimental observations with image simulations in a quantitative manner, the experimentally acquired ADF STEM images were normalized using the so-called “detector scan”. To obtain the detector scan, a sharp image of the probe was created on the detector plane in the absence of a specimen and the image of the probe is scanned over the detector under vacuum conditions. Figure 3.2a shows the acquired experimental detector scan. Here, it can be seen that the sensitivity of the detector is not homogeneous; instead, the intensities are proportional to the local sensitivity of the ADF STEM detector surface.^{152,156,242} For example, the area right to the inner hole shows a more variable response as compared to the other regions.

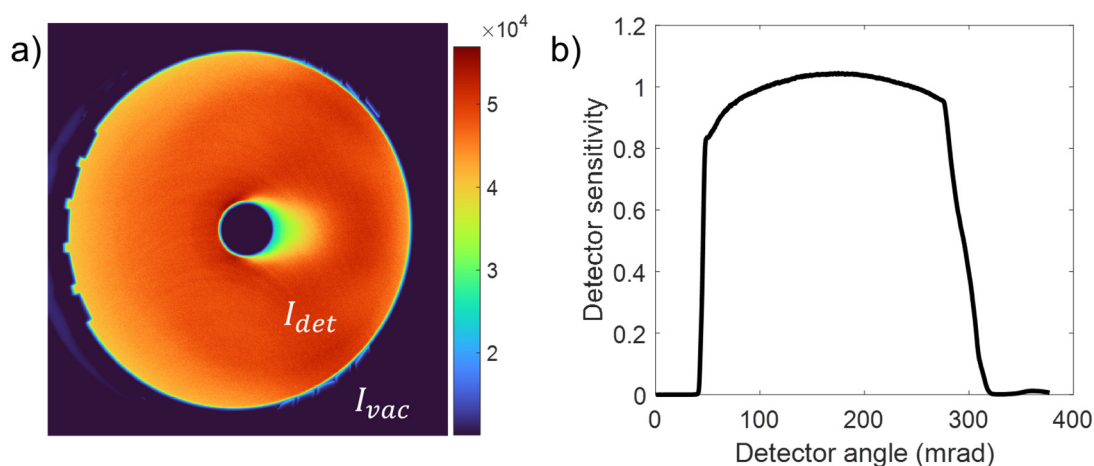


Figure 3.2 a) ADF STEM detector scan. b) Radial sensitivity curve.

For normalizing the experimental images, the first step is to measure the image mean intensity in vacuum I_{vac} , and the averaged detector intensity I_{det} (Figure 3.2a). Both values were extracted from the detector scan by using a threshold value with Otsu’s method.²⁴³ Otsu’s method is a multilevel image thresholding algorithm for the reduction of a gray level image to a binary image. These measured values were used to normalize the experimental ADF STEM images:^{152,156,244}

$$I_{norm} = \frac{I_{raw} - I_{vac}}{I_{det} - I_{vac}}, \quad (3.1)$$

where I_{raw} and I_{norm} represent the intensity of an experimental image before and after normalization.

3.2.4. Multislice simulations to create library values

In the combined simulation and statistics-based atom counting method, experimental observations were quantitatively validated by means of independent multislice simulations. For this purpose, a so-called library of simulated SCS was created by multislice simulations. In order to accurately simulate thermal diffuse scattering during the multislice simulations, the frozen phonon model with 100 phonon configurations was used. The simulation parameters were chosen in accordance with the experimental imaging conditions, which are tabulated in Table 3.1. For the defocus value, the Scherzer condition was assumed. Moreover, the temperature effect was included in the simulations by defining the temperature-dependent RMSD values based on the parameterized DWF, as explained in Section 2.1.

To perform reliable simulations, the non-uniform detector sensitivity was also taken into account.^{153,155,242} To do so, after normalizing the detector scan by using Equation 3.1, the scan was averaged azimuthally, resulting in a radial sensitivity curve as shown in Figure 3.2b. For multislice simulations by the MULTEM software, a 2D detector sensitivity map should be supplied. Therefore, a new 2D detector map was created by the interpolation of the 1D radial sensitivity curve. Afterward, the interpolated detector sensitivity was set to 0 for the regions corresponding to angles that are smaller than the detector inner angle or larger than the outer angle. The final detector map was then loaded into the MULTEM software. Although azimuthal averaging neglects the anisotropy of the experimental detector, it has been stated that it is a reasonable approach if the scattering distribution is approximately rotationally symmetric. Previous studies have shown that high angle scattering, which forms ADF STEM signals, well fulfill this approximation.^{156,242}

For the simulations of the SCS library values as a function of thickness, one unit cell of a periodic Au FCC structure along a [110] zone axis was scanned, corresponding to the experimentally investigated Au NP shown in Figure 3.1. The library values were computed by measuring the total intensity corresponding to the simulated unit cell for each thickness and dividing the measured total intensity by the total number of Au atoms in one unit cell. The scanned unit cell of Au FCC structure from [110] zone axis is shown in Figure 3.3a. In Figure 3.3b, the computed library SCS values as a function of thickness are compared in the presence and absence of the detector sensitivity map and the temperature effect. The latter accounts for the increase in thermal diffuse scattering with temperature. It can be seen that, for example, when ignoring the nonhomogeneous detector sensitivity and temperature effect, a specified SCS would be matched with a thickness of 13 atoms, whereas it actually corresponds to around 15 atoms (see green dashed arrows in Figure 3.3b), limiting the error by around ~2 atoms per atomic column. Including the detector sensitivity and temperature effect is therefore of crucial importance in order to generate a correct library of simulated SCS values. Moreover, the individual effect of temperature and nonhomogeneous ADF

STEM detector surface on the simulated SCS library values are shown in Figure 3.3c and Figure 3.3d, respectively.

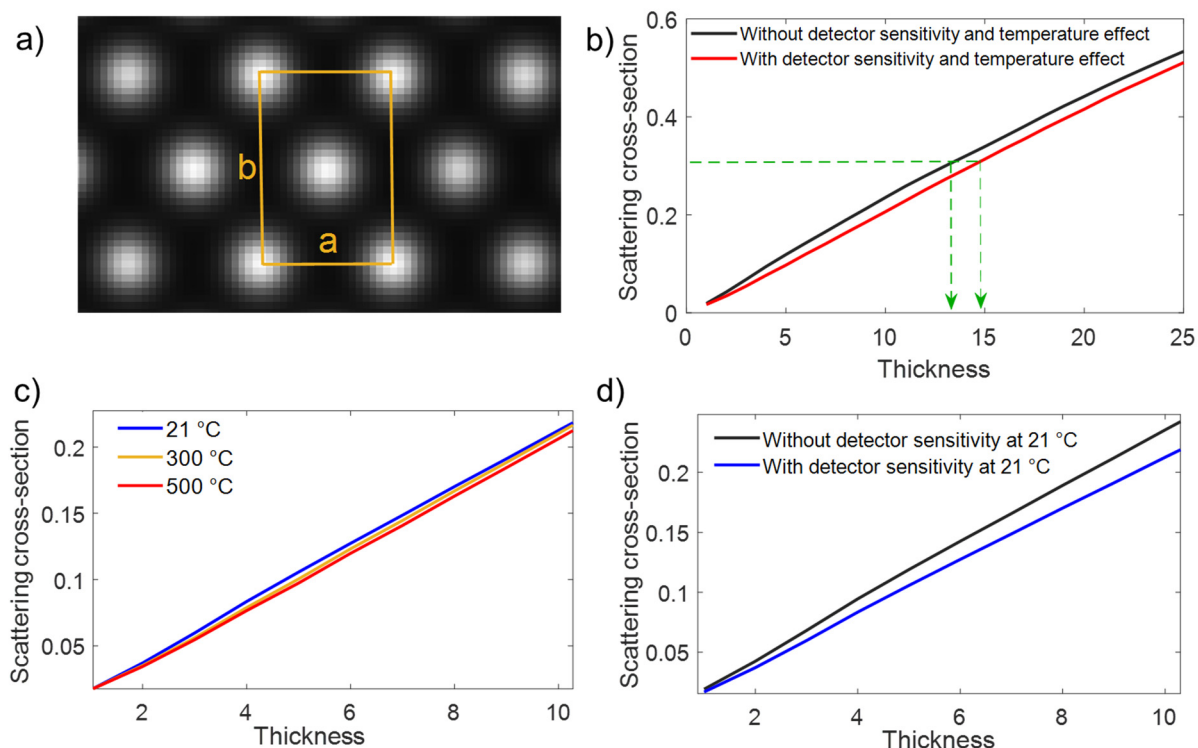


Figure 3.3 Multislice simulations to create library SCS values. a) Periodic Au FCC structure along a [110] zone axis. The scanned unit cell of the structure is shown by a yellow box. b) Simulated SCS library values including the detector nonuniformity and temperature effect into multislice simulations. Individual effect of temperature (c) and detector sensitivity map (d) on the library values.

3.2.5. Combined simulation and statistics-based atom counting

The statistics-based counting procedure was first performed independently from the multislice simulations.^{96,99} In this method, as introduced in Section 2.2, the intensities in the ADF STEM images were modeled as a superposition of 2D Gaussian functions. Then, the unknown parameters and the volumes under the Gaussian peaks, i.e. the SCSs, were estimated by fitting an incoherent parametric imaging model to the experimental images using the criterion of goodness of fit.

As an example, the parametric model of the normalized and averaged STEM image of the Au NP at room temperature (Figure 3.1e) is presented in Figure 3.4a. Next, from the volume under the Gaussian peaks of the parametric model, the SCS of each atomic column was measured. In a subsequent analysis, the distribution of the SCSs of all atomic columns was decomposed into overlapping normal distributions using a Gaussian mixture model analysis. The histogram of the estimated SCSs, together with the estimated mixture model and its individual components, is shown in Figure 3.4b. In order to identify the correct number of components in the Gaussian mixture model, the ICL criterion was evaluated as a function of the number of components (Figure 3.4c). Since there is more than one local minimum in the ICL criterion, a validation step was required.¹⁷³

Therefore, the computed library SCSs values from multislice simulations using the MULTEM software were used to validate the statistics-based atom counting results. Figure 3.4d shows the experimental mean SCSs corresponding to the selected 19 component number in the ICL criterion (Figure 3.4c) together with the computed library values under the same experimental conditions. The excellent match of the experimental and simulated SCSs validates the choice for 19 components. Here, the number of atoms associated with the first component corresponds to 2, and there are no atomic columns with 3, 4 and 5 atoms. The estimated number of Au atoms per column resulting from the combined simulation and statistics-based atom counting method is shown Figure 3.4e.

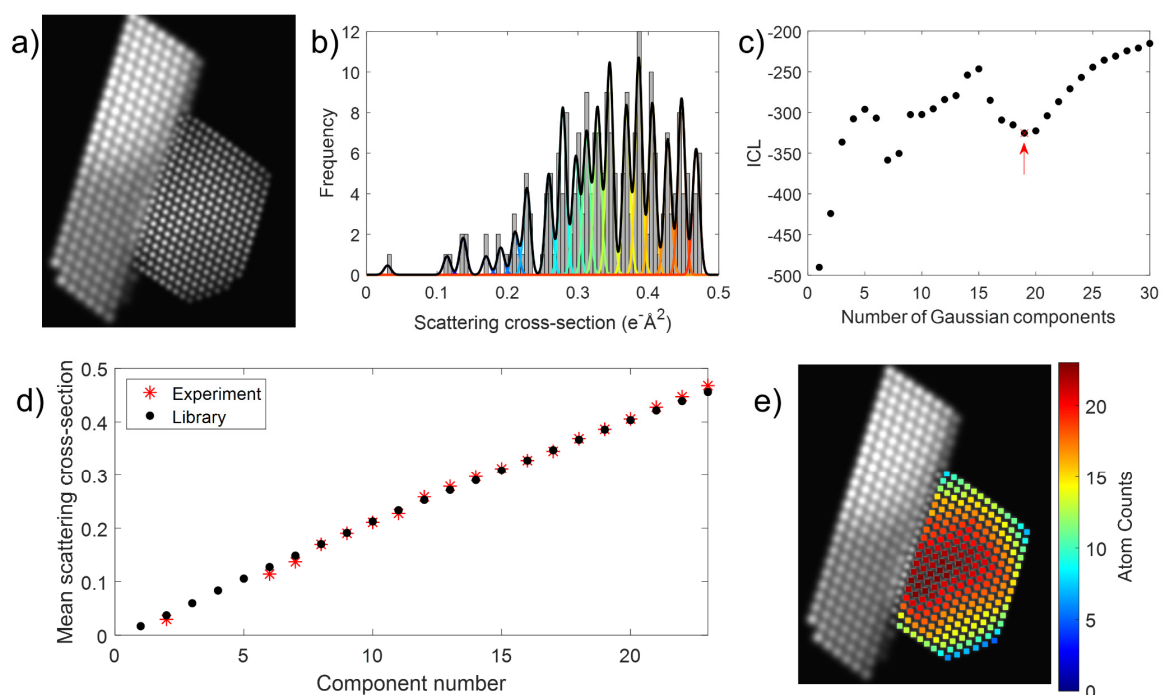


Figure 3.4 Summary of the combined simulation and statistics-based atom counting method. a) The parametric model of the normalized and averaged STEM image of the Au NP at room temperature presented in Figure 3.1e. b) Histogram of SCSs of the Au columns together with the estimated mixture model (black line) and its individual components. c) Evaluation of the ICL criterion. d) Comparison of the experimentally estimated mean SCSs with the simulated library SCSs. e) Number of Au atoms per column.

3.3. 3D equilibrium structure of supported Au NPs as a function of temperature

The averaged and normalized ADF STEM images of a supported Au NP at different temperatures are displayed in Figure 3.5a. It can be seen that the 2D projected shape of the NP remains almost the same up to 500 °C. Applying the combined simulation and statistics-based atom counting, it is found that the total number of detected atoms decreases from 3785 to 3676 (Figure 3.5b). Considering the total number of atomic columns indicated in Figure 3.5b, this means that on average less than one atom per column disappears, likely because of sputtering caused by the electron beam or due to the increased thermal vibrations, which may complicate the atom detection.

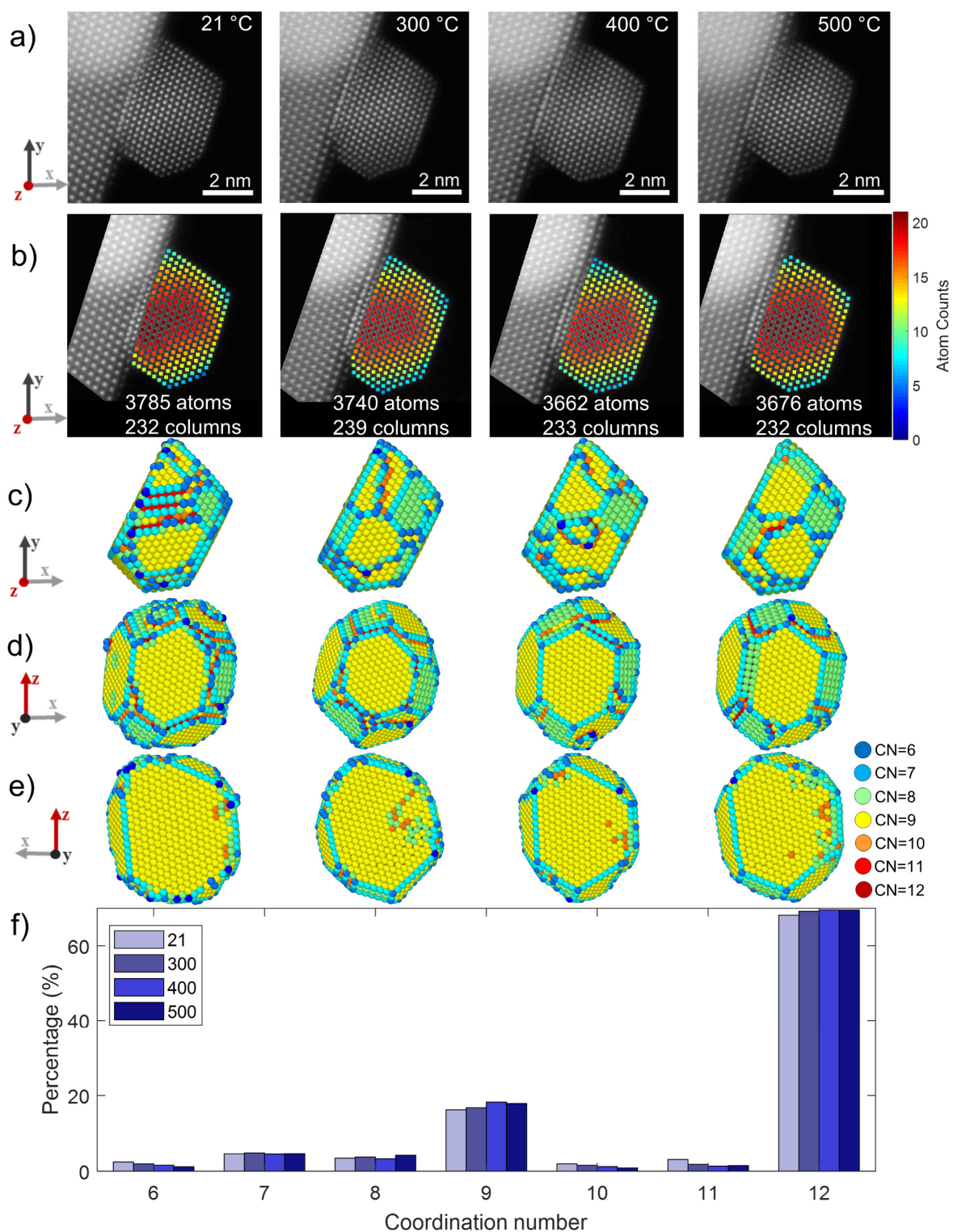


Figure 3.5 Structural characterization of a supported Au NP at different temperatures. a) Averaged and normalized ADF STEM images. b) Atom counting results. The total number of atoms and total number of atomic columns are labeled for each temperature. c-e) Side, top and bottom view of the relaxed structures. The atoms are presented in different colors according to the coordination numbers (CN). $\{111\}$ facets: yellow atoms, $\{100\}$ facets: green atoms, $\{110\}$ facets: light blue atoms. f) Coordination number histogram of all atoms at different temperatures.

The atom counting results were then used to generate 3D starting configurations by positioning the atoms in each atomic column parallel to the beam direction based on the Au FCC crystal structure and a [110] specimen orientation. All atoms were placed symmetrically around the central plane. First, the energy of the 3D models was minimized using the conjugate gradient method. Then, to obtain the equilibrium structures of the Au NP at different temperatures, a full MD structural relaxation with the EAM¹⁹⁰ was performed for each experimental temperature in the canonical ensemble for 5 ns. Hereby, the substrate was assumed to have a constant thickness, and a model for CeO₂ was generated based on the fluorite structure.^{245,246} To incorporate the interaction between the particle and the substrate, the LJ potential was used. The simulations were carried out without periodic boundary conditions and with a time step of 0.5 fs. Also, the total linear and angular momenta were conserved to avoid drift or rotation throughout the simulations of the supported Au NPs. All the 3D structures were visualized by the OVITO open visualization tool.²⁴⁷

Figure 3.5c-e show the side, top, and bottom view of the relaxed 3D structures. In order to further quantify our results, the coordination numbers of the atoms at different temperatures were determined (Figure 3.5f). The coordination analysis was applied through OVITO Python open-source scripts.²⁴⁸ The cutoff radius is an important parameter to control the range of neighbors taken into account during the coordination analysis. Here, the first minimum of the pair distribution function was used as a cutoff radius, which was found 3.48 Å.

In accordance with the literature,^{212,249} the NP has a truncated octahedron shape at room temperature, which is enclosed by {100} and {111} surface facets, as indicated by the color codes in Figure 3.5e, although small variations can be observed in the coordination number of the atoms located at the {111} interface due to the lattice mismatch between the NP and substrate. As the temperature increases, the percentage of atoms with a coordination number equal to 12 gradually increases, whereas the percentage of atoms with coordination number 10 and 11 decreases since the shape of the NP becomes more symmetric and round. Hereby, atoms displace from the surface to the interior of the particle. Although there is little change for the coordination numbers as a function of temperature, it should be noted that the shape of the local surface facets changes, as can be seen by comparing the results for different temperatures in Figure 3.5c-e. Since the coordination numbers are important in terms of the activity of the NP during catalysis, our quantitative 3D results prove that this specific particle is indeed expected to be thermally stable up to at least 500 °C.

It is known that the equilibrium shape of supported Au NPs depends on their size. Therefore, a comparison for NPs with different sizes was made in Figure 3.6, where the particle at the right is the same as the one in Figure 3.5. ADF STEM images of the NPs having a different number of atoms are shown in the first row. In addition to the size effect, the lattice mismatch between the Au NP (4.08 Å) and oxide substrate (5.41 Å) can also affect the shape of the supported NPs.^{190,212,245} Therefore, the positions of the atomic columns were fitted using statistical parameter estimation theory, and the projected atomic displacement maps of each NP were extracted according to the ideal positions of the Au atoms. The displacement maps are shown in the second row of Figure 3.6. Then, the same methodology as explained above was used to extract the shape and the coordination numbers as a function of temperature. The side and the bottom view of the relaxed 3D structures

are illustrated in the third and the fourth row, respectively. Finally, the coordination numbers are shown in the fifth row.

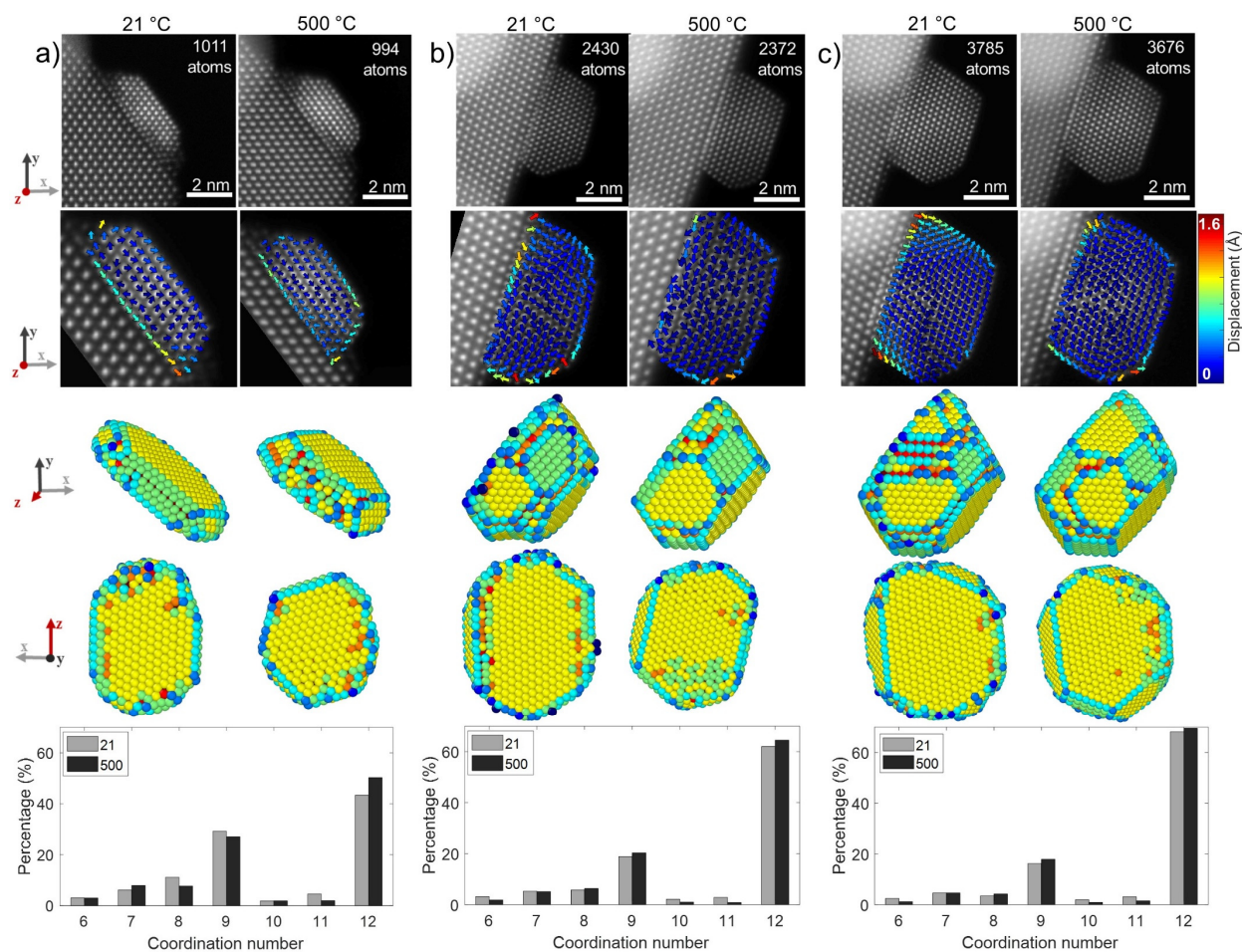


Figure 3.6 3D structural characterization of the supported Au NPs with different sizes at 21 °C and 500 °C. a) Au NP having around 1000 atoms. b) Au NP having around 2400 atoms. c) Au NP having around 3700 atoms. The atoms are presented in different colors according to the CNs (see Figure 3.5).

According to Figure 3.6a, high strain can be observed at the interface between the particle and the oxide substrate at room temperature. At 500 °C, on the other hand, the projected displacement map shows that the strain at the interface of this particle is more relaxed. This is likely related to the observation that the interface area is also reduced from approximately 13.7 nm² to 11.9 nm², which was measured from the 3D models. Accordingly, the NP grows in height and becomes more rounded and the percentage of 12-coordinated atoms increases significantly. Moreover, the contribution of the edge atoms (7-coordinated atoms) increases, accompanied by a decrease in {100} and {111} facets corresponding to 8 and 9-coordinated atoms. A similar mechanism is observed for the larger particle shown in Figure 3.6b. To relax the strain at the interface at high temperature, the area of the interface between the NP and the substrate is decreased from 20.6 nm² to 19.4 nm², which leads to a small rise in the percentage of atoms with a coordination number equal to 12. On the other hand, as the size of the Au NP increases (Figure 3.6c), the transformation of the morphology at higher temperature becomes less apparent, in accordance with literature.²¹²

As discussed above, although the contribution of the energetically more favorable {100} and {111} facets increases slightly, the interfacial area for the largest Au NP (Figure 3.6c) remains stable (around 23 nm²). Also, the morphology is maintained while increasing the temperature.

3.4. Non-equilibrium transformations of supported Au NPs at high temperature

To investigate the non-equilibrium shape transformations for this type of supported Au NPs, a time series of images at 400 °C was acquired after an initial acquisition time of 0.14 seconds (Figure 3.7a). At these temperatures, it has been shown previously that entire surface layers of atoms abruptly displace, a phenomenon which is referred to as “layer jumping”.¹¹⁶ To reliably count the number of atoms from a time series of images, a hidden Markov model, which explicitly models the possibility of structural changes over time, was used. The hidden Markov model was performed by Dr. Annelies De wael and detailed information about this model can be found in ref²⁵⁰. The atom counting results are displayed in Figure 3.7b. The total number of atoms was found to be close to 1125 for all frames, except for frame 3, for which the number of atoms was equal to 1103. This observation is related to the layer jump, which can be seen more clearly in Figure 3.7c, illustrating the counting difference between the consecutive frames. The blue colour code indicates a decreasing number of atoms, and the red colour code corresponds to an increase in the number of atoms. Figure 3.7 demonstrates that a layer on the (010) surface facet disappears on the third frame and reappears in frame 4.

Based on the counting results, input structures for MD simulations were again created, and the results are illustrated in Figure 3.7d and Figure 3.7e. It is clear that the NP in Figure 3.7 has a similar morphology as the particle in Figure 3.5, with {100} and {111} surface facets. Based on the 3D models, it can be seen that an entire (010) plane disappears and reappears (pink atoms in Figure 3.7e). Moreover, from the MD simulations, the potential energy was extracted for each system. In the potential energy curve, shown in Figure 3.7e, it can be seen that the energy slightly increases after frame 2. This means that the particle becomes less stable around the event of the layer jump. Afterwards, the potential energy decreases and the particle becomes more stable again. It can be seen in Figure 3.7e that for the model corresponding to frame 4, the layer (in pink) is not in exact agreement with the original plane (frame 1 and 2) and deviates from a perfect (010) facet. In frame 5, however, the facet is recovered, and the potential energy decreases. Our 3D models indicate that the process of layer jumping cannot be simply considered as a reversible rigid displacement of an entire facet. Indeed, there is a significant change in the surface structure and sites (e.g. frame 3 and 4).

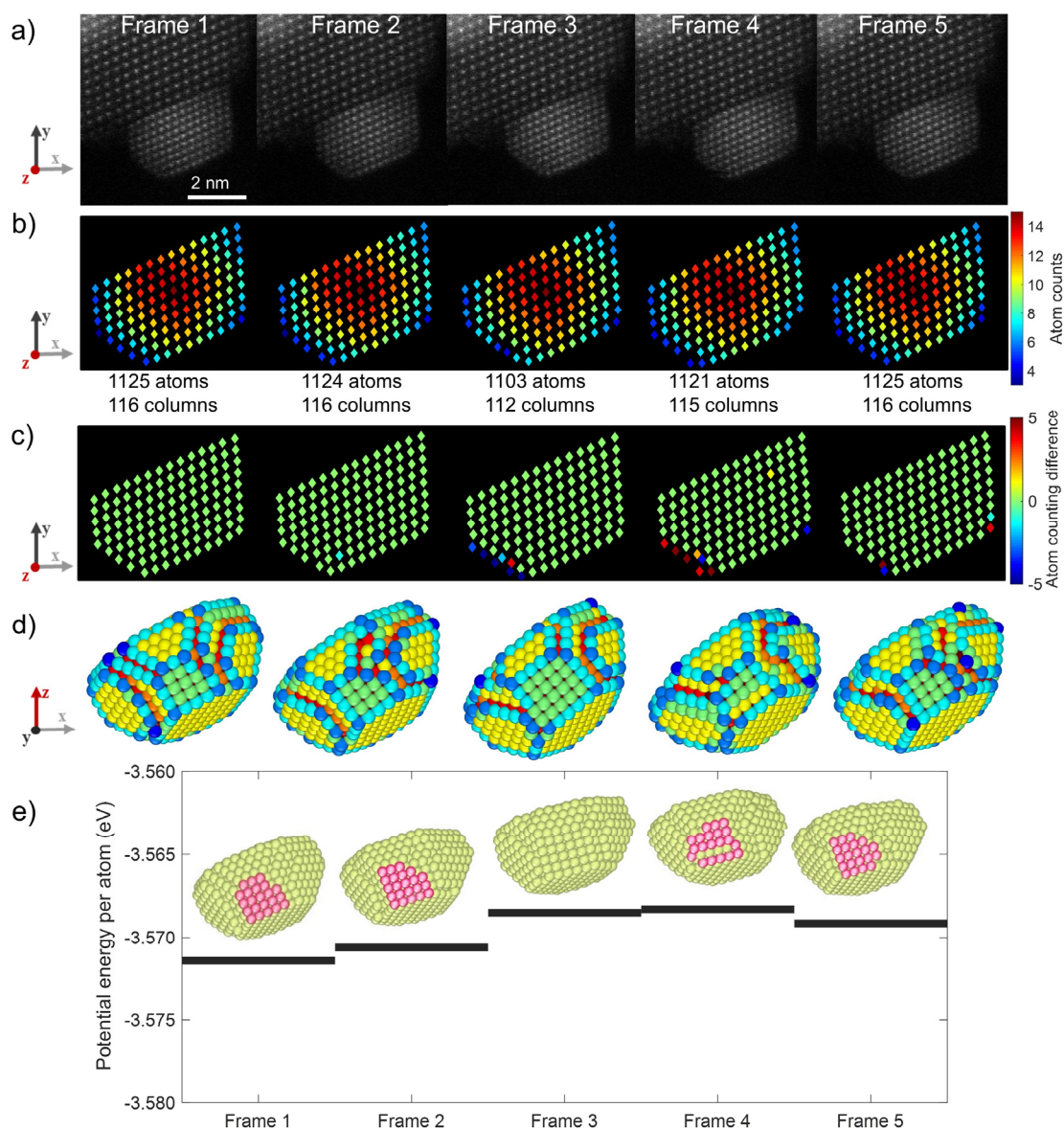


Figure 3.7 Reversible shape transformation of a supported Au NP. a) Time series ADF STEM images of a supported Au NP at 400 °C. b) Atom counting results of the Au NP at different time frames. The total number of atomic columns and the total number of atoms are listed for each time snapshot. c) The change in the number of atoms for all atomic columns between consecutive time frames. d) 3D relaxed structure of the Au NP at each time frame. The atoms are presented in different colors according to the CNs (see Figure 3.5). e) Averaged total potential energy per atom and 3D relaxed structures for each time snapshot.

Finally, in addition to changes in the surface structure, crystalline transformations that appear for the entire NP at 500 °C was also characterized. It has been reported that Au NPs in an oxygen atmosphere can transform between two crystalline orientations by electron irradiation or thermal heating since the potential energies of these two orientations are close.¹¹⁷ These orientations are referred to as Type I: (111)[−110]CeO₂ // (111)[−110]Au and Type II: (111)[−110]CeO₂ // (111)[1−10]Au. Figure 3.8 shows an example of a crystalline transformation of a NP which alternates between a Type I and Type II structure, albeit here under high vacuum conditions. The

number of atoms for each atomic column is presented in Figure 3.8b. Figure 3.8c displays the 3D models based on MD simulations, whereas in Figure 3.8d, the percentage of internal atoms that can be classified as FCC or HCP is presented, together with the contribution of the disordered atoms. For the structural classification, polyhedral template-matching approach was applied through OVITO Python open-source scripts.²⁵¹ Also the average potential energy per atom for the Au NP was extracted from MD simulations and is displayed in Figure 3.8d.

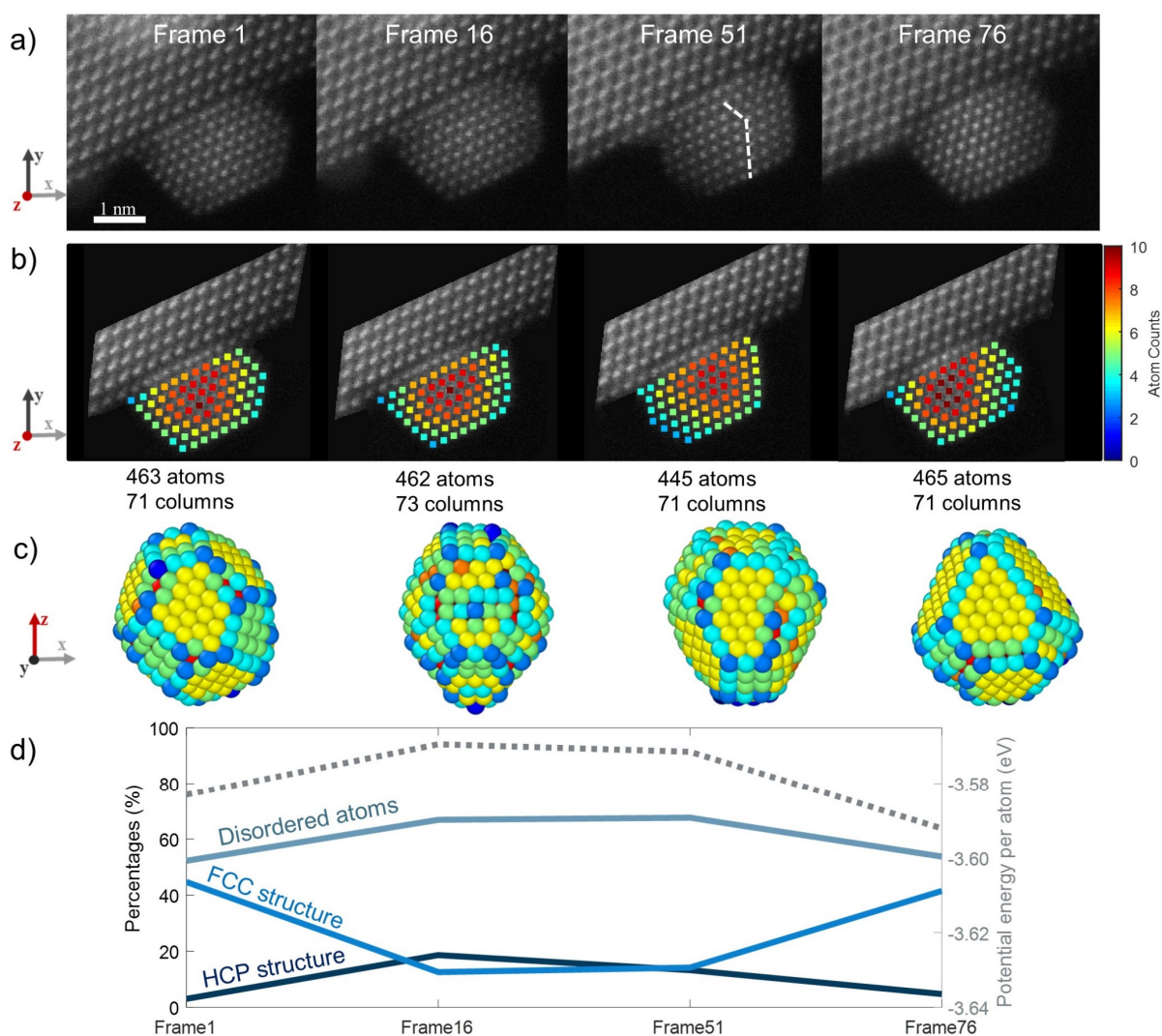


Figure 3.8 Crystalline orientation transformation of a supported Au NP. a) Raw ADF STEM images of the supported Au NP at different time frames at 500 °C. b) Atom counting results of the Au NP at different time frames. The number of atomic columns and the total number of atoms are listed for each time snapshot. c) 3D models of the supported Au NP. The atoms are presented in different colors according to the CNs (see Figure 3.5). d) Structural changes and the average potential energy change per atom with the reversible structural transformation.

In frame 1 and frame 76, the NP yields a Type II structure, with an FCC internal structure according to the graph in Figure 3.8d. In between frame 1 and frame 76, a structural transformation takes place. First, a disordered structure (frame 16) is observed without any ordered facet on the surface

(Figure 3.8c). Then, a Type I structure is found to be dominant in frame 51, and a twin boundary appears within the NP, which is marked by a dashed white line in Figure 3.8a. As it can be seen in Figure 3.8d, this structural transformation is reflected as an increase in the average potential energy per atom and HCP internal structure. In frame 76, the NP has completely transformed back to Type II by having energetically stable $\{111\}$ and $\{100\}$ facets, and the potential energy drops again. Moreover, during this reversible transformation, it should be noted that there is always one layer at the interface between the Au NP and oxide support that remains Type II, which indicates the strong interaction between Au and CeO₂.

3.5. Conclusion

The surface dynamics of CeO₂ supported Au NPs have been previously investigated by high-resolution TEM. However, given that such images invariably correspond to 2D projections of 3D objects, the interpretation of the particle morphology might be challenging. Conventional electron tomography is not applicable to evaluate the surface structure due to the fast dynamics of the atom movement. The methodology that is presented here enables going beyond these limitations since it has been possible to directly describe dynamic changes in the 3D atomic structure in a quantitative manner, also at high temperatures. Moreover, it is clear from our experiments that events such as layer jumping or crystalline transformation between type I and II structure are accompanied by intermediate disordered structures with higher potential energies, which may have an influence on the catalytic activity of the particle.

In conclusion, by combining atom counting based on aberration-corrected ADF STEM images and MD relaxation, an atomic-resolution 3D investigation of supported Au NPs was performed. In this manner, the 3D equilibrium structure of single NPs was investigated as a function of temperature. It has been observed that the overall shape appears to become more rounded at higher temperatures, especially for relatively small NPs, which might be related to the relaxation of interfacial strain. Moreover, an analysis of the surface dynamics was performed, including atomic layer jumping, which is most likely driven by surface atom diffusion. Finally, the crystalline transformation of a supported NP in 3D at high temperatures was characterized.

In Chapter 4, the capabilities and limitations of this method are further discussed in detail, and then a new approach is presented to overcome the limitations of this approach.

Chapter 4. 3D atomic structure of supported metallic nanoparticles: a combination of atom counting and a local minima search algorithm[†]

As illustrated in the previous chapter, determining the 3D atomic structure of NPs is critical to understand their structure-dependent properties. It is hereby important to perform such analyses under conditions relevant for the envisioned application. Here, the 3D structures of supported Au NPs are investigated at high temperatures, which is of importance to understand their behavior during catalytic reactions. To overcome limitations related to conventional high-resolution electron tomography at high temperature, 3D characterization of NPs with the atomic resolution has been performed by applying atom counting using atomic resolution ADF STEM images followed by structural relaxation. However, at high temperatures, thermal displacements, which affect the ADF STEM intensities, should be taken into account. Moreover, it is very likely that the structure of a NP investigated at elevated temperature deviates from a ground state configuration, which is difficult to determine using purely computational energy minimization approaches. Therefore, in this chapter, an optimized approach is proposed by using an iterative local minima search algorithm followed by MD structural relaxation of candidate structures associated with each local minimum. In this manner, it becomes possible to investigate the 3D atomic structure of supported NPs, which may deviate from their ground state configuration.

[†] This chapter is based on the following paper:

Arslan Irmak, E., Liu, P., Bals, S., Van, S. 3D Atomic Structure of Supported Metallic Nanoparticles Estimated from 2D ADF STEM Images: A Combination of Atom-Counting and a Local Minima Search Algorithm. *Small Methods* (2021) doi: 10.1002/smt.202101150.

My contribution consisted of applying the atom counting method, designing and performing molecular dynamics simulations, proposing, designing, and implementing the local minima search algorithm for 3D characterization of nanoparticles based on atom counting results, as well as their analysis and discussion.

4.1. Introduction

An accurate description of the morphology and the structure of metallic NPs is of great importance since these aspects determine many of their physical and chemical properties. Supported Au NPs smaller than 3-5 nm are highly reactive for a variety of important catalytic applications where the reacting molecules adsorb on the catalytically active surface.^{33,34} It has been shown that the binding energy of the reacting molecules decreases with the presence of stepped facets or decreasing coordination number of Au atoms at the surface. In addition, the metal-support interaction between the NP and the oxide support, often CeO₂, plays a critical role. The Au-CeO₂ interface may yield active sites leading to high catalytic activities during e.g., CO oxidation and water-gas shift reactions.²⁵²⁻²⁵⁴ However, the general shape and surface facets of supported NPs are also highly dependent on environmental conditions, such as pressure^{116,235,236} or temperature²³²⁻²³⁴. Therefore, it is essential to characterize the structure of the catalytic NPs at the atomic scale under relevant conditions and to hereby consider the role of the support.

Among different experimental techniques, ADF STEM is a valuable technique to investigate materials at the atomic scale. ADF STEM images can be obtained with atomic resolution and the image intensity is sensitive to sample thickness and the atomic number of the elements that are present.^{95,153,255,256} Nonetheless, these 2D images are usually inadequate to analyze the structure-property relation of nanomaterials because they only provide a projected image of a 3D structure. Electron tomography is one of the most known and powerful methods to retrieve the 3D atomic structure of NPs.^{68,72,257} However, as explained in Chapter 1, it is not always straightforward to apply conventional electron tomography since the approach requires a tilt series of many images to be acquired over a tilt range that is as large as possible. Conventional electron tomography therefore becomes very challenging when one wants to investigate very small or electron beam-sensitive NPs. Moreover, performing 3D *in situ* experiments or 3D characterization of dynamic processes is nearly impossible using conventional electron tomography since the NPs will change during the acquisition of the tilt series. Although the recently developed fast tomography approach shows great promise to accelerate the acquisition of tomographic tilt series from hours to minutes, the resolution is currently limited to the nanometer regime.^{121,258}

As an alternative method, 3D characterization of NPs with atomic resolution has been performed by combining atom counting on 2D ADF STEM images using statistical parameter estimation and structural relaxation.^{81,107,109,110} ADF STEM is a valuable technique to investigate materials at the atomic scale since they can be obtained with atomic resolution and the image intensity is sensitive to sample thickness and the atomic number of the elements that are present.^{95,153,255,256} Hereby, a high-resolution ADF STEM image is considered as a data plane to estimate the total number of atoms in each atomic column with the highest possible precision and accuracy.^{96,173} Next, the unknown positions of the atoms are determined based on the atom counting results by performing atomistic simulations, such as MC or MD simulations.^{81,109,110} Since the data acquisition is much faster in comparison to electron tomography, this approach enables one to study 3D dynamical changes of nanomaterials at the atomic scale during *in situ* experiments.

The present work is focused on the 3D characterization of Au NPs deposited on CeO₂ at high temperatures, at which catalytic reactions are often performed.^{33,254} In order to reliably count the number of atoms for NPs at high temperatures, it is shown that thermal displacements of the atoms need to be taken into account since this may affect the ADF STEM intensities and hence the quantification, especially for small NPs. Moreover, it is expected that supported NPs at high temperature may significantly deviate from their ground state configuration. At high temperatures, kinks and steps at the surface of the NP, acting as active sites for catalytic reactions, may appear. Also, the particle-support interaction will influence the atomic configuration at the surface of a supported NP. Hence, it is very likely that the structures of interest in this study can have a metastable state located in one of the local minima in the energy landscape, containing a huge number of local minima, each corresponding to a different atomic arrangement.²⁵⁹ Purely computational energy minimization approaches, such as MC or MD simulations, may easily result in a closest local minimum where the reconstructed structure may deviate from the experimental observation. To overcome the aforementioned limitations and obtain a reliable 3D model of supported NPs at high temperatures, the energy landscape should be exhaustively explored to find the local minimum corresponding to the experimentally observed structure.^{260–264} Therefore, an iterative local minima search algorithm is proposed, which is followed by MD structural relaxation at the experimental temperature and by including the particle-support interaction.

In the following part, the methodology for atom counting and 3D reconstruction is explained. Moreover, simulations of small Au NPs at high temperatures are performed to evaluate the accuracy of the atom counting and validate the proposed 3D reconstruction methodology.

4.2. Experimental details

Au NPs on CeO₂ were prepared by a physical sputtering coating method. ADF STEM projection images of the samples were acquired using a Thermo Fisher Scientific Themis Z microscope. The electron microscope was operated at 300 kV with a 30.4 mrad probe convergence semi-angle and a beam current of 50 pA. The inner and outer detector collection angles of the ADF detector were equal to 46.1 mrad and 198.6 mrad, respectively. For the acquisition of the high-resolution projection images of the supported Au NP, a DENSsolutions *in situ* heating holder (Wildfire) was used. During the experiment, images of 1024×1024 pixels in size with a frame time of 0.629 s were recorded at 400 °C under vacuum conditions. Figure 4.1.a shows an experimental ADF STEM image of a supported Au NP along a [110] zone axis. It can be seen that the epitaxial relationship between the support and the NP is Au{111}//CeO₂{111}, which is extensively observed for ceria-supported Au NPs.^{117,235} Experimental analysis, including sample preparation and the acquisition of ADF STEM experimental images, was performed by Dr. Pei Liu.

In order to compare the experimental data with multislice simulations in a quantitative manner, the acquired ADF STEM images were first normalized using a so-called detector scan, as explained in Subsection 3.2.3.

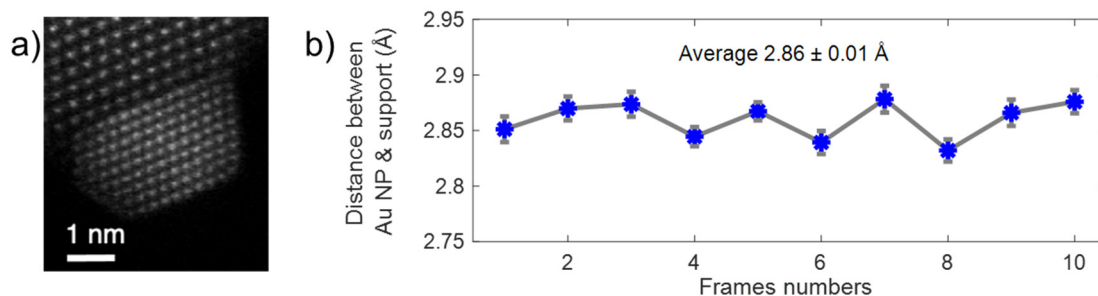


Figure 4.1 a) Experimental ADF STEM image of a supported Au NP. b) Measured interface distance between the Au NP and support.

4.3. Details of MD simulations and particle-support interaction

In order to evaluate the ability to reliably count the number of atoms in NPs from experimental ADF STEM images acquired at high temperatures, atom counting was first tested using accurate ADF STEM image simulations in which all factors affecting the image intensities were accounted for. As a test structure, a truncated octahedral Au NP (1215 atoms) was created with a size comparable to the experimentally imaged NP in Figure 4.1a. Moreover, to include the NP-support interaction, a CeO₂ substrate was created according to the fluorite structure and the experimentally observed epitaxial relationship between the support and the NP. This structure was relaxed by MD simulations at different temperatures (21°C, 400°C and 800°C) for 10 ns with NVT ensemble. During structural relaxations, non-periodic boundary conditions were applied in all three directions with a large vacuum area. The equations of motion were integrated using the velocity Verlet algorithm with a time step of 0.5 fs. Also, the total linear and angular momenta were conserved so that the supported Au NPs do not drift or rotate throughout our simulation. To define the interaction between Au-Au atoms during the structural relaxation, the EAM¹⁹⁰ was used. For the interaction between the CeO₂ support and the Au NP, the LJ potential was used. Since the interaction between the Au NP and oxide support is sensitive to several parameters, such as the size of the NP, the orientation of the NP on the support, the epitaxial relationship between the NP and the support, steps or defects on the oxide surface as well as the experimental environment,^{212,265,266} it is important to define the particle-support interaction directly based on the experimental observation. Therefore, the average interface spacing between the NP and the CeO₂ support observed from the experimental observation (Figure 4.1b), was taken as a reference to define the LJ parameters used in MD simulations. To measure the interface distance, the atomic column positions of the Au NP and CeO₂ support were obtained after fitting the ADF STEM images by statistical parameter estimation theory.⁹⁶

Figure 4.1b shows that the interface spacing between the Au{111} and CeO₂{111} surface is approximately 2.86 Å and the spacing remains the same for the consecutive time frames under vacuum conditions. Therefore, this observation was taken as a reference while adjusting the LJ parameters. For this purpose, MD simulations were performed with the combination of five different LJ parameters that define the interaction between Au-Ce and Au-O ($\epsilon_{\text{Ce-Au}}$, $\epsilon_{\text{O-Au}}$, $\sigma_{\text{Ce-Au}}$,

$\sigma_{\text{O-Au}}$, cut-off). After each iteration, the distance between the Au atoms, located at the bottom of the particle and the surface of the support is measured. Then, the LJ parameters were selected for which the distance between the NP and support showed good agreement with the experimental observation. Figure 4.2 shows the change in the NP-support distance during a MD simulation where the following LJ parameters were used: $\epsilon_{\text{Ce-Au}} = 0.3$, $\epsilon_{\text{O-Au}} = 0.1$, $\sigma_{\text{Ce-Au}} = 3.0$, $\sigma_{\text{O-Au}} = 2.0$, cut-off = 5.5 Å. It can be seen that the mean distance between the particle and support is approximately 2.87 Å and this distance remains almost constant for the consecutive MD simulation steps. This result is very close to the experimental observation, 2.86 Å. Moreover, it is important to note that although the LJ parameters defined here are system-specific, these parameters can be adjusted based on the experimental observations of the different systems i.e. for different NP orientation, or different particle-support epitaxial relationship.

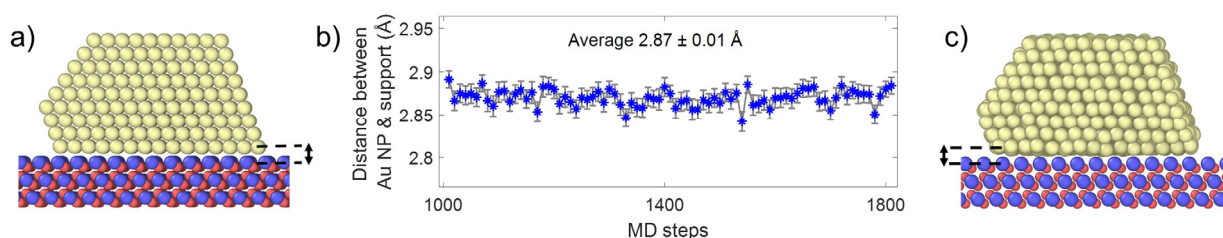


Figure 4.2 a) Input structure of a Au NP on a CeO₂ support. b) Measured interface distance between the Au NP and support at different steps during MD simulations at constant temperature. c) Au NP on CeO₂ support after the successive MD steps performed by using the following LJ parameters: $\epsilon_{\text{Ce-Au}} = 0.3$, $\epsilon_{\text{O-Au}} = 0.1$, $\sigma_{\text{Ce-Au}} = 3.0$, $\sigma_{\text{O-Au}} = 2.0$, cut-off = 5.5 Å.

4.4. Atom counting for NPs at high temperatures

4.4.1. Accuracy of the atom counting approach evaluated on simulated images

The atomic positions of the relaxed structures at different temperatures (Figure 4.3a) were used as an input for ADF STEM image simulations. Multislice calculations within the frozen phonon framework were used to accurately simulate thermal diffuse scattering in ADF STEM images. Hereby, the simulation parameters were chosen in accordance with the experimental imaging conditions. Moreover, a temperature-dependent DWF¹⁵⁰ and experimentally determined detector characteristics were included.¹⁵⁶ Next, the simulated image was convoluted with a 2D Gaussian to mimic the source size effect and Poisson noise was included corresponding to the experimental electron dose (5843 e-/Å²). The simulated ADF STEM images of the Au NP imaged along the [110] zone axis at 21°C, 400°C and 800 °C are presented in Figure 4.3b. Hereby, it can be seen that as the temperature increases, larger thermal displacements of Au atoms destroy the coherence along the beam direction so that a reduction in the intensities was observed at high temperatures.

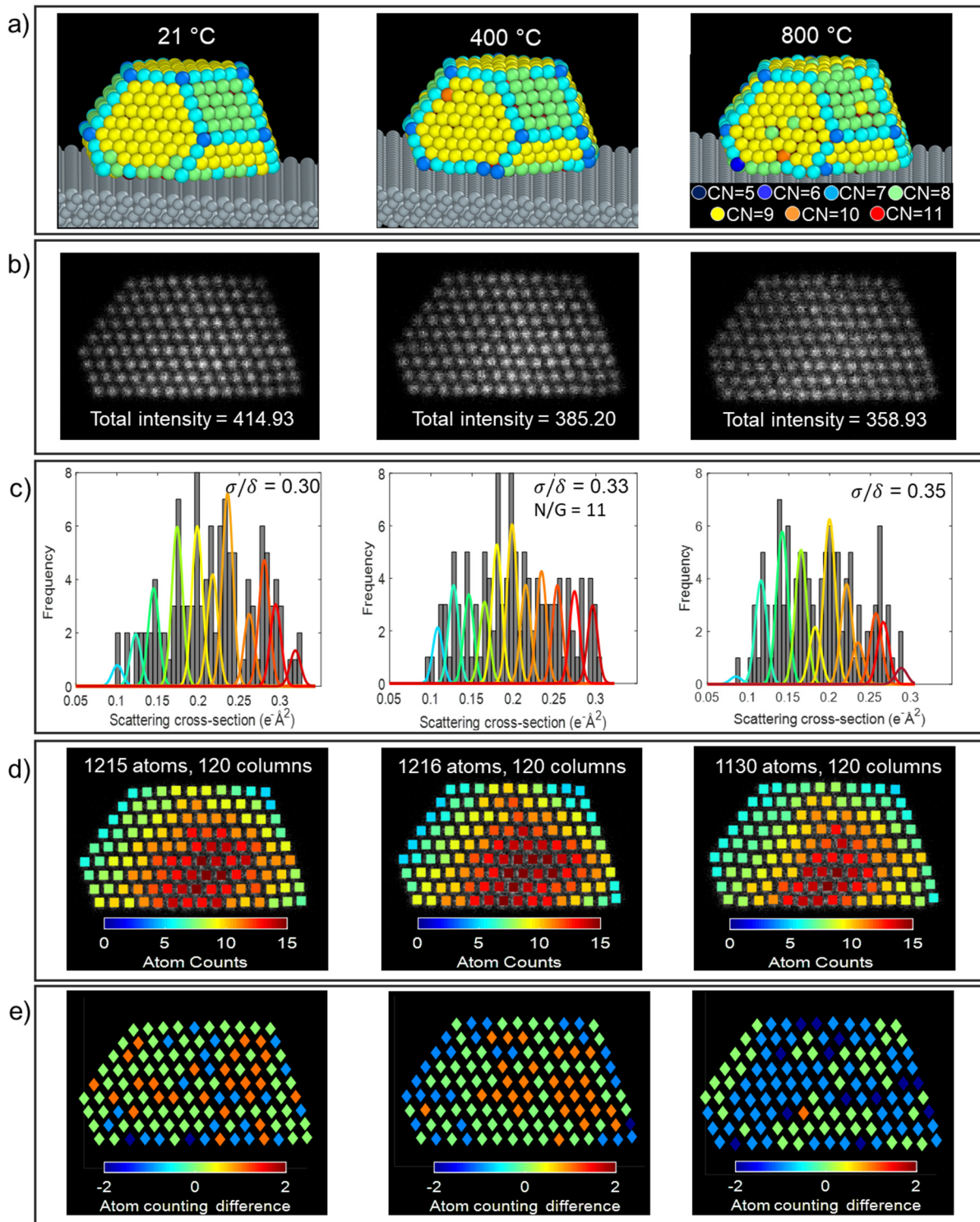


Figure 4.3 Temperature effect on atom counting performed at 21 °C, 400 °C, 800 °C. a) Relaxed 3D models of the Au NP on a CeO₂ support at the given temperature. Au atoms are presented in different colors according to their coordination numbers. b) Simulated ADF STEM images of the relaxed structures shown in (a). c) Histogram of estimated SCSs together with Gaussian components. d) Number of atoms in each atomic column. e) Difference in the total number of atoms in each projected atomic column between the reference model and the estimated number of atoms using the atom counting method.

To determine the number of atoms in each atomic column from the simulated images, the SCS corresponding to each atomic column was extracted from the ADF STEM images using statistical parameter estimation theory as explained in Section 2.2.^{97,168,173} Using this approach, the images were first modeled by a superposition of Gaussian peaks located at the atomic column positions. Based on the estimated height and width, the volume under the modeled Gaussian peak, i.e., the SCS was determined for each projected atomic column (Figure 4.3c). Next, the distribution of SCSs from all the atomic columns was decomposed into overlapping normal distributions using the Gaussian mixture model analysis,¹⁷⁴ enabling one to determine the locations and the width of each Gaussian component (Figure 4.3c). The number of Gaussian components, corresponding to the number of atoms found in the thickest atomic column of the NPs, was here selected based on the known size and shape of the original structures (Figure 4.3a). To determine the number of atoms in each atomic column of the simulated images, each estimated SCS was assigned to the Gaussian component with the largest probability (Figure 4.3d).

The precision of the atom counts is limited by overlap of the Gaussian components as shown in in Section 2.2.^{168,173} The overlap can be quantified in terms of the relative width of the Gaussian components (σ/δ) where σ is the width of the normal component and δ is the distance between the location of two neighboring components. This overlap is set by different factors including experimental detection noise, different vertical onset of columns of the same height, relaxation at the boundaries, but also by the increased thermal vibration of Au atoms at high temperature. From Figure 4.3c, it can be seen that the overlap (σ/δ) increases with increasing temperature. This affects the precision of the atom counting method (Figure 4.3d). For example, it can be seen that the total number of atoms estimated from atom counting method for the NP at 21 °C is identical to the total number of atoms in the original input structure, 1215 atoms. For the ADF STEM image of the relaxed Au NP at 400 °C, the difference between the ground truth used as an input for the simulation and the estimated number of atoms for each atomic column is ± 2 at maximum (Figure 4.3e) but far less on average. This demonstrates the high accuracy and precision of the atom counting methodology for NPs imaged at 21 °C and 400 °C temperature. However, at 800 °C, the increased overlap (Figure 4.3c) causes a larger discrepancy between the estimated number of atoms per column in the simulated image and the original input (Figure 4.3e).

4.4.2. Counting the number of atoms from experimental images

In Subsection 4.4.1, a priori knowledge concerning the shape and size of the 3D original structures could be used to determine the number of components of the Gaussian mixture model. On the other hand, the number of components from experimental images is typically determined using the ICL criterion.^{96,174,267} However, a correct interpretation of the ICL is affected by the overlap (σ/δ) between the normal components and the number of columns having a specific thickness.⁹⁶ Previous studies have shown that the number of atomic columns present in the experimental images should be sufficiently large to allow for a correct interpretation of the ICL and hence for reliable atom counting.^{96,98,267} If the relative width of the components (σ/δ) is of the order of 0.33, as expected from the simulation of the Au NP at 400 °C (see Figure 4.3c), the required average number of

Chapter 4. 3D atomic structure of supported metallic nanoparticles: a combination of atom counting and a local minima search algorithm

atomic columns per component (N/G) should be around 90 in order to correctly count 95 % of all atomic columns, whereas it is only equal to around 11 for the small NPs investigated in this study. To overcome this problem, a time series consisting of ten frames of the same particle of interest is collected (Figure 4.4a). By collectively analyzing all SCSs resulting from these experimental time frames, the average number of atomic columns per component (N/G) will increase to around 100, enabling a reliable interpretation of the ICL.

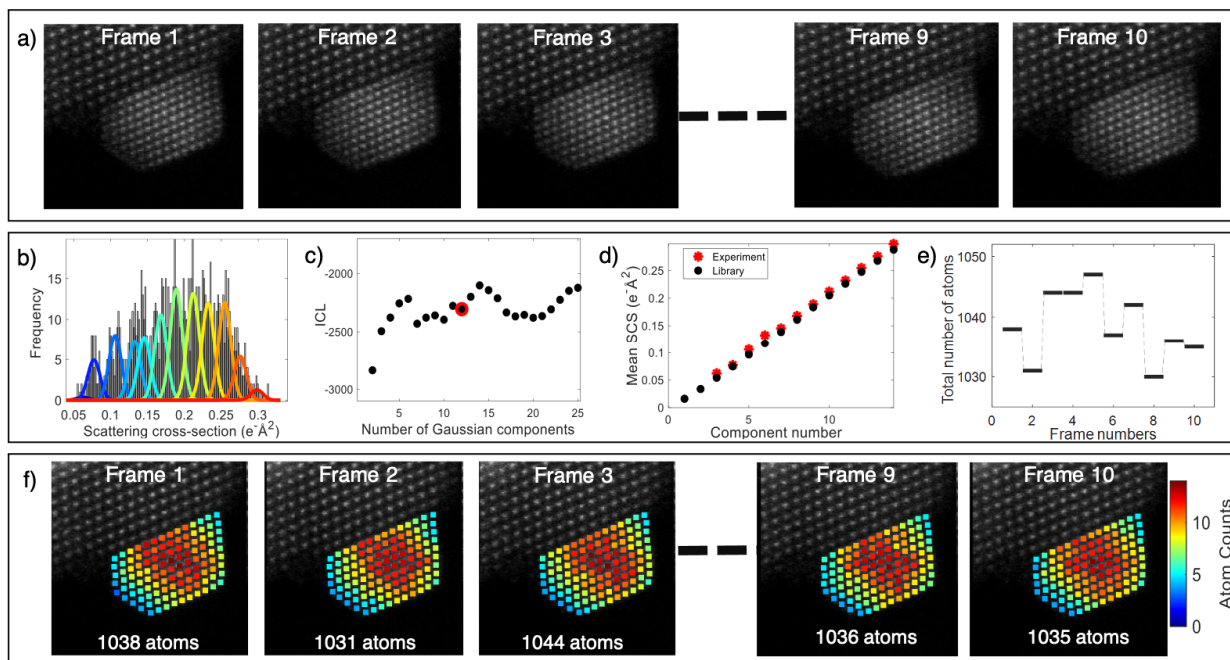


Figure 4.4 The ADF STEM quantification of the experimentally imaged supported Au NP at 400 °C. a) Ten consecutive time frames. b) Histogram of the set of SCSs of the Au columns collectively obtained from the time frames and normal components of the estimated Gaussian mixture model. c) Evaluation of the ICL criterion. d) Comparison of the experimentally estimated mean SCSs with the simulated library SCSs. e) Estimated total number of atoms with respect to the frame number. f) Atom counting maps for all time frames.

The estimated SCS values of the Au atomic columns obtained from ten consecutive frames are visualized in the histogram of Figure 4.4b and the evaluation of the ICL criterion as a function of the number of components of the Gaussian mixture model is shown in Figure 4.4c. The true number of components often corresponds to a local minimum, but the presence of more than one minimum complicates the analysis. Therefore, to confirm the choice of twelve components (highlighted in red in Figure 4.4c), the experimental mean SCSs (corresponding to the component locations in Figure 4.4b) were compared with SCSs resulting from independent multislice simulations.^{133,267} To obtain these so-called simulated library values for increasing number of Au atoms, it is important to use the actual microscope settings, to include the contribution of thermal diffuse scattering through the frozen phonon approximation, to model the non-uniform experimentally determined detector sensitivity, and to incorporate the temperature effect by the DWF. The details regarding the multislice simulations and the effect of the detector sensitivity and temperature on

the simulated library values are given in Section 2.1 and Section 3.2. As shown in Figure 4.4d, a nearly perfect match is observed between the simulated and experimentally estimated SCSs validating the choice for twelve components where the number of atoms associated with the first component corresponds to three.

The total number of atoms in the NP and estimated number of atoms for each atomic column for the individual frames are shown in Figure 4.4e and Figure 4.4f, respectively. It can be seen that the estimated total number of atoms in the Au NP for the ten time frames remains almost constant over time. The remaining fluctuations result from the inherent experimental uncertainties and the statistical nature of the methodology. Therefore, it can be concluded that also at high temperatures and with a limited number of atomic columns, it is possible to accurately count the number of atoms for each atomic column provided that the analysis is based on a times series of images rather than on a single image and that the temperature effect is taken into account in the simulated SCSs.

4.5. 3D reconstruction based on atom counting results

4.5.1. Validation of the method on the simulated image

Based on the estimated number of atoms for each atomic column, our final goal is to reconstruct the 3D atomic structure. The proposed method was validated on the simulated NP relaxed at 400 °C at which experiments were performed. The atom counts from the simulated ADF STEM image of the NP relaxed at 400 °C, shown in Figure 4.3d, were used to create a starting 3D model for the Au NP by placing the atoms symmetrically around the central plane using prior knowledge about the [110] specimen orientation and the FCC crystal structure. The distance between neighboring Au atoms, parallel to the beam direction, has been fixed according to the lattice parameter. This provided a reliable starting input model (Figure 4.5a) for the next steps in our study since Au NPs on an oxide support are fairly close to being symmetrically distributed according to the thermodynamics perspective.²¹²

Next, an iterative local minima search algorithm was applied to reconstruct the final 3D structure from the starting input model. The role of this step is to provide a broad sampling of the energy landscape to avoid being stuck in the closest local minimum. During each iteration of this algorithm, a random atomic column was selected and shifted upwards or downwards in the range $[-a, 0, a]$, where a is the lattice parameter of the FCC Au structure. Based on the resulting change in the energy of the system, ΔE , the Boltzmann probability factor (P) was computed:^{259,268,269}

$$P = \exp(\Delta E/k_B T) \quad (4.1)$$

with k_B the Boltzmann's constant and T the temperature which was chosen as 673 K. If the value of P corresponding to the candidate structure with the displaced atoms was equal to or larger than a specified threshold, the candidate structure was accepted and used as a starting point for the next iteration. Otherwise, the previous configuration was used for the next step. This process continued until the morphology of the candidate structure deviates from a convex shape due to the displaced

atomic columns. A threshold value of 0.9 was chosen to efficiently explore neighboring configurations within the energy range close to the created input model. Although a high threshold imposes a narrow energy range, this threshold value works efficiently when the algorithm already starts with a reliable input model. Moreover, it brings computational advantages since this narrow energy range enables for a neighborhood search through a relatively small number of local minima, rather than a global search with a huge number of local minima.²⁶² This process took around six hours with two CPU cores. However, the computational time can be further decreased by using larger number of CPU cores or GPU. The obtained neighborhood energy landscape resulting from the iterative local minima search algorithm is illustrated as a gray line in Figure 4.5b. Here, points having the lowest value in regions where at least ten previous points showed a continuously decreasing trend were selected as local minima and are indicated by black dots.

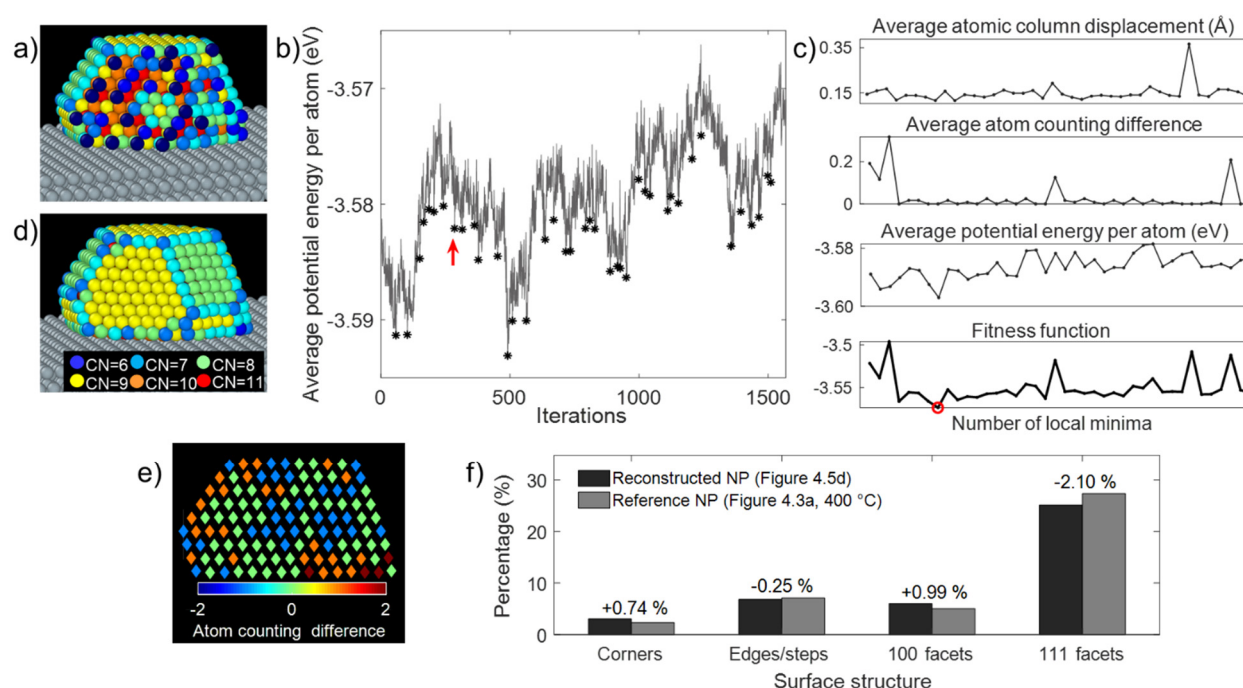


Figure 4.5 Main steps of the iterative local minima search algorithm demonstrated for the simulated Au NP. a) Starting 3D model created based on the atom counting results shown in Figure 4.3d. b) Neighborhood energy landscape obtained by the iterative local minima search algorithm. c) The components of the defined fitness function. d) Reconstructed final Au NP on the support. Au atoms are presented in different colors according to their coordination numbers. e) Difference in number of atoms in each projected atomic column between the original input and reconstructed model. f) Comparison of the surface structure of the reconstructed NP and the original NP. The histogram is obtained from the coordination numbers of the atoms.

Afterward, each candidate structure associated with a local minimum (black dots in Figure 4.5b) was relaxed by MD simulations in a canonical ensemble at 400 °C for 5 ns with Nose-Hoover thermostat to locate the low energy structures from the explored local minima. Structural relaxation of each candidate structure took around eighty minutes with six CPU cores. Standard energy

minimization algorithms, i.e. a conjugate gradient method, are typically performed without temperature parameter, at 0K, where the surface energy anisotropy is maximal. However, at high temperatures, the surface energy anisotropy decreases, and rounded parts in the equilibrium shape or some kinks and steps at the surface which act as sources of atoms or growth sites for diffusing adatoms may appear.²¹² Therefore, rather than applying a standard energy minimization,²⁷⁰ MD structural relaxation was applied at a specified temperature, enabling one to investigate atomic structures that may be observed at high temperatures.

During the iterative local minima search algorithm and MD simulations, the EAM potential was used to define the interaction between the Au atoms. Moreover, the presence of the support has a strong influence on the stability of the catalytic NP and certainly affects its morphology and structure, especially under the heating environment. Therefore, the interaction between the CeO₂{111} support and the particle, which is often neglected in many of the previous studies,^{81,107,109,110} was taken into account using a LJ interaction as explained in Section 4.3.

Afterwards, to select the most plausible 3D structure corresponding to the explored local minima, a fitness function (f) has been defined:

$$f = \frac{E}{atom} + \alpha\chi \quad (4.2)$$

$$\chi = \frac{\sum_{n=1}^N \sqrt{(G_{candidate}(n) - G_{ref}(n))^2}}{N} + \frac{\sum_{n=1}^N \sqrt{(x_{candidate}(n) - x_{ref}(n))^2 + (y_{candidate}(n) - y(n))^2}}{N} \quad (4.3)$$

Equation 4.2 includes the average potential energy per atom ($E/atom$) and a quantitative measure of the goodness of fit of each candidate structure located in a local minimum with the reference observation (χ). A weighting parameter α was chosen empirically to make variations in the $E/atom$ term and the χ term of the same order of magnitude. The choice of the fitness function is based on the work of Yu et al.,²⁷¹ where instead of image matching, the atom counts and projected atomic column displacements were used to define the discrepancy between the relaxed 3D structure and the observation (Equation 4.3). The first term of Equation 4.3 determines the average difference between the number of atoms located in each projected atomic column of a candidate model and the estimated atom counts resulting from an ADF STEM image. Here, N and G represent the number of projected atomic columns and the corresponding number of atoms in an atomic column, respectively. The second term in Equation 4.3 measures the average shift in the projected atomic column positions of each candidate structure compared to the atomic column positions observed in the ADF STEM image. The projected atomic column positions of the candidate structures were

estimated by averaging the xy-coordinates of atoms located in the same column along the z-direction.

The evolution of the fitness function for each candidate structure and the three contributing terms are shown in Figure 4.5c. The minimum value in the fitness graph (indicated with a red circle in Figure 4.5c) provides the final 3D structure that has the best agreement with the reference ADF STEM image (in terms of number of atoms for each atomic column and projected atomic column position) among all relaxed candidate structures associated with different local minima. The retrieved structure (Figure 4.5d) is mainly composed of {100} (green atoms) and {111} (yellow atoms) facets which are separated by edges (light blue atoms) and corners (dark blue atoms). Since the exact 3D model (Figure 4.3a) of the reference ADF STEM image is available, a one-to-one comparison has been made to quantitatively verify the proposed methodology. For this purpose, the difference in the number of atoms in each projected atomic column between the reconstructed NP and original input model used for MULTEM simulations was determined (Figure 4.5e). It can be seen that the total number of atoms in each atomic column differs maximum ± 2 atoms but far less on average. This discrepancy results from the limited precision of the statistics-based atom counting method and the atom movement between the atomic columns during MD structural relaxations. Furthermore, a surface structure analysis was performed by determining the coordination number of all surface atoms. The comparison between the surface structures of the reconstructed NP and the original 3D model has been shown in Figure 4.5f. According to the results, it can be concluded that the surface structure of the reconstructed Au NP has been identified with an accuracy of more than 95 % where the maximum difference of 2.22 % was observed in the percentage of {111} facets as indicated in Figure 4.5f.

4.5.2. Experimental results

Once validated, the iterative local minima search algorithm was applied to reconstruct the 3D structure of the experimentally investigated NP (Figure 4.4). The reconstructed 3D atomic structures of the supported NP from ten consecutive time frames and their surface structures are illustrated in Figure 4.6. According to the percentage of the average coordination number from each reconstructed NP and the standard deviation from the mean value, indicated in Figure 4.6b, the surface structure of the NP was reconstructed with high precision. The standard deviation is mainly due to atom diffusion under the electron beam, limited precision of the atom counting method and the optimization algorithm. Around 3.5 % of the atoms are located at the corners, 7.7 % of the atoms are on edges or surface steps, 5.0 % and 25.8 % of the atoms are located on {100} and {111} surface facets, respectively.

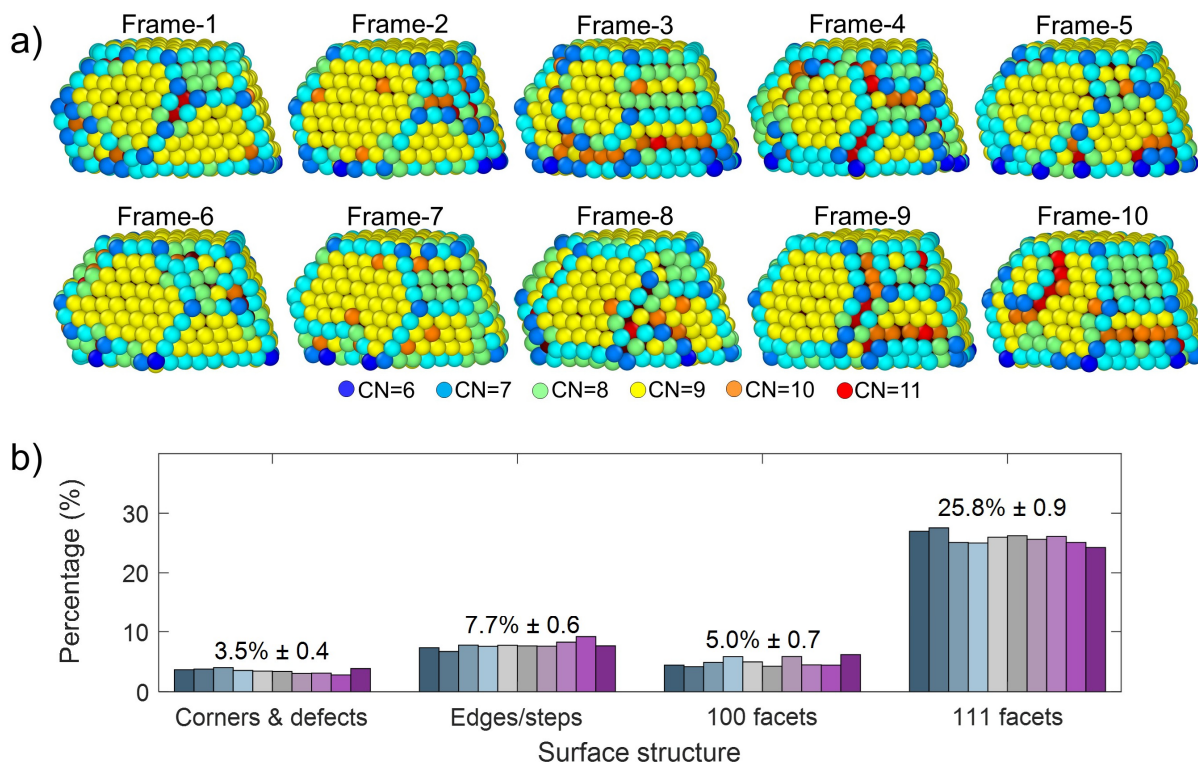


Figure 4.6 3D characterization of the experimentally observed Au NP on CeO₂ retrieved from 10 consecutive time frames. a) 3D structures where atoms are presented in different colors according to their coordination numbers. b) Surface structure of the reconstructed NPs. The histogram is obtained from the coordination number of the atoms.

4.6. Comparison to other approaches

The performance of the proposed methodology was tested by comparing it to the outcome determined using previously applied approaches in the literature where 3D atom counting results were combined with a MC approach or MD simulations. For this purpose, energy minimization by a MC approach and full structural relaxation by MD simulations were performed on the same starting 3D model shown in Figure 4.5a. Then, the outcome of each method was compared with the original 3D structure (Figure 4.3a at 400 °C and Figure 4.7a).

When using the MC approach, movement of atoms between the atomic columns was not allowed and only the z-positions of the atomic columns moved up and downwards for each iteration while keeping the number of atoms in each atomic column fixed. The new configuration is accepted only if the potential energy decreases. This process was repeated until the potential energy of the system remains unchanged. The final 3D model obtained from this methodology is shown in Figure 4.7b. Since the atoms were not permitted to move between the atomic columns during the MC approach, the final structure was likely affected by the limited precision of atom counting.¹¹⁰ The counting imprecision, with an error of ± 2 as explained in Section 4.4, and the restriction in the atomic movement between columns resulted in more roughness at the surface of the 3D reconstructed NP

compared to the original model in Figure 4.7a. In the second approach, full structural relaxation at 400 °C was performed by MD simulations for 5 ns where the NP-support interaction is ignored. According to the 3D model shown in Figure 4.7c, MD simulations ended up with relatively large structural deviations from the original model due to the large atomic movement between the columns during the structural relaxation at high temperature. However, when using the method proposed in this work (Figure 4.7d), there is visually a very good agreement with the original structure.

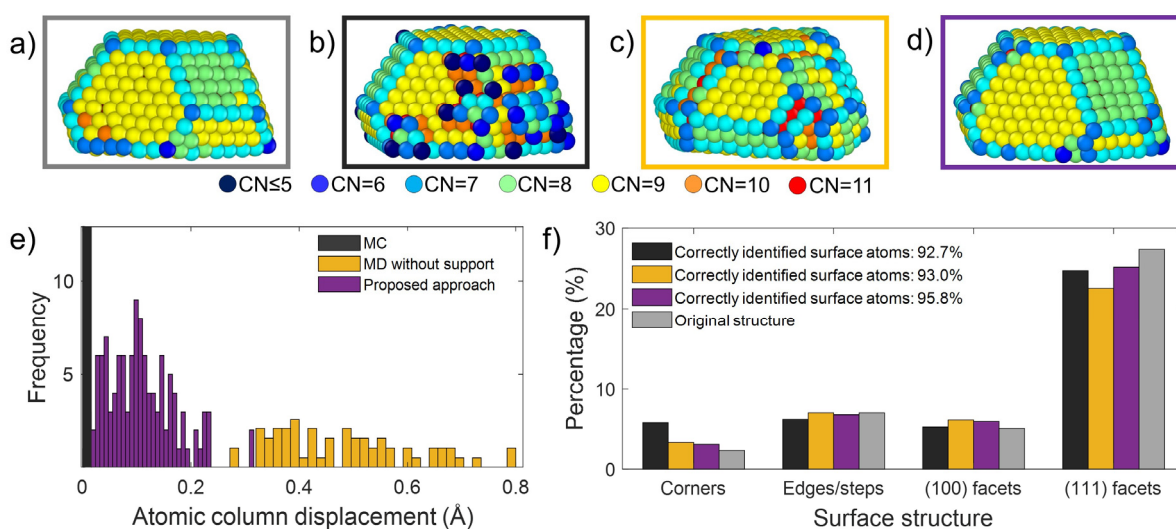


Figure 4.7 Comparison of different approaches. a) Original structure. b-d) The final structures obtained from MC approach, MD simulations, and local minima search algorithm. e) Projected atomic column displacement compared to the target structure. f) Comparison of the surface structure of the reconstructed NPs and the original NP. The histogram is obtained from the coordination number of the atoms.

Moreover, a quantitative comparison has been performed between the different approaches. Figure 4.7e shows the difference in the projected atomic column positions of each reconstructed NP with respect to the atomic column positions of the original structure. Here, larger atomic column displacements indicate a large deviation of the projected structure from the observed structure in the reference ADF STEM image. Since atomic movement was not allowed during energy minimization by the MC approach, no atomic column displacements were observed (black color in Figure 4.7e) so that the reconstructed particle had the same projected shape as observed in the ADF STEM image. However, more roughness was observed at the surface due to the restriction in the atomic movement between the columns. This is clear from Figure 4.7f where the surface structure is determined from a coordination number analysis. Indeed, a larger percentage in the low-coordinated corner atoms is observed for the particle reconstructed using the MC approach. As it has already been observed in Figure 4.7c, the discrepancy between the NP shape retrieved from MD structural relaxations and the original structure can also be seen from the large atomic column displacements (yellow color in Figure 4.7e). However, the proposed local minima search algorithm (Figure 4.7d) successfully reproduced the target structure both in terms of the projected atomic column positions and the atomic configuration at the surface.

To evaluate the overall accuracy of each approach, the fraction of atoms in the final 3D structures that have the same coordination number as in the original structure was calculated. It was found that iterative local minima search algorithm, which is followed by MD structural relaxation at the experimental temperature by including the particle-support interaction, correctly identified the coordination number of 94.50 % atoms in the 3D structure. However, this value remained below 90 % for the MC approach (84.29 %) and MD structural relaxation (87.42 %).

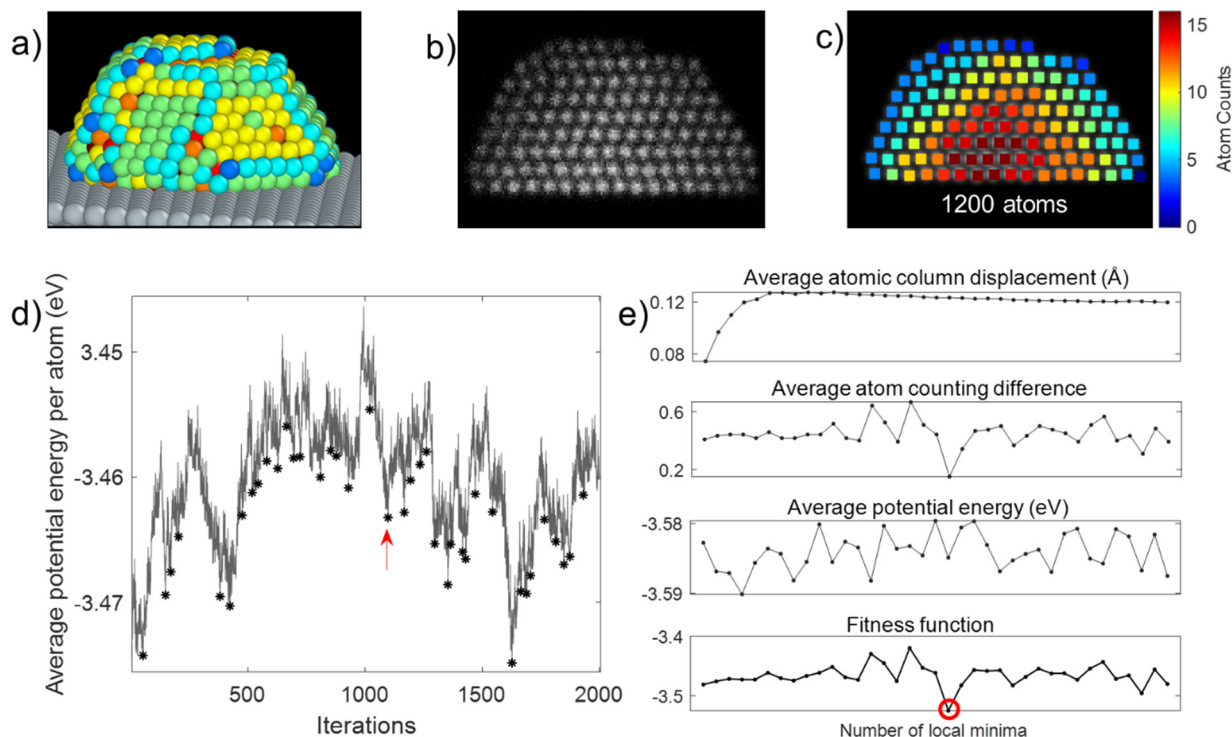


Figure 4.8 a) A metastable Au NP on a CeO₂ support at 400 °C obtained from melting and rapid quenching of the structure shown in Figure 4.3a. b) Simulated ADF STEM image. c) Number of atoms in each atomic column. d) Neighborhood energy landscape. e) Fitness function components.

The original test structure (Figure 4.3a), a truncated octahedron, is a thermodynamically stable structure for Au NPs with clear surface facets. On the other hand, it is known that metastable structures have rough surfaces containing some defects. Therefore, our approach was also tested on a metastable structure. A metastable structure was created by melting the Au NP, shown in Figure 4.3a, at 1300K for 20 ns and rapid quenching to 673 K at which the structure was relaxed for 10 ns with NVT ensemble. The obtained structure is displayed in Figure 4.8a and its corresponding ADF STEM image is shown in Figure 4.8b. The same imaging parameters as in Figure 4.3b were used for the ADF STEM simulations. The number of atoms in each atomic column in the simulated ADF STEM image (Figure 4.3b) was estimated by the atom counting method explained in Subsection 4.4.1. The resultant atom counting map is displayed in Figure 4.8c and the detected total number of atoms was found as 1200. Considering the total number of atoms in the original structure in Figure 4.8a (1215 atoms), the discrepancy in the estimated number of atoms, which corresponds to less than one atom per column on average, most likely comes from

the large displacement of Au atoms in the metastable structure. By using the atom counts, a starting model was created as it is explained in Subsection 4.5.1 and the iterative local minima search algorithm was applied (Figure 4.8d and Figure 4.8e.) taking both the effect of temperature and particle-support interaction into account.

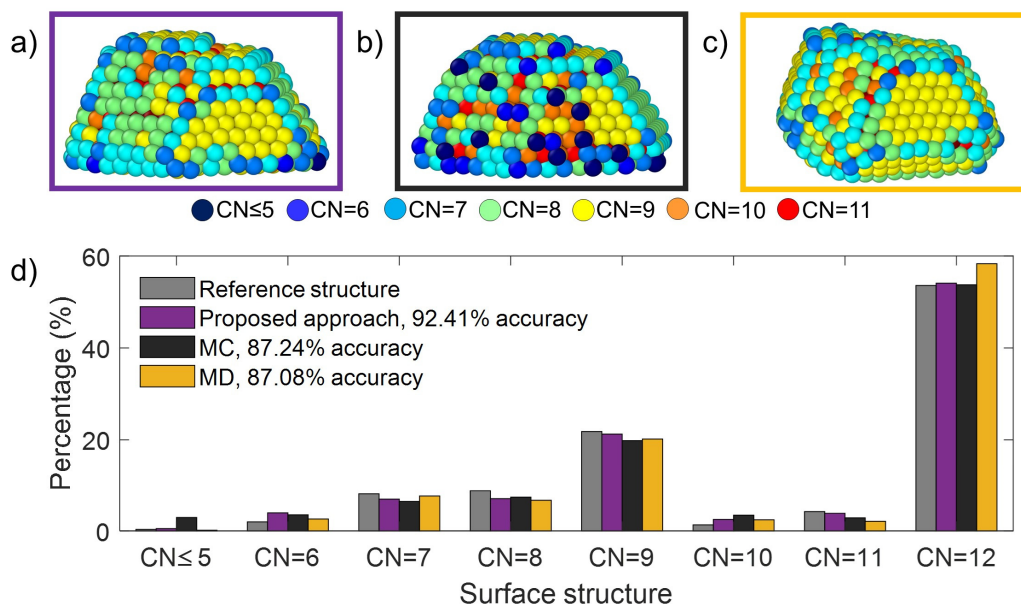


Figure 4.9 Comparison of different approaches on the same metastable Au NP at 400 °C. a-c) The final structures obtained from the proposed local minima search algorithm, MC approach and MD simulations. d) Coordination number histogram of all atoms in the final structures.

The reconstructed 3D model obtained from the local minima search algorithm is displayed in Figure 4.9a. Moreover, to compare the outcome of this approach, again, energy minimization by MC and structural relaxation by MD at 400 °C were applied to the same starting model created based on the atom counting map (Figure 4.8c). The final structures obtained from MC approach and MD simulations are displayed in Figure 4.9b and Figure 4.9c, respectively. Similar to the observations in Figure 4.7, the restriction of atomic movement between the projected atomic columns caused more roughness at the surface of the 3D reconstruction (Figure 4.9b) and large atomic movement during MD structural relaxation resulted in a rounder shape (Figure 4.9c) compared to the original structure (Figure 4.8a). These observations were also reflected in the coordination number histogram of atoms in the final structures (Figure 4.9d). While a higher fraction in the low-coordinated atoms was observed in the particle reconstructed using the MC approach, a larger percentage of atoms with coordination number 12 was found in the NP retrieved from MD relaxation due to having a rounded shape. On the other hand, according to Figure 4.9a and Figure 4.9d, the proposed approach in this chapter successfully reconstructed the imaged NP and correctly identified the coordination number of 92.41% atoms in the structure.

It should be noted that our approach shows similarities with the basin-hopping algorithm.^{259,260,272} However, due to the system-specific needs, it was necessary to adapt the algorithm for our system. In the basin-hopping algorithm, a standard energy minimization approach is performed at each step

without temperature parameter, at 0K. Since the structure of NPs depends on temperature, MD structural relaxation was preferred to apply at a specified temperature rather than an energy minimization approach. Since performing structural relaxations at each step by including the particle-support interaction and the effect of temperature is computationally expensive, a computationally more efficient model was employed without sacrificing accuracy. For this purpose, first the neighborhood energy landscape was obtained. Afterward, to use computer resources efficiently, the local maxima and unstable points of the energy landscape were eliminated and MD simulations were applied only for the structures located in regions of interest of the energy landscape where at least ten previous points showed a continuously decreasing trend.

Overall, with the combination of atom counting and an iterative local minima search algorithm, where both the temperature effect and particle-support interaction were taken into account, the 3D structure of the simulated and experimentally imaged supported NPs were successfully reconstructed with high accuracy and precision. Since the proposed method does not only rely on energy minimization, it outperforms the previously applied approaches, where 3D atom counting results were combined with a MC approach or MD simulations.^{81,109,110} Figure 4.7 and Figure 4.9 show that the MC approach may lead to wrong interpretations for the surface-catalytic property relation, while the full MD structural relaxation can easily end up with a different structure from the originally imaged NP. However, the proposed approach in this study enables us to overcome those limitations. Due to its ability to search the local energy landscape and to find the local minimum that corresponds to the imaged NP, the original target structures observed from ADF STEM images can be successfully estimated both in terms of atomic column positions and atomic configuration at the surface. Therefore, the proposed methodology provides a powerful approach to retrieve the 3D atomic scale information of both stable and metastable structures under a catalytic environment, i.e., at high temperature.

4.7. Conclusion

In conclusion, it has been demonstrated that a local minima search algorithm based on atom counts resulting from ADF STEM images can be used to successfully reconstruct the 3D atomic structure of supported Au NPs even at high temperatures. This approach is initiated with a reliable starting configuration based on the atom counting results where the atoms are positioned symmetrically along the beam direction. The proposed method, taking both the effect of experimental temperature and particle-support interaction into account, explores different local minima in the energy landscape while quantitatively validating the reconstructed structure with the observations from ADF STEM images. In this manner, the atomic scale information of supported NPs observed at high temperatures were accurately reconstructed from 2D ADF STEM images acquired along a single viewing direction. The accuracy of this method was tested on a simulated Au NP lying on a support by considering all experimental parameters that may affect the image intensities and quantification. According to the results, the proposed method predicts the 3D atomic structure of a simulated Au NP on a CeO₂ support with high accuracy and outperforms the previously reported approaches. This method, therefore, enables an accurate refinement of experimentally observed 3D

Chapter 4. 3D atomic structure of supported metallic nanoparticles: a combination of atom counting and a local minima search algorithm

atomic structures providing critical information to understand the structure-property relationship from limited data.

Chapter 5. Unravelling Pt-driven morphological transformations in Au@Pt nanorods upon heating[‡]

Understanding the thermal stability of bimetallic NPs is of vital importance to preserve their functionalities during a variety of applications. In contrast to well-studied bimetallic systems such as Ag-coated Au (Au@Ag), heat-induced morphological and compositional changes of Pt-coated Au (Au@Pt) NPs are less understood, even though Au@Pt is an important material for catalytic applications. To investigate the thermal instability of Au@Pt nanorods (NRs) at temperatures below their bulk melting point, in this chapter, different 2D and 3D electron microscopy techniques are applied, including EDX spectroscopy, HAADF STEM, and combined with *in situ* heating. By using the experimental results as an input for MD simulations, the mechanisms behind the morphological transformations of Au@Pt core-shell NRs are unravelled. In this chapter, it is demonstrated that the thermal stability of Au@Pt core-shell NRs is influenced by both the continuity and the detailed morphology of the Pt shell surrounding the Au core.

[‡] This chapter is based on the following paper:

Pedraza-Tardajos, A.[†], Arslan Irmak, E.[†], Kumar, V., Sánchez-Iglesias, A., Chen, Q., Wirix, M., Freitag, B., Albrecht, W., Van Aert, S., Liz-Marzán, L. M., Bals, S. Thermal Activation of Gold Atom Diffusion in Au@Pt Nanorods. (*Submitted*)

[†] Equal contribution to the published work.

My contribution consisted of creating input structures for MD simulations based on the 3D electron tomography reconstructions of the experimental nanoparticles, designing and performing molecular dynamics simulations, as well as their analysis and discussion.

5.1. Introduction

Colloidal Au@Pt bimetallic NPs have attracted considerable interest due to the possibility to synthesize them in a wide variety of shapes and with different chemical compositions, making their properties easily tunable for multiple plasmonic and catalytic applications.^{273–275} Particularly interesting bimetallic systems are Au@Pt NPs, resulting from the combination of excellent plasmonic properties of Au^{276,277} and attractive catalytic properties of Pt.²⁷⁸ This synergy has enabled novel applications in various fields, such as nanoenzymes,²⁷⁹ antibacterials,²⁸⁰ and catalysts for formic acid electro-oxidation.^{281,282} Since the properties of NPs are directly connected to their 3D structure, including surface facets^{23,283,284} and composition,¹¹¹ controlling the shape and elemental distribution during the synthesis of bimetallic systems is crucial.^{285–293} In a recent development, a micelle-directed seeded approach using chiral additives was shown to direct the growth of regular surface Pt spikes on Au NRs, potentially showing chiral features.²⁹⁴ Such systems are of great interest as they present tunable catalytic and optical properties by controlling the structure improve the overall catalytic activity and may have promising applications in biocatalysis, disease diagnostics and bioassays.^{279,295,296}

Despite of the interesting properties of this system, its application has been hindered by their sensitivity to environmental conditions, such as annealing²⁹³ and gaseous environments,²⁹⁷ which often result in complex changes of their morphology and elemental distribution.²⁹⁸ As a first step toward preserving the carefully designed structure and functionalities of bimetallic NPs, it is necessary to understand the mechanisms underlying unwanted modifications.^{299,300} Among the limited number of investigations concerning the stability of Au@Pt NRs, TEM has been a preferred technique. He et al.³⁰¹ studied the stability of Au@Pt NRs by *ex situ* annealing at 200 °C followed by TEM characterization. It should be noted however, that only 2D images were acquired in this study which in general provide insufficient information regarding complex transformations in nanostructures with 3D morphological features.⁷⁶ A more appropriate tool for the study of morphological and compositional changes in bimetallic NPs at a local scale is *in situ* TEM,³⁰² which even allows 3D *in situ* measurements when combined with electron tomography.^{114,303–305}

In this chapter, a systematic investigation of thermal effects on the morphology and composition of Au@Pt NRs with different structures of the Pt shell, obtained by applying a surfactant-driven seed-mediated approach, either with and without chiral additives. Electron tomography was used as a key tool to investigate changes in the surface features and morphology of Au@Pt NRs during *in situ* heating up to 200 °C. In this manner, a deformation of the particles was observed at temperatures hundreds of degrees below the bulk melting temperatures of the individual elemental components (1769 °C for Pt¹⁴² and 1024 °C for Au³⁰⁶). To gain a detailed understanding of the atomistic mechanisms behind the observed instabilities, MD simulations were performed by using the results of the electron tomography experiments as an input. From the combined experimental and theoretical analysis, it was shown that the observed thermal instability is strongly influenced by a delicate balance between Pt shell thickness and coverage of the Au core.

5.2. Synthesis and 3D characterization of Au@Pt NRs

The samples investigated in this chapter were provided by the group of Prof. Dr. Luis Liz-Marzán (research center CIC BiomaGUNE in San Sebastian). Moreover, HAADF STEM imaging, tomography and EDX STEM measurements in this chapter were performed by Dr. Adrián Pedraza Tardajos. Au@Pt NRs were obtained using a micelle-directed seeded approach following previous work.²⁹⁴ Single-crystalline (SC) Au NRs were hereby used as seeds to grow shells with a variety of Pt patterning. Different Pt-shell configurations were obtained by a precise control in the Pt deposition. Different continuity of the shell and its thickness was obtained by combining both a chiral additive and changing the temperature during the synthesis.

An overview of different samples, imaged by HAADF STEM, is presented in Figure 5.1. HAADF STEM imaging was performed using a ThermoFischer Scientific™ Osiris electron microscope operated at 200 kV at a camera length of 115 mm. It can be seen that samples grown without chiral additives (Figure 5.1a), resulted in Au NRs covered with a rough and seemingly continuous Pt shell. On the other hand, in the presence of a chiral additive (BINAMINE) during the synthesis at 20 °C, Au@Pt NRs featured Pt spikes growing radially outward from the central Au NR surface (Figure 5.1b). Furthermore, Au@Pt NRs synthesized using BINAMINE at a temperature of 40 °C resulted in Au@Pt NRs with a Pt shell composed of longer spikes (Figure 5.1c). The measured sizes and aspect ratios for these samples are summarized in Table 5.1. The values correspond to the average size of the particles observed in each sample including the Pt shell. The elemental distribution for these three samples was investigated by EDX STEM measurements. Figure 5.2a illustrates a clear core-shell structure and Pt/Au ratios ranging from 0.1 to 1, as extracted from the EDX STEM measurements (Table 5.1).

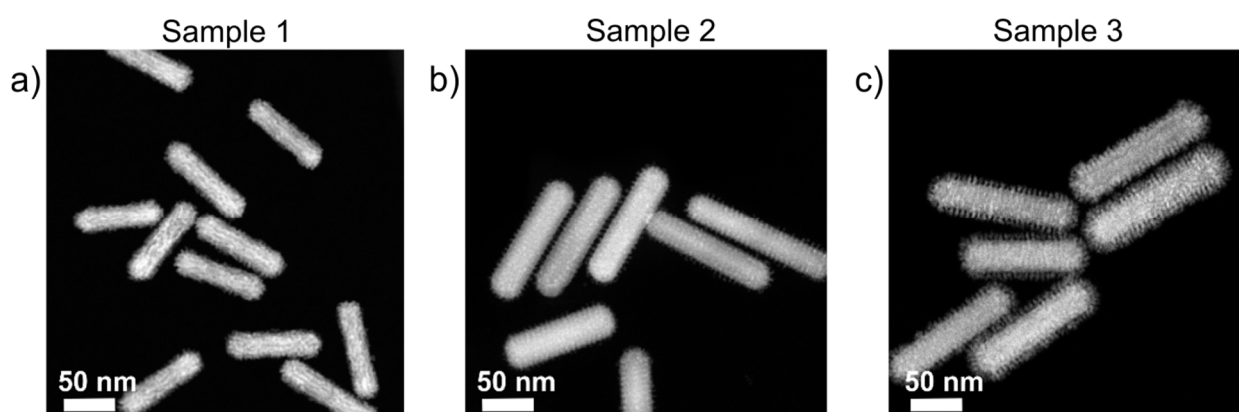


Figure 5.1 HAADF STEM overview of the three different Au@Pt NRs. a) Au@Pt NRs synthesized without chiral additives. b) Au@Pt NRs synthesized using chiral additives at 20 °C. c) Au@Pt NRs synthesized using chiral additives at 40 °C.

Table 5.1 Average morphological and compositional parameters of the different samples investigated by HAADF STEM and EDX at room temperature.

Sample ID	Size	Aspect ratio	[Pt/Au] ratio
Sample-1	100 x 30 nm	~3.30	0.8 ± 0.4
Sample -2	130 x 37 nm	~3.50	0.1 ± 0.3
Sample-3	130 x 43 nm	~3.00	0.3 ± 0.1

However, as these results were obtained from single 2D HAADF STEM images, HAADF STEM tomography was performed to investigate the 3D morphology of the Pt shell. HAADF STEM tomography tilt series were acquired within a $\pm 70^\circ$ tilt range and a tilt increment of 3° in a ThermoFischer Scientific Osiris electron microscope operated at 200 kV and a camera length of 115 mm. Tomographic reconstructions were retrieved by using the reconstruction algorithm developed by Dr. Ivan Lobato at EMAT.⁸¹ 3D visualizations of the electron tomography reconstructions are presented in Figure 5.2b which confirms the presence of regularly arranged spikes for Sample-2 and Sample-3, whereas Sample-1 contains a rough (disordered) Pt shell, with no obvious Pt spikes. From a careful analysis of orthoslices acquired through the 3D reconstructions, it can be confirmed that the Pt spikes in Sample-2 and Sample-3 show a periodic distribution. The helical nature of this ordering is furthermore clear from the 3D visualizations of the electron tomography reconstructions for Sample-2 and Sample-3.

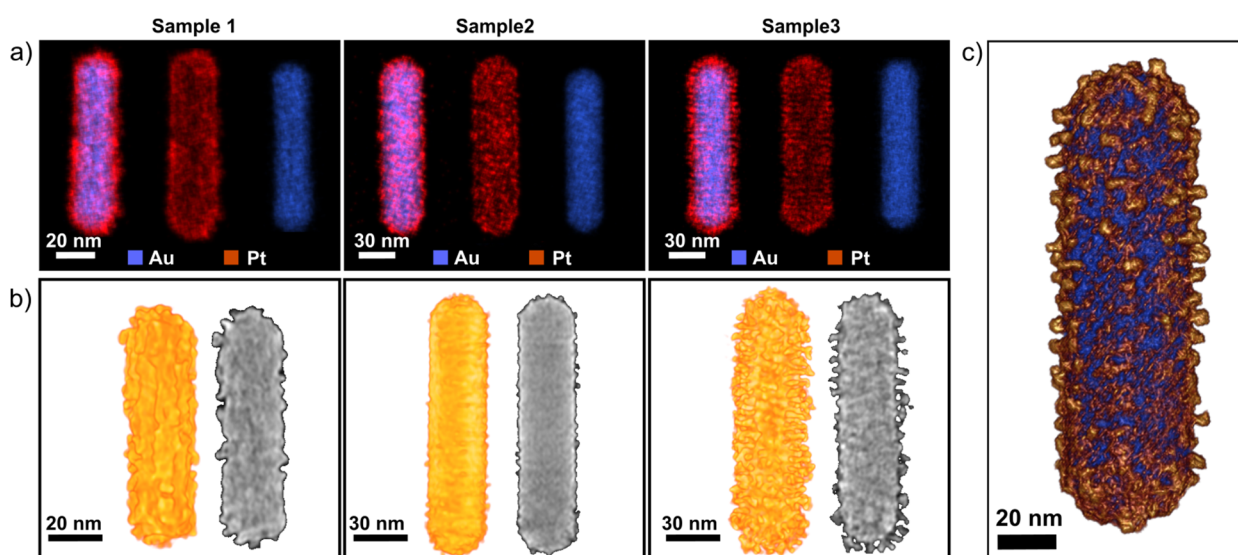


Figure 5.2 a) EDX STEM maps of the different Au@Pt NPs, as labeled. From left to right, the [Pt/Au] ratios calculated from the EDX STEM data obtained from the three different samples are: 0.80, 0.11 and 0.34. b) 3D visualizations and orthoslices (right sides) through the HAADF STEM tomography reconstructions obtained for the different samples at room temperature. c) 3D visualization of the EDX STEM tomography reconstruction obtained from a representative sample prepared using chiral additives.

The difference in atomic number Z for Au and Pt is too small to generate sufficient contrast difference in a 3D HAADF STEM reconstruction. To visualize the Au-Pt interface and investigate the coverage of Au by Pt in more detail, an EDX STEM tilt series were acquired by exploiting the high efficiency of a novel Ultra-XTM EDX detector. A 3D visualization of the EDX STEM tomography reconstruction of a representative Au@Pt NR, prepared in the presence of BINAMINE, is presented in Figure 5.2c. The high SNR of EDX STEM tomography reconstruction enables to conclude that the Pt shell is solely composed of Pt spikes, directly grown on the Au surface and that no intermediate Pt layer is present at the surface of the Au NR.

5.3. Thermal stability of Au@Pt NRs

To study heat-induced morphological transformations, a DENSsolutions Wildfire heating tomography holder was used.³⁰⁷ Au@Pt NRs were deposited on a dedicated silicon nitride (Si_3N_4) MEMS heating chip and heated to 200 °C (temperature selected to compare our *in situ* results with *ex situ* results in ref.³⁰¹). After heating the NRs for 5 min, they were instantaneously cooled down to room temperature (in ~ 1 s) to prevent further transformations while imaging. HAADF STEM images (Figure 5.3a) indicated the heat-induced formation of indentations or voids in all investigated samples. Such voids are especially noticeable in Sample-3, whereas a smaller one is indicated by an arrow for Sample-1. Sample-2 mostly showed indentations, rather than voids.

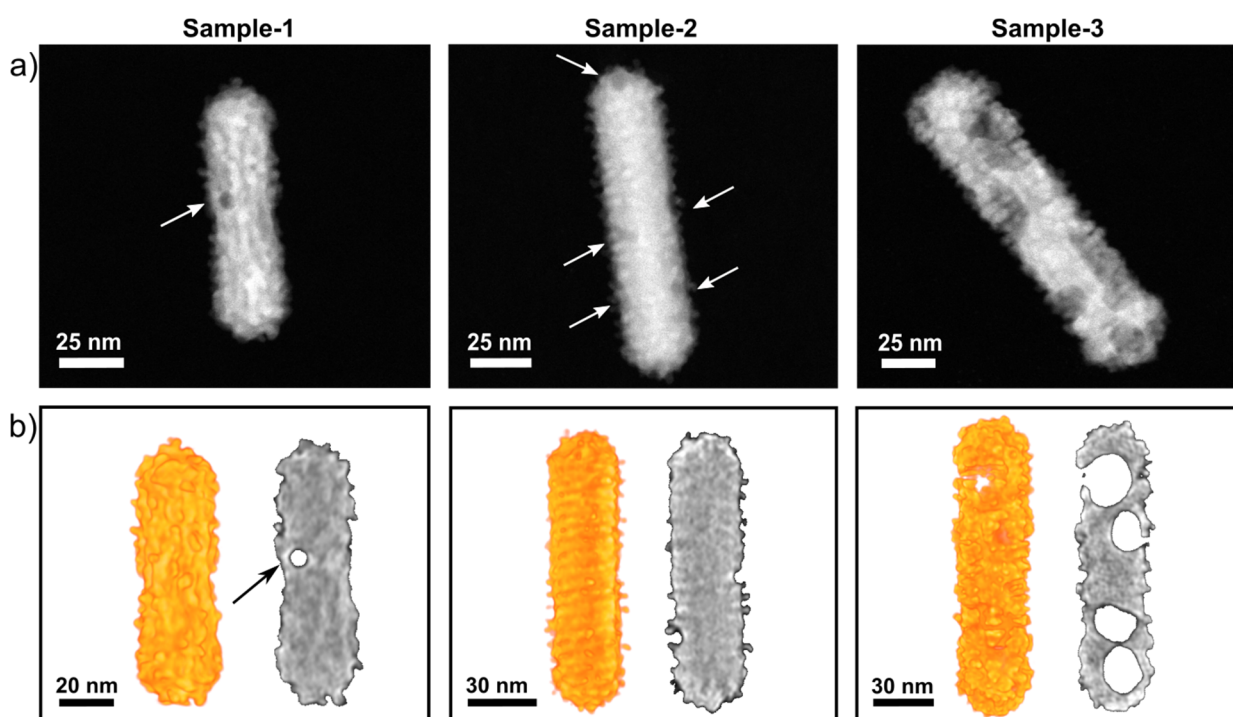


Figure 5.3 *In situ* STEM experiments for the three different samples as labeled. a) 2D HAADF STEM images and b) 3D visualizations with orthoslices (right sides) through the HAADF STEM tomography reconstructions obtained after heating at 200 °C for 5 minutes. Small voids and indentations observed in Sample-1 and Sample-2 are marked in the 2D images by white arrows and by black arrows in the orthoslices.

A better understanding of this complex transformation required additional investigation in 3D, which was achieved by using *in situ* electron tomography.^{114,304,305,308} 3D reconstructions of NRs

from the three different samples after heating to 200 °C are shown in Figure 5.3b. From the orthoslices through the 3D reconstructions of Sample-1, which originally had a rough, but continuous Pt shell, small voids were observed close to the surface, along with narrow channels connecting the void to the surface (Figure 5.4). Moreover, for all samples, depleted Au was found to form Au clusters on the otherwise empty regions of the Si₃N₄ support as confirmed by EDX STEM measurements (Figure 5.5). Based on these observations, it can be hypothesized that the observed channels formed a pathway for Au atoms to diffuse out of the core, which ultimately resulted in the creation of voids inside the Au NRs, in agreement with the postulation by He et al.

301

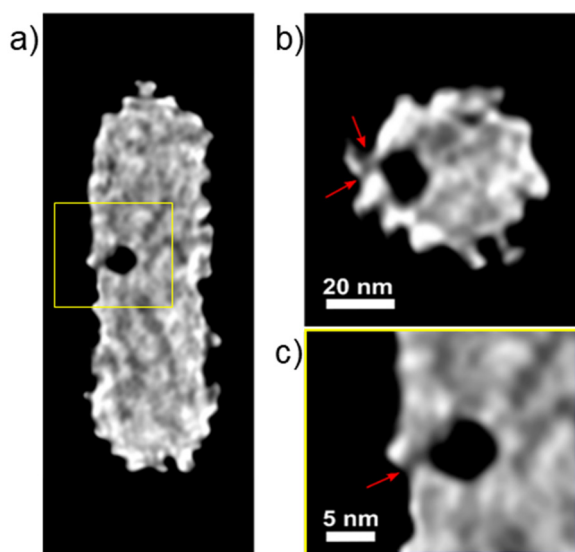


Figure 5.4 3D reconstruction of a Au@Pt NR from Sample-1 after heating to 200 °C. Orthoslice through the 3D reconstruction along the (a) yz plane and (b) xy plane. (c) A magnified region from panel (a). The presence of diffusion pathways for Au atoms are marked by red arrows.

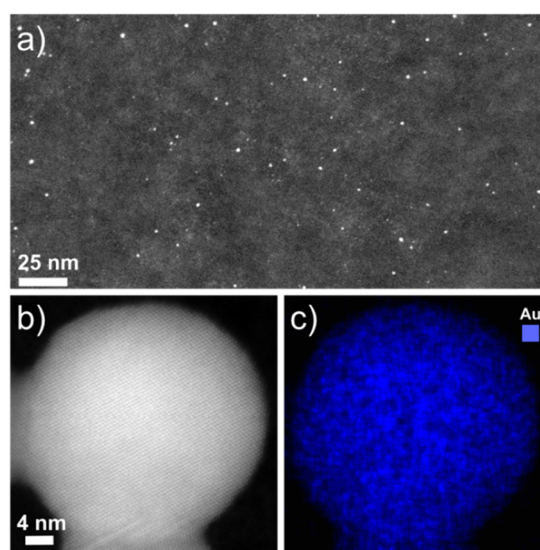


Figure 5.5 Au clusters depleted from the Au@Pt NRs after heating to 200 °C. (a) HAADF STEM image of the Si₃N₄ MEMS heating chip covered by small Au NPs. (b) Higher magnification image of one of those Au NPs. (c) EDX map of the NP in panel (b), showing a composition of 100% Au.

On the other hand, Sample-2 did not contain any voids inside the NR, but indentations were clearly observed at the surface of the particle in agreement with the 2D projection image shown in Figure 5.3a. For Sample-3, it was observed that the large voids extended far inside the NP (Figure 5.3b). Since the degree of void formation significantly varied for different samples, it is likely that the local Pt surface morphology has an effect on Au migration. However, the details of the underlying processes are difficult to understand from the experimental observations alone. To gain insight into these mechanistic details, MD simulations were performed.

5.4. MD simulations

5.4.1. MD simulations by using experimental morphology

MD simulations started by using the experimentally measured morphologies for Samples 1-3. Based on literature reports³⁰⁹ and electron tomography reconstructions obtained for Au NRs used

during synthesis (Figure 5.6a-c), the input structure of the Au NR was constructed to have eight $\{520\}$ lateral facets and $\{100\}$, $\{110\}$, $\{111\}$ facets at its tips. For that, an FCC Au structure in a rectangular prism was created. The ends of the prism, having the configurations of $\{100\}$ crystal facets, were then truncated to form $\{110\}$ and $\{111\}$ facets. Afterward, the lateral facets were truncated according to a $\{520\}$ configuration. The side view of the created NR is shown in Figure 5.6d.

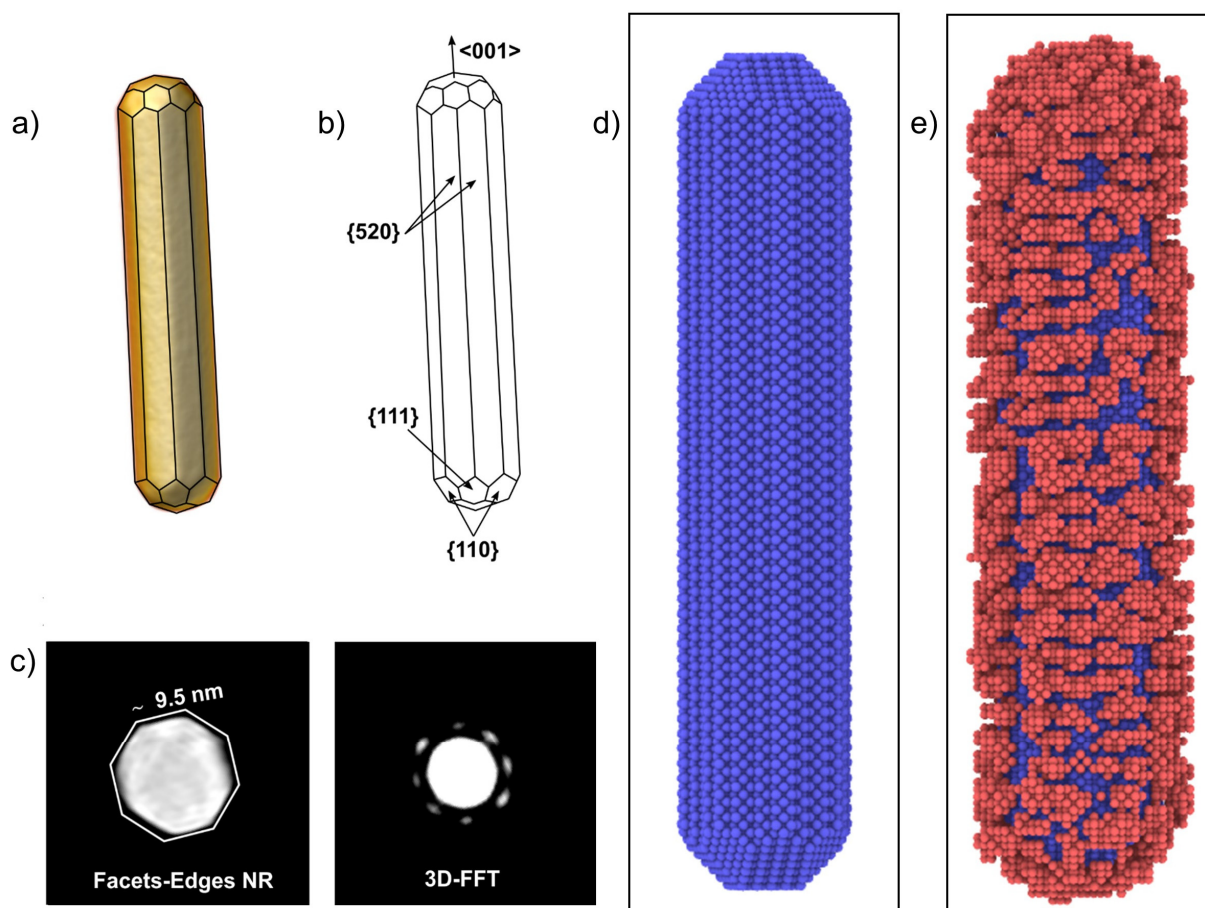


Figure 5.6 a) Visualization of the HAADF STEM tomography reconstruction of a Au NR with the corresponding crystallographic facets highlighted. b) Analysis of the crystallographic facets of the rod according to the model presented in reference ³⁰⁹, suggesting the presence of $\{520\}$ lateral facets. c) Symmetry of the side of the facets and 3D-FFT projection image confirming the symmetry of $\{520\}$ lateral facets. Electron tomography experiments and 3D-FFT analysis were performed by Dr. Adrián Pedrazo-Tardajos. d) Created 3D Au NR model with eight $\{520\}$ lateral facets. e) Model of the Au@Pt NR based on the experimentally determined morphology.

The Pt-shell around the input structure of Au NR was created based on the morphology of the 3D reconstructions shown in Figure 5.2b. The reconstructed volumes were first binarized by setting the values above a threshold to 1 and setting the others to 0. Hereby, the threshold value was defined by using Otsu's method. ²⁴³ Next, each binarized 3D volume was filtered with a 3-D Gaussian smoothing kernel to create a mask. At the same time, an FCC Pt structure (lattice parameter = 3.9764 Å) ¹⁹² was created in a rectangular simulation box. Then, Pt structures were extracted by

applying the created masks to the FCC rectangular simulation box. Finally, the previously created Au NR was placed at the center of the created Pt structures. Since using the actual size of the experimental NPs (Table 5.1) in MD simulations requires vast computational power, overall sizes of the created Au@Pt NRs were scaled down. However, for all the other parameters, such as aspect ratio and Pt/Au ratios, experimentally determined values were used. As an example, a created input structure of Au@Pt NR for MD simulations is shown in Figure 5.6e.

After creating input structures corresponding to the Au@Pt NRs, conjugate gradient energy minimization³¹⁰ was applied by controlling the maximum distance that an atom can move in a one-time step. The maximum displacement distance was set as 0.01 Å. A time step of 1 fs was used to track the movements of atoms and the EAM was used to define the interaction between the atoms.¹⁹² Non-periodic boundary conditions were applied in all three directions with a large vacuum area. Also, the total linear and angular momenta were conserved so that the rod did not drift nor rotate throughout our simulation. Next, the NRs were relaxed for 20 ns at room temperature with the canonical ensemble and a damping factor of 0.1. Subsequently, to mimic the experimental observations, temperature was increased with a constant heating rate of 0.5 K/ps and relaxed for 20 ns at 200 °C.

In Figure 5.7a-c, the resulting 3D morphologies based on Samples (1-3) are shown before and after heating. Also, orthoslices through the simulated NRs after heating are presented (right sides). After heating of the simulated NRs, indentations were found for all samples, indicating a good agreement between the experiments and simulations. It should be noted that the size of these indentations, appearing during MD simulations, are relatively small compared to the size of the indentations and voids observed in the experiments. This apparent discrepancy is related to the limited time scale and smaller input structures used during MD simulations. Moreover, our simulations were performed without the presence of a Si₃N₄ sample support and with the constraint of keeping the total volume of the NRs constant, which explains why indentations rather than voids are formed.

These simulations allowed to capture the *dynamics* of void formation, which could not be extracted from the experiments, in which only the structure before and after heating could be investigated. The MD results in Figure 5.7d demonstrate that Au atoms close to the Au-Pt interface (indicated in black for better visualization) created diffusion channels and migrated towards the NR surface during heating, as hypothesized from our experiments. This process resulted in the formation of a small indentation, as shown in Figure 5.7a,d. The MD simulations further showed that during heating at 200 °C, 2.8% of Au atoms in Sample-1 (Figure 5.7a) migrated towards the NR surface, whereas this percentage increased to 8.2% for Sample-2 and 9.0% for Sample-3 (Figure 5.7b,c). As expected, it can also be seen that higher percentages of Au migration lead to larger indentations. This percentage of migrated Au atoms was defined as the ratio between the number of migrated Au atoms and the total number of Au atoms that were initially in the core.

Figure 5.7 moreover suggests that the size and location of the formed indentations is different for the different samples, in agreement with the experimental observations. For instance, it can be seen that the NR in Figure 5.7c, which had a Pt surface coverage of 65% (to mimic Sample-3), yielded a larger number of indentations in comparison to the NR in Figure 5.7a, which had initially a 99%

surface coverage (to mimic Sample-1). The surface coverage of the Pt shell was defined as the ratio between the number of Au surface atoms covered by the Pt-shell and the total number of atoms at the surface of the Au core. In addition to surface coverage, also the thickness of the Pt spikes apparently played a role during Au migration. The NR in Figure 5.7b, which initially had short spikes, mimicking Sample-2, yielded smaller indentations at 200 °C in comparison to the NR in Figure 5.7c, which initially had thicker spikes but a similar coverage, in agreement with Sample-3.

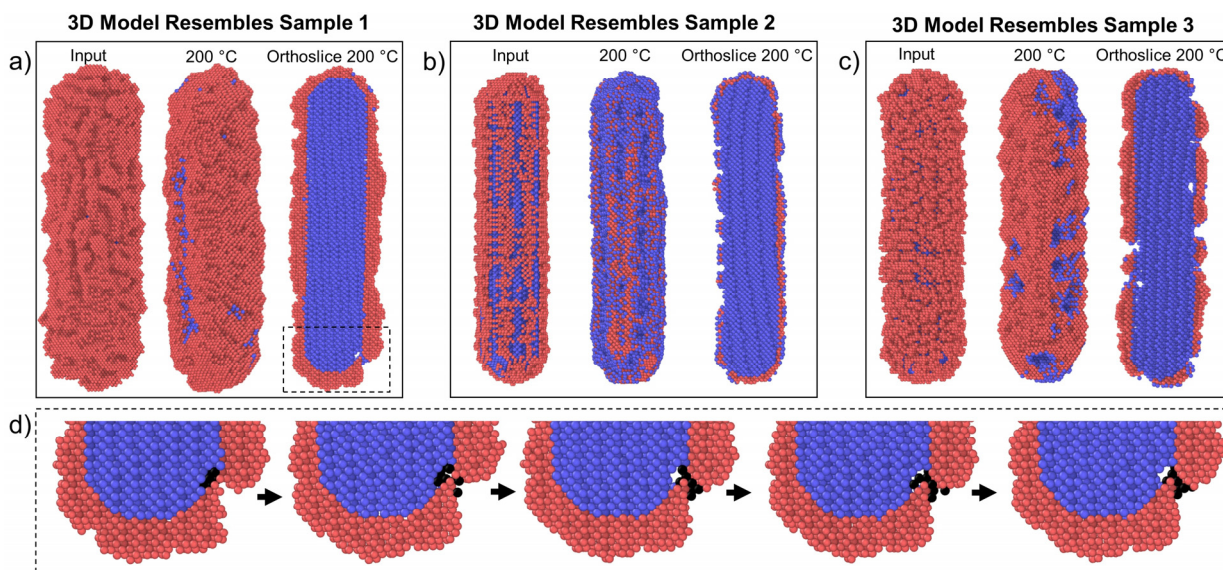


Figure 5.7 MD simulations based on electron tomography reconstructions. a-c) Tomography-based 3D models and orthoslices (right sides) of Au@Pt NRs before and after heating at 200 °C resembling Sample-1, Sample-2 and Sample-3 represented in Figure 5.2b. Pt atoms are shown in red and Au atoms are shown in blue. d) Snapshots of the intermediate steps during the transformation of the NR in Figure 5.7a. Black dots represent Au atoms migrating towards the NR surface during heating at 200 °C.

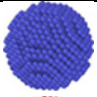
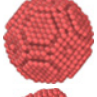
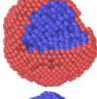
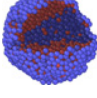
The very good agreement between the simulations and the experimental observations confirms that the MD approach can be used to model the mechanistic processes explaining the instability of these samples at elevated temperature. MD simulations in this section showed that there is a direct relationship between the morphology of Pt-shell and the percentage of migrated Au atoms towards the NR surface and so the size of the appeared voids at 200 °C. Herein, it is also important to get an insight into the thermodynamic behavior of bimetallic Au-Pt NPs to be able to interpret the reason behind the migration of Au atoms toward the NR surface at high temperatures. Therefore, in the next section, the core-shell preference of Au-Pt bimetallic systems is overviewed on a model-like spherical NPs before a detailed investigation of the Pt surface morphology effect on the thermal instability of NRs (Section 5.4.3).

5.4.2. Thermodynamic behavior of Au-Pt NPs

Recent studies revealed that the cohesive energy and Wigner-Seitz radius, which is defined as the radius occupied by one atom,³¹¹ are the two primary factors affecting the preference for an element

to be at the core or the shell in core-shell bimetallic NPs. In general, the less cohesive element with a larger Wigner-Seitz radius prefers to segregate at the surface to minimize compressive strain within the bimetallic NP arising from the size mismatch.^{312–315} The total cohesive energies per atom for Au and Pt NPs were determined from conjugate gradient energy minimization by employing EAM potential.¹⁹² It was found that Au is less cohesive, -2.89 eV, compared to Pt, -5.19 eV (Table 5.2) which is consistent with literature.^{312,314,315} Moreover, Au has a larger Wigner-Seitz radius (3.01 Bohr radius) than Pt (2.90 Bohr radius).³¹⁶ Therefore, from a thermodynamics point of view, Au atoms prefer to be located on the surface in Au-Pt bimetallic systems.

Table 5.2 Formation energies of Au-Pt bimetallic systems.

3D models	Type of structures	Component	Average cohesive energy per atom (eV)	Total formation energy (eV)
	Pure Au NP	1865 atoms	-2.89	-
	Pure Pt NP	2123 atoms	-5.19	-
	Pt-shell/ Au-core	1865 Au atoms 1952 Pt atoms	-4.01	236.5
	Au-shell/ Janus-like structure	1865 Au atoms 1952 Pt atoms	-4.18	-473.6

This hypothesis was supported by MD simulations of spherical Au@Pt and Pt@Au with 5 nm diameter and a double-layer shell. MD simulations started with conjugate gradient energy minimization.²⁶³ Then, the NPs were relaxed for 10 ns at room temperature with the NVT ensemble and a damping factor of 0.1. Subsequently, to observe the thermal stability of each bimetallic NP, the temperature was increased with a constant heating rate of 0.5 K/ps to 2000K. The change in elemental distribution in the Pt@Au NP as a function of temperature is displayed in Figure 5.8a, and at the same temperatures, the snapshots of Au@Pt NP are shown in Figure 5.8b.

Since Au segregation at the surface is thermodynamically preferable, Pt@Au NP in Figure 5.8a preserved its initial elemental distribution even at a high temperatures. On the other hand, as the temperature increased, the Au atoms in Au@Pt NP (Figure 5.8b) started to move from the core to the outer shell. The migration of Au atoms became pronounced at 600 °C, and eventually, Au atoms completely covered the surface at 800 °C and formed a segregated Janus-like structure. Moreover, the formation energies of Au@Pt (the left-most row of Figure 5.8b) and the final Janus-like structure (the right-most row of Figure 5.8b) were calculated from the difference of the cohesive energies of bimetallic NPs and their pure components (Table 5.2). The negative formation energy of the final Janus-like structure demonstrates its thermal stability. Therefore, it can be concluded that heat-induced movement of Au atoms arises from the tendency to minimize the energy of the

Au@Pt NP and to reach a thermodynamically more stable configuration. Although these simulations are performed on relatively simple systems, they provide an insight regarding the thermodynamic behavior of Au@Pt NPs at high temperatures. However, these observations are still inadequate to enlighten the experimentally observed void formation, which significantly varied for different samples having different Pt-shell morphology. Therefore, as a next step, the effect of Pt surface morphology on the thermal instability of Au@Pt NRs at mild temperatures is investigated in detail.

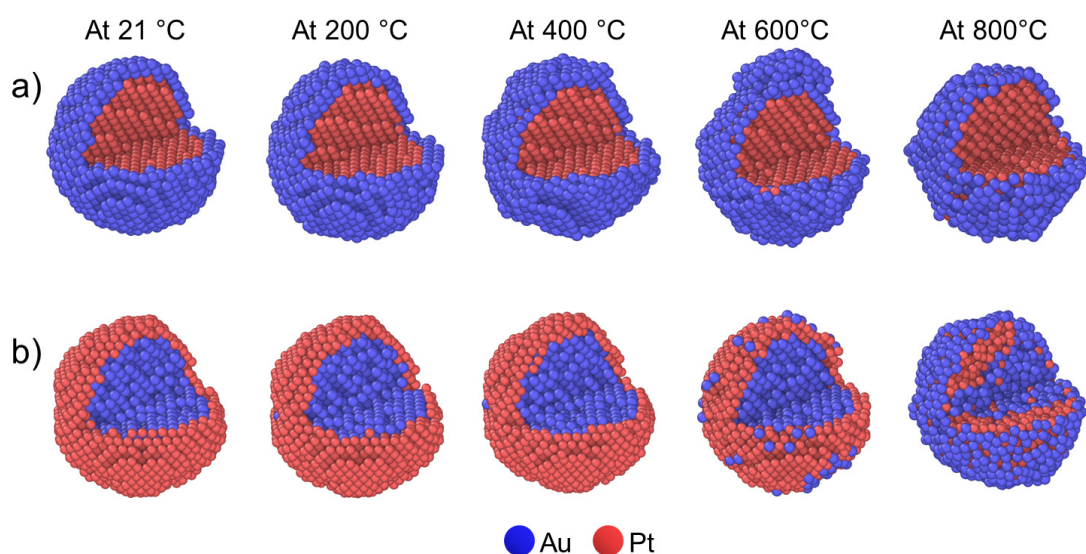


Figure 5.8 MD simulations of the thermal stability of spherical Au-Pt NPs having different structure in the core-shell. The snapshots of Pt@Au (a) and Au@Pt (b) NPs are shown as a function of temperature.

5.4.3. The effect of Pt surface morphology on thermal stability of NRs

In this section, the morphological parameters of the Pt shell, namely the thickness of Pt spikes and the surface coverage are decoupled. To investigate the latter, different Pt islands, mimicking Pt spikes were placed on an Au(111) surface (Figure 5.9). All islands had the same Au-Pt interfacial area, but they all had a different height corresponding to 2, 4 or 5 atomic layers. Prior to the heating simulations, the Au(111) surface was relaxed for 10 ns at room temperature. During the relaxation, periodic boundary conditions were applied in the x and y-directions and a non-periodic boundary condition was applied along the z-direction. Also, the bottom layer in the z-direction was frozen. After different Pt islands were placed on the relaxed Au(111) surface, a full relaxation was performed for 20 ns at room temperature. Then, the relaxed Pt islands on Au(111) surface were gradually heated with a 0.5 K/ps heating rate. Side- and top-views of these islands are presented in Figure 5.9a-c, as a function of temperature.

Already at room temperature, Au atoms were observed to move towards the top of the Pt islands, independent of the thickness of the islands. As a result, small indentations were formed at the surface (as indicated by grey dots). However, after 10 ns this process did not propagate any further. Next, the temperature was increased to 200 °C and the system was relaxed for 20 ns. From Figure

5.9, it can be seen that the higher temperature significantly enhanced Au migration toward the top of the Pt islands, resulting in larger indentations at the Au surface. Because of larger thermal vibrations, it is typically expected that the potential energy of a system monotonically increases with increasing temperature, prior to reaching the melting point. On the contrary, Figure 5.9d shows that the average potential energy of the Pt atoms decreased as temperature was increased from room temperature to 400 °C.

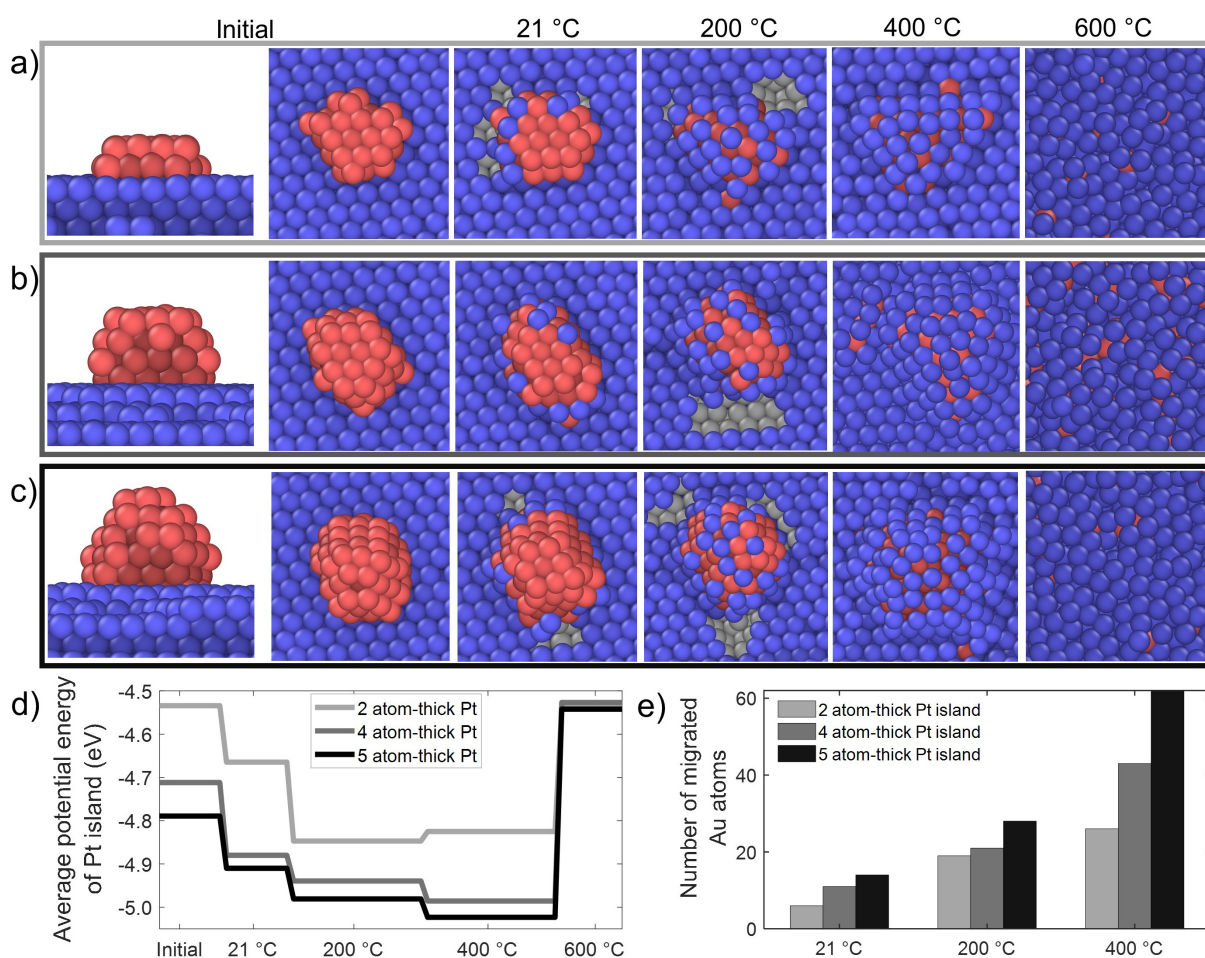


Figure 5.9 Effect of the thickness of Pt(111) islands on the number of Au atoms migrating to the surface of Au@Pt NRs. Pt atoms are presented in red, Au atoms in blue and voids in gray. a-c) Side-views of 2, 4, and 5 atoms-thick Pt-islands, and top views illustrating their structural evolution as a function of temperature. d) Average change of potential energy per atom for the Pt islands as a function of temperature. e) Histogram of the number of migrated Au atoms as a function of temperature and thickness of the Pt-islands.

These observations can be rationalized from a thermodynamics point of view as it has already been explained in the previous subsection. Since Au is less cohesive and has a larger Wigner-Seitz radius than Pt,³¹⁶ Au atoms prefer to migrate toward the surface, so as to reduce strain at the Au-Pt interface and to consequently minimize the overall energy (Figure 5.9d). It is important to note that although Au migration continued at higher temperatures, the formation of the voids and indentations at the Au surface prevailed at mild temperatures only. When the temperature was increased further to 400 °C and above, it was observed that the voids diminished since a higher

thermal vibration results in larger spacing between Au atoms at the surface. This was followed by surface melting (sharp increase in Figure 5.9d) at 600 °C.

As a consequence of the thermodynamic instability, thicker Pt islands induced the formation of larger indentations on the Au surface, as more Au atoms were required to cover the thicker Pt-islands. Figure 5.9e shows the increase in the total number of migrated Au atoms as a function of temperature, for each system. This explains why the voids became more pronounced in our experiments for samples with larger Pt spikes (Sample-3).

Next, the influence of Pt shell completeness (coverage of the Au core surface) was investigated. Therefore, Pt-coatings with helical shapes were created by extending Pt-islands, with similar thickness, on Au NR surfaces (Figure 5.10). The reason of using helical coatings is that it gives one good control over the coverage (by simply changing the number of spirals) while making it possible to keep the thickness of the coating the same. Moreover, the experimental observations demonstrated that the Pt coating contains helical features for Sample-2 and Sample-3 (see Figure 5.2b).

By changing the number of helices, Au@Pt NRs with different Pt surface coverage, ranging from 44.5% (leftmost) to 89% (rightmost) were obtained (Figure 5.10a). The structures, obtained after heating to 200 °C, are shown in Figure 5.10b, along with a visualization of Au atoms only (Figure 5.10c). The resulting percentages of Au atoms that migrated from the core to the surface of the Pt shell are plotted in Figure 5.10d. Since the same Au core was used for all Au@Pt NRs shown in Figure 5.10, these percentages can also be interpreted in an absolute manner. As the surface coverage increased from 44.5% to 65.3%, the number of migrated Au atoms increased. This can be expected from the results above, demonstrating the tendency of Au atoms to cover the Pt islands. However, for Pt coverages above 65.3%, a decrease in the number of migrated Au atoms was observed. This is not surprising since for higher Pt coverage less Au diffusion pathways between the Pt spikes are present. Consequently, for an Au@Pt NR with 89% Pt coverage, the number of Au atoms that could migrate upon heating was significantly reduced and the initial shape of the core Au NR was almost fully preserved after heating (Figure 5.10c).

Finally, to obtain a complete understanding of the interplay between surface coverage and thickness of dendrites, MD simulations were carried out for different Pt-coatings by varying both the surface coverage and the thickness of the Pt islands. The created input structures used for the simulations are shown in Figure 5.11. The results of the simulations for the 40 combinations of different morphologies are summarized in Table 5.3, which shows the percentage of diffused Au atoms at 200 °C. For the sake of visualization, the results in Table 5.3 are color-coded, with red representing the largest number of diffused Au atoms and blue corresponding to negligible migration of Au atoms.

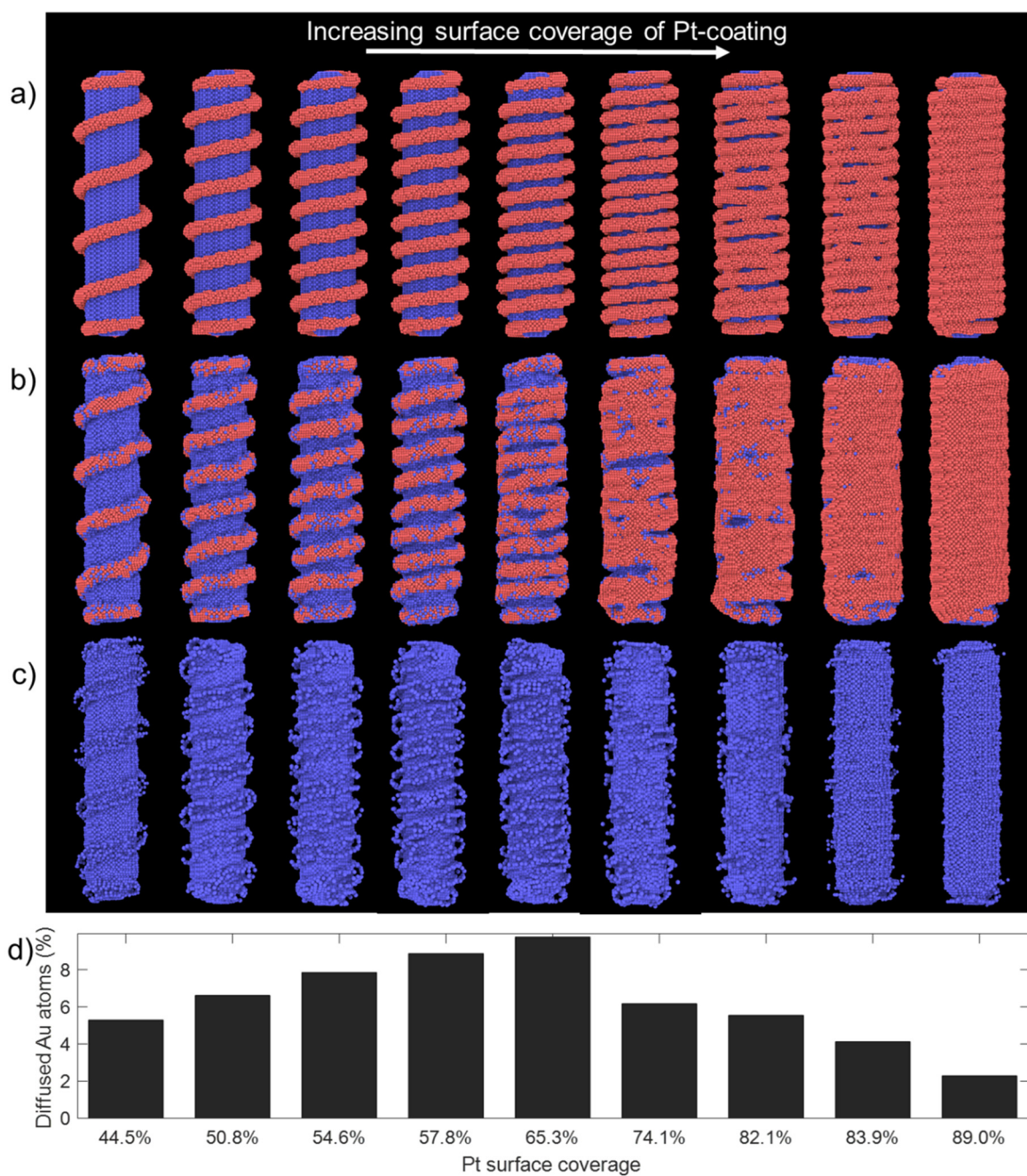


Figure 5.10 Surface-coverage effect of the Pt shell around the Au NR, on the number of migrated Au atoms. a) Created input structures. b) Structures after heating at 200 °C. c) Au atoms within the Au@Pt NR after heating to 200 °C. d) The percentage of migrated Au atoms from structures with different Pt surface coverage.

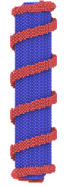
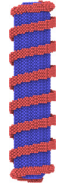
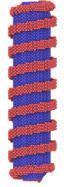
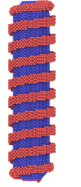
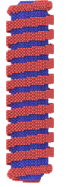

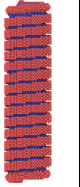
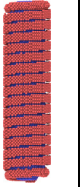
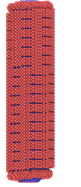
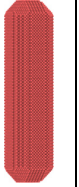
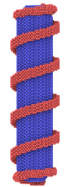
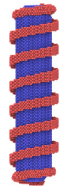
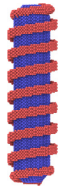
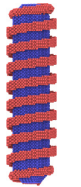
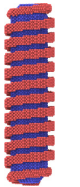
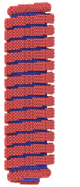


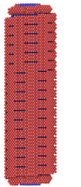
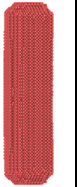
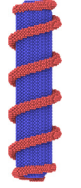
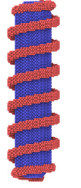
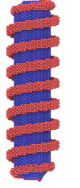
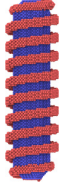
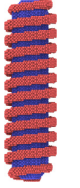


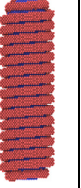
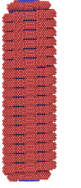
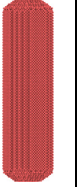
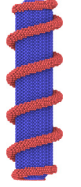
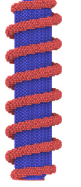

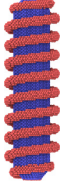



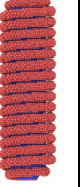

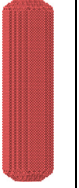
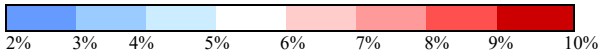
		Surface Coverage of Pt-Shell									
		44.5%	50.8%	54.6%	57.8%	65.3%	74.1%	82.1%	83.9%	89.0 %	100%
Thickness of Pt-shell ↓	2 atom-thick										
	3 atom-thick										
	4 atom-thick										
	5 atom-thick										

Figure 5.11 Input structures of Au@Pt NRs used in the MD simulations from which Table 5.3 was obtained.

Two different trends can be observed from Table 5.3. At Pt surface coverages below 74%, an increasing number of Pt atoms, in terms of either surface coverage or thickness of the Pt islands, resulted in a higher percentage of migrated Au atoms. Therefore, the highest percentage of Au diffusion was observed for NRs with 65% Pt surface coverage and 5 atom-thick Pt dendrites. This system had long-enough Pt-spikes to stimulate the diffusion of Au atoms, while at the same time yielding sufficient Pt-free Au surface to enable Au migration. On the other hand, once the Pt surface coverage reached 74%, fewer Au atoms could diffuse because of the lack of Pt free pathways. Obviously, this effect was most dominant for NRs with a continuous Pt-shell (rightmost column), for which Au atoms would have to create diffusion channels toward the surface and hereby overcome the energy barrier imposed by the Pt shell.

Table 5.3 Percentage of diffused Au atoms after heating at 200 °C by MD simulations for Au@Pt NRs with different Pt surface coverage and thickness of the Pt shell.

		Surface Coverage of Pt Shell									
		44.5%	50.8%	54.6%	57.8%	65.3%	74.1%	82.1%	83.9%	89.0%	100%
Thickness of Pt shell ↓	2 atom-thick	4.9 %	6.4 %	7.2 %	8.1 %	9.7 %	9.8 %	9.2 %	7.6	3.3	2.0 %
	3 atom-thick	5.1 %	6.6 %	7.2 %	8.1 %	9.7 %	7.3 %	5.6%	3.4	2.0	0.5 %
	4 atom-thick	5.1 %	6.5 %	7.4 %	8.5 %	9.6 %	6.3 %	5.4%	3.8	2.2	0.0 %
	5 atom-thick	5.3 %	6.8 %	7.8 %	8.9 %	9.8 %	6.2 %	5.5 %	4.1 %	2.3 %	0.0 %



To be more precise on the effect of continuous Pt-shell thickness on the thermal stability of Au@Pt NRs, the required energy barriers of Au@Pt NRs having a continuous but varying thickness of Pt-shell was estimated. Hereby, NRs with a continuous Pt-shell (rightmost column of Figure 5.11) were heated to 1350K with a heating rate of 0.5 K/ps. Then, the required energy was simply calculated as the energy difference between the initial state and the state where the first Au atom appeared on the surface of the Pt-shell. It should be noted that the energy difference was determined based on the defined inter-atomic potential, EAM, during MD simulations, and so it should be interpreted in a relative manner. 3D models of the NR having a continuous 2 atom layer-thick Pt-shell before and after heating are shown in Figure 5.12a-c. The calculated energy barriers for NRs having continuous Pt-shells with 2 atom layer, 3 atom layer and 4 atom layer-thick are shown in Figure 5.12d. As illustrated in Figure 5.12, due to the thin coating around the NR having a 2 atom-thick Pt-shell, Au atoms could easily diffuse through the outer surface even at room temperature. However, for a thicker Pt-shell, heating to higher temperatures was required to overcome the energy barrier and to create a Pt-free pathway for the diffusion of Au atoms. Although the imposed energy barrier was overcome at 200 °C for the NR with a 3 atom-layer Pt-shell, the first Au atom on the surface was observed only at around 1300 K for the NR with a 4 atom-layer Pt-shell. During heating of the Au@Pt NR having a 5 atom-thick Pt-shell, none of the Au atoms could overcome the energy barrier and diffuse through the Pt-surface below the melting temperature. These results hence indicate that Au surfaces with a high Pt coverage or larger Pt spikes can significantly improve the thermal stability of Au@Pt NRs due to a stronger kinetic trapping effect against the heating-induced migration of Au atoms.

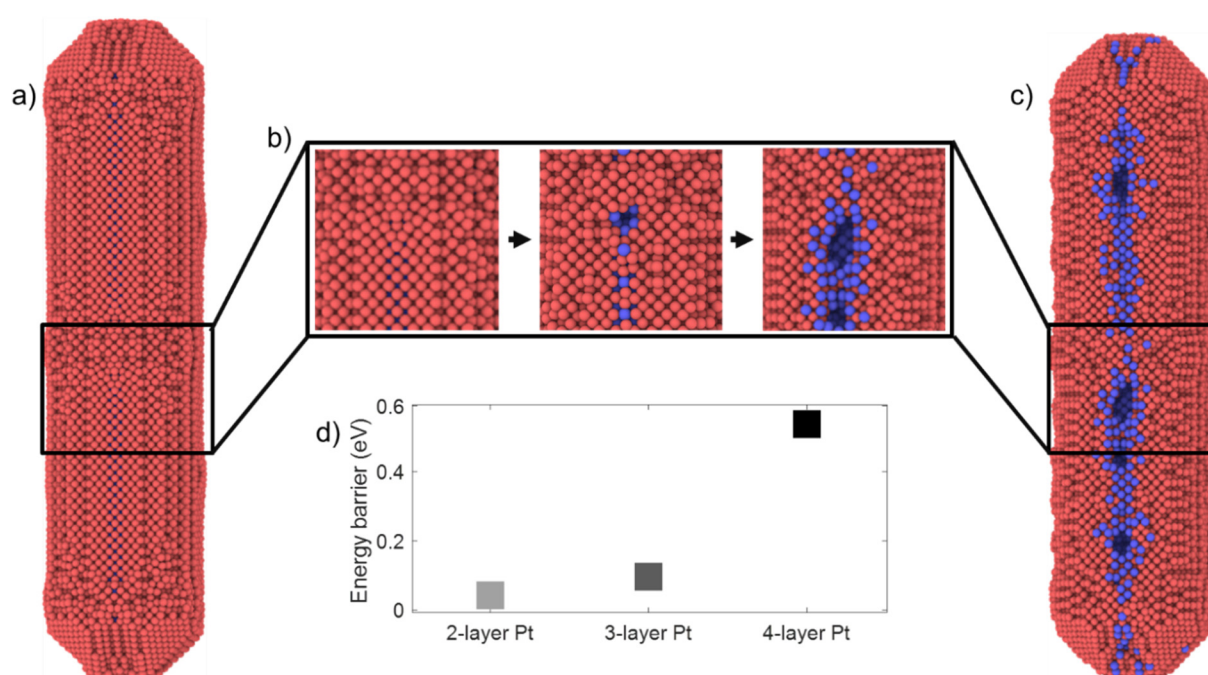


Figure 5.12 MD simulations of Au@Pt NRs which were fully covered by Pt-shell. a) 3D model having continuous Pt-shells with 2 atom layer before heating. b) Magnified visualization that shows the intermediate steps of creation of gaps on the continuous Pt shell and the diffusion of Au atoms through the appeared gap upon heating. c) The final structure of the NR at 200 °C. Pt atoms are shown in red and Au atoms are shown in blue. d) Energy barrier against the heat-induced diffusion of Au atoms in Au@Pt NRs with different thicknesses of the Pt-shell.

5.5. Discussion and conclusion

All of the results presented in this chapter contribute to understanding the driving forces behind Au migration and the resulting thermal instability of Au@Pt NRs. It has been shown that the experimentally-observed heat-induced transformations depend on the exact morphology of the nanostructure, where Pt surface coverage as well as the thickness of Pt spikes on the Au surface were the main factors influencing the thermal stability. At elevated temperatures, Au atoms diffuse from the core to the outer part of the Pt shell to reach a thermodynamically more stable configuration, with Pt spikes acting as the nucleation sites for Au atoms. Longer Pt spikes lead to an increased number of migrated Au atoms and consequently larger voids. However, this process was mainly dominated by the continuity of the Pt shell. At Pt surface coverage exceeding 74%, the Pt coating was found to act as a barrier against Au atom diffusion, thereby reversing the mechanism: longer Pt spikes lead to a decrease in the percentage of diffused Au atoms.

There is general agreement with literature reports showing that core-shell formation in Pt-Au bimetallic NPs is affected by the atomic size and cohesive energy of the constituent elements.^{312–315} In addition to such previous reports, the findings presented in this chapter show that heat-induced deformation at mild temperatures can be explained by a delicate interplay between thermodynamics and kinetics. This study therefore provides an atomistic insight towards tuning

the thermal stability of Au@Pt NPs by changing the morphology of Pt shells, for relevant applications at which elevated temperatures are needed.

In conclusion, the thermodynamic behavior of Au@Pt NPs with different spatial distributions of Pt-shell was investigated by electron microscopy and MD simulations. Combined results from both techniques enabled to understand the complex cooperative effect between Au and Pt at the atomic scale. In brief, the experiments revealed that Au@Pt NRs exhibited structural deformation at temperatures well below the melting point of both Au and Pt, creating voids and indentations in the Au core. It has been observed that such structural transformations largely depended on the morphology and coverage of the Pt shell. Using the experimentally determined 3D morphology of the real particles as an input, MD simulations enabled to conclude that the observed deformations take place because the system aims to reduce its total energy by migration of Au atoms from the core through the interface to the outer surface, leading to a thermodynamically favorable structure. The process is highly influenced by the amount of Pt in the coating spikes, as well as Pt surface coverage. The findings in this chapter can be ultimately exploited to improve the design of these systems to preserve their functionalities for electro- and photo catalytic applications operated at elevated temperatures.

Chapter 6. 3D atomic-scale dynamics of laser light induced restructuring of nanoparticles unraveled by electron tomography and molecular dynamics simulations[§]

In the previous chapters, the transformations of morphology and composition in NPs have been measured as a function of temperature by combining *in situ* heating experiments and atomistic simulations. However, the investigation of NP transformations becomes more challenging when the specific environmental triggers cannot be applied *in situ*. For example, due to the ultrafast time scales of laser-light-induced restructuring of NPs, these transformations cannot be monitored by simply heating the particles during the experiments.

Understanding light-matter interactions in nanomaterials is crucial for optoelectronic, photonic and plasmonic applications. Specifically, metal NPs strongly interact with light and can undergo shape transformations, fragmentation and ablation upon (pulsed) laser excitation. Despite being vital for technological applications, insights into the underlying atomistic processes is still lacking due to the complexity of such measurements. In this chapter, atomic resolution electron tomography on the same mesoporous silica-coated Au NR, before and after femtosecond laser irradiation, is performed. By performing MD simulations based on the experimentally determined 3D atomic scale morphology, the complex atomistic rearrangements, causing shape deformations and defect generation, are unraveled. These rearrangements are simultaneously driven by surface diffusion, facet restructuring and strain formation, and are influenced by subtleties in the atomic distribution at the surface.

* This chapter is based on the following paper:

Albrecht, W.[†], Arslan Irmak, E.[†], Altantzis, T., Pedraza-Tardajos, A., Skorikov, A., Deng, T.-S., van der Hoeven, J. E. S., van Blaaderen, A., Van Aert, S., Bals, S. Three-Dimensional Atomic Scale Dynamics of Laser Light Induced Restructuring of Nanoparticles Unraveled by Electron Tomography. *Advanced Materials* (2021) doi: 10.1002/adma.202100972.

[†] Equal contribution to the published work.

My contribution consisted of the determination of surface facets of an experimentally imaged nanoparticle from high-resolution electron tomography, creating input models for molecular dynamics simulations, developing numerical calculations to model femtosecond laser induced heating, designing and performing molecular dynamics simulations, as well as their analysis and discussion.

6.1. Introduction

The interaction of metal NPs with ultrashort laser pulses has been an intensive research topic due to their unique optical and photothermal properties, which led to numerous applications in, amongst others, biomedicine,^{317,318} sensing,^{319–321} imaging,^{322,323} data storage^{324–326} and catalysis.^{327–329} These properties stem from the efficient interaction of metal NPs with light via LSPRs. Specifically, the electronic absorption of the laser energy and subsequent electron-phonon scattering heats up the NP's crystal lattice, possibly leading to atomic restructuring.^{330–333} This reshaping depends on the laser pulse width,³³⁴ fluence^{331,333,335} and repetition rate.³³⁶ Excitation with femtosecond laser pulses generally results in more uniform reshaping of anisotropic NPs, whereas nanosecond pulses are likely to induce fragmentation and irregular morphologies.³³⁴

Next to the above-mentioned factors, the NP's environment plays a pivotal role due to possible hindrance of surface atom diffusion and its effect on heat dissipation.^{335,337–341} To improve the robustness and durability in applications, surface coating of NPs was investigated, with silica-coated Au NPs emerging as one of the most well-suited systems in practice.^{342,343} For biomedical applications, for example, silica coatings were shown to provide biocompatibility, large surface areas for drug delivery and prevent aggregation of NPs inside cells.³⁴⁴ Next to their increased colloidal and thermal stability, silica-coated Au NPs also exhibited superior performance for imaging applications such as photoacoustic imaging³⁴⁵ and a higher dynamic range for optical data storage.³³⁶ In the case of catalytic applications, porous silica coatings provide accessibility to the NP's surface while inhibiting sintering,^{299,346} which is one of the main deactivation channels of catalytic metal NPs.

Despite their relevance in applications, little is known about the atomistic processes occurring in (porous) silica-coated Au NRs when exposed to high temperatures or laser irradiation as most work so far has focused on bare Au NPs. For uncoated NRs, surface atom diffusion is believed to be the driving mechanism of photothermal reshaping for absorbed energies below the melting energy,³³² but internal crystal defects in irradiated NPs have also been reported.^{333,347} Matsumura and co-workers observed twinning and different crystallographic orientations in initially single-crystalline and defect-free Au NRs upon excitation with nanosecond laser pulses.³⁴⁸ Several MD studies reported the creation of stacking faults, which originated at the NP surface upon heating.^{223,349} Moreover, more accurate modeling of laser heating of a Au NR revealed that surface pre-melting predominantly occurred at {110} lattice planes and started before the creation of parallel twin boundaries, appearing in the middle of the NR.³⁵⁰

Unfortunately, accessible time and length scales are generally different between experiments and simulations. Most experimental work to understand photothermal reshaping has been performed at the ensemble level using optical techniques. Although optical single-particle studies gained additional insight on this mechanism,^{331,332} few reports exist on structural changes of excited NPs. Such studies were mainly performed by SEM^{331,332} or TEM at medium spatial resolution and via observing 2D projections of the 3D NP.^{338,348,351} On the other hand, simulation studies are generally

performed at the single particle level using short time and atomic spatial scales. A complete picture of the reshaping and defect formation mechanism, combining experiments and simulations, is still lacking. In this chapter, to bridge the gap between simulations and experiments, atomic resolution electron tomography of the same mesoporous silica-coated Au NR is performed before and after femtosecond laser excitation. The experiments enabled to perform MD simulations using the experimentally determined morphology, thereby extending previous simulation studies to an experimental system with realistic surface morphologies.

6.2. Synthesis and femtosecond laser excitation

Au NRs were obtained by a modified version of the method by Ye et al.³⁵², in which the seed concentration was increased. The CTAB stabilized Au NRs were coated with a 18nm mesoporous silica shell via the method of Gorelikov et al.³⁵²

For femtosecond laser excitation, a Leica SP8 confocal setup (63×/1.4 oil-immersion objective) equipped with a Coherent Chameleon II Ti:Sapphire laser (80 MHz repetition rate, 140 fs laser pulses) was used. The laser wavelength was set at the ensemble-averaged longitudinal plasmon resonance of the corresponding silica-coated Au NRs immersed in glycerol. During the laser excitation, the early stages of below-melting-point deformation were investigated as these contain most information about the interplay between structural and morphological changes. Furthermore, below-melting-point deformation is highly relevant for applications since it can, for example, be used to shape or weld NPs into desired configurations.^{340,353} Consequently, a laser fluence that induced only mild NR reshaping was selected.

6.3. 2D STEM characterization

To understand the impact of the absorbed laser energy on the structure and morphology, the same mesoporous silica coated and uncoated Au NRs were imaged before and after multi-shot femtosecond laser excitation at their ensemble-average LSPR. Hereby, the NRs were deposited on a TEM grid. For bare NRs, this leads to symmetry breaking and hindered deformation of the NR side touching the support. A mesoporous silica coating around the Au NRs, on the other hand, guarantees a homogenous surrounding, while enhancing the thermal stability of Au NRs.^{335,336}

Figure 6.1 shows bright-field scanning TEM (BF STEM) images of bare Au NRs before and after laser irradiation with two different applied fluences. BF-TEM images were acquired using a TECNAI12 electron microscope by Dr. Wiebke Albrecht. It can be seen that a range of defects, such as stacking faults and twinning planes, appeared for bare NRs after laser irradiation. In addition, the formation of irregular, asymmetric shapes and volume loss are observed. The irregularity in shapes for uncoated NRs mainly stems from non-uniform properties of their environment, specifically its rigidity and heat conductivity due to the contact with the TEM support, which is prevented by the silica shell.¹¹²

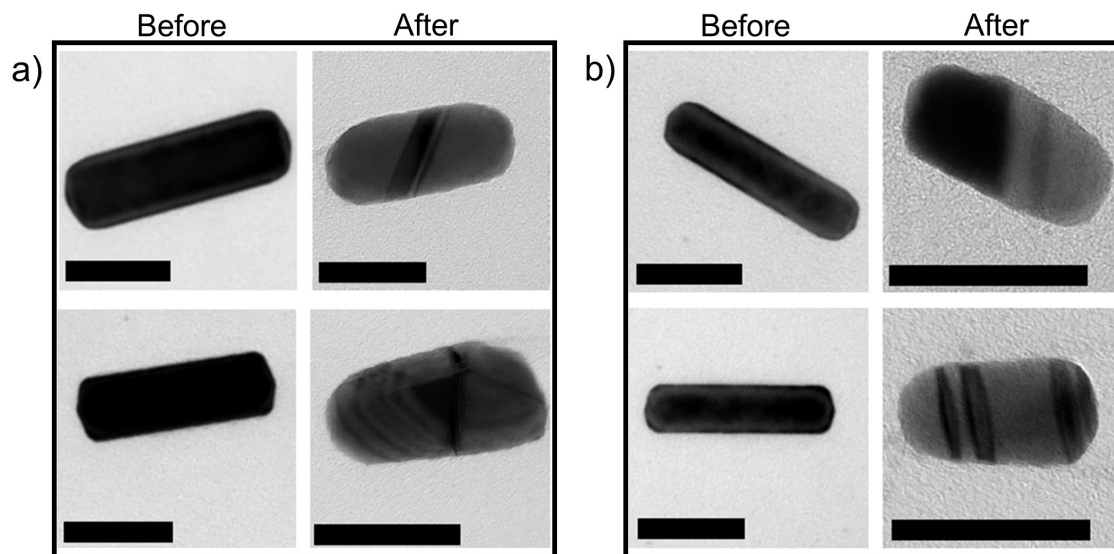


Figure 6.1 BF-TEM images of the same Au NRs without a silica shell, before and after laser irradiation at 890 nm with a fluence of 7.9 mJ/cm² (a) and 10.4 mJ/cm² (b). All scale bars represent 50 nm.

Figure 6.2a and Figure 6.2b show HAADF STEM images of two silica-coated NRs before and after laser excitation. HAADF STEM images were acquired by Prof. Dr. Thomas Altantzis and Dr. Wiebke Albrecht using an aberration-corrected ‘cubed’ FEI-Titan electron microscope, operated at 300 kV. The NR shown in Figure 6.2a was defect-free before laser excitation. Upon laser excitation, its aspect ratio (AR), which is the ratio of NR’s length to its width, decreased from 4.4 to 3.8 and twinning planes occurred. Similarly to the NR in Figure 6.2a, a defect-free NR in Figure 6.2b contained lattice defects after femtosecond laser excitation and its AR reduced from 4.3 to 3.5. Mostly, twin boundaries were observed and for the majority of the investigated NRs, these were perfectly parallel to each other (Figure 6.2a and Figure 6.2b). However, Figure 6.2c suggests that under the same irradiation conditions twin boundaries were also found along more than one direction. In addition to twinning boundaries, the deformed NRs in Figure 6.2a-c show a bullet-like intermediate shape, as was also previously observed for silica-coated Au NRs after femtosecond laser excitation.¹¹²

Interestingly, almost all silica-coated Au NRs did not show crystal defects when heated in a furnace at 500°C for 2 hours (as illustrated in Figure 6.2d as an example). Moreover, the silica-coated Au NRs did not fully transform into a spherical shape under these conditions, as expected for as-synthesized Au NRs without a silica shell.³⁵⁴ This is due to the hindrance of surface atoms induced by the silica confinement. For all of these observations, however, caution needs to be taken when interpreting the shape of a 3D object from 2D projection images. To unambiguously determine the 3D morphology and to understand the role of surface facets during reshaping, a 3D analysis is indispensable.

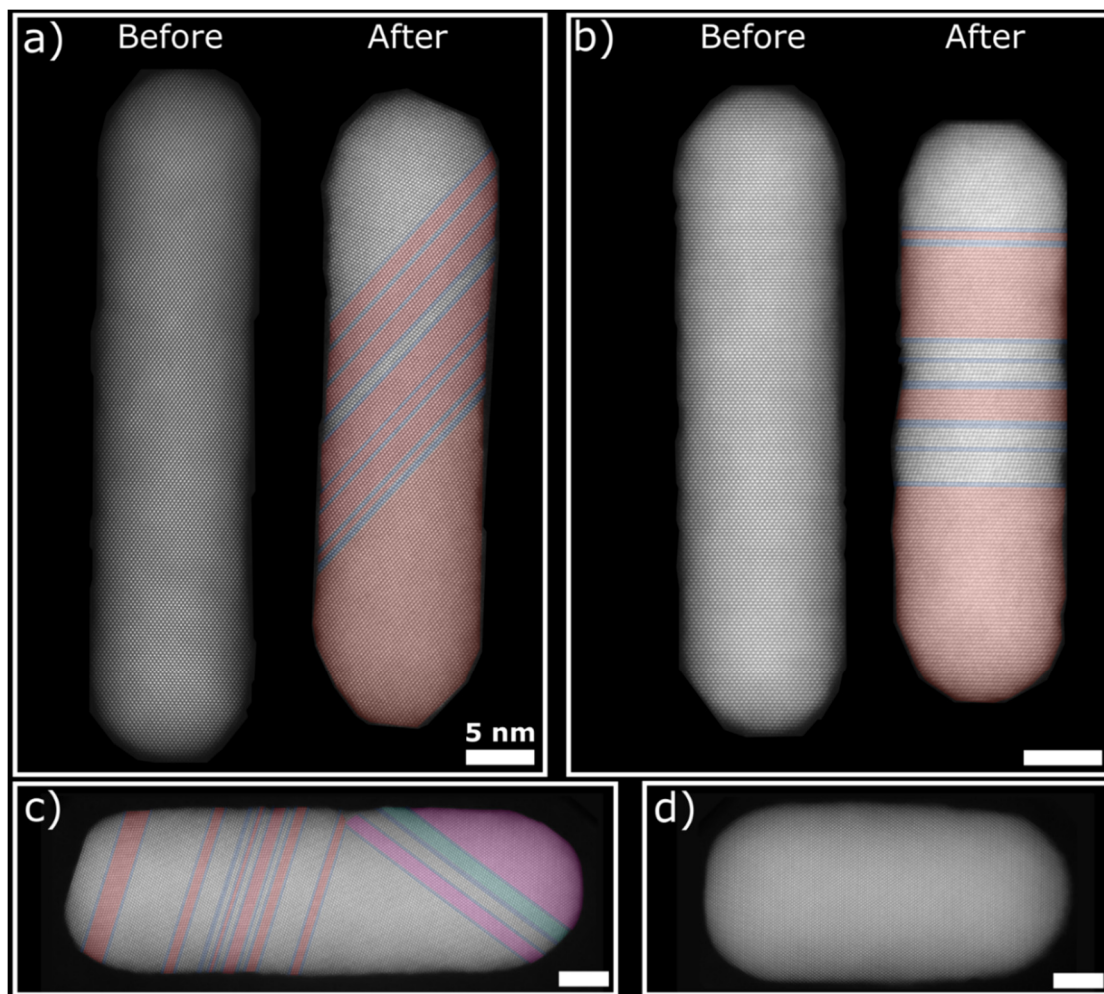


Figure 6.2 Defect creation upon femtosecond laser excitation at 925nm with a fluence of 6.5 mJ/cm². a) HAADF STEM images of a mesoporous silica-coated Au NR with an initial length of 51.2nm and width of 11.6 nm before and after laser excitation. b) HAADF STEM images of a mesoporous silica-coated Au NR with an initial length and width of 40.9nm and 9.6 nm before and after laser excitation. c) Another silica-coated Au NR of the same sample batch after laser excitation. d) Silica-coated Au NR of the same sample batch after oven heating at 500°C for 2 h. The colors in (a)-(c) correspond to different crystal orientations. It should be noted that although the silica coating is surrounding the NRs, it is not visible in the HAADF STEM images due to the large contrast difference between silica and Au. All scale bars represent 5 nm.

6.4. 3D characterization by electron tomography

High-resolution electron tomography tilt series from the NR shown in Figure 6.2a were acquired before and after laser excitation within a tilt range from -69° to +72° and from -68° to +74°, with a tilt increment of 3° and 2°, respectively. The high-resolution electron tomography of silica-coated Au NRs was performed by Dr. Adrián Pedraza-Tardajos using the 3D reconstruction algorithm developed by Dr. Ivan Lobato.⁸¹ The 3D visualization of the reconstructions are presented in Figure 6.3a.

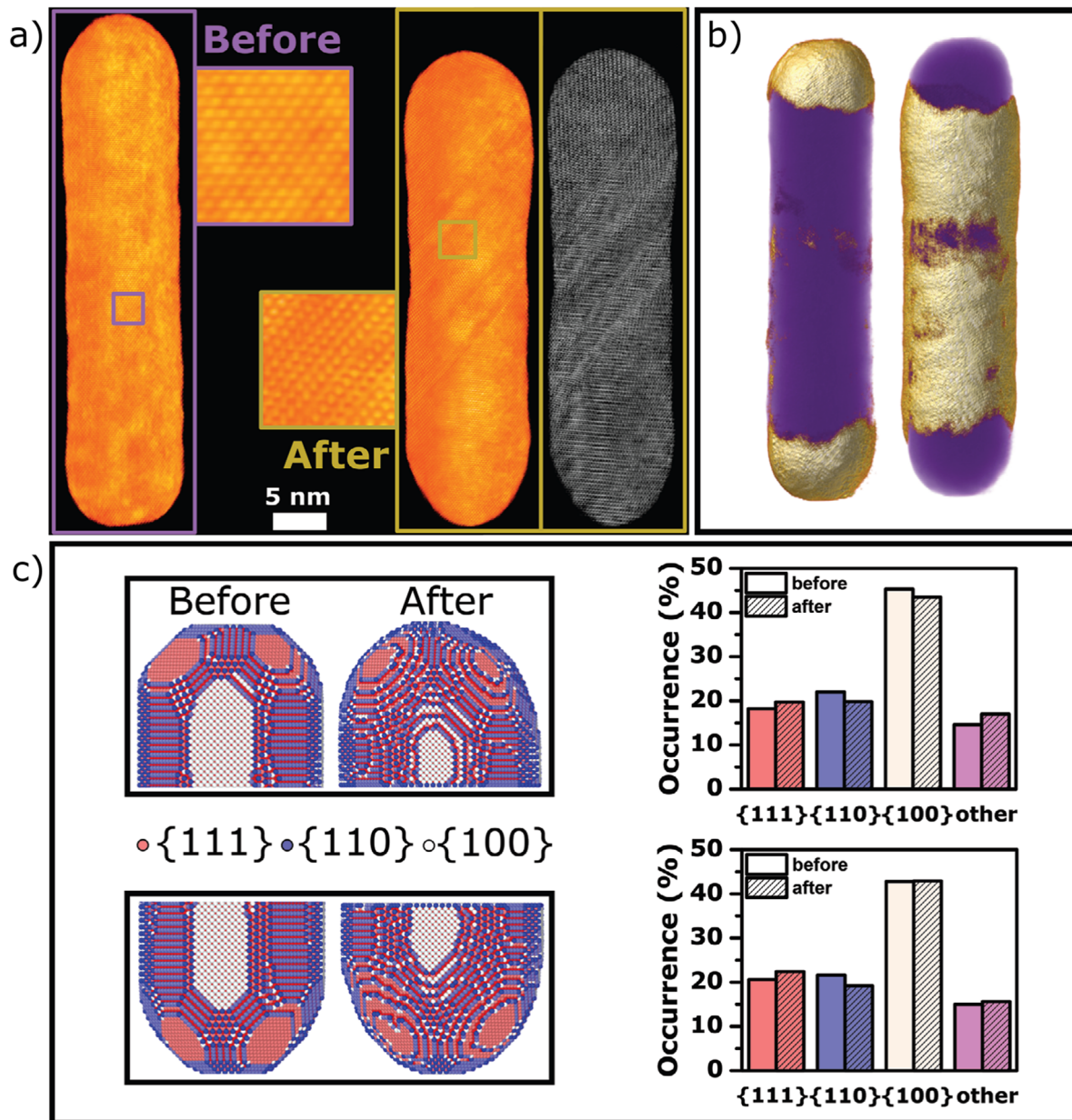


Figure 6.3 3D characterization of the mesoporous silica-coated Au NR shown in Figure 6.2a before and after femtosecond laser excitation. a) 3D visualization of the high-resolution electron tomography before and after excitation along the same viewing direction. A magnified visualization shows the single-crystalline nature of the particle before laser excitation. After excitation, a magnified visualization and a slice through the middle of the NR (right box) confirm twinning defects. b) 3D visualization of redistributed volume upon laser excitation. The left and right sides show areas of local volume decrease and increase, respectively, overlaid on visualization of the segmented original NR (purple). c) Visualization and quantification of the facet distribution at the two tips before and after laser excitation.

As expected, prior to laser excitation, the Au NR yielded a defect-free FCC lattice, without significant surface roughness (Figure 6.3a left side). After exposure to about 10^4 femtosecond laser pulses, the NR's surface roughened (Figure 6.3a right side) along with the appearance of twin boundaries, which is common for FCC lattices. Because the 3D information of the same NR before

and after laser excitation were extracted, the redistributed volume could be calculated, displayed in Figure 6.3b. The overall volume of the NR was $5.16 \times 10^3 \text{ nm}^3$ and did not change after laser excitation. 9% of the NR's volume redistributed upon laser excitation. During this redistribution, about 28 000 atoms diffused from the tips of the NR (left image in Figure 6.3b) to its side (right image in Figure 6.3b).

The surface facets of the NR before and after femtosecond laser irradiation were determined by using the 3D reconstructions. To determine the facet distribution of the experimental NR before femtosecond laser irradiation, first the reconstructed volume (Figure 6.3a left side) was scaled according to the pixel size of the experimental image. Then, the rescaled 3D volume was binarized by setting the values above a threshold to 1 and setting the others to 0. Here, the threshold value was defined by using Otsu's method.²⁴³ Later, the 3D volume was filtered with a 3D Gaussian smoothing kernel to create a mask. Meantime, a Au structure was created in a rectangular simulation box according to the defect-free FCC structure of the NR before laser irradiation which was proven by the high-resolution electron tomography. Then, the Au NR was extracted by applying the created mask to the FCC Au structure created in a rectangular simulation box. Finally, to identify the surface facets, coordination analysis was applied through Ovito Python open source scripts.²⁴⁷ To control the range of neighbors taken into account during the coordination analysis, a cutoff radius of 3.48 Å, which corresponds to the first minimum of the pair distribution function, was defined.

According to determined surface facets, the Au NR before laser excitation yielded 35% {100}, 22% {110}, and 20% {111} as well as higher-order surface facets. When the same approach was applied to the 3D reconstruction after laser excitation (Figure 6.3a right side), it has been observed that the volume redistribution (Figure 6.3b) did not only lead to the observed AR reduction but also to facet restructuring (Figure 6.3c), where the more stable {111} surface facets expanded at the expense of less stable {100} and {110} facets.

6.5. MD simulations for femtosecond laser excitation of NRs

In Sections 6.3 and 6.4, it has been observed that a range of morphological deformations and structural defects may appear upon femtosecond laser excitation. Considering many promising applications of Au NRs, a full understanding of the mechanisms behind the observed deformations is crucial. Although 3D electron tomography allows to measure the structural and morphological properties of the NRs before and after femtosecond laser excitation, presently it is impossible to experimentally capture dynamic information of the underlying processes. Therefore, to unravel the mechanism behind the atomic scale transformations causing morphological changes and defect generation upon femtosecond laser irradiation, MD simulations were performed.

Hereby, a representative heating regime of the laser irradiation is crucial for MD simulations because the laser-induced structural changes in a Au NR depend on the heating rate and the maximum temperature that is reached.²²³ However, for experiments, it is not straightforward to measure the temperatures of NPs. On the one hand, the absorbed laser energy, and thus the

temperature of a Au NR depends on its exact AR, volume and orientation with respect to the laser polarization. On the other hand, inhomogeneities in the TEM grid can lead to changes in the absorbed energy when illuminating a NR. Therefore, to reliably mimic the experiments, the heating regime of a femtosecond laser pulse was modelled as explained in Subsection 6.5.1 and the temperature profiles were obtained for mesoporous silica coated and bare Au NRs with three different ARs (3.0, 3.5, 4.5).

In Subsection 6.5.2, the AR effect on the deformation of NRs is investigated by using model-like facet distribution as typically applied for MD simulations.^{223,349,350} The experimental observations indicate that, in addition to the importance of the AR, the mesoporous silica coating around bare Au NRs influences the final structure after laser excitation. However, the role of coating on the laser-induced deformation mechanism of the Au NRs was never investigated in the simulations. Therefore, in contrast to previous studies, the effect of mesoporous silica coating around Au NRs is investigated in Subsection 6.5.2.

In Subsection 6.5.3, the information from high-resolution electron tomography (Figure 6.3a) is directly used to construct an input structure, which resembles the experimental NR more accurately than the model-like systems. In this manner, the deformation dynamics of the experimental NR can be better understood.

6.5.1. Modelling heating regime of a femtosecond laser pulse

The absorption of a femtosecond laser pulse by the NP can be summarized in three main steps: electronic absorption, electron-phonon thermalization and heat dissipation. In this study, the approach proposed by Baffou et al. in refs^{355,356} was followed to model electronic absorption and electron-phonon thermalization. It has been found that this approach is a simpler approach than the so-called two-temperature model^{357,358} and can reliably reproduce the experimental results in this study. To model the heat dissipation, the lumped capacitance method was applied.³⁵⁹

Electronic absorption

When exciting the longitudinal plasmon resonance with a high-energy femtosecond laser pulse, the photon energy is absorbed by the free electrons of the Au NR. The electronic gas thermalizes very fast over a timescale of around 100 fs.^{355,356,360,361} This leads to a state of non-equilibrium within the NR where the temperature of the free electron gas increases whereas the temperature of the phonons (lattice) remains unchanged. The total energy transferred from the laser pulse to the electron density can be expressed by:

$$E = \sigma_{abs}F \quad , \quad (6.1)$$

where σ_{abs} is absorption cross section and F is the applied fluence, which are given in Appendix A.

Electron-phonon thermalization

Subsequent to the electronic absorption process, the hot electron gas relaxes through the internal electron-phonon interaction.³⁵⁵ This electron-phonon interaction leads to a temperature increase in the lattice. The characteristic time scale of the electron-phonon scattering is often independent from the size of the NP. It has been stated that, for the use of Ti:sapphire laser, a typical electron-phonon relaxation time (τ_{ep}) approximately corresponds to 1.7 ps.^{355,356,362,363} For femtosecond laser pulses, the energy transfer from the electrons to the lattice occurs according to an exponential decay function:³⁵⁵

$$p(t) = \frac{1}{\tau_{ep}} \exp\left(-\frac{t}{\tau_{ep}}\right) . \quad (6.2)$$

Therefore, the femtosecond laser-induced temperature increase in the Au NR with respect to time ($\partial T/\partial t$) can be expressed by:³⁵⁵

$$c_p \rho V \frac{\partial T}{\partial t} = \sigma_{abs} F p(t) , \quad (6.3)$$

where c_p represents the specific heat capacity of Au, ρ is the density of Au and V is the volume of the Au NR.³⁵⁹ The physical constants are tabulated in Table 6.1.

Heat dissipation

Finally, the absorbed heat dissipates through the surrounding medium which leads to a cooling in the lattice and heating of the surrounding medium. The heat dissipation usually occurs at longer time scales, depending on the size of the NP and its surrounding medium, compared to the time scales of electronic absorption or electron-phonon thermalization. For example, a typical heat dissipation time for silica-coated Au NPs is around 50-100 ps for water and ethanol environments.³⁶⁴ To mimic the cooling regime of the NRs during heat dissipation, the lumped capacitance method was used.³⁵⁹ The lumped capacitance suggests a uniform temperature distribution in the particle during heat dissipation, depending on the volume-to-surface ratio of the NP under investigation, the thermal conductivity of the NP and the heat transfer coefficient of the surrounding medium. The validity of this approach is confirmed by calculating a dimensionless number, the so-called Biot number, which provides a measure of the temperature drop in the NP relative to the temperature difference between the NP surface and the surrounding medium.³⁵⁹ When the Biot number smaller than 0.1, the temperature gradients within a particle remains negligible during the heat transfer between the particle and its surroundings.³⁵⁹ As shown in Appendix A, Biot number was calculated by considering the size and surface-to-volume ratio of the experimental NR with a length of 51.2 nm and width of 11.6 nm (Figure 6.3a), and so the validity of the lumped capacitance method was confirmed for this study. Consequently, the heat dissipation of the NP can be summarized as:

$$c_p \rho V \frac{\partial T}{\partial t} = U_{medium} A (T - T_{medium}) \quad (6.4)$$

where A is the surface area of the NP and U represents the thermal resistance which is calculated by using Equation 6.5 for a glycerol medium (uncoated Au NRs) or by using Equation 6.6 for a glycerol/silica medium (Au NRs coated with mesoporous silica).

$$U_{glycerol} = \frac{1}{\frac{1}{h_{glycerol}} + \frac{L_c}{k_{Au}}} \quad (6.5)$$

$$U_{glycerol/silica} = \frac{1}{\frac{1}{h_{glycerol}} + \frac{L_{coating}}{k_{porous\ silica}} + \frac{L_c}{k_{Au}}} \quad (6.6)$$

Hereby, $L_{coating}$ represents the thickness of the mesoporous silica coating (18 nm) which is filled with glycerol and L_c is the volume-to-surface ratio of the Au NP. Moreover, k_{Au} is the thermal conductivity of Au, $k_{porous\ silica}$ is the thermal conductivity of the porous silica filled with glycerol and $h_{glycerol}$ is the convective heat transfer coefficient of glycerol. The calculation of these coefficients including nano-size effects section are given in Appendix A and the physical constants are tabulated in Table 6.1.

Due to the sufficiently short duration of femtosecond laser excitation and the small size of the NR in this study, it can be assumed that there is no overlap between these successive steps. This is also the reason why femtosecond-heating is more efficient than nanosecond-heating since the total energy from the laser pulse can be transferred to the crystal completely before lattice cooling takes place.^{355,356,361} Moreover, because of the same reasons (short duration of femtosecond laser excitation and small size), it has been assumed that the temperature uniformly changes within the NP during laser excitation. The details of the validation of the assumptions and derivation of the heating-cooling model are explained in Appendix A.

The obtained temperature profile for mesoporous silica coated and uncoated Au NRs with three different ARs (3.0, 3.5 and 4.5) are shown in Figure 6.5. According to the calculated temperature profiles of the laser irradiation, the maximum temperature that the NR reached during laser heating increased with increasing AR and volume due to the shape-dependent plasmonic properties. The heat dissipation was slower for silica-coated NRs due to the additional heat resistance at the surface. The latter indicates the crucial importance of including the cooling process in the simulations.

6.5.2. MD simulations by using model-like inputs

Creating input structures

Based on earlier works^{223,349,350} and the determined surface facets of the Au NR using electron tomography (Figure 6.3), model-like input structures of Au NRs with three different ARs (3.0, 3.5 and 4.5) were constructed to have {110} and {100} lateral facets, and a combination of {100}, {110}, {111} facets at its tips. As generally known, high computational costs limit the size range

and time scales of MD simulations. Hence, using the actual size of common realistic experimental NPs remains challenging. Therefore, Au NR models with a diameter of 4 nm were used throughout the MD simulations. These NRs were constructed by cutting out octagonal prisms from an FCC Au matrix with a lattice parameter of 4.08 Å. The two base faces of the octagonal prisms correspond to Au {100} facets, and the other eight faces were alternate {100} and {110} facets. The ends of the prism were truncated to form {110} and {111} facets.

A realistic mesoporous silica structure was created based on the study of Patil et al.³⁶⁵ First, a β -cristobalite silica structure was created because it has a density of 2.17 g cm^{-3} , which is close to that of amorphous silica. In this structure, the silicon atoms occupy the positions they take in the diamond structure, while the oxygen atoms form bridges between them. Next, a random velocity was assigned to atoms at 7000 K which was followed by a rapid quenching to 300 K using the NVT ensemble. Then, energy minimization was applied using the conjugate gradient method. Afterward, the system was relaxed to atmospheric conditions (300 K and 1 bar) for 7.5 ps using the NPT ensemble followed by an instantaneous expansion to the desired density. The expanded system was then heated to 3000 K for 50 ps and relaxed using the NVT ensemble. The final porous silica structure was formed by quenching the system to 0 K, followed by energy minimization. The consecutive annealing and quenching processes to obtain the porous silica structure are illustrated in Figure 6.4. During these simulations, a time step size of 0.5 fs was used. The obtained structure exhibited a porosity around 70%, which is close to typical values of 60-70 % for mesoporous silica coating around NRs.³⁶⁶

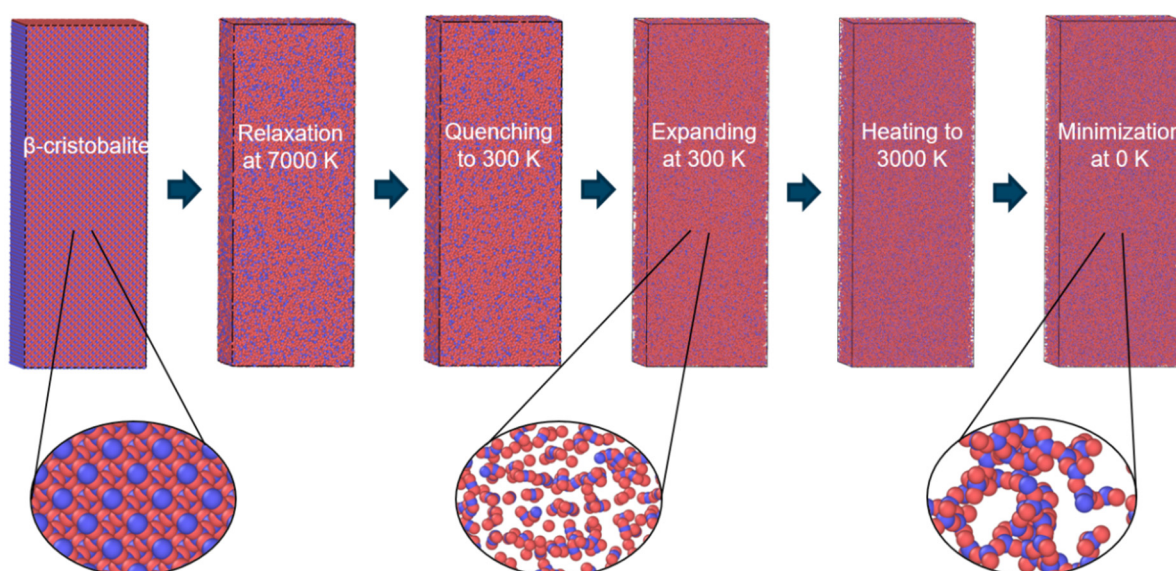


Figure 6.4 The main steps for the creation of the mesoporous silica.

The created input structures of Au NRs were then placed at the center of the simulation box, which was filled with the created porous silica. Next, the input structures of Au NRs with a 4 nm mesoporous silica coating were extracted. Then, the mesoporous silica coated Au NRs were placed in a larger simulation box with enough vacuum area in all three directions and relaxed for 10 ns at

room temperature before starting the MD simulations for laser heating. During the MD simulations, EAM¹⁹⁰ was used for the interaction between Au atoms. Moreover, the inter-atomic potential of Vashishta et al. was defined for the interaction between the atoms of silica.²⁰³ For the interaction between the Au atoms and the mesoporous silica coating, the Lennard-Jones potential was applied where the following LJ parameters were used: $\epsilon_{O-Au} = 0.1$, $\epsilon_{Si-Au} = 0.1$, $\sigma_{O-Au} = 3.5$, $\sigma_{Si-Au} = 3.5$, cut-off = 6.0 Å. In addition, since the density of the porous silica was low and the interaction between the Au and the coating was weak, a low spring force of 0.0002 was applied on the atoms of silica.

The results of the MD simulations for femtosecond laser excitation

Side views and interior structures of the NRs before and after the modeled laser excitation from MD simulations, as well as the obtained temperature profiles are shown in Figure 6.5. For the internal structure identification of the NRs, the polyhedral template matching (PTM) approach was used with Ovito Python open-source scripts.^{247,251} In the PTM method, a convex hull is formed by the set of neighboring atoms to construct a small set of candidate structures. Then, local crystalline order is identified by matching the local atomic neighborhood to the templates of the structural types determined by the PTM algorithm, which is sensitive to the RMSD value. RMSD is a measure of the spatial deviation of the atoms from their expected positions in the crystal phase. Therefore, defining accurate RMSD values is essential to avoid errors in the local structure identification due to the increased thermal displacements at high temperatures during laser heating. In this study, the temperature-dependent RMSD was calculated based on the parameterization of the temperature dependence of DWF presented in the study of Gao et al.¹⁵⁰ Since the PTM approach considers the effect of thermal vibration, it promises greater reliability to describe the local structure around an atom, especially in the presence of strong thermal fluctuations and strain, compared to other structural identification methods, such as Voronoi analysis or the common neighbor analysis.^{248,367}

Figure 6.5 shows that MD simulations of femtosecond laser heating resulted in an increase in {111} as well as the formation of twinning planes resulting from internal restructuring from pure FCC to FCC with twinning planes (Figure 6.5b,c). It can be seen that the density of twinning planes after laser excitation differed according to the initial AR and the presence of a coating. Hereby, the twin density increased with increasing AR (red atoms in Figure 6.5b,c). Moreover, the effect of the silica coating resulted in the development of a multiple parallel twin structure, whereas for uncoated particles a range of defects, e.g. stacking faults and twinning planes, along the long axis of the NR were also observed. These observations are in excellent agreement with the experiments as we observed parallel twin planes for the coated NRs (Figure 6.2 and Figure 6.3), and a range of defects for uncoated NRs (Figure 6.1). It is important to note that, depending on the view, twins appear to extend in different directions, although they have the same 3D nature (Figure 6.5b,c). This explains the reason why twinning planes seemed to occur along seemingly different crystallographic directions in 2D HAADF STEM images (Figure 6.2a-c).

A quantitative comparison of the change in AR, {111} facets and HCP of NRs after laser excitation is presented in Figure 6.6. As already visually observed in Figure 6.5, the uncoated NR with the highest AR, 4.5, deformed the most. This is confirmed by the significant change in the AR,

Chapter 6. 3D atomic-scale dynamics of laser light induced restructuring of nanoparticles unraveled by electron tomography and molecular dynamics simulations

percentage of {111} surface facets, and HCP structure in Figure 6.6. Moreover, it is clear that the mesoporous silica coating improved the stability of the NRs. The coating hindered the atomic surface diffusion and consequently led to a decrease in the percentage of {111} facets change and AR change. For the uncoated NRs, the AR decreased by 34%, 36% and 56% for initial ARs of 3.0, 3.5 and 4.5, respectively. For the coated Au NRs the AR changes were smaller with 0%, 5% and 24%, respectively. The stronger deformation at larger ARs in the simulation can be attributed to the higher maximum heating temperature (Figure 6.5b,c) due to the shape dependent plasmonic properties of the NRs.

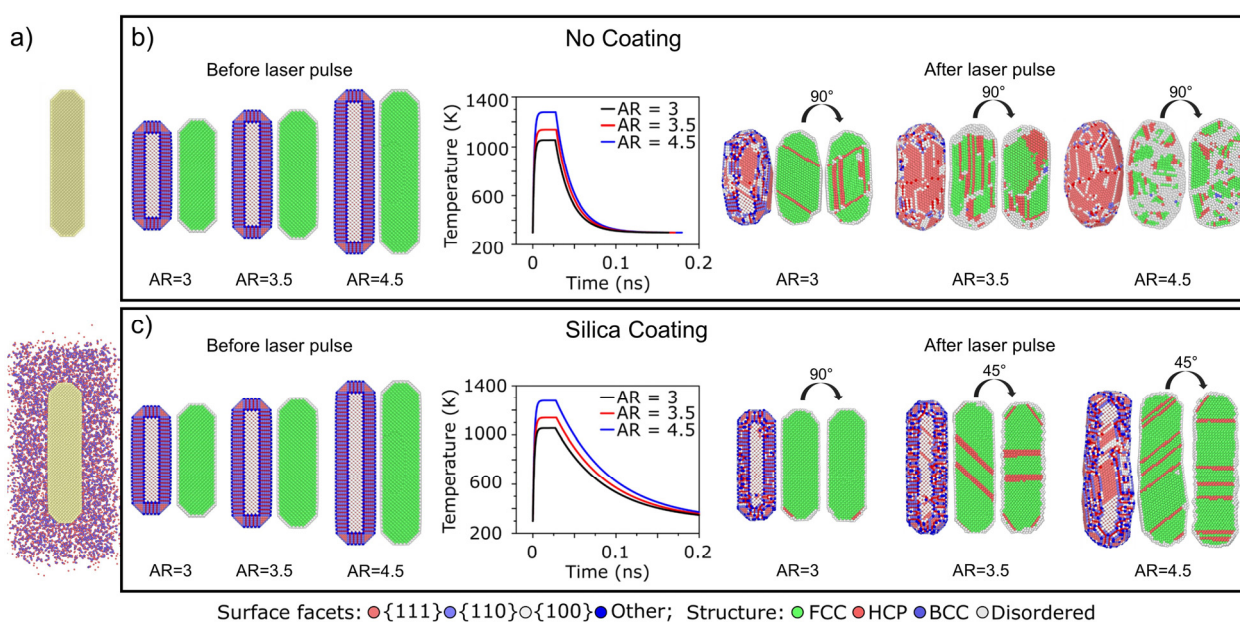


Figure 6.5 MD simulations of laser-heated Au NRs with a model-like input structure. a) Cut through the input structures. b) Side views (left sides) and interior structure (right sides) before and after simulated laser pulse excitation and the calculated temperature profile for three different bare Au NRs with varying ARs. c) Side views (left sides) and interior structure (right sides) before and after simulated laser pulse excitation and the calculated temperature profiles for three different mesoporous silica-coated Au NRs with varying ARs. The silica coating is omitted in the visualizations. The cross sectional views of the deformed NRs after femtosecond laser irradiation are shown from two different viewing directions.

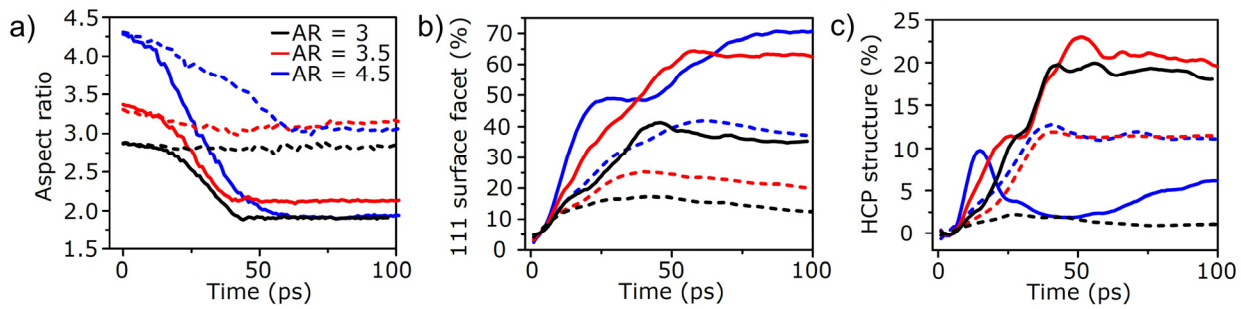


Figure 6.6 Comparison of the change in (a) AR, (b) $\{111\}$ facets and (c) HCP internal structure for the NRs from Figure 6.5. The uncoated NRs are represented by the solid lines and the coated ones by the dashed lines.

6.5.3. MD simulations based on the experimentally determined morphology

To capture dynamic information of the underlying processes of the experimental NRs, which is presently impossible to assess experimentally, the information from atomic resolution electron tomography (Figure 6.3c) was directly used to construct an input structure. To compare with the model-like input structure of the coated 4.5-AR Au NR (Figure 6.5), the experimentally-based input structure was scaled down to the same diameter of 4 nm but all the other parameters, such as the percentage of surface facets and AR were preserved. The same heating profile of the model-like coated 4.5-AR Au NR was used (Figure 6.7a) since the volume and AR of the two NRs are very similar. The main difference between the experimental-based and the model-like structure is the facet distribution. The rescaled experimental input structure contained a larger amount of $\{111\}$ facets (18.3% compared to 3.4%) and a smaller amount of $\{100\}$ and $\{110\}$ facets.

Upon laser heating, the shape transformation started almost immediately by a drop in the AR (Figure 6.7b), which did not change significantly during the rest of the cooling. Around 1024K (point 2 in Figure 6.7d) hexagonal close-packed (HCP) and body-centered cubic (BCC) interior regions occurred within the FCC structure. Afterwards, the percentage of HCP and BCC atoms and $\{111\}$ facets increased continuously (point 3 in Figure 6.7c,d). Upon reaching the maximum temperature (point 4 in Figure 6.7d), the growth of the HCP structure resulted in stacking faults that concentrated in the middle of the NR. Disordering continued until the NR cooled down to about 1150K (point 7 in Figure 6.7d), when the minimum of internal FCC structure was reached. During cooling, the distance between the twin planes increased while surface reorganization continued until 500K (point 9 in Figure 6.7c,d). The slower heat dissipation for coated NRs, compared to uncoated NRs, resulted in more time for the HCP internal regions to grow into twinning (Figure 6.7d). It has been experimentally confirmed that the ordering into multiple twins occurred after surface diffusion as twins extended over multiple NPs which welded together upon laser excitation.

To evaluate whether the internal lattice defects were caused by induced strain due to the surface transformation, atomic strain analysis was performed (Figure 6.8a). The local shear strain was determined based on the displacement vector of each atom using OVITO Python open-source

scripts.³⁶⁸ Calculation of the local strain requires a reference configuration, which was defined as the atomic configuration of the Au NR at the beginning of the simulations. This method also considers the relative displacement of the neighbor atoms within a cutoff radius when computing the atomic deformation gradient tensor for a particle. Here, the cutoff radius was again taken as 3.48 Å.

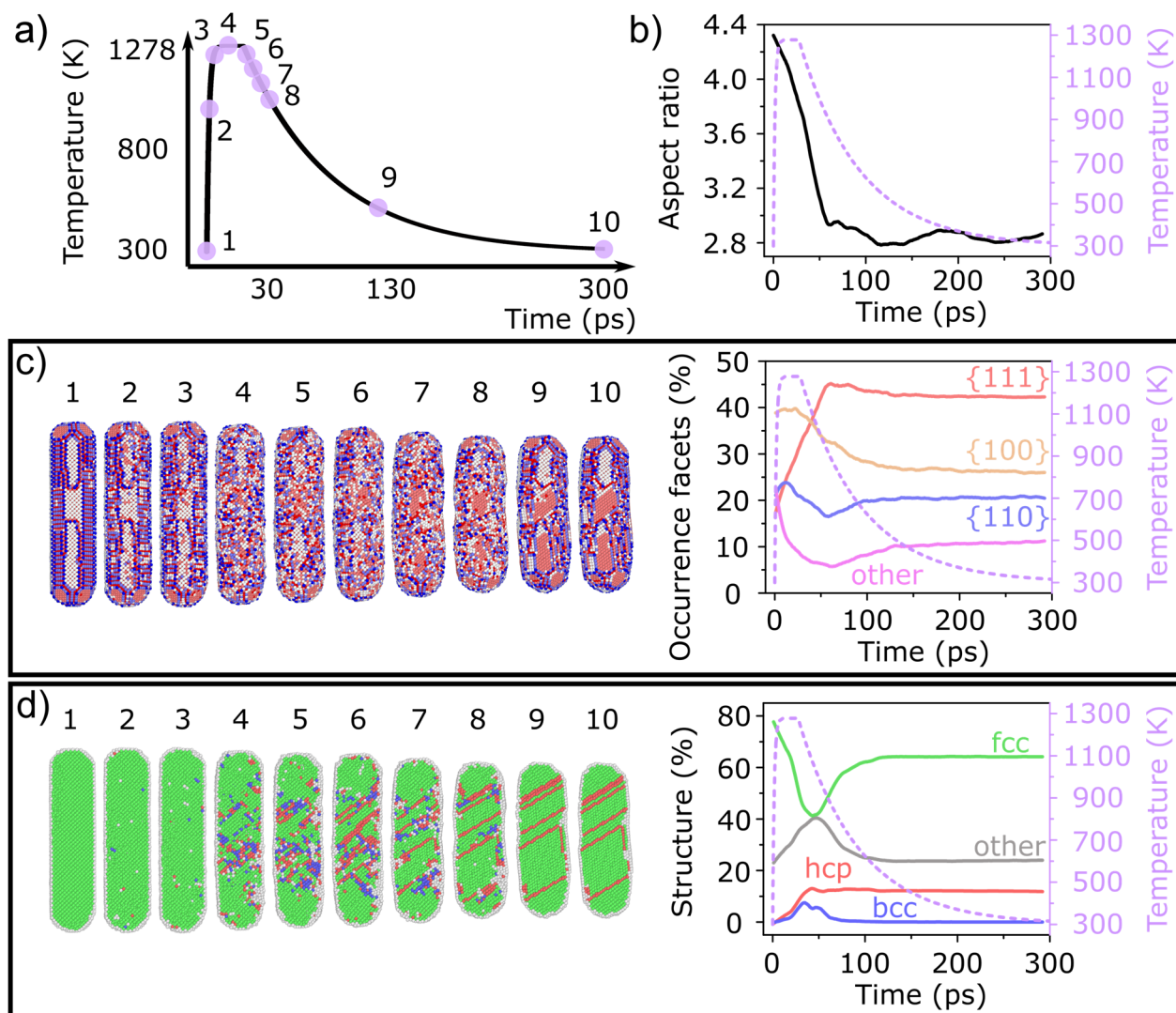


Figure 6.7 MD simulations for a mesoporous silica-coated Au NR with the experimentally measured surface facets as input structure (silica not shown). a) Applied laser heating profile (same as blue curve in Figure 6.5c.). b) AR change overlaid with the heating profile. c) Side views at the time points indicated in a) and quantification of corresponding facet changes. d) Internal structure at the time points indicated in a) and quantification of structural changes. All colors in the graphs correspond to the same colors in the visualizations.

Figure 6.8b connects the change in AR, shear strain, occurrence of {111} surface facets and HCP internal transformation. At the beginning of laser heating, the shear strain increased almost instantaneously due to the displacement of atoms out of their equilibrium position (magenta arrow

in Figure 6.8b). The onset of surface diffusion was reflected in the increase in $\{111\}$ surface facets and change in AR. Simultaneously, the first HCP interior atoms appeared prior to localized melting in accordance with literature.³³³ Until the maximum temperature was reached (point 4 in Figure 6.8a), the atomic strain was only related to displaced atoms due to heating. Then, localized stress propagated from the surface through the internal structure (white arrows in Figure 6.8a). The sharp increase in potential energy around point 4 (as labeled in Figure 6.8c) indicates local melting after the occurrence of the first point defects (point 3). Together with localized melting around the interior areas with HCP and BCC defects occurring around point 4, internal planes shifted, forming stacking faults in the middle of the NR. During cooling at 1080K (around point 8) the HCP percentage reached its maximum. The change in AR and $\{111\}$ facets was maximal at around 900 K, while the shear strain continued to slowly increase until around 660 K, causing the separation of neighbouring stacking fault HCP layers, which resulted in multi-twin boundaries.

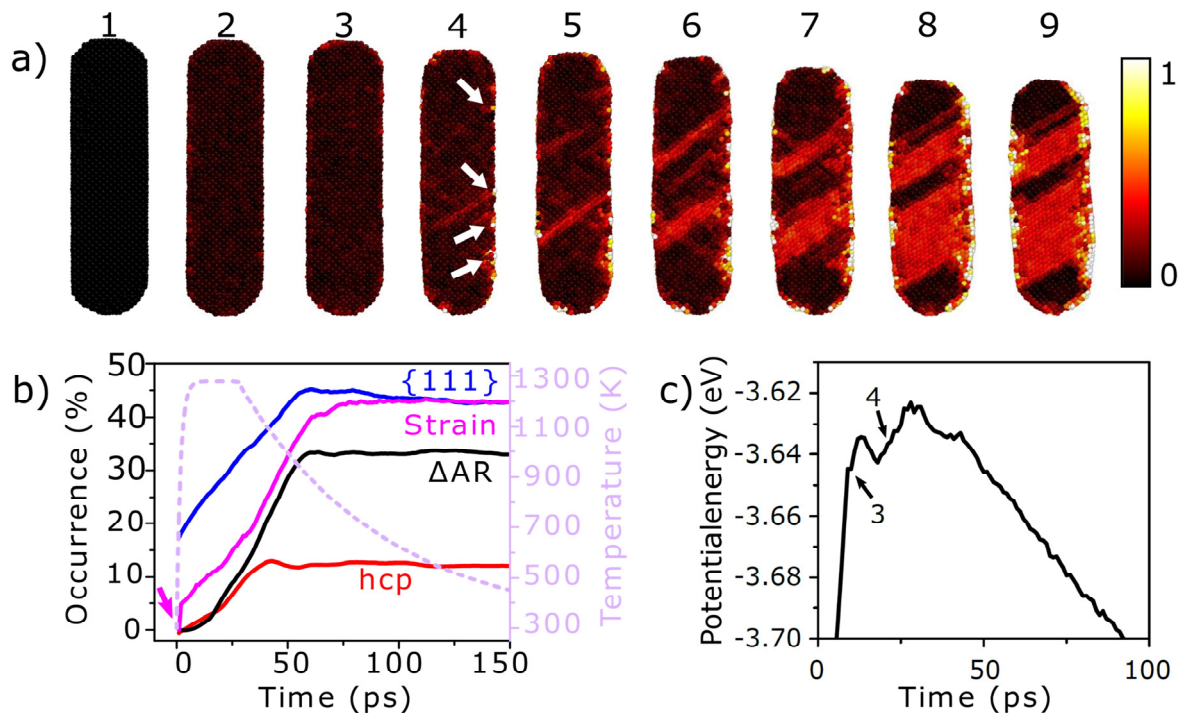


Figure 6.8 Strain analysis of the simulated silica-coated Au NR in Figure 6.7. a) Atomic shear strain maps taken at the same time points as in Figure 6.7. The atoms are colored according to their local shear strain, which is measured by the displacement gradient of atoms with respect to their initial positions and taking into account the relative displacements of the neighboring atoms. b) Comparison of strain, AR change, $\{111\}$ facet evolution and HCP atoms occurrence. c) Average potential energy of Au atoms shown for the first 100 ps.

Although the final morphology of the model-like (Figure 6.5) and the experimental (Figure 6.7) input structures appear qualitatively similar, quantitative differences exist. Figure 6.9b demonstrates the relative difference in the final shapes of the NRs from the top and side view. Also, in Figure 6.9c-e, the relative change in AR, HCP occurrence and the change in $\{111\}$ facets are shown, respectively. The NR based on the experimental input facets was less stable as evident from

the larger change in shape (Figure 6.9b) and AR (Figure 6.9c). Although the transformation of the internal structure was almost identical (Figure 6.9d), the relative facet changes (Figure 6.9e) differed significantly. The relative $\{111\}$ facet transformation occurred faster for the model-like input structure in the initial stage and also an additional 10% of the surface facets were transformed into $\{111\}$ facets (Figure 6.9e) compared to the experimental input structure. This observation clearly shows the importance of using experimental structures as input for simulations. Moreover, it demonstrates that morphology-dependent surface diffusion and facet restructuring simultaneously drive the deformation of metal NPs.

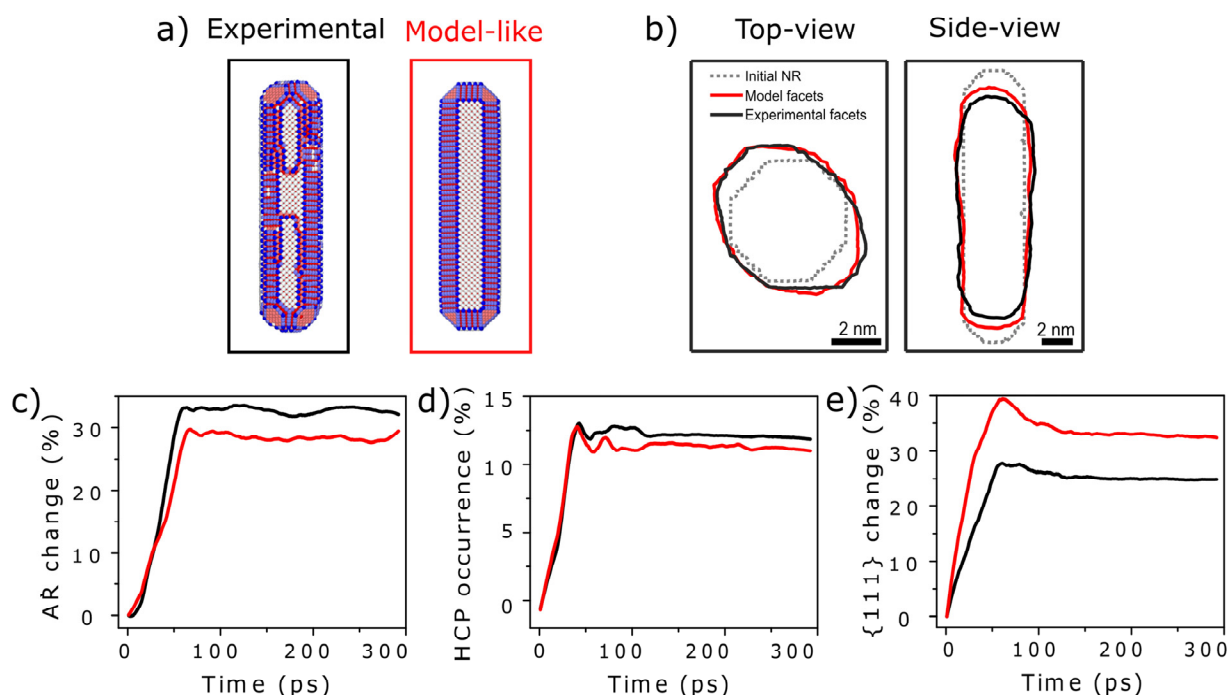


Figure 6.9 a) Comparison of input structures for the experimental-based (black curves) and model-like (red curves). (b) Change in the shape of NRs from top and side view, c) AR change, d) HCP occurrence and e) relative change in $\{111\}$ facets after the MD simulations of laser heating.

6.6. Discussion

From a thermodynamics point of view, all anisotropic Au NPs are unstable or far out of equilibrium and will strive to reach an equilibrium shape. According to the Wulff theorem, the equilibrium shape of our Au NPs is a truncated octahedron exposing $\{100\}$ and $\{111\}$ facets.²⁴⁹ On the other hand, surface coatings can kinetically stabilize an out-of-equilibrium shape, at least at room temperature. At elevated temperatures, these kinetic barriers can be overcome and the particles will transform towards their thermodynamically stable shapes. Two critical parameters of this transformation process are heating temperature and time.^{112,333,354} For heating temperatures above the melting point, the NP will melt and recrystallize into its thermodynamically stable shape. For laser-heated NRs, the heating time and the achievable deformation is limited.³⁵⁴ Allowing the NR more time to reach its thermodynamically stable state, led to a stronger deformation despite the

same maximum heating temperature as shown in Figure 6.10.

As demonstrated in the previous sections, the NR did not only lower its AR but also developed multiple twin boundaries after laser illumination. Concerning the atomistic mechanism in creating lattice defects, the results presented in this chapter bridge different studies in literature. On the one hand, surface diffusion was responsible for the start of the deformation,^{223,349} which resulted in stress propagating from the surface to the interior and facilitating internal point defects to evolve into stacking faults, accompanied by local melting as suggested by Link et al.³⁴⁷ Then, the high strain around stacking faults caused a transformation into multiple twin structures. On the other hand, although observed in,³⁵⁰ surface melting did not happen prior to the occurrence of planar defects. A plausible reason for the discrepancy is that the common neighbor analysis used in³⁵⁰ ignores thermal displacement of the atoms that can easily cause inaccuracies in detecting point defects of HCP structures at high temperatures. Although extended twin and double twin boundaries were observed to be almost free from atomic displacements compared to an ideal FCC lattice,³⁶⁹ the ideal thermodynamic minimum corresponds to a single-crystalline FCC structure. For laser-heated NRs, the heating and cooling rates are too fast to allow reorganization into a single crystalline lattice. With enough time at higher temperatures and during cooling, the Au NR will strive towards eliminating the internal defects resulting in NRs with reduced twin boundaries (Figure 6.2d and Figure 6.11).

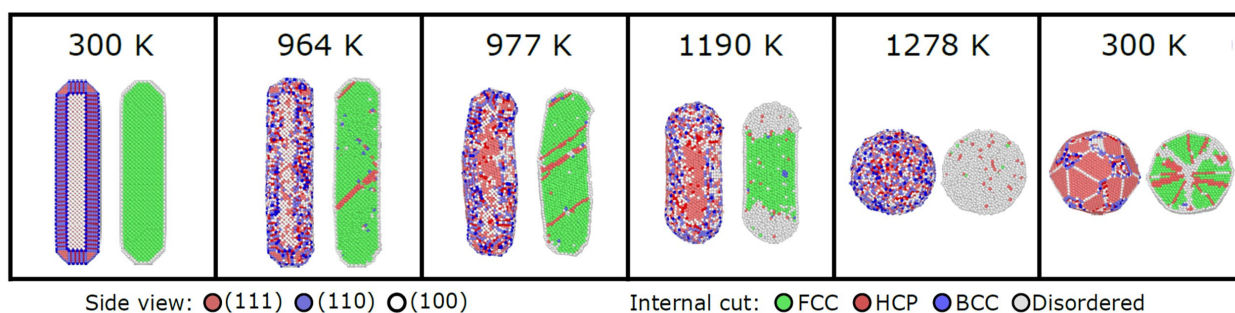


Figure 6.10 Snapshots of a “slow” heating process of a bare Au NR with an initial aspect ratio of 4.5. The NR was heated to the same maximum temperature as for the laser heating (Figure 6.5b) with a constant heating rate of 0.1 K/ps and then cooled to room temperature with a cooling rate of 0.1 K/ps. The NR deformed more compared to laser heating.

The results in this chapter thus show that laser-induced deformation is a complex process defined by a delicate interplay between thermodynamics and kinetics. The actual kinetic pathway of the transformation is difficult to predict and a controversy exists between curvature-driven,³³² defect-driven³⁴⁷ and facet-driven^{349,350} below-melting-point deformation. By performing slow heating experiments inside the TEM, it was proposed that the shape determines the kinetic pathway.³⁷⁰ Whereas for NRs, curvature was the dominant factor with reshaping to rounder shapes with higher index facets, deformation of triangular nanoplates was driven by surface faceting. Indeed, in our case the NP's tips became more rounded indicating curvature-driven surface diffusion. However, the changes in surface facets can only be quantified based on 3D information as done here. The

change in morphology actually allows for an increase of stable $\{111\}$ surface facets and decrease of more unstable facets. Despite having the same curvature with the NR from the experimental input, the facets of the model-like NR were found to change more, reducing the overall energy. Thus, curvature and facet-driven below-melting-point deformation are not necessarily competing processes but are rather intertwined.

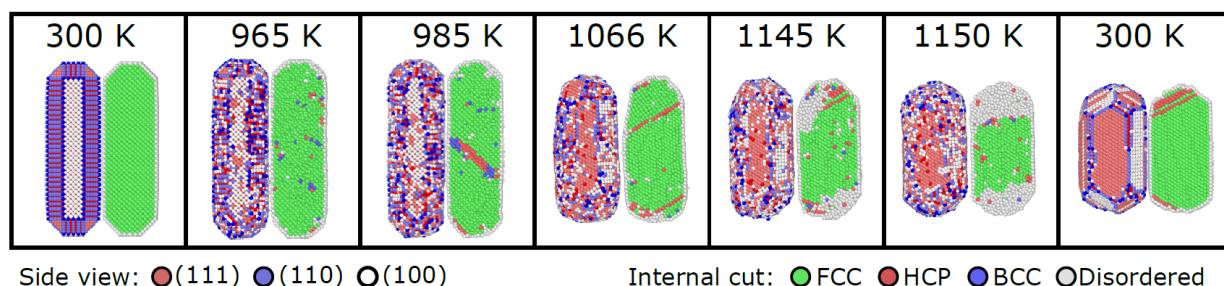


Figure 6.11 Snapshots of a “slow” heating process of a bare Au NR with an initial aspect ratio of 3.5 simulated by MD. The NR was heated to the same maximum temperature as for the laser heating (Figure 6.5b) with a constant heating rate of 0.1 K/ps and then cooled to room temperature with a cooling rate of 0.1 K/ps. The NR exhibited fewer internal defects compared to laser heating.

The amount of facet transformation was indeed linked to the initial facet distribution and the same initial AR and volume of the NR did not result in the same deformation dynamics (Figure 6.9). This becomes clear from the comparison of the model-like NR with the morphology based on experiments. In the latter case, the amount of stable $\{111\}$ facets were higher but yet it deformed more. This can be explained by the fact that the initial surface disorder present for the experimental NR influenced the deformation dynamics, providing kinks and steps on the side of the NR as a low-energy path for atoms diffusing from the tips. On the contrary, the nucleation of new atomic planes was necessary for diffusing atoms for the model-like structure,³⁷¹ leading to an increase in stability. This will not only depend on the amount of disorder but also on the exact ratio of initial facets.

Deeper knowledge about reshaping and restructuring is tremendously important for the routine use of silica-coated metal NPs in actual applications. For this purpose, the results presented in this chapter provide an understanding concerning the conditions under which defects are formed and reshaping occurs. For most plasmonic applications such as imaging, sensing and biomedicine, reshaping and atomic restructuring is unwanted because it changes the carefully designed optical properties. Moreover, the creation of even a single lattice defect already causes plasmon broadening.³⁰ Our work demonstrates that local temperatures of more than 1000K can be achieved for silica-coated Au NRs without inducing structural and morphological modifications, which is not possible for bare Au NRs. Furthermore, it is essential to particularly highlight the importance of controlled restructuring for catalytic applications. It was recently demonstrated that a high density of stacking faults in Ag NPs immensely increased the activity for the hydrogen evolution reaction, thereby outperforming conventional Pt catalysts.³¹ Being able to control the internal restructuring as well as occurrence of specific surface facets will be a powerful tool in future catalytic research.³⁷² As shown in our work, a mesoporous silica coating gives a significantly better

control over the density of stacking faults, strain and surface coordination numbers compared to bare Au NPs. Our work paves the way towards tuning these parameters by changing the amount of absorbed heat (either by changing the AR of the NP or excitation power) to create highly active and stable future catalysts.

6.7. Conclusion

By combining experimentally retrieved 3D atomic scale information and MD simulations, it has been shown that femtosecond laser induced deformation with energies below the melting point proceeds twofold: 1) the NR deforms towards its thermodynamic equilibrium shape by curvature-driven surface diffusion and 2) the nanocrystal additionally lowers its free energy by creating more low-energy surface facets at the cost of internal twin boundaries. The latter are induced by a combination of atomic strain and localized melting. To reproduce the experimental data, femtosecond laser heating regime was modelled where the cooling process was specifically included in the simulations. By doing so, it has been observed that a mesoporous silica coating did not only stabilize Au NRs upon laser heating but also influenced the structure after deformation, which is due to the combination of a modified cooling profile and hindrance of surface diffusion. Finally, it has been demonstrated that subtleties in atomic scale morphology can significantly influence the physical properties of nanomaterials and their transformation mechanisms. Hence, the actual experimental morphology needs to be considered when studying dynamic atomistic processes. Therefore, incorporating realistic morphologies in models and simulations will be imperative for understanding and predicting the behavior of nanomaterials in practically relevant conditions. The methodology and insights demonstrated in the present study are expected to be valuable for open questions such as the effect of atomic distribution and crystal defects in NPs on their optical properties and catalytic performance.

Appendix A: Derivation of heating-cooling model to mimic femtosecond laser pulse

The validity of the heating model and the approximations were first checked by considering the experimental NR shown in Figure 6.3a (initial length and width of 51.2 nm and 11.6 nm, respectively). After the validation, the heating model was applied to simulated Au NRs having a 4 nm diameter. It should be noted that, although the validity of some approximations was tested by using the concepts of "effective diameter" or "characteristic length", the heat equations were solved by considering the size of the Au NR.

Validation of Approximation 1: Uniform temperature increase within the NP during electron-phonon scattering

During electron-phonon scattering, the temperature within a NP does not necessarily increase uniformly. When the lattice temperature starts to increase while the NP is still being illuminated, i.e. in nanosecond laser excitation, the temperature possibly differs radially inside the NP. On the

other hand, the time scale of electron-phonon thermalization is much longer than the pulse duration of femtosecond laser excitation. Therefore, it is reasonable to assume that there is no overlap between electron absorption and electron-phonon thermalization as long as the size of the NP is sufficiently small. Studies have shown that this approximation is valid if the size of the NP is smaller than 50 nm.^{355,356,361} To test the validity of this assumption for the anisotropic systems, the effective diameter (D_{eff}) is calculated as follows:

$$D_{eff} = \left(\frac{6V}{\pi} \right)^{(1/3)} . \quad (6.7)$$

Hereby, V represents the volume. The volume of the Au NR shown in Figure 6.3a (initial length and width of 51.2nm and 11.6 nm, respectively) was calculated by considering the geometry as a hemispherically capped cylinder:

$$V = \frac{\pi D^2}{4} (L - D) + \pi \frac{D^3}{6} , \quad (6.8)$$

where D is the diameter and L is the length of the NR. According to Equation 6.7 and Equation 6.8, the effective diameter of the Au NR was found to be around 21 nm, which is smaller than 50 nm. Hence, it is reasonable to assume that the temperature is not dependent on the distance and it changes only as a function of time $T(r, t) \approx T(t)$.

Validation of Approximation 2: Lumped capacitance approach for heat dissipation

To check the validity of this Lumped capacitance method, the Biot number was calculated as a ratio of convection at the surface of a particle to the conduction within the particle is given by:³⁵⁹

$$Bi = \frac{h_{medium} L_C}{k_{Au}} \quad (6.9)$$

where h_{medium} is the convective heat transfer coefficient of the surrounding medium, k_{Au} is the thermal conductivity of Au, and L_C is the volume-to-surface ratio of the NP. The Biot number smaller than 0.1 means that the resistance to conduction within the solid is much less than the resistance to convection across the boundary to the surrounding medium, which leads to a uniform temperature distribution in the particle during heat dissipation. h_{medium} was calculated as follows:

$$h_{medium} = k_{medium} \times Nu / D_{eff} , \quad (6.10)$$

where Nu represents the Nusselt number for natural convection and more detailed information can be found in ref³⁵⁹ and k_{medium} is the thermal conductivity of the surrounding medium, which is either glycerol or silica/glycerol in our case and is detailed below.

Thermal conductivity of Au NR

The thermal conductivity of Au k_{Au} for bulk systems is 317 W/m.K.³⁵⁹ However, when the size of the system gets close to the electron mean free path, the thermal conductivity decreases and when the ratio between the size and the mean free path becomes close to 1, the nano-size effect needs to be taken into account for the thermal conductivity, which can be determined by:³⁷³

$$\frac{k_{Au}}{k_{Au,bulk}} = \frac{1}{1 + K_n} \quad (6.11)$$

Here, K_n is the Knudsen number and it equals $\frac{\lambda_{mfp}}{D_{eff}}$.³⁷³ The electron mean free path, λ_{mfp} , of Au is equal to 31 nm³⁵⁹ and the effective diameter of the experimental Au NR was already calculated as 21 nm. Since the ratio between the electron mean free path and the effective diameter is close to 1, the nano-size effect was included into the calculations and the thermal conductivity of the Au NR (k_{Au}) was hence estimated as 128.8 W/m.K. As a consequence, the Biot number was calculated as 0.0008 for glycerol and 0.0006 for glycerol/silica medium, and hence the assumption of uniform temperature distribution within the NR is reasonable which allows to approximate $T(r, t) \approx T(t)$ during heat dissipation.

Thermal conductivity of porous silica filled with glycerol

The thermal conductivity of the porous silica filled with glycerol $k_{porous\ silica}$ was calculated by:³⁵⁹

$$k_{porous\ silica} = porosity \times k_{glycerol} + (1 - porosity) \times k_{silica} \quad (6.12)$$

where $k_{glycerol}$ is the thermal conductivity of glycerol and k_{silica} is the thermal conductivity of the silica.³⁵⁹ The constants are tabulated in Table 6.1.

Table 6.1 Physical constants.

Parameter	Symbol	Value
Density of Au	ρ (kg/m ³)	19300 ³⁵⁹
Dielectric constant marginally changes for silica-glycerol	$\epsilon_{silica-glycerol}$	2.17 ³⁶⁶
Dielectric constant marginally changes for glycerol	$\epsilon_{glycerol}$	2.1 ³⁶⁶
Electron mean free path of Au	λ_{mfp} (nm)	31 ³⁵⁹
Specific heat capacity of Au	c_p (j/kg.K)	129 ³⁵⁹
Thermal conductivity of Au for bulk systems	k_{Au} (W/m.K)	317 ³⁵⁹
Thermal conductivity of glycerol	$k_{glycerol}$ (W/m.K)	0.286 ³⁵⁹
Thermal conductivity of the silica	k_{silica} (W/m.K)	0.014 ³⁵⁹

Absorbed energy for simulated NPs

Due to the time and size differences between the experimental and simulated NRs, the absorbed

energy, $\sigma_{abs}F$, was carefully determined for the much smaller simulated NRs to fit the experimental conditions. This is necessary because the laser fluence F , which is used for the experiments, cannot be directly applied to calculate the excitation energy for the simulations due to the differences in volume between the experimental and simulated NRs.³⁷⁴ Therefore, the change in absorption cross section (σ_{abs}) was calculated using the MNPBEM toolbox³⁷⁴ by Dr. Wiebke Albrecht for the average experimental sizes of the NRs with three different ARs which is depicted in Figure 6.12.

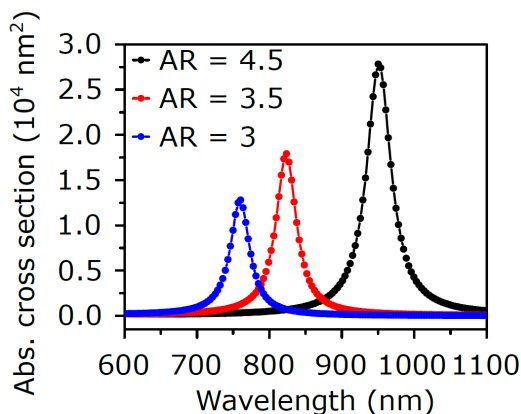


Figure 6.12 Calculated absorption cross sections of mesoporous silica-coated Au NRs with three different ARs.

Furthermore, as described in the section ‘Synthesis and femtosecond laser excitation’, the absorbed energy, inducing mild NR reshaping, was generally below the melting energy of the NRs. In order not to apply more energy than the melting threshold in the simulations, the melting energy of the smaller simulated NRs (with a constant diameter of 4 nm) was calculated as shown in Table 6.2

Table 6.2 Calculated melting energies Q_{melt} and applied heating energies $\sigma_{abs}F$ for the simulated NRs.

AR	Q_{melt} (fJ)	$\sigma_{abs}F$ (gJ)
3	0.51	0.25
3.5	0.61	0.33
4.5	0.80	0.51

To stay below the melting threshold, half of Q_{melt} was used as an excitation energy for AR=3. Based on the absorption cross section ratios calculated in Figure 6.12, the appropriate excitation energies for simulated NRs have an AR of 3.5 and 4.5. The resulting applied excitation energies in the simulations are summarized in Table 6.2. It should be noted that these energies do not change for the uncoated NRs, because the surrounding dielectric constant marginally changes from 2.17 for silica-glycerol to 2.1 for glycerol.

Chapter 6. 3D atomic-scale dynamics of laser light induced restructuring of nanoparticles unraveled by electron tomography and molecular dynamics simulations

Chapter 7. General conclusion & Outlook

In this chapter, a general conclusion of the methodologies and insights presented in this thesis is drawn, future perspectives for the research presented in this thesis are discussed, and promising results to be further explored are demonstrated.

7.1. General conclusion

Metallic NPs, in comparison to their bulk counterparts, exhibit unique physical and chemical properties that make them attractive for an increasing number of applications in various fields, such as (photo-)catalysis, biomedicine, sensing, and data storage. The emergent properties of metallic NPs are directly linked to their size, shape, structural defects, surface facets, and elemental distribution. However, when these NPs are exposed to environmental stimuli, such as heating and intense light illumination, rapid structural and morphological transformations are often observed in NPs. Since any small change in the local structure of the NPs may significantly modify their performance, to gain control over their structure-dependent properties and to relate their design for specific applications, an atomic scale understanding is of primary importance. Therefore, this thesis was devoted to presenting robust approaches by joining the STEM imaging techniques and theoretical calculations in an adequate way to capture 3D atomic-scale transformations of metallic NPs when they are exposed to the application-relevant conditions. Within this framework, the research presented in this thesis was conducted twofold.

First, I focused on the 3D atomic-resolution structural characterization of metallic NPs lying on a support from ADF STEM images acquired along a single viewing direction during *in situ* heating experiments. Previously reported studies demonstrated that 3D characterization of nanoparticles, combining atom counting on 2D high-resolution STEM images acquired along a single viewing direction and structural relaxation by atomistic simulations, was a very useful tool. This method enabled the 3D atomic structure of NPs in a quantitative manner, as was explained in Chapter 1 and Chapter 2. However, prior to the research presented in this thesis, this approach was applied to free-standing particles roughly symmetrical along the electron beam direction in the electron microscope. In order to obtain reliable 3D atomic-scale characterization of the supported metallic NPs at high temperatures, which is typical for catalytic applications, several critical steps in the methodology were further optimized in Chapter 3. Moreover, in Chapter 4, I introduced the local minima search algorithm followed by MD structural relaxation at experimental temperature by including the particle-support interaction. This method explores different local minima in the energy landscape while quantitatively validating the reconstructed structure in terms of the projected atomic column positions and atom counts in atomic columns. It has been shown that the proposed approach outperforms the previously applied methodologies and enables the 3D investigation of both stable and metastable states of the experimentally imaged particles that may appear at high temperatures.

On the other hand, atomic-scale transformations cannot be visualized by only experimental techniques when *in situ* STEM experiments do not provide the necessary time or spatial resolution. The 3D investigation of atomic-scale transformations becomes even more challenging when the triggers cannot be applied *in situ*. To overcome this limitation, I used the outcome of the electron tomography experiments as realistic input models for the atomistic simulations. This approach is unique and highly important as it enables performing simulations based on the experimentally measured surface facets, the distribution of which is tremendously important for nanoscale

processes. Moreover, this method provides a powerful approach since it enables us to capture the ongoing processes at atomic scale, which cannot be achievable by experimental observations, as well as to understand the driving mechanisms behind the complex atomistic rearrangements, causing shape deformations and defect generation.

The methodologies and insights demonstrated in this thesis are expected to be valuable for controlling the desired structure-dependent functional properties of metallic NPs for medical and optical applications as well as in the field of catalysis. For example, an accurate refinement of experimentally observed 3D atomic structures of supported metallic NPs in a realistic environment can provide critical information for the structure-dependent properties of catalytic NPs. Moreover, a full understanding of the mechanisms behind the transformations by incorporating realistic morphologies in simulations can allow improving the thermal stability of photo- and electrocatalytic NPs and to overcome the degradation of nanostructures, e.g. during biomedical applications triggered by laser irradiation.

7.2. Outlook

Several development directions that are yet to be addressed for the proposed methods in this thesis can be further explored. Promising developments for the research presented in this thesis can be carried out in three main topics:

- 3D characterization of different types of nanomaterials
- 3D *operando* studies
- Combination of 3D *operando* studies and atomistic simulations

7.2.1. 3D characterization of different types of nanomaterials

All the methods in this thesis have been developed for metallic NPs, which are relatively stable to the incident electron beam. However, the application of the proposed methodologies is by far not limited to metallic systems. This approach can also enable an accurate 3D characterization of different classes of materials, such as semiconductor nanocrystals. As a semiconductor nanocrystal, Indium Phosphide (InP) quantum dots have become a subject of intense interest in recent years. The tunable electronic properties of InP quantum dots make them promising for many applications, such as in electronic devices, sensors, and catalysis. Considering their shape and size-dependent functionalities, 3D characterizations of InP quantum dots are essential to control their functionality.

These quantum dots are too electron beam-sensitive to be studied by conventional electron tomography. Therefore, the local minima search algorithm based on atom counting results, as introduced in Chapter 4, can be employed to retrieve the 3D structure of these quantum dots from STEM images acquired along a single viewing direction. However, in order to obtain a reliable 3D model, some challenges need to be pursued. In the HAADF STEM imaging mode, visualizing light P-atomic columns together with heavy In-atomic columns can be challenging since light elements only scatter electrons weakly to high detector angles leading to low intensities in HAADF STEM images (Figure 7.1a). Recently introduced integrated differential phase-contrast (iDPC) imaging

method enables direct imaging of the phase transmission function for non-magnetic samples.³⁷⁵ This imaging mode is of great interest to observe both light and heavy elements since the image contrast varies approximately linear according to the atomic number Z of the elements in a sample.³⁷⁶ On the other hand, quantification of an iDPC image is not straightforward due to the high sensitivity of the image to phase modifications and amplified frequency noise during the integration step.⁶¹

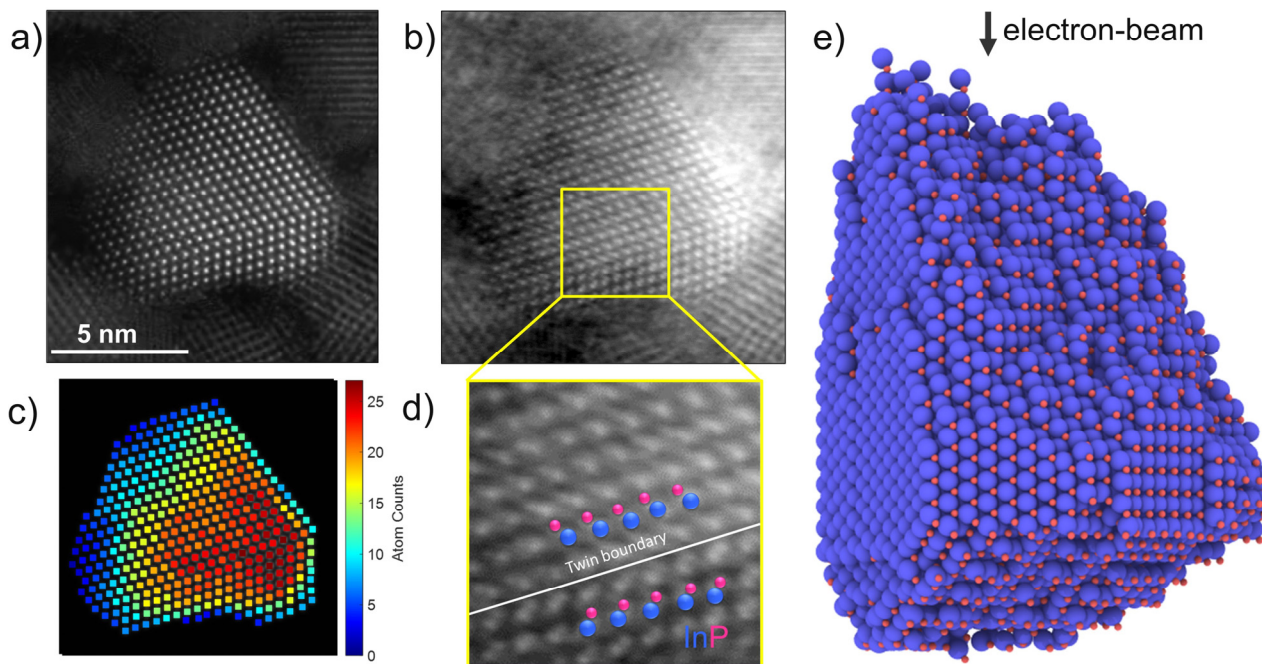


Figure 7.1 3D modelling of an InP quantum dot. a) Simultaneously acquired (a) HAADF STEM and (b) iDPC images of the same InP quantum dot. The imaged InP quantum dots were synthesized by Kim Dürnberg and the STEM images were acquired by Dr. Nadine Schrenker. c) Number of atoms in each In-atomic column acquired by applying the combined simulation and statistics-based atom counting on the HAADF STEM image shown in (a). d) A close-up image of the highlighted area of the iDPC image shown in (b). From this magnified image, both light P-atomic columns and heavier In-atomic columns can be distinguished. e) A final 3D model of InP quantum dots from the local minima search algorithm where a starting model was created based on (c), (d), and zinc blend crystalline structure of InP quantum dots. To define the interaction between the atoms during the 3D reconstruction algorithm, the Vashishta inter-atomic potential³⁷⁷ was used.

To overcome these limitations, the advantages of the simultaneously acquired HAADF STEM (Figure 7.1a) and iDPC (Figure 7.1b) images have been exploited for the 3D characterization of InP quantum dots. On the one hand, the use of combined simulation and statistics-based atom counting on a high-resolution HAADF STEM image enabled us to count the number of atoms in In-atomic columns (Figure 7.1c). The estimated atom counts were then used to create a starting model according to the sample zone axis and the configuration of In atoms in a zinc blend³⁷⁸ crystalline structure of InP quantum dots. On the other hand, based on the relative positions of projected P-atomic columns with respect to In-atomic columns, as observed in the iDPC STEM

image (Figure 7.1d), and zinc blend structure of the InP quantum dots, the P-atoms could be located in the created starting model. Afterwards, the created starting model was used as an input for the local minima search algorithm to obtain the final 3D structure of the InP quantum dots as shown in Figure 7.1e. These results demonstrate the power of the proposed approach by simultaneously using different STEM imaging modes for high throughput 3D structural investigation of promising classes of materials with minimum electron irradiation damage.

7.2.2. 3D operando studies

The 3D *in situ* heating studies are insightful and crucial to understand the structural and morphological changes of a catalytic NP upon heating. In this thesis, I have demonstrated that NPs change their surface faceting during *in situ* experiments. However, to link the surface structure of a nanocatalyst to its catalytic activity, one must also be able to measure reactant and product species generated in real-time combined with the simultaneous observation of the working catalyst. This can be achieved by *operando* studies using a dedicated mass spectrometer in TEM.

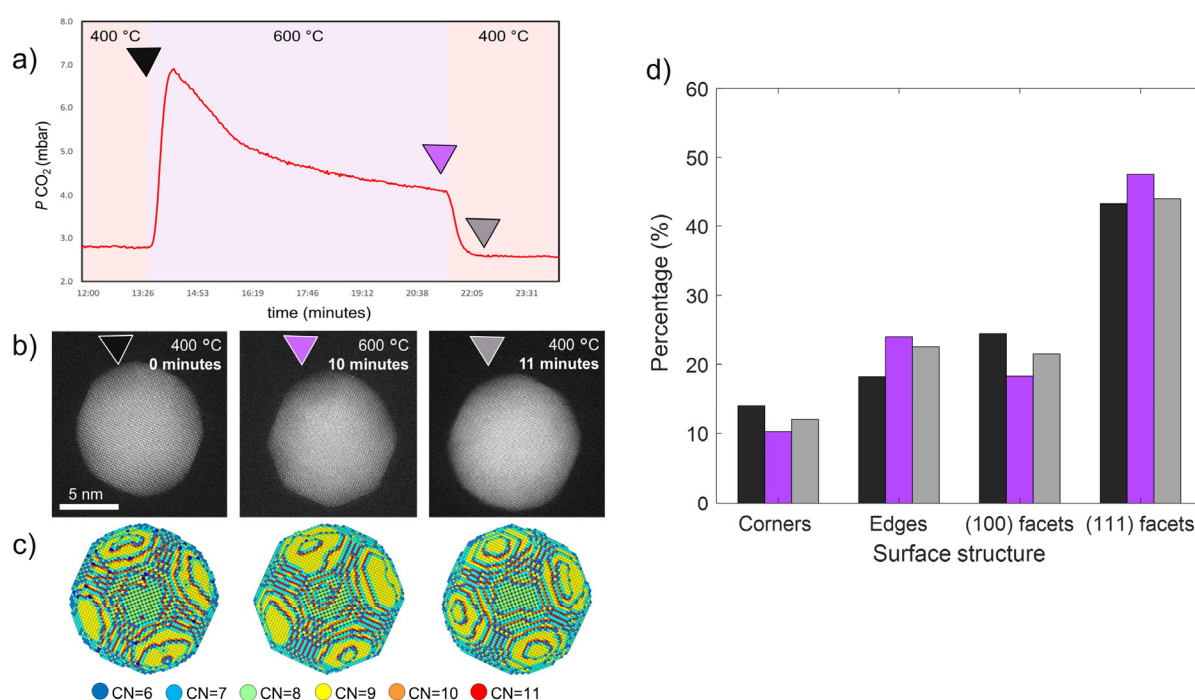


Figure 7.2 Correlation of the activity and 3D surface structure of Pt NP catalyzing CO oxidation. a) Mass spectrometry of the CO pressures. b) ADF STEM images of the same Pt NP acquired at the different states of the reaction, as indicated by triangles. c) 3D models retrieved from the ADF STEM images shown in (b). The atoms are presented in different colors according to the coordination numbers (CN). d) Surface structure of the reconstructed NPs. The histogram is obtained from the coordination number of the atoms. The samples were provided by the group of Prof. Dr. Luis Liz-Marzán, and *operando* STEM experiments were performed by Dr. Kellie Jenkinson.

To this end, an *operando* STEM study of a Pt NP was performed during CO oxidation with mass spectrometry measurements in real-time (Figure 7.2). The CO oxidation reaction is a benchmark heterogeneous reaction catalyzed by costly precious metals such as Pt, Pd and Au, and is primarily

focused on for its automotive emission control to convert the toxic and hazardous CO to CO₂. From mass spectrometry of CO pressure shown in Figure 7.2a, it can be seen that the catalytic activity of Pt NP for CO oxidation drops with respect to time (from black triangle to purple triangle). It is commonly hypothesized that this activity drop is associated with the reduction in under-coordinated atoms at the surface. However, to date, most of the reported *operando* studies are based on 2D information only, which is not sufficient to connect the entire 3D structure of the catalysts to their activity. To go beyond the current studies, the 3D characterization techniques presented for *in situ* studies in this thesis can be extended to *operando* studies. Since, the tilting range of most gas cell holders does not allow one to perform electron tomography experiments based on continuous tilt series, the 3D characterizations of the Pt NP at different stages of CO oxidation reactions were performed from ADF STEM images (Figure 7.2b) acquired along a single zone axis of the sample. The reconstructed 3D models of the same Pt NP are shown in Figure 7.2c. As the 3D structures of the same NP at the different states of the reaction were extracted, I could also quantify the changes in facet evolution throughout the reaction (Figure 7.2d). In this manner, it has been possible to relate the quantitative change in the surface facets to the catalyst performance of the NP. In the future, it would be highly important to extend this framework for 3D *operando* studies of anisotropic and bimetallic NPs to investigate their structure-dependent performance.

7.2.3. Combination of 3D *operando* studies and atomistic simulations

In this thesis, it has been shown that the combination of 3D experimental characterization techniques and MD simulations is a powerful approach to understand a wide variety of atomic scale transformations. Extending this approach to systematically investigate the effect of size, shape, surface structure, crystalline defects, and alloying on the catalytic performance of the experimentally observed NPs under a gaseous environment will be highly important. However, due to their size and time constraints, classical MD simulations are limited to relatively small systems. Also, due to the same limitations of the classical MD simulations, this approach may have poor performance in investigating the diffusion, alloying, or defect migration observed in experimental systems since these processes take orders of magnitude longer (beyond microseconds) than MD simulations are able to address. Recent studies have shown that machine learning-based MD simulations can provide accurate and fast predictions addressing a variety of problems in chemistry, physics, and materials science at reduced computational cost and for larger length and time scales that cannot be accessible by conventional MD simulations.³⁴⁻³⁷ Therefore, using experimentally determined 3D structures of NPs in machine learning-assisted simulations can enable one to capture atomistic transformations, including alloying, defect formation and morphological transformations, on experimentally relevant time and length scales. Since machine learning-based simulations can be trained to accurately reproduce the quantum mechanical behavior of NPs, coupling 3D reconstructed NPs to such simulations performed under a gaseous environment can provide valuable information to enlighten the complicated dynamics of experimental NPs at the atomic scale and their elusive structure-activity relationship during catalytic reactions. In this manner, the developments of novel nanocatalysts possessing the optimum catalytic activity and selectivity for specific applications can be triggered.

References

- (1) Schodek, D.; Ferreira, P.; Ashby, M. *Nanomaterials, Nanotechnologies and Design*; 2009. <https://doi.org/10.1016/B978-0-7506-8149-0.X0001-3>.
- (2) Claes, N. 3D Characterization of Coated Nanoparticles and Soft-Hard Nanocomposites. 2018.
- (3) Luther, J. M.; Jain, P. K.; Ewers, T.; Alivisatos, A. P. Localized Surface Plasmon Resonances Arising from Free Carriers in Doped Quantum Dots. *Nat. Mater.* **2011**. <https://doi.org/10.1038/nmat3004>.
- (4) Louis, C.; Pluchery, O. *Gold Nanoparticles for Physics, Chemistry and Biology*; 2012. <https://doi.org/10.1142/P815>.
- (5) Baffou, G.; Quidant, R.; Girard, C. Heat Generation in Plasmonic Nanostructures: Influence of Morphology. *Appl. Phys. Lett.* **2009**. <https://doi.org/10.1063/1.3116645>.
- (6) Bayda, S.; Adeel, M.; Tuccinardi, T.; Cordani, M.; Rizzolio, F. The History of Nanoscience and Nanotechnology: From Chemical-Physical Applications to Nanomedicine. *Molecules*. 2020. <https://doi.org/10.3390/molecules25010112>.
- (7) Barber, D. J.; Freestone, I. C. An Investigation of the Origin of the Colour of the Lycurgus Cup by Analytical Transmission Electron Microscopy. *Archaeometry* **1990**. <https://doi.org/10.1111/j.1475-4754.1990.tb01079.x>.
- (8) Singh, A. K. Introduction to Nanoparticles and Nanotoxicology. In *Engineered Nanoparticles*; 2016. <https://doi.org/10.1016/b978-0-12-801406-6.00001-7>.
- (9) Reibold, M.; Paufler, P.; Levin, A. A.; Kochmann, W.; Pätzke, N.; Meyer, D. C. Materials: Carbon Nanotubes in an Ancient Damascus Sabre. *Nature* **2006**. <https://doi.org/10.1038/444286a>.
- (10) Feynman, R. There's Plenty of Room at the Bottom. In *Feynman and Computation*; 2018. <https://doi.org/10.1201/9780429500459>.
- (11) Pearce, A. K.; Wilks, T. R.; Arno, M. C.; O'Reilly, R. K. Synthesis and Applications of Anisotropic Nanoparticles with Precisely Defined Dimensions. *Nature Reviews Chemistry*. 2021. <https://doi.org/10.1038/s41570-020-00232-7>.
- (12) Šimon, P.; Chaudhry, Q.; Bakoš, D. Migration of Engineered Nanoparticles from Polymer Packaging to Food - A Physicochemical View. *J. Food Nutr. Res.* **2008**.
- (13) Chen, C. H.; Li, S. Y.; Chiang, A. S. T.; Wu, A. T.; Sun, Y. S. Scratch-Resistant Zeolite Anti-Reflective Coating on Glass for Solar Applications. *Sol. Energy Mater. Sol. Cells* **2011**. <https://doi.org/10.1016/j.solmat.2011.01.032>.
- (14) Zhao, H. E.; Shen, F. The Applied Research of Nanophase Materials in Sports Engineering. In *Advanced Materials Research*; 2012. <https://doi.org/10.4028/www.scientific.net/AMR.496.126>.
- (15) Newman, M. D.; Stotland, M.; Ellis, J. I. The Safety of Nanosized Particles in Titanium Dioxide- and Zinc Oxide-Based Sunscreens. *Journal of the American Academy of*

References

- Dermatology*. 2009. <https://doi.org/10.1016/j.jaad.2009.02.051>.
- (16) Jiang, C.; Hosono, E.; Zhou, H. Nanomaterials for Lithium Ion Batteries. *Nano Today* **2006**. [https://doi.org/10.1016/S1748-0132\(06\)70114-1](https://doi.org/10.1016/S1748-0132(06)70114-1).
- (17) Mahmood, N.; Hou, Y. Electrode Nanostructures in Lithium-Based Batteries. *Advanced Science*. 2014. <https://doi.org/10.1002/advs.201400012>.
- (18) Lu, J.; Chen, Z.; Ma, Z.; Pan, F.; Curtiss, L. A.; Amine, K. The Role of Nanotechnology in the Development of Battery Materials for Electric Vehicles. *Nature Nanotechnology*. 2016. <https://doi.org/10.1038/nnano.2016.207>.
- (19) Su, J. Portable and Sensitive Air Pollution Monitoring. *Light: Science and Applications*. 2018. <https://doi.org/10.1038/s41377-018-0017-x>.
- (20) Willner, M. R.; Vikesland, P. J. Nanomaterial Enabled Sensors for Environmental Contaminants. *J. Nanobiotechnology* **2018**. <https://doi.org/10.1186/s12951-018-0419-1>.
- (21) Becher, J.; Sanchez, D. F.; Doronkin, D. E.; Zengel, D.; Meira, D. M.; Pascarelli, S.; Grunwaldt, J. D.; Sheppard, T. L. Chemical Gradients in Automotive Cu-SSZ-13 Catalysts for NO_x Removal Revealed by Operando X-Ray Spectrotomography. *Nat. Catal.* **2021**. <https://doi.org/10.1038/s41929-020-00552-3>.
- (22) Lanzafame, P.; Perathoner, S.; Centi, G.; Gross, S.; Hensen, E. J. M. Grand Challenges for Catalysis in the Science and Technology Roadmap on Catalysis for Europe: Moving Ahead for a Sustainable Future. *Catal. Sci. Technol.* **2017**. <https://doi.org/10.1039/c7cy01067b>.
- (23) Tian, N.; Zhou, Z.-Y.; Sun, S.-G.; Ding, Y.; Wang, Z. L. Synthesis of Tetrahedral Platinum Nanocrystals with High-Index Facets and High Electro-Oxidation Activity. *Science (80-.)*. **2007**, *316* (5825), 732–735. <https://doi.org/10.1126/science.1140484>.
- (24) Zhao, Q.; Hazarika, A.; Chen, X.; Harvey, S. P.; Larson, B. W.; Teeter, G. R.; Liu, J.; Song, T.; Xiao, C.; Shaw, L.; Zhang, M.; Li, G.; Beard, M. C.; Luther, J. M. High Efficiency Perovskite Quantum Dot Solar Cells with Charge Separating Heterostructure. *Nat. Commun.* **2019**. <https://doi.org/10.1038/s41467-019-10856-z>.
- (25) Hu, L.; Zhao, Q.; Huang, S.; Zheng, J.; Guan, X.; Patterson, R.; Kim, J.; Shi, L.; Lin, C. H.; Lei, Q.; Chu, D.; Tao, W.; Cheong, S.; Tilley, R. D.; Ho-Baillie, A. W. Y.; Luther, J. M.; Yuan, J.; Wu, T. Flexible and Efficient Perovskite Quantum Dot Solar Cells via Hybrid Interfacial Architecture. *Nat. Commun.* **2021**. <https://doi.org/10.1038/s41467-020-20749-1>.
- (26) Jean, J. Getting High with Quantum Dot Solar Cells. *Nature Energy*. 2020. <https://doi.org/10.1038/s41560-019-0534-8>.
- (27) Kennedy, L. C.; Bickford, L. R.; Lewinski, N. A.; Coughlin, A. J.; Hu, Y.; Day, E. S.; West, J. L.; Drezek, R. A. A New Era for Cancer Treatment: Gold-Nanoparticle-Mediated Thermal Therapies. *Small*. 2011. <https://doi.org/10.1002/sml.201000134>.
- (28) Bromma, K.; Chithrani, D. B. Advances in Gold Nanoparticle-Based Combined Cancer Therapy. *Nanomaterials*. 2020. <https://doi.org/10.3390/nano10091671>.
- (29) Carabineiro, S. A. C. Applications of Gold Nanoparticles in Nanomedicine: Recent Advances in Vaccines. *Molecules*. 2017. <https://doi.org/10.3390/molecules22050857>.

References

- (30) Milagres de Oliveira, T.; Albrecht, W.; González-Rubio, G.; Altantzis, T.; Lobato Hoyos, I. P.; Béché, A.; Van Aert, S.; Guerrero-Martínez, A.; Liz-Marzán, L. M.; Bals, S. 3D Characterization and Plasmon Mapping of Gold Nanorods Welded by Femtosecond Laser Irradiation. *ACS Nano* **2020**, *14* (10), 12558–12570. <https://doi.org/10.1021/acsnano.0c02610>.
- (31) Li, Z.; Fu, J. Y.; Feng, Y.; Dong, C. K.; Liu, H.; Du, X. W. A Silver Catalyst Activated by Stacking Faults for the Hydrogen Evolution Reaction. *Nat. Catal.* **2019**. <https://doi.org/10.1038/s41929-019-0365-9>.
- (32) Vendelbo, S. B.; Elkjær, C. F.; Falsig, H.; Puspitasari, I.; Dona, P.; Mele, L.; Morana, B.; Nelissen, B. J.; Van Rijn, R.; Creemer, J. F.; Kooyman, P. J.; Helveg, S. Visualization of Oscillatory Behaviour of Pt Nanoparticles Catalysing CO Oxidation. *Nat. Mater.* **2014**. <https://doi.org/10.1038/nmat4033>.
- (33) Hvolbæk, B.; Janssens, T. V. W.; Clausen, B. S.; Falsig, H.; Christensen, C. H.; Nørskov, J. K. Catalytic Activity of Au Nanoparticles. *Nano Today*. 2007. [https://doi.org/10.1016/S1748-0132\(07\)70113-5](https://doi.org/10.1016/S1748-0132(07)70113-5).
- (34) Zhang, C.; Michaelides, A.; Jenkins, S. J. Theory of Gold on Ceria. *Phys. Chem. Chem. Phys.* **2011**. <https://doi.org/10.1039/c0cp01123a>.
- (35) Hofer, W. A. Challenges and Errors: Interpreting High Resolution Images in Scanning Tunneling Microscopy. In *Progress in Surface Science*; 2003. [https://doi.org/10.1016/S0079-6816\(03\)00005-4](https://doi.org/10.1016/S0079-6816(03)00005-4).
- (36) Tseng, A. A. Advancements and Challenges in Development of Atomic Force Microscopy for Nanofabrication. *Nano Today*. 2011. <https://doi.org/10.1016/j.nantod.2011.08.003>.
- (37) Suga, M.; Asahina, S.; Sakuda, Y.; Kazumori, H.; Nishiyama, H.; Nokuo, T.; Alfredsson, V.; Kjellman, T.; Stevens, S. M.; Cho, H. S.; Cho, M.; Han, L.; Che, S.; Anderson, M. W.; Schüth, F.; Deng, H.; Yaghi, O. M.; Liu, Z.; Jeong, H. Y.; Stein, A.; Sakamoto, K.; Ryoo, R.; Terasaki, O. Recent Progress in Scanning Electron Microscopy for the Characterization of Fine Structural Details of Nano Materials. *Progress in Solid State Chemistry*. 2014. <https://doi.org/10.1016/j.progsolidstchem.2014.02.001>.
- (38) Henderson, R. The Potential and Limitations of Neutrons, Electrons and X-Rays for Atomic Resolution Microscopy of Unstained Biological Molecules. *Q. Rev. Biophys.* **1995**. <https://doi.org/10.1017/S003358350000305X>.
- (39) Pennycook, S. J. Fulfilling Feynman's Dream: "Make the Electron Microscope 100 Times Better" - Are We There Yet? In *MRS Bulletin*; 2015. <https://doi.org/10.1557/mrs.2014.307>.
- (40) Segal, M. Surely You're Happy, Mr Feynman! *Nature Nanotechnology*. 2009. <https://doi.org/10.1038/nnano.2009.360>.
- (41) Heintzmann, R.; Ficz, G. Breaking the Resolution Limit in Light Microscopy. *Briefings in Functional Genomics and Proteomics*. 2006. <https://doi.org/10.1093/bfgp/ell036>.
- (42) Knoll, M.; Ruska, E. Das Elektronenmikroskop. *Zeitschrift für Physik*. 1932. <https://doi.org/10.1007/BF01330526>.
- (43) Williams, D. B.; Carter, C. B. *Transmission Electron Microscopy: A Textbook for Materials Science*; 2009. <https://doi.org/10.1007/978-0-387-76501-3>.

References

- (44) Erni, R.; Rossell, M. D.; Kisielowski, C.; Dahmen, U. Atomic-Resolution Imaging with a Sub-50-Pm Electron Probe. *Phys. Rev. Lett.* **2009**, *102*, 096101. <https://doi.org/10.1103/PhysRevLett.102.096101>.
- (45) Batson, P. E.; Dellby, N.; Krivanek, O. L. Sub-Angstrom Resolution Using Aberration Corrected Electron Optics. *Nature* **2002**, *418*, 617–620.
- (46) Kabius, B.; Haider, M.; Uhlemann, S.; Schwan, E.; Urban, K.; Rose, H. First Application of a Spherical-Aberration Corrected Transmission Electron Microscope in Materials Science. *J. Electron Microsc. (Tokyo)*. **2002**, *51*, S51–S58. <https://doi.org/10.1093/jmicro/51.supplement.s51>.
- (47) Haider, M.; Rose, H.; Uhlemann, S.; Schwan, E.; Kabius, B.; Urban, K. A Spherical-Aberration-Corrected 200 KV Transmission Electron Microscope. *Ultramicroscopy* **1998**, *75* (1), 53–60. [https://doi.org/10.1016/S0304-3991\(98\)00048-5](https://doi.org/10.1016/S0304-3991(98)00048-5).
- (48) Van Dyck, D.; Chen, J. H. A Simple Theory for Dynamical Electron Diffraction in Crystals. *Solid State Commun.* **1999**. [https://doi.org/10.1016/S0038-1098\(98\)00599-7](https://doi.org/10.1016/S0038-1098(98)00599-7).
- (49) van Dyck, D. High-Resolution Electron Microscopy. *Adv. Imaging Electron Phys.* **2002**. [https://doi.org/10.1016/S1076-5670\(02\)80062-3](https://doi.org/10.1016/S1076-5670(02)80062-3).
- (50) Pennycook, S. J.; Nellist, P. D. Z-Contrast Scanning Transmission Electron Microscopy BT - Impact of Electron and Scanning Probe Microscopy on Materials Research; Rickerby, D. G., Valdrè, G., Valdrè, U., Eds.; Springer Netherlands: Dordrecht, 1999; pp 161–207. https://doi.org/10.1007/978-94-011-4451-3_7.
- (51) Allen, L. J.; McBride, W.; O’Leary, N. L.; Oxley, M. P. Exit Wave Reconstruction at Atomic Resolution. *Ultramicroscopy* **2004**. <https://doi.org/10.1016/j.ultramic.2004.01.012>.
- (52) Erni, R.; Rossell, M. D.; Nakashima, P. N. H. Optimization of Exit-Plane Waves Restored from HRTEM through-Focal Series. *Ultramicroscopy* **2010**. <https://doi.org/10.1016/j.ultramic.2009.10.015>.
- (53) Van Dyck, D. Wave Reconstruction in TEM Using a Variable Phase Plate. *Ultramicroscopy* **2010**. <https://doi.org/10.1016/j.ultramic.2009.12.016>.
- (54) Linck, M.; Freitag, B.; Kujawa, S.; Lehmann, M.; Niermann, T. State of the Art in Atomic Resolution Off-Axis Electron Holography. *Ultramicroscopy* **2012**. <https://doi.org/10.1016/j.ultramic.2012.01.019>.
- (55) Van Aert, S.; De Backer, A.; Martinez, G. T.; Den Dekker, A. J.; Van Dyck, D.; Bals, S.; Van Tendeloo, G. Advanced Electron Crystallography through Model-Based Imaging. *IUCrJ* **2016**. <https://doi.org/10.1107/S2052252515019727>.
- (56) Kirkland, E. J. *Advanced Computing in Electron Microscopy*; 2013. <https://doi.org/10.1007/978-1-4757-4406-4>.
- (57) Nellist, P. D. The Principles of STEM Imaging. In *Scanning Transmission Electron Microscopy*; 2011. https://doi.org/10.1007/978-1-4419-7200-2_2.
- (58) Nellist, P. D.; Pennycook, S. J. The Principles and Interpretation of Annular Dark-Field Z-Contrast Imaging. *Adv. Imaging Electron Phys.* **2000**. [https://doi.org/10.1016/S1076-5670\(00\)80013-0](https://doi.org/10.1016/S1076-5670(00)80013-0).

References

- (59) Cowley, J. M. Image Contrast in a Transmission Scanning Electron Microscope. *Appl. Phys. Lett.* **1969**. <https://doi.org/10.1063/1.1652901>.
- (60) Rose, H.; Kisielowski, C. F. On the Reciprocity of TEM and STEM. *Microsc. Microanal.* **2005**. <https://doi.org/10.1017/s1431927605507761>.
- (61) Gauquelin, N.; van den Bos, K. H. W.; Béch e, A.; Krause, F. F.; Lobato, I.; Lazar, S.; Rosenauer, A.; Van Aert, S.; Verbeeck, J. Determining Oxygen Relaxations at an Interface: A Comparative Study between Transmission Electron Microscopy Techniques. *Ultramicroscopy* **2017**. <https://doi.org/10.1016/j.ultramic.2017.06.002>.
- (62) Nellist, P. D. Scanning Transmission Electron Microscopy. In *Springer Handbooks*; 2019. https://doi.org/10.1007/978-3-030-00069-1_2.
- (63) Hartel, P.; Rose, H.; Dinges, C. Conditions and Reasons for Incoherent Imaging in STEM. *Ultramicroscopy* **1996**. [https://doi.org/10.1016/0304-3991\(96\)00020-4](https://doi.org/10.1016/0304-3991(96)00020-4).
- (64) Lobato, I.; Van Dyck, D. MULTEM: A New Multislice Program to Perform Accurate and Fast Electron Diffraction and Imaging Simulations Using Graphics Processing Units with CUDA. *Ultramicroscopy* **2015**. <https://doi.org/10.1016/j.ultramic.2015.04.016>.
- (65) Cliff, G.; Lorimer, G. W. The Quantitative Analysis of Thin Specimens. *J. Microsc.* **1975**. <https://doi.org/10.1111/j.1365-2818.1975.tb03895.x>.
- (66) Watanabe, M.; Williams, D. B. The Quantitative Analysis of Thin Specimens: A Review of Progress from the Cliff-Lorimer to the New ζ -Factor Methods. *Journal of Microscopy*. 2006. <https://doi.org/10.1111/j.1365-2818.2006.01549.x>.
- (67) Egerton, R. F. Electron Energy-Loss Spectroscopy in the TEM. *Reports Prog. Phys.* **2009**. <https://doi.org/10.1088/0034-4885/72/1/016502>.
- (68) Bals, S.; Goris, B.; Liz-Marz an, L. M.; Van Tendeloo, G. Three-Dimensional Characterization of Noble-Metal Nanoparticles and Their Assemblies by Electron Tomography. *Angew. Chemie - Int. Ed.* **2014**. <https://doi.org/10.1002/anie.201401059>.
- (69) Bals, S.; Goris, B.; De Backer, A.; Van Aert, S.; Van Tendeloo, G. Atomic Resolution Electron Tomography. *MRS Bull.* **2016**, *41* (7), 525–530. <https://doi.org/10.1557/mrs.2016.138>.
- (70) Midgley, P. A.; Weyland, M. 3D Electron Microscopy in the Physical Sciences: The Development of Z-Contrast and EFTEM Tomography. *Ultramicroscopy* **2003**, *96* (3–4), 413–431. [https://doi.org/10.1016/S0304-3991\(03\)00105-0](https://doi.org/10.1016/S0304-3991(03)00105-0).
- (71) Midgley, P. A.; Dunin-Borkowski, R. E. Electron Tomography and Holography in Materials Science. *Nat. Mater.* **2009**, *8*, 271–280. <https://doi.org/10.1038/nmat2406>.
- (72) Midgley, P. A.; Weyland, M. 3D Electron Microscopy in the Physical Sciences: The Development of Z-Contrast and EFTEM Tomography. In *Ultramicroscopy*; 2003. [https://doi.org/10.1016/S0304-3991\(03\)00105-0](https://doi.org/10.1016/S0304-3991(03)00105-0).
- (73) Bals, S.; Batenburg, K. J.; Liang, D.; Lebedev, O.; Van Tendeloo, G.; Aerts, A.; Martens, J. A.; Kirschhock, C. E. A. Quantitative Three-Dimensional Modeling of Zeolite through Discrete Electron Tomography. *J. Am. Chem. Soc.* **2009**. <https://doi.org/10.1021/ja8089125>.

References

- (74) Zanaga, D.; Altantzis, T.; Polavarapu, L.; Liz-Marzán, L. M.; Freitag, B.; Bals, S. A New Method for Quantitative XEDS Tomography of Complex Heteronanostructures. *Part. Part. Syst. Charact.* **2016**. <https://doi.org/10.1002/ppsc.201600021>.
- (75) Möbus, G.; Doole, R. C.; Inkson, B. J. Spectroscopic Electron Tomography. In *Ultramicroscopy*; 2003. [https://doi.org/10.1016/S0304-3991\(03\)00106-2](https://doi.org/10.1016/S0304-3991(03)00106-2).
- (76) Albrecht, W.; Van Aert, S.; Bals, S. Three-Dimensional Nanoparticle Transformations Captured by an Electron Microscope. *Acc. Chem. Res.* **2021**. <https://doi.org/10.1021/acs.accounts.0c00711>.
- (77) Ke, X.; Bals, S.; Cott, D.; Hantschel, T.; Bender, H.; Van Tendeloo, G. Three-Dimensional Analysis of Carbon Nanotube Networks in Interconnects by Electron Tomography without Missing Wedge Artifacts. *Microsc. Microanal.* **2010**. <https://doi.org/10.1017/S1431927609991371>.
- (78) Radon, J. ON THE DETERMINATION OF FUNCTIONS FROM THEIR INTEGRAL VALUES ALONG CERTAIN MANIFOLDS. *IEEE Trans. Med. Imaging* **1986**. <https://doi.org/10.1109/tmi.1986.4307775>.
- (79) Gilbert, P. Iterative Methods for the Three-Dimensional Reconstruction of an Object from Projections. *J. Theor. Biol.* **1972**. [https://doi.org/10.1016/0022-5193\(72\)90180-4](https://doi.org/10.1016/0022-5193(72)90180-4).
- (80) Heidari Mezerji, H.; Van den Broek, W.; Bals, S. A Practical Method to Determine the Effective Resolution in Incoherent Experimental Electron Tomography. *Ultramicroscopy* **2011**. <https://doi.org/10.1016/j.ultramic.2011.01.021>.
- (81) Altantzis, T.; Lobato, I.; De Backer, A.; Béché, A.; Zhang, Y.; Basak, S.; Porcu, M.; Xu, Q.; Sánchez-Iglesias, A.; Liz-Marzán, L. M.; Van Tendeloo, G.; Van Aert, S.; Bals, S. Three-Dimensional Quantification of the Facet Evolution of Pt Nanoparticles in a Variable Gaseous Environment. *Nano Lett.* **2019**. <https://doi.org/10.1021/acs.nanolett.8b04303>.
- (82) Jones, L.; Nellist, P. D. Identifying and Correcting Scan Noise and Drift in the Scanning Transmission Electron Microscope. In *Microscopy and Microanalysis*; 2013. <https://doi.org/10.1017/S1431927613001402>.
- (83) Jones, L.; Yang, H.; Pennycook, T. J.; Marshall, M. S. J.; Van Aert, S.; Browning, N. D.; Castell, M. R.; Nellist, P. D. Smart Align—a New Tool for Robust Non-Rigid Registration of Scanning Microscope Data. *Adv. Struct. Chem. Imaging* **2015**. <https://doi.org/10.1186/s40679-015-0008-4>.
- (84) Lebeau, J. M.; Findlay, S. D.; Allen, L. J.; Stemmer, S. Quantitative Atomic Resolution Scanning Transmission Electron Microscopy. *Phys. Rev. Lett.* **2008**. <https://doi.org/10.1103/PhysRevLett.100.206101>.
- (85) Dwyer, C.; Maunders, C.; Zheng, C. L.; Weyland, M.; Tiemeijer, P. C.; Etheridge, J. Sub-0.1 Nm-Resolution Quantitative Scanning Transmission Electron Microscopy without Adjustable Parameters. *Appl. Phys. Lett.* **2012**. <https://doi.org/10.1063/1.4711766>.
- (86) Hýtch, M. J.; Stobbs, W. M. Quantitative Comparison of High Resolution TEM Images with Image Simulations. *Ultramicroscopy* **1994**. [https://doi.org/10.1016/0304-3991\(94\)90034-5](https://doi.org/10.1016/0304-3991(94)90034-5).
- (87) Van Aert, S.; Verbeeck, J.; Erni, R.; Bals, S.; Luysberg, M.; Dyck, D. Van; Tendeloo, G. Van. Quantitative Atomic Resolution Mapping Using High-Angle Annular Dark Field

References

- Scanning Transmission Electron Microscopy. *Ultramicroscopy* **2009**. <https://doi.org/10.1016/j.ultramic.2009.05.010>.
- (88) Jones, L.; Wenner, S.; Nord, M.; Ninive, P. H.; Løvvik, O. M.; Holmestad, R.; Nellist, P. D. Optimising Multi-Frame ADF-STEM for High-Precision Atomic-Resolution Strain Mapping. *Ultramicroscopy* **2017**. <https://doi.org/10.1016/j.ultramic.2017.04.007>.
- (89) Liu, P.; Arslan Irmak, E.; De Backer, A.; De Wael, A.; Lobato, I.; Béch e, A.; Van Aert, S.; Bals, S. Three-Dimensional Atomic Structure of Supported Au Nanoparticles at High Temperature. *Nanoscale* **2021**. <https://doi.org/10.1039/d0nr08664a>.
- (90) Gonnissen, J.; Batuk, D.; Nataf, G. F.; Jones, L.; Abakumov, A. M.; Van Aert, S.; Schryvers, D.; Salje, E. K. H. Direct Observation of Ferroelectric Domain Walls in LiNbO₃: Wall-Meanders, Kinks, and Local Electric Charges. *Adv. Funct. Mater.* **2016**. <https://doi.org/10.1002/adfm.201603489>.
- (91) E, H.; MacArthur, K. E.; Pennycook, T. J.; Okunishi, E.; D'Alfonso, A. J.; Lugg, N. R.; Allen, L. J.; Nellist, P. D. Probe Integrated Scattering Cross Sections in the Analysis of Atomic Resolution HAADF STEM Images. *Ultramicroscopy* **2013**. <https://doi.org/10.1016/j.ultramic.2013.07.002>.
- (92) Boschker, H.; Huijben, M.; Vailionis, A.; Verbeeck, J.; Van Aert, S.; Luysberg, M.; Bals, S.; Van Tendeloo, G.; Houwman, E. P.; Koster, G.; Blank, D. H. A.; Rijnders, G. Optimized Fabrication of High-Quality La_{0.67}Sr_{0.33}MnO₃ Thin Films Considering All Essential Characteristics. *J. Phys. D. Appl. Phys.* **2011**. <https://doi.org/10.1088/0022-3727/44/20/205001>.
- (93) Huijben, M.; Koster, G.; Kruize, M. K.; Wenderich, S.; Verbeeck, J.; Bals, S.; Slooten, E.; Shi, B.; Molegraaf, H. J. A.; Kleibeuker, J. E.; Van Aert, S.; Goedkoop, J. B.; Brinkman, A.; Blank, D. H. A.; Golden, M. S.; Van Tendeloo, G.; Hilgenkamp, H.; Rijnders, G. Defect Engineering in Oxide Heterostructures by Enhanced Oxygen Surface Exchange. *Adv. Funct. Mater.* **2013**. <https://doi.org/10.1002/adfm.201203355>.
- (94) Martinez, G. T.; Rosenauer, A.; De Backer, A.; Verbeeck, J.; Van Aert, S. Quantitative Composition Determination at the Atomic Level Using Model-Based High-Angle Annular Dark Field Scanning Transmission Electron Microscopy. *Ultramicroscopy* **2014**. <https://doi.org/10.1016/j.ultramic.2013.11.001>.
- (95) Lebeau, J. M.; Findlay, S. D.; Allen, L. J.; Stemmer, S. Standardless Atom Counting in Scanning Transmission Electron Microscopy. *Nano Lett.* **2010**. <https://doi.org/10.1021/nl102025s>.
- (96) De Backer, A.; Martinez, G. T.; Rosenauer, A.; Van Aert, S. Atom Counting in HAADF STEM Using a Statistical Model-Based Approach: Methodology, Possibilities, and Inherent Limitations. *Ultramicroscopy* **2013**. <https://doi.org/10.1016/j.ultramic.2013.05.003>.
- (97) De Backer, A.; van den Bos, K. H. W.; Van den Broek, W.; Sijbers, J.; Van Aert, S. StatSTEM: An Efficient Approach for Accurate and Precise Model-Based Quantification of Atomic Resolution Electron Microscopy Images. *Ultramicroscopy* **2016**. <https://doi.org/10.1016/j.ultramic.2016.08.018>.
- (98) De wael, A.; De Backer, A.; Jones, L.; Nellist, P. D.; Van Aert, S. Hybrid Statistics-Simulations Based Method for Atom-Counting from ADF STEM Images. *Ultramicroscopy*

References

2017. <https://doi.org/10.1016/j.ultramic.2017.01.010>.
- (99) Van Den Bos, K. H. W.; De Backer, A.; Martinez, G. T.; Winckelmans, N.; Bals, S.; Nellist, P. D.; Van Aert, S. Unscrambling Mixed Elements Using High Angle Annular Dark Field Scanning Transmission Electron Microscopy. *Phys. Rev. Lett.* **2016**. <https://doi.org/10.1103/PhysRevLett.116.246101>.
- (100) van den Bos, K. H. W.; Altantzis, T.; De Backer, A.; Van Aert, S.; Bals, S. Recent Breakthroughs in Scanning Transmission Electron Microscopy of Small Species. *Adv. Phys. X* **2018**. <https://doi.org/10.1080/23746149.2018.1480420>.
- (101) MacArthur, K. E.; D'Alfonso, A. J.; Ozkaya, D.; Allen, L. J.; Nellist, P. D. Optimal ADF STEM Imaging Parameters for Tilt-Robust Image Quantification. *Ultramicroscopy* **2015**. <https://doi.org/10.1016/j.ultramic.2015.04.010>.
- (102) Martinez, G. T.; De Backer, A.; Rosenauer, A.; Verbeeck, J.; Van Aert, S. The Effect of Probe Inaccuracies on the Quantitative Model-Based Analysis of High Angle Annular Dark Field Scanning Transmission Electron Microscopy Images. *Micron* **2014**. <https://doi.org/10.1016/j.micron.2013.12.009>.
- (103) Van Aert, S.; Batenburg, K. J.; Rossell, M. D.; Erni, R.; Van Tendeloo, G. Three-Dimensional Atomic Imaging of Crystalline Nanoparticles. *Nature* **2011**. <https://doi.org/10.1038/nature09741>.
- (104) Bals, S.; Casavola, M.; Van Huis, M. A.; Van Aert, S.; Batenburg, K. J.; Van Tendeloo, G.; Vanmaekelbergh, D. Three-Dimensional Atomic Imaging of Colloidal Core-Shell Nanocrystals. *Nano Lett.* **2011**. <https://doi.org/10.1021/nl201826e>.
- (105) Goris, B.; Bals, S.; Van Den Broek, W.; Carbó-Argibay, E.; Gómez-Graña, S.; Liz-Marzán, L. M.; Van Tendeloo, G. Atomic-Scale Determination of Surface Facets in Gold Nanorods. *Nat. Mater.* **2012**. <https://doi.org/10.1038/nmat3462>.
- (106) Goris, B.; De Backer, A.; Van Aert, S.; Gómez-Graña, S.; Liz-Marzán, L. M.; Van Tendeloo, G.; Bals, S. Three-Dimensional Elemental Mapping at the Atomic Scale in Bimetallic Nanocrystals. *Nano Lett.* **2013**. <https://doi.org/10.1021/nl401945b>.
- (107) Bals, S.; Van Aert, S.; Romero, C. P.; Lauwaet, K.; Van Bael, M. J.; Schoeters, B.; Partoens, B.; Yücelen, E.; Lievens, P.; Van Tendeloo, G. Atomic Scale Dynamics of Ultrasmall Germanium Clusters. *Nat. Commun.* **2012**. <https://doi.org/10.1038/ncomms1887>.
- (108) Geuchies, J. J.; Van Overbeek, C.; Evers, W. H.; Goris, B.; De Backer, A.; Gantapara, A. P.; Rabouw, F. T.; Hilhorst, J.; Peters, J. L.; Konovalov, O.; Petukhov, A. V.; Dijkstra, M.; Siebbeles, L. D. A.; Van Aert, S.; Bals, S.; Vanmaekelbergh, D. *In situ* Study of the Formation Mechanism of Two-Dimensional Superlattices from PbSe Nanocrystals. *Nat. Mater.* **2016**. <https://doi.org/10.1038/nmat4746>.
- (109) Jones, L.; Macarthur, K. E.; Fauske, V. T.; Van Helvoort, A. T. J.; Nellist, P. D. Rapid Estimation of Catalyst Nanoparticle Morphology and Atomic-Coordination by High-Resolution Z-Contrast Electron Microscopy. *Nano Lett.* **2014**. <https://doi.org/10.1021/nl502762m>.
- (110) De Backer, A.; Jones, L.; Lobato, I.; Altantzis, T.; Goris, B.; Nellist, P. D.; Bals, S.; Van Aert, S. Three-Dimensional Atomic Models from a Single Projection Using: Z -Contrast

References

- Imaging: Verification by Electron Tomography and Opportunities. *Nanoscale* **2017**. <https://doi.org/10.1039/c7nr02656k>.
- (111) Albrecht, W.; van der Hoeven, J. E. S.; Deng, T.-S.; de Jongh, P. E.; van Blaaderen, A. Fully Alloyed Metal Nanorods with Highly Tunable Properties. *Nanoscale* **2017**, *9* (8), 2845–2851. <https://doi.org/10.1039/C6NR08484B>.
- (112) Albrecht, W.; Deng, T. S.; Goris, B.; Van Huis, M. A.; Bals, S.; Van Blaaderen, A. Single Particle Deformation and Analysis of Silica-Coated Gold Nanorods before and after Femtosecond Laser Pulse Excitation. *Nano Lett.* **2016**. <https://doi.org/10.1021/acs.nanolett.5b04851>.
- (113) Albrecht, W.; Arslan Irmak, E.; Altantzis, T.; Pedraza-Tardajos, A.; Skorikov, A.; Deng, T. S.; van der Hoeven, J. E. S.; van Blaaderen, A.; Van Aert, S.; Bals, S. 3D Atomic-Scale Dynamics of Laser-Light-Induced Restructuring of Nanoparticles Unraveled by Electron Tomography. *Adv. Mater.* **2021**. <https://doi.org/10.1002/adma.202100972>.
- (114) Vanrompay, H.; Bladt, E.; Albrecht, W.; Béché, A.; Zakhozheva, M.; Sánchez-Iglesias, A.; Liz-Marzán, L. M.; Bals, S. 3D Characterization of Heat-Induced Morphological Changes of Au Nanostars by Fast: *In situ* Electron Tomography. *Nanoscale* **2018**. <https://doi.org/10.1039/c8nr08376b>.
- (115) Cheng, Y.; Zhang, L.; Zhang, Q.; Li, J.; Tang, Y.; Delmas, C.; Zhu, T.; Winter, M.; Wang, M. S.; Huang, J. Understanding All Solid-State Lithium Batteries through *in situ* Transmission Electron Microscopy. *Materials Today*. **2021**. <https://doi.org/10.1016/j.mattod.2020.09.003>.
- (116) Liu, P.; Madsen, J.; Schiøtz, J.; Wagner, J. B.; Hansen, T. W. Reversible and Concerted Atom Diffusion on Supported Gold Nanoparticles. *J. Phys. Mater.* **2020**. <https://doi.org/10.1088/2515-7639/ab82b4>.
- (117) Liu, P.; Wu, T.; Madsen, J.; Schiøtz, J.; Wagner, J. B.; Hansen, T. W. Transformations of Supported Gold Nanoparticles Observed by: *In situ* Electron Microscopy. *Nanoscale* **2019**. <https://doi.org/10.1039/c9nr02731a>.
- (118) Zheng, H.; Meng, Y. S.; Zhu, Y. Frontiers of *in situ* Electron Microscopy. *MRS Bulletin*. **2015**. <https://doi.org/10.1557/mrs.2014.305>.
- (119) Albrecht, W.; Bals, S. Fast Electron Tomography for Nanomaterials. *J. Phys. Chem. C* **2020**. <https://doi.org/10.1021/acs.jpcc.0c08939>.
- (120) Vanrompay, H.; Skorikov, A.; Bladt, E.; Béché, A.; Freitag, B.; Verbeeck, J.; Bals, S. Fast versus Conventional HAADF-STEM Tomography: Advantages and Challenges. **2020**, *221* (October 2020). <https://doi.org/10.1016/j.ultramic.2020.113191>.
- (121) Vanrompay, H.; Skorikov, A.; Bladt, E.; Béché, A.; Freitag, B.; Verbeeck, J.; Bals, S. Fast versus Conventional HAADF-STEM Tomography of Nanoparticles: Advantages and Challenges. *Ultramicroscopy* **2021**. <https://doi.org/10.1016/j.ultramic.2020.113191>.
- (122) Fujiwara, K. Relativistic Dynamical Theory of Electron Diffraction. *J. Phys. Soc. Japan* **1961**. <https://doi.org/10.1143/JPSJ.16.2226>.
- (123) Kirkland, E. J. *Advanced Computing in Electron Microscopy: Second Edition*; 2010. <https://doi.org/10.1007/978-1-4419-6533-2>.

References

- (124) Kirkland, E. J. Computation in Electron Microscopy. *Acta Crystallogr. Sect. A Found. Adv.* **2016**. <https://doi.org/10.1107/S205327331501757X>.
- (125) de Beeck, M. O. Comments on the Use of the Relativistic Schrodinger Equation in High-Energy Electron Diffraction. In *Proceedings - Annual Meeting, Microscopy Society of America*; 1993. <https://doi.org/10.1017/s0424820100151891>.
- (126) Rother, A.; Scheerschmidt, K. Relativistic Effects in Elastic Scattering of Electrons in TEM. *Ultramicroscopy* **2009**. <https://doi.org/10.1016/j.ultramic.2008.08.008>.
- (127) Ferwerda, H. A.; Hoenders, B. J.; Slump, C. H.; Slump, C. H. Fully Relativistic Treatment of Electron-Optical Image Formation Based on the Dirac Equation. *Opt. Acta (Lond)*. **1986**. <https://doi.org/10.1080/713821923>.
- (128) Jagannathan, R. Quantum Theory of Electron Lenses Based on the Dirac Equation. *Phys. Rev. A* **1990**. <https://doi.org/10.1103/PhysRevA.42.6674>.
- (129) Jagannathan, R.; Simon, R.; Sudarshan, E. C. G.; Mukunda, N. Quantum Theory of Magnetic Electron Lenses Based on the Dirac Equation. *Phys. Lett. A* **1989**. [https://doi.org/10.1016/0375-9601\(89\)90685-3](https://doi.org/10.1016/0375-9601(89)90685-3).
- (130) Kirkland, E. J. On the Optimum Probe in Aberration Corrected ADF-STEM. *Ultramicroscopy* **2011**. <https://doi.org/10.1016/j.ultramic.2011.09.002>.
- (131) Scherzer, O. The Theoretical Resolution Limit of the Electron Microscope. *J. Appl. Phys.* **1949**. <https://doi.org/10.1063/1.1698233>.
- (132) Haider, M.; Uhlemann, S.; Zach, J. Upper Limits for the Residual Aberrations of a High-Resolution Aberration-Corrected STEM. *Ultramicroscopy* **2000**. [https://doi.org/10.1016/S0304-3991\(99\)00194-1](https://doi.org/10.1016/S0304-3991(99)00194-1).
- (133) Lobato, I.; van Aert, S.; Verbeeck, J. Progress and New Advances in Simulating Electron Microscopy Datasets Using MULTEM. *Ultramicroscopy* **2016**. <https://doi.org/10.1016/j.ultramic.2016.06.003>.
- (134) Cowley, J. M.; Moodie, A. F. The Scattering of Electrons by Atoms and Crystals. I. A New Theoretical Approach. *Acta Crystallogr.* **1957**. <https://doi.org/10.1107/s0365110x57002194>.
- (135) Goodman, P.; Moodie, A. F. Numerical Evaluations of N-beam Wave Functions in Electron Scattering by the Multi-slice Method. *Acta Crystallogr. Sect. A* **1974**. <https://doi.org/10.1107/S056773947400057X>.
- (136) van Dyck, D. The Path Integral Formalism as a New Description for the Diffraction of High-energy Electrons in Crystals. *Phys. status solidi* **1975**. <https://doi.org/10.1002/pssb.2220720135>.
- (137) Jap, B. K.; Glaeser, R. M. The Scattering of High-energy Electrons. I. Feynman Path-integral Formulation. *Acta Crystallogr. Sect. A* **1978**. <https://doi.org/10.1107/S0567739478000170>.
- (138) Ishizuka, K.; Uyeda, N. A New Theoretical and Practical Approach to the Multislice Method. *Acta Crystallogr. Sect. A* **1977**. <https://doi.org/10.1107/S0567739477001879>.
- (139) Alania, M.; Lobato, I.; Van Aert, S. Frozen Lattice and Absorptive Model for High Angle

- Annular Dark Field Scanning Transmission Electron Microscopy: A Comparison Study in Terms of Integrated Intensity and Atomic Column Position Measurement. *Ultramicroscopy* **2018**. <https://doi.org/10.1016/j.ultramic.2017.08.021>.
- (140) Abe, E.; Pennycook, S. J.; Tsai, A. P. Direct Observation of a Local Thermal Vibration Anomaly in a Quasicrystal. *Nature* **2003**. <https://doi.org/10.1038/nature01337>.
- (141) Aveyard, R.; Ferrando, R.; Johnston, R. L.; Yuan, J. Modeling Nanoscale Inhomogeneities for Quantitative HAADF STEM Imaging. *Phys. Rev. Lett.* **2014**. <https://doi.org/10.1103/PhysRevLett.113.075501>.
- (142) Wang, Z. L.; Petroski, J. M.; Green, T. C.; El-Sayed, M. A. Shape Transformation and Surface Melting of Cubic and Tetrahedral Platinum Nanocrystals. *J. Phys. Chem. B* **1998**, *102* (32), 6145–6151. <https://doi.org/10.1021/jp981594j>.
- (143) Wang, Z. L. Thermal Diffuse Scattering in Sub-Angstrom Quantitative Electron Microscopy - Phenomenon, Effects and Approaches. In *Micron*; 2003. [https://doi.org/10.1016/S0968-4328\(03\)00024-6](https://doi.org/10.1016/S0968-4328(03)00024-6).
- (144) Van Dyck, D. Is the Frozen Phonon Model Adequate to Describe Inelastic Phonon Scattering? *Ultramicroscopy* **2009**. <https://doi.org/10.1016/j.ultramic.2009.01.001>.
- (145) Rosenauer, A.; Schowalter, M.; Titantah, J. T.; Lamoen, D. An Emission-Potential Multislice Approximation to Simulate Thermal Diffuse Scattering in High-Resolution Transmission Electron Microscopy. *Ultramicroscopy* **2008**. <https://doi.org/10.1016/j.ultramic.2008.04.002>.
- (146) Martinez, G. T. Quantitative Model-Based High Angle Annular Dark Field Scanning Transmission Electron Microscopy, 2014.
- (147) Muller, D. A.; Edwards, B.; Kirkland E, E. J.; Silcox, J. Simulation of Thermal Diffuse Scattering Including a Detailed Phonon Dispersion Curve. *Ultramicroscopy* **2001**. [https://doi.org/10.1016/S0304-3991\(00\)00128-5](https://doi.org/10.1016/S0304-3991(00)00128-5).
- (148) Croitoru, M. D.; Van Dyck, D.; Van Aert, S.; Bals, S.; Verbeeck, J. An Efficient Way of Including Thermal Diffuse Scattering in Simulation of Scanning Transmission Electron Microscopic Images. *Ultramicroscopy* **2006**. <https://doi.org/10.1016/j.ultramic.2006.04.006>.
- (149) Schowalter, M.; Rosenauer, A.; Titantah, J. T.; Lamoen, D. Computation and Parametrization of the Temperature Dependence of Debye-Waller Factors for Group IV, III-V and II-VI Semiconductors. *Acta Crystallogr. Sect. A Found. Crystallogr.* **2009**. <https://doi.org/10.1107/S0108767308031437>.
- (150) Cao, H. X.; Peng, L. M. Parameterization of the Temperature Dependence of the Debye-Waller Factors. *Acta Crystallogr. Sect. A Found. Crystallogr.* **1999**. <https://doi.org/10.1107/s0108767399005176>.
- (151) Sears, V. F.; Shelley, S. A. Debye–Waller Factor for Elemental Crystals. *Acta Crystallogr. Sect. A* **1991**. <https://doi.org/10.1107/S0108767391002970>.
- (152) LeBeau, J. M.; Stemmer, S. Experimental Quantification of Annular Dark-Field Images in Scanning Transmission Electron Microscopy. *Ultramicroscopy* **2008**. <https://doi.org/10.1016/j.ultramic.2008.07.001>.

References

- (153) Jones, L. Quantitative ADF STEM: Acquisition, Analysis and Interpretation. In *IOP Conference Series: Materials Science and Engineering*; 2016. <https://doi.org/10.1088/1757-899X/109/1/012008>.
- (154) Goodman, J. W. Introduction to Fourier Optics 3ed. *Roberts & Company Publishers*. 2005.
- (155) Martinez, G. T.; Jones, L.; De Backer, A.; Béch e, A.; Verbeeck, J.; Van Aert, S.; Nellist, P. D. Quantitative STEM Normalisation: The Importance of the Electron Flux. *Ultramicroscopy* **2015**. <https://doi.org/10.1016/j.ultramic.2015.07.010>.
- (156) Krause, F. F.; Schowalter, M.; Grieb, T.; M uller-Caspary, K.; Mehrrens, T.; Rosenauer, A. Effects of Instrument Imperfections on Quantitative Scanning Transmission Electron Microscopy. *Ultramicroscopy* **2016**. <https://doi.org/10.1016/j.ultramic.2015.10.026>.
- (157) Verbeeck, J.; B ech e, A.; Van den Broek, W. A Holographic Method to Measure the Source Size Broadening in STEM. *Ultramicroscopy* **2012**. <https://doi.org/10.1016/j.ultramic.2012.05.007>.
- (158) Klenov, D. O.; Stemmer, S. Contributions to the Contrast in Experimental High-Angle Annular Dark-Field Images. *Ultramicroscopy* **2006**. <https://doi.org/10.1016/j.ultramic.2006.03.007>.
- (159) Richardson, M. H. Fundamentals of the Discrete Fourier Transform. *S V Sound Vib*. **1978**.
- (160) Van Aert, S.; Den Dekker, A. J.; Van Den Bos, A.; Van Dyck, D.; Chen, J. H. Maximum Likelihood Estimation of Structure Parameters from High Resolution Electron Microscopy Images. Part II: A Practical Example. *Ultramicroscopy* **2005**. <https://doi.org/10.1016/j.ultramic.2005.03.002>.
- (161) Den Dekker, A. J.; Van Aert, S.; Van Den Bos, A.; Van Dyck, D. Maximum Likelihood Estimation of Structure Parameters from High Resolution Electron Microscopy Images. Part I: A Theoretical Framework. *Ultramicroscopy* **2005**. <https://doi.org/10.1016/j.ultramic.2005.03.001>.
- (162) van den Bos, A.; den Dekker, A. J. Resolution Reconsidered-Conventional Approaches and an Alternative. *Adv. Imaging Electron Phys.* **2001**. [https://doi.org/10.1016/S1076-5670\(01\)80114-2](https://doi.org/10.1016/S1076-5670(01)80114-2).
- (163) Van Aert, S.; Den Dekker, A. J.; Van Dyck, D.; Van Den Bos, A. Optimal Experimental Design of STEM Measurement of Atom Column Positions. *Ultramicroscopy* **2002**. [https://doi.org/10.1016/S0304-3991\(01\)00152-8](https://doi.org/10.1016/S0304-3991(01)00152-8).
- (164) Van Aert, S.; Geuens, P.; Van Dyck, D.; Kisielowski, C.; Jinschek, J. R. Electron Channelling Based Crystallography. *Ultramicroscopy* **2007**. <https://doi.org/10.1016/j.ultramic.2006.04.031>.
- (165) Klenov, D. O.; Findlay, S. D.; Allen, L. J.; Stemmer, S. Influence of Orientation on the Contrast of High-Angle Annular Dark-Field Images of Silicon. *Phys. Rev. B - Condens. Matter Mater. Phys.* **2007**. <https://doi.org/10.1103/PhysRevB.76.014111>.
- (166) Nellist, P. D.; Rodenburg, J. M. Beyond the Conventional Information Limit: The Relevant Coherence Function. *Ultramicroscopy* **1994**. [https://doi.org/10.1016/0304-3991\(94\)90092-2](https://doi.org/10.1016/0304-3991(94)90092-2).

References

- (167) Van Aert, S.; Den Dekker, A. J.; Van Den Bos, A.; Van Dyck, D. High-Resolution Electron Microscopy: From Imaging toward Measuring. *IEEE Trans. Instrum. Meas.* **2002**. <https://doi.org/10.1109/TIM.2002.802250>.
- (168) De Backer, A.; Martinez, G. T.; Rosenauer, A.; Van Aert, S. Atom Counting in HAADF STEM Using a Statistical Model-Based Approach: Methodology, Possibilities, and Inherent Limitations. *Ultramicroscopy* **2013**. <https://doi.org/10.1016/j.ultramic.2013.05.003>.
- (169) van den Bos, A. *Parameter Estimation for Scientists and Engineers*; 2007. <https://doi.org/10.1002/9780470173862>.
- (170) Van Aert, S.; Van den Broek, W.; Goos, P.; Van Dyck, D. Model-Based Electron Microscopy: From Images toward Precise Numbers for Unknown Structure Parameters. *Micron* **2012**. <https://doi.org/10.1016/j.micron.2011.10.019>.
- (171) van den Bos, K. H. W.; Krause, F. F.; Béch e, A.; Verbeeck, J.; Rosenauer, A.; Van Aert, S. Locating Light and Heavy Atomic Column Positions with Picometer Precision Using ISTEM. *Ultramicroscopy* **2017**. <https://doi.org/10.1016/j.ultramic.2016.10.003>.
- (172) Fatermans, J. Quantitative Atom Detection from Atomic-Resolution Transmission Electron Microscopy Images, 2019.
- (173) Van Aert, S.; De Backer, A.; Martinez, G. T.; Goris, B.; Bals, S.; Van Tendeloo, G.; Rosenauer, A. Procedure to Count Atoms with Trustworthy Single-Atom Sensitivity. *Phys. Rev. B - Condens. Matter Mater. Phys.* **2013**. <https://doi.org/10.1103/PhysRevB.87.064107>.
- (174) McLachlan, G. J.; Lee, S. X.; Rathnayake, S. I. Finite Mixture Models. *Annu. Rev. Stat. Its Appl.* **2019**. <https://doi.org/10.1146/annurev-statistics-031017-100325>.
- (175) Hasselblad, V. Estimation of Finite Mixtures of Distributions from the Exponential Family. *J. Am. Stat. Assoc.* **1969**. <https://doi.org/10.1080/01621459.1969.10501071>.
- (176) DAY, N. E. Estimating the Components of a Mixture of Normal Distributions. *Biometrika* **1969**. <https://doi.org/10.1093/biomet/56.3.463>.
- (177) Wolfe, J. H. Pattern Clustering by Multivariate Mixture Analysis. *Multivariate Behav. Res.* **1970**. https://doi.org/10.1207/s15327906mbr0503_6.
- (178) Dempster, A. P.; Laird, N. M.; Rubin, D. B. Maximum Likelihood from Incomplete Data Via the EM Algorithm . *J. R. Stat. Soc. Ser. B* **1977**. <https://doi.org/10.1111/j.2517-6161.1977.tb01600.x>.
- (179) LeSar, R. *Introduction to Computational Materials Science*; 2013. <https://doi.org/10.1017/cbo9781139033398>.
- (180) Rapaport, D. C. *The Art of Molecular Dynamics Simulation*; 2004. <https://doi.org/10.1017/cbo9780511816581>.
- (181) Frenkel, D.; Smit, B. *Understanding Molecular Simulation: From Algorithms to Applications*; 2002.
- (182) Norman, G. E.; Stegailov, V. V. Stochastic Theory of the Classical Molecular Dynamics Method. *Math. Model. Comput. Simulations* **2013**. <https://doi.org/10.1134/S2070048213040108>.

References

- (183) Singraber, A.; Behler, J.; Dellago, C. Library-Based LAMMPS Implementation of High-Dimensional Neural Network Potentials. *J. Chem. Theory Comput.* **2019**. <https://doi.org/10.1021/acs.jctc.8b00770>.
- (184) Cai, J.; Ye, Y. Simple Analytical Embedded-Atom-Potential Model Including a Long-Range Force for Fcc Metals and Their Alloys. *Phys. Rev. B - Condens. Matter Mater. Phys.* **1996**. <https://doi.org/10.1103/PhysRevB.54.8398>.
- (185) Ercolessi, F.; Parrinello, M.; Tosatti, E. Simulation of Gold in the Glue Model. *Philos. Mag. A Phys. Condens. Matter, Struct. Defects Mech. Prop.* **1988**. <https://doi.org/10.1080/01418618808205184>.
- (186) Finnis, M. W.; Sinclair, J. E. A Simple Empirical N-Body Potential for Transition Metals. *Philos. Mag. A Phys. Condens. Matter, Struct. Defects Mech. Prop.* **1984**. <https://doi.org/10.1080/01418618408244210>.
- (187) Chen, S. P.; Srolovitz, D. J.; Voter, A. F. Computer Simulation on Surfaces and [001] Symmetric Tilt Grain Boundaries in Ni, Al, and Ni₃Al. *J. Mater. Res.* **1989**. <https://doi.org/10.1557/JMR.1989.0062>.
- (188) Daw, M. S.; Baskes, M. I. Embedded-Atom Method: Derivation and Application to Impurities, Surfaces, and Other Defects in Metals. *Phys. Rev. B* **1984**. <https://doi.org/10.1103/PhysRevB.29.6443>.
- (189) Ercolessi, F.; Adams, J. B. Interatomic Potentials from First-Principles Calculations: The Force-Matching Method. *EPL* **1994**. <https://doi.org/10.1209/0295-5075/26/8/005>.
- (190) Grochola, G.; Russo, S. P.; Snook, I. K. On Fitting a Gold Embedded Atom Method Potential Using the Force Matching Method. *J. Chem. Phys.* **2005**. <https://doi.org/10.1063/1.2124667>.
- (191) Sheng, H. W.; Kramer, M. J.; Cadien, A.; Fujita, T.; Chen, M. W. Highly Optimized Embedded-Atom-Method Potentials for Fourteen FCC Metals. *Phys. Rev. B - Condens. Matter Mater. Phys.* **2011**. <https://doi.org/10.1103/PhysRevB.83.134118>.
- (192) O'Brien, C. J.; Barr, C. M.; Price, P. M.; Hattar, K.; Foiles, S. M. Grain Boundary Phase Transformations in PtAu and Relevance to Thermal Stabilization of Bulk Nanocrystalline Metals. *J. Mater. Sci.* **2018**. <https://doi.org/10.1007/s10853-017-1706-1>.
- (193) Verlet, L. Computer "Experiments" on Classical Fluids. I. Thermodynamical Properties of Lennard-Jones Molecules. *Phys. Rev.* **1967**. <https://doi.org/10.1103/PhysRev.159.98>.
- (194) Swope, W. C.; Andersen, H. C.; Berens, P. H.; Wilson, K. R. A Computer Simulation Method for the Calculation of Equilibrium Constants for the Formation of Physical Clusters of Molecules: Application to Small Water Clusters. *J. Chem. Phys.* **1982**. <https://doi.org/10.1063/1.442716>.
- (195) Allen, M. P.; Tildesley, D. J. *Computer Simulation of Liquids: Second Edition*; 2017. <https://doi.org/10.1093/oso/9780198803195.001.0001>.
- (196) Hoover, W. G. Canonical Dynamics: Equilibrium Phase-Space Distributions. *Phys. Rev. A* **1985**. <https://doi.org/10.1103/PhysRevA.31.1695>.
- (197) Grønbech-Jensen, N. Complete Set of Stochastic Verlet-Type Thermostats for Correct Langevin Simulations. *Mol. Phys.* **2020**. <https://doi.org/10.1080/00268976.2019.1662506>.

References

- (198) Jang, S.; Pak, Y.; Shin, S. Multicanonical Ensemble with Nosé-Hoover Molecular Dynamics Simulation. *J. Chem. Phys.* **2002**. <https://doi.org/10.1063/1.1453398>.
- (199) Frenkel, D.; Smit, B.; Tobochnik, J.; McKay, S. R.; Christian, W. Understanding Molecular Simulation. *Comput. Phys.* **1997**. <https://doi.org/10.1063/1.4822570>.
- (200) Gubicza, J. *Defect Structure in Nanomaterials*; 2012. <https://doi.org/10.1533/9780857096142>.
- (201) Thompson, A. P.; Aktulga, H. M.; Berger, R.; Bolintineanu, D. S.; Brown, W. M.; Crozier, P. S.; in 't Veld, P. J.; Kohlmeyer, A.; Moore, S. G.; Nguyen, T. D.; Shan, R.; Stevens, M. J.; Tranchida, J.; Trott, C.; Plimpton, S. J. LAMMPS - a Flexible Simulation Tool for Particle-Based Materials Modeling at the Atomic, Meso, and Continuum Scales. *Comput. Phys. Commun.* **2022**, 271, 108171. <https://doi.org/10.1016/j.cpc.2021.108171>.
- (202) He, Y.; Liu, J. C.; Luo, L.; Wang, Y. G.; Zhu, J.; Du, Y.; Li, J.; Mao, S. X.; Wang, C. Size-Dependent Dynamic Structures of Supported Gold Nanoparticles in CO Oxidation Reaction Condition. *Proc. Natl. Acad. Sci. U. S. A.* **2018**. <https://doi.org/10.1073/pnas.1800262115>.
- (203) Vashishta, P.; Nakano, A.; Kalia, R. K.; Ebbsjö, I. Molecular Dynamics Simulations of Covalent Amorphous Insulators on Parallel Computers. *J. Non. Cryst. Solids* **1995**. [https://doi.org/10.1016/0022-3093\(94\)00576-1](https://doi.org/10.1016/0022-3093(94)00576-1).
- (204) Pregler, S. K.; Sinnott, S. B. Molecular Dynamics Simulations of Electron and Ion Beam Irradiation of Multiwalled Carbon Nanotubes: The Effects on Failure by Inner Tube Sliding. *Phys. Rev. B - Condens. Matter Mater. Phys.* **2006**. <https://doi.org/10.1103/PhysRevB.73.224106>.
- (205) Durrant, J. D.; McCammon, J. A. Molecular Dynamics Simulations and Drug Discovery. *BMC Biology*. 2011. <https://doi.org/10.1186/1741-7007-9-71>.
- (206) Wang, Y. G.; Mei, D.; Glezakou, V. A.; Li, J.; Rousseau, R. Dynamic Formation of Single-Atom Catalytic Active Sites on Ceria-Supported Gold Nanoparticles. *Nat. Commun.* **2015**. <https://doi.org/10.1038/ncomms7511>.
- (207) Martinez, G. T.; van den Bos, K. H. W.; Alania, M.; Nellist, P. D.; Van Aert, S. Thickness Dependence of Scattering Cross-Sections in Quantitative Scanning Transmission Electron Microscopy. *Ultramicroscopy* **2018**. <https://doi.org/10.1016/j.ultramic.2018.01.005>.
- (208) Ali, S.; Myasnichenko, V. S.; Neyts, E. C. Size-Dependent Strain and Surface Energies of Gold Nanoclusters. *Phys. Chem. Chem. Phys.* **2015**. <https://doi.org/10.1039/c5cp06153a>.
- (209) Grzelczak, M.; Pérez-Juste, J.; Mulvaney, P.; Liz-Marzán, L. M. Shape Control in Gold Nanoparticle Synthesis. *Chem. Soc. Rev.* **2008**. <https://doi.org/10.1039/b711490g>.
- (210) Holec, D.; Dumitraschkewitz, P.; Vollath, D.; Fischer, F. D. Surface Energy of Au Nanoparticles Depending on Their Size and Shape. *Nanomaterials* **2020**. <https://doi.org/10.3390/nano10030484>.
- (211) Holec, D.; Mayrhofer, P. H. Surface Energies of AlN Allotropes from First Principles. *Scr. Mater.* **2012**. <https://doi.org/10.1016/j.scriptamat.2012.07.027>.
- (212) Henry, C. R. Morphology of Supported Nanoparticles. *Progress in Surface Science*. 2005. <https://doi.org/10.1016/j.progsurf.2005.09.004>.

References

- (213) Lee, B. J.; Shim, J. H.; Baskes, I. Semiempirical Atomic Potentials for the Fcc Metals Cu, Ag, Au, Ni, Pd, Pt, Al, and Pb Based on First and Second Nearest-Neighbor Modified Embedded Atom Method. *Phys. Rev. B - Condens. Matter Mater. Phys.* **2003**. <https://doi.org/10.1103/PhysRevB.68.144112>.
- (214) Crljen; Lazić, P.; Šokčević, D.; Brako, R. Relaxation and Reconstruction on (111) Surfaces of Au, Pt, and Cu. *Phys. Rev. B - Condens. Matter Mater. Phys.* **2003**. <https://doi.org/10.1103/PhysRevB.68.195411>.
- (215) McCrum, I. T.; Hickner, M. A.; Janik, M. J. First-Principles Calculation of Pt Surface Energies in an Electrochemical Environment: Thermodynamic Driving Forces for Surface Faceting and Nanoparticle Reconstruction. *Langmuir* **2017**. <https://doi.org/10.1021/acs.langmuir.7b01530>.
- (216) Singh-Miller, N. E.; Marzari, N. Surface Energies, Work Functions, and Surface Relaxations of Low-Index Metallic Surfaces from First Principles. *Phys. Rev. B - Condens. Matter Mater. Phys.* **2009**. <https://doi.org/10.1103/PhysRevB.80.235407>.
- (217) Brown, W. A.; Kose, R.; King, D. A. Femtomole Adsorption Calorimetry on Single-Crystal Surfaces. *Chem. Rev.* **1998**. <https://doi.org/10.1021/cr9700890>.
- (218) Foiles, S. M.; Baskes, M. I.; Daw, M. S. Embedded-Atom-Method Functions for the Fcc Metals Cu, Ag, Au, Ni, Pd, Pt, and Their Alloys. *Phys. Rev. B* **1986**. <https://doi.org/10.1103/PhysRevB.33.7983>.
- (219) Vitos, L.; Ruban, A. V.; Skriver, H. L.; Kollár, J. The Surface Energy of Metals. *Surf. Sci.* **1998**. [https://doi.org/10.1016/S0039-6028\(98\)00363-X](https://doi.org/10.1016/S0039-6028(98)00363-X).
- (220) Galanakis, I.; Papanikolaou, N.; Dederichs, P. H. Applicability of the Broken-Bond Rule to the Surface Energy of the Fcc Metals. *Surf. Sci.* **2002**. [https://doi.org/10.1016/S0039-6028\(02\)01547-9](https://doi.org/10.1016/S0039-6028(02)01547-9).
- (221) Tyson, W. R.; Miller, W. A. Surface Free Energies of Solid Metals: Estimation from Liquid Surface Tension Measurements. *Surf. Sci.* **1977**. [https://doi.org/10.1016/0039-6028\(77\)90442-3](https://doi.org/10.1016/0039-6028(77)90442-3).
- (222) Olivier, S.; Conte, R.; Fortunelli, A. Derivation of an Empirical Potential for Gold with Angular Corrections. *Phys. Rev. B - Condens. Matter Mater. Phys.* **2008**. <https://doi.org/10.1103/PhysRevB.77.054104>.
- (223) Opletal, G.; Grochola, G.; Chui, Y. H.; Snook, I. K.; Russo, S. P. Stability and Transformations of Heated Gold Nanorods. *J. Phys. Chem. C* **2011**. <https://doi.org/10.1021/jp1074913>.
- (224) Opletal, G.; Feigl, C. A.; Grochola, G.; Snook, I. K.; Russo, S. P. Elucidation of Surface Driven Crystallization of Icosahedral Clusters. *Chem. Phys. Lett.* **2009**. <https://doi.org/10.1016/j.cplett.2009.10.009>.
- (225) Zheng, H.; Cao, A.; Weinberger, C. R.; Huang, J. Y.; Du, K.; Wang, J.; Ma, Y.; Xia, Y.; Mao, S. X. Discrete Plasticity in Sub-10-Nm-Sized Gold Crystals. *Nat. Commun.* **2010**. <https://doi.org/10.1038/ncomms1149>.
- (226) Wei Wang, J.; Narayanan, S.; Yu Huang, J.; Zhang, Z.; Zhu, T.; Mao, S. X. Atomic-Scale Dynamic Process of Deformation-Induced Stacking Fault Tetrahedra in Gold Nanocrystals.

- Nat. Commun.* **2013**. <https://doi.org/10.1038/ncomms3340>.
- (227) Sun, X. Y.; Xu, G. K.; Li, X.; Feng, X. Q.; Gao, H. Mechanical Properties and Scaling Laws of Nanoporous Gold. *J. Appl. Phys.* **2013**. <https://doi.org/10.1063/1.4774246>.
- (228) Haruta, M.; Yamada, N.; Kobayashi, T.; Iijima, S. Gold Catalysts Prepared by Coprecipitation for Low-Temperature Oxidation of Hydrogen and of Carbon Monoxide. *J. Catal.* **1989**. [https://doi.org/10.1016/0021-9517\(89\)90034-1](https://doi.org/10.1016/0021-9517(89)90034-1).
- (229) Paier, J.; Penschke, C.; Sauer, J. Oxygen Defects and Surface Chemistry of Ceria: Quantum Chemical Studies Compared to Experiment. *Chemical Reviews*. **2013**. <https://doi.org/10.1021/cr3004949>.
- (230) Meyer, R.; Lemire, C.; Shaikhutdinov, S. K.; Freund, H. J. Surface Chemistry of Catalysis by Gold. *Gold Bull.* **2004**. <https://doi.org/10.1007/BF03215519>.
- (231) Mills, G.; Gordon, M. S.; Metiu, H. Oxygen Adsorption on Au Clusters and a Rough Au(111) Surface: The Role of Surface Flatness, Electron Confinement, Excess Electrons, and Band Gap. *J. Chem. Phys.* **2003**. <https://doi.org/10.1063/1.1542879>.
- (232) Schlexer, P.; Andersen, A. B.; Sebok, B.; Chorkendorff, I.; Schiøtz, J.; Hansen, T. W. Size-Dependence of the Melting Temperature of Individual Au Nanoparticles. *Part. Part. Syst. Charact.* **2019**. <https://doi.org/10.1002/ppsc.201800480>.
- (233) Barnard, A. S.; Young, N. P.; Kirkland, A. I.; Van Huis, M. A.; Xu, H. Nanogold: A Quantitative Phase Map. *ACS Nano* **2009**. <https://doi.org/10.1021/nn900220k>.
- (234) Foster, D. M.; Pavloudis, T.; Kioseoglou, J.; Palmer, R. E. Atomic-Resolution Imaging of Surface and Core Melting in Individual Size-Selected Au Nanoclusters on Carbon. *Nat. Commun.* **2019**. <https://doi.org/10.1038/s41467-019-10713-z>.
- (235) Uchiyama, T.; Yoshida, H.; Kuwauchi, Y.; Ichikawa, S.; Shimada, S.; Haruta, M.; Takeda, S. Systematic Morphology Changes of Gold Nanoparticles Supported on CeO₂ during Co Oxidation. *Angew. Chemie - Int. Ed.* **2011**. <https://doi.org/10.1002/anie.201102487>.
- (236) Yoshida, H.; Kuwauchi, Y.; Jinschek, J. R.; Sun, K.; Tanaka, S.; Kohyama, M.; Shimada, S.; Haruta, M.; Takeda, S. Visualizing Gas Molecules Interacting with Supported Nanoparticulate Catalysts at Reaction Conditions. *Science (80-.)*. **2012**. <https://doi.org/10.1126/science.1213194>.
- (237) Li, Z. Y.; Young, N. P.; Di Vece, M.; Palomba, S.; Palmer, R. E.; Bleloch, A. L.; Curley, B. C.; Johnston, R. L.; Jiang, J.; Yuan, J. Three-Dimensional Atomic-Scale Structure of Size-Selected Gold Nanoclusters. *Nature* **2008**. <https://doi.org/10.1038/nature06470>.
- (238) Sang, X.; LeBeau, J. M. Revolving Scanning Transmission Electron Microscopy: Correcting Sample Drift Distortion without Prior Knowledge. *Ultramicroscopy* **2014**. <https://doi.org/10.1016/j.ultramic.2013.12.004>.
- (239) Kroon, D. J.; Slump, C. H. MRI Modality Transformation in Demon Registration. In *Proceedings - 2009 IEEE International Symposium on Biomedical Imaging: From Nano to Macro, ISBI 2009*; 2009. <https://doi.org/10.1109/ISBI.2009.5193214>.
- (240) Wang, H.; Dong, L.; O'Daniel, J.; Mohan, R.; Garden, A. S.; Kian Ang, K.; Kuban, D. A.; Bonnen, M.; Chang, J. Y.; Cheung, R. Validation of an Accelerated “demons” Algorithm

References

- for Deformable Image Registration in Radiation Therapy. *Phys. Med. Biol.* **2005**. <https://doi.org/10.1088/0031-9155/50/12/011>.
- (241) Pennec, X.; Cachier, P.; Ayache, N. Understanding the “Demon’s Algorithm”: 3D Non-Rigid Registration by Gradient Descent BT - Medical Image Computing and Computer-Assisted Intervention – MICCAI’99; Taylor, C., Colchester, A., Eds.; Springer Berlin Heidelberg: Berlin, Heidelberg, 1999; pp 597–605. https://doi.org/https://doi.org/10.1007/10704282_64.
- (242) Findlay, S. D.; LeBeau, J. M. Detector Non-Uniformity in Scanning Transmission Electron Microscopy. *Ultramicroscopy* **2013**. <https://doi.org/10.1016/j.ultramic.2012.09.001>.
- (243) Otsu, N. Threshold Selection Method from Gray-Level Histograms. *IEEE Trans Syst Man Cybern* **1979**. <https://doi.org/10.1109/tsmc.1979.4310076>.
- (244) Rosenauer, A.; Gries, K.; Müller, K.; Pretorius, A.; Schowalter, M.; Avramescu, A.; Engl, K.; Lutgen, S. Measurement of Specimen Thickness and Composition in Al_xGa_{1-x}N / GaN Using High-Angle Annular Dark Field Images. *Ultramicroscopy* **2009**. <https://doi.org/10.1016/j.ultramic.2009.05.003>.
- (245) Balaji Gopal, C.; García-Melchor, M.; Lee, S. C.; Shi, Y.; Shavorskiy, A.; Monti, M.; Guan, Z.; Sinclair, R.; Bluhm, H.; Vojvodic, A.; Chueh, W. C. Equilibrium Oxygen Storage Capacity of Ultrathin CeO_{2-δ} Depends Non-Monotonically on Large Biaxial Strain. *Nat. Commun.* **2017**. <https://doi.org/10.1038/ncomms15360>.
- (246) Da Silva, J. L. F.; Ganduglia-Pirovano, M. V.; Sauer, J.; Bayer, V.; Kresse, G. Hybrid Functionals Applied to Rare-Earth Oxides: The Example of Ceria. *Phys. Rev. B - Condens. Matter Mater. Phys.* **2007**. <https://doi.org/10.1103/PhysRevB.75.045121>.
- (247) Stukowski, A. Visualization and Analysis of Atomistic Simulation Data with OVITO-the Open Visualization Tool. *Model. Simul. Mater. Sci. Eng.* **2010**, *18* (1), 015012. <https://doi.org/10.1088/0965-0393/18/1/015012>.
- (248) Stukowski, A. Structure Identification Methods for Atomistic Simulations of Crystalline Materials. *Model. Simul. Mater. Sci. Eng.* **2012**. <https://doi.org/10.1088/0965-0393/20/4/045021>.
- (249) Marks, L. D.; Peng, L. Nanoparticle Shape, Thermodynamics and Kinetics. *Journal of Physics Condensed Matter*. 2016. <https://doi.org/10.1088/0953-8984/28/5/053001>.
- (250) De Wael, A.; De Backer, A.; Jones, L.; Varambhia, A.; Nellist, P. D.; Van Aert, S. Measuring Dynamic Structural Changes of Nanoparticles at the Atomic Scale Using Scanning Transmission Electron Microscopy. *Phys. Rev. Lett.* **2020**. <https://doi.org/10.1103/PhysRevLett.124.106105>.
- (251) Larsen, P. M.; Schmidt, S.; Schiøtz, J. Robust Structural Identification via Polyhedral Template Matching. *Model. Simul. Mater. Sci. Eng.* **2016**. <https://doi.org/10.1088/0965-0393/24/5/055007>.
- (252) Ziemba, M.; Ganduglia-Pirovano, M. V.; Hess, C. Insight into the Mechanism of the Water-Gas Shift Reaction over Au/CeO₂ catalysts Using Combined: Operando Spectroscopies. *Faraday Discuss.* **2021**. <https://doi.org/10.1039/c9fd00133f>.
- (253) Centeno, M. A.; Reina, T. R.; Ivanova, S.; Laguna, O. H.; Odriozola, J. A. Au/CeO₂

References

- Catalysts: Structure and CO Oxidation Activity. *Catalysts*. 2016. <https://doi.org/10.3390/catal6100158>.
- (254) Fu, Q.; Saltsburg, H.; Flytzani-Stephanopoulos, M. Active Nonmetallic Au and Pt Species on Ceria-Based Water-Gas Shift Catalysts. *Science* (80-.). **2003**. <https://doi.org/10.1126/science.1085721>.
- (255) Krivanek, O. L.; Chisholm, M. F.; Nicolosi, V.; Pennycook, T. J.; Corbin, G. J.; Dellby, N.; Murfitt, M. F.; Own, C. S.; Szilagy, Z. S.; Oxley, M. P.; Pantelides, S. T.; Pennycook, S. J. Atom-by-Atom Structural and Chemical Analysis by Annular Dark-Field Electron Microscopy. *Nature* **2010**. <https://doi.org/10.1038/nature08879>.
- (256) Rosenauer, A.; Mehtens, T.; Müller, K.; Gries, K.; Schowalter, M.; Venkata Satyam, P.; Bley, S.; Tessarek, C.; Hommel, D.; Sebald, K.; Seyfried, M.; Gutowski, J.; Avramescu, A.; Engl, K.; Lutgen, S. Composition Mapping in InGaN by Scanning Transmission Electron Microscopy. *Ultramicroscopy* **2011**. <https://doi.org/10.1016/j.ultramic.2011.04.009>.
- (257) Möbus, G.; Inkson, B. J. Nanoscale Tomography in Materials Science. *Materials Today*. 2007. [https://doi.org/10.1016/S1369-7021\(07\)70304-8](https://doi.org/10.1016/S1369-7021(07)70304-8).
- (258) Koneti, S.; Roiban, L.; Dalmás, F.; Langlois, C.; Gay, A. S.; Cabiác, A.; Grenier, T.; Banjak, H.; Maxim, V.; Epicier, T. Fast Electron Tomography: Applications to Beam Sensitive Samples and *in situ* TEM or Operando Environmental TEM Studies. *Mater. Charact.* **2019**. <https://doi.org/10.1016/j.matchar.2019.02.009>.
- (259) Ferrando, R. Determining the Equilibrium Structures of Nanoalloys by Computational Methods. *Journal of Nanoparticle Research*. 2018. <https://doi.org/10.1007/s11051-018-4267-6>.
- (260) Yang, S.; Day, G. M. Exploration and Optimization in Crystal Structure Prediction: Combining Basin Hopping with Quasi-Random Sampling. *J. Chem. Theory Comput.* **2021**. <https://doi.org/10.1021/acs.jctc.0c01101>.
- (261) Woodley, S. M.; Catlow, R. Crystal Structure Prediction from First Principles. *Nature Materials*. 2008. <https://doi.org/10.1038/nmat2321>.
- (262) Oganov, A. R.; Glass, C. W. Crystal Structure Prediction Using Ab Initio Evolutionary Techniques: Principles and Applications. *J. Chem. Phys.* **2006**. <https://doi.org/10.1063/1.2210932>.
- (263) Zhu, Q.; Oganov, A. R.; Glass, C. W.; Stokes, H. T. Constrained Evolutionary Algorithm for Structure Prediction of Molecular Crystals: Methodology and Applications. *Acta Crystallogr. Sect. B Struct. Sci.* **2012**. <https://doi.org/10.1107/S0108768112017466>.
- (264) Bazterra, V. E.; Ferraro, M. B.; Facelli, J. C. Modified Genetic Algorithm to Model Crystal Structures. II. Determination of a Polymorphic Structure of Benzene Using Enthalpy Minimization. *J. Chem. Phys.* **2002**. <https://doi.org/10.1063/1.1458548>.
- (265) Han, Y.; Ferrando, R.; Li, Z. Y. Atomic Details of Interfacial Interaction in Gold Nanoparticles Supported on MgO(001). *J. Phys. Chem. Lett.* **2014**. <https://doi.org/10.1021/jz4022975>.
- (266) Lin, Y.; Wu, Z.; Wen, J.; Ding, K.; Yang, X.; Poepelmeier, K. R.; Marks, L. D. Adhesion and Atomic Structures of Gold on Ceria Nanostructures: The Role of Surface Structure and

References

- Oxidation State of Ceria Supports. *Nano Lett.* **2015**. <https://doi.org/10.1021/acs.nanolett.5b02694>.
- (267) Van Aert, S.; De Backer, A.; Martinez, G. T.; Goris, B.; Bals, S.; Van Tendeloo, G.; Rosenauer, A. Procedure to Count Atoms with Trustworthy Single-Atom Sensitivity. *Phys. Rev. B* **2013**, *87* (6), 064107. <https://doi.org/10.1103/PhysRevB.87.064107>.
- (268) Kirkpatrick, S.; Gelatt, C. D.; Vecchi, M. P. Optimization by Simulated Annealing. *Science* (80-.). **1983**. <https://doi.org/10.1126/science.220.4598.671>.
- (269) Metropolis, N.; Rosenbluth, A. W.; Rosenbluth, M. N.; Teller, A. H.; Teller, E. Equation of State Calculations by Fast Computing Machines. *J. Chem. Phys.* **1953**. <https://doi.org/10.1063/1.1699114>.
- (270) Wales, D. J.; Doye, J. P. K. Global Optimization by Basin-Hopping and the Lowest Energy Structures of Lennard-Jones Clusters Containing up to 110 Atoms. *J. Phys. Chem. A* **1997**. <https://doi.org/10.1021/jp970984n>.
- (271) Yu, M.; Yankovich, A. B.; Kaczmarowski, A.; Morgan, D.; Voyles, P. M. Integrated Computational and Experimental Structure Refinement for Nanoparticles. *ACS Nano* **2016**. <https://doi.org/10.1021/acs.nano.5b05722>.
- (272) Rossi, G.; Ferrando, R. Searching for Low-Energy Structures of Nanoparticles: A Comparison of Different Methods and Algorithms. *J. Phys. Condens. Matter* **2009**. <https://doi.org/10.1088/0953-8984/21/8/084208>.
- (273) Wang, D.; Li, Y. Bimetallic Nanocrystals: Liquid-Phase Synthesis and Catalytic Applications. *Adv. Mater.* **2011**. <https://doi.org/10.1002/adma.201003695>.
- (274) DeSantis, C. J.; Weiner, R. G.; Radmilovic, A.; Bower, M. M.; Skrabalak, S. E. Seeding Bimetallic Nanostructures as a New Class of Plasmonic Colloids. *J. Phys. Chem. Lett.* **2013**, *4* (18), 3072–3082. <https://doi.org/10.1021/jz4011866>.
- (275) Gilroy, K. D.; Ruditskiy, A.; Peng, H. C.; Qin, D.; Xia, Y. Bimetallic Nanocrystals: Syntheses, Properties, and Applications. *Chem. Rev.* **2016**. <https://doi.org/10.1021/acs.chemrev.6b00211>.
- (276) Liz-Marzán, L. M. Tailoring Surface Plasmons through the Morphology and Assembly of Metal Nanoparticles. *Langmuir* **2006**, *22* (1), 32–41. <https://doi.org/10.1021/la0513353>.
- (277) Pérez-Juste, J.; Pastoriza-Santos, I.; Liz-Marzán, L. M.; Mulvaney, P. Gold Nanorods: Synthesis, Characterization and Applications. *Coord. Chem. Rev.* **2005**, *249* (17), 1870–1901. <https://doi.org/https://doi.org/10.1016/j.ccr.2005.01.030>.
- (278) Zorić, I.; Zäch, M.; Kasemo, B.; Langhammer, C. Gold, Platinum, and Aluminum Nanodisk Plasmons: Material Independence, Subradiance, and Damping Mechanisms. *ACS Nano* **2011**, *5* (4), 2535–2546. <https://doi.org/10.1021/nn102166t>.
- (279) He, W.; Liu, Y.; Yuan, J.; Yin, J. J.; Wu, X.; Hu, X.; Zhang, K.; Liu, J.; Chen, C.; Ji, Y.; Guo, Y. Au@Pt Nanostructures as Oxidase and Peroxidase Mimetics for Use in Immunoassays. *Biomaterials* **2011**. <https://doi.org/10.1016/j.biomaterials.2010.09.040>.
- (280) Zhao, Y.; Ye, C.; Liu, W.; Chen, R.; Jiang, X. Tuning the Composition of AuPt Bimetallic Nanoparticles for Antibacterial Application. *Angew. Chemie Int. Ed.* **2014**, *53* (31), 8127–

References

8131. <https://doi.org/10.1002/anie.201401035>.
- (281) Wang, S.; Kristian, N.; Jiang, S.; Wang, X. Controlled Deposition of Pt on Au Nanorods and Their Catalytic Activity towards Formic Acid Oxidation. *Electrochem. commun.* **2008**. <https://doi.org/10.1016/j.elecom.2008.04.018>.
- (282) Iyyamperumal, R.; Zhang, L.; Henkelman, G.; Crooks, R. M. Efficient Electrocatalytic Oxidation of Formic Acid Using Au@Pt Dendrimer-Encapsulated Nanoparticles. *J. Am. Chem. Soc.* **2013**. <https://doi.org/10.1021/ja4010305>.
- (283) Zhou, Z.-Y.; Tian, N.; Li, J.-T.; Broadwell, I.; Sun, S.-G. Nanomaterials of High Surface Energy with Exceptional Properties in Catalysis and Energy Storage. *Chem. Soc. Rev.* **2011**, *40* (7), 4167–4185. <https://doi.org/10.1039/C0CS00176G>.
- (284) Zhang, Q.; Wang, H. Facet-Dependent Catalytic Activities of Au Nanoparticles Enclosed by High-Index Facets. *ACS Catal.* **2014**. <https://doi.org/10.1021/cs501445h>.
- (285) Fennell, J.; He, D.; Tanyi, A. M.; Logsdail, A. J.; Johnston, R. L.; Li, Z. Y.; Horswell, S. L. A Selective Blocking Method To Control the Overgrowth of Pt on Au Nanorods. *J. Am. Chem. Soc.* **2013**, *135* (17), 6554–6561. <https://doi.org/10.1021/ja4003475>.
- (286) Grzelczak, M.; Pérez-Juste, J.; Rodríguez-González, B.; Liz-Marzán, L. M. Influence of Silver Ions on the Growth Mode of Platinum on Gold Nanorods. *J. Mater. Chem.* **2006**. <https://doi.org/10.1039/b606887a>.
- (287) Xu, Z.; Carlton, C. E.; Allard, L. F.; Shao-Horn, Y.; Hamad-Schifferli, K. Direct Colloidal Route for Pt-Covered AuPt Bimetallic Nanoparticles. *J. Phys. Chem. Lett.* **2010**, *1* (17), 2514–2518. <https://doi.org/10.1021/jz100896p>.
- (288) Ataee-Esfahani, H.; Wang, L.; Nemoto, Y.; Yamauchi, Y. Synthesis of Bimetallic Au@Pt Nanoparticles with Au Core and Nanostructured Pt Shell toward Highly Active Electrocatalysts. *Chem. Mater.* **2010**, *22* (23), 6310–6318. <https://doi.org/10.1021/cm102074w>.
- (289) Habas, S. E.; Lee, H.; Radmilovic, V.; Somorjai, G. A.; Yang, P. Shaping Binary Metal Nanocrystals through Epitaxial Seeded Growth. *Nat. Mater.* **2007**, *6* (9), 692–697. <https://doi.org/10.1038/nmat1957>.
- (290) Suntivich, J.; Xu, Z.; Carlton, C. E.; Kim, J.; Han, B.; Lee, S. W.; Bonnet, N.; Marzari, N.; Allard, L. F.; Gasteiger, H. A.; Hamad-Schifferli, K.; Shao-Horn, Y. Surface Composition Tuning of Au–Pt Bimetallic Nanoparticles for Enhanced Carbon Monoxide and Methanol Electro-Oxidation. *J. Am. Chem. Soc.* **2013**, *135* (21), 7985–7991. <https://doi.org/10.1021/ja402072r>.
- (291) Garcia-Gutierrez, D. I.; Gutierrez-Wing, C. E.; Giovanetti, L.; Ramallo-López, J. M.; Requejo, F. G.; Jose-Yacaman, M. Temperature Effect on the Synthesis of Au–Pt Bimetallic Nanoparticles. *J. Phys. Chem. B* **2005**, *109* (9), 3813–3821. <https://doi.org/10.1021/jp048114a>.
- (292) Feng, L.; Wu, X.; Ren, L.; Xiang, Y.; He, W.; Zhang, K.; Zhou, W.; Xie, S. Well-Controlled Synthesis of Au@Pt Nanostructures by Gold-Nanorod-Seeded Growth. *Chem. – A Eur. J.* **2008**, *14* (31), 9764–9771. <https://doi.org/10.1002/chem.200800544>.
- (293) Chi, M.; Wang, C.; Lei, Y.; Wang, G.; Li, D.; More, K. L.; Lupini, A.; Allard, L. F.;

References

- Markovic, N. M.; Stamenkovic, V. R. Surface Faceting and Elemental Diffusion Behaviour at Atomic Scale for Alloy Nanoparticles during *in situ* Annealing. *Nat. Commun.* **2015**, *6* (1), 8925. <https://doi.org/10.1038/ncomms9925>.
- (294) González-Rubio, G.; Mosquera, J.; Kumar, V.; Pedraza-Tardajos, A.; Llombart, P.; Solís, D. M.; Lobato, I.; Noya, E. G.; Guerrero-Martínez, A.; Taboada, J. M.; Obelleiro, F.; MacDowell, L. G.; Bals, S.; Liz-Marzán, L. M. Micelle-Directed Chiral Seeded Growth on Anisotropic Gold Nanocrystals. *Science (80-.)*. **2020**, *368* (6498), 1472 LP – 1477. <https://doi.org/10.1126/science.aba0980>.
- (295) Wang, S.; Kristian, N.; Jiang, S.; Wang, X. Controlled Deposition of Pt on Au Nanorods and Their Catalytic Activity towards Formic Acid Oxidation. *Electrochem. commun.* **2008**, *10* (7), 961–964. <https://doi.org/https://doi.org/10.1016/j.elecom.2008.04.018>.
- (296) Zhao, D.; Xu, B. Q. Platinum Covering of Gold Nanoparticles for Utilization Enhancement of Pt in Electrocatalysts. *Phys. Chem. Chem. Phys.* **2006**. <https://doi.org/10.1039/b610269g>.
- (297) Plodinec, M.; Nerl, H. C.; Girgsdies, F.; Schlögl, R.; Lunkenbein, T. Insights into Chemical Dynamics and Their Impact on the Reactivity of Pt Nanoparticles during CO Oxidation by Operando TEM. *ACS Catal.* **2020**, *10* (5), 3183–3193. <https://doi.org/10.1021/acscatal.9b03692>.
- (298) Deng, L.; Hu, W.; Deng, H.; Xiao, S. Surface Segregation and Structural Features of Bimetallic Au–Pt Nanoparticles. *J. Phys. Chem. C* **2010**, *114* (25), 11026–11032. <https://doi.org/10.1021/jp100194p>.
- (299) Joo, S. H.; Park, J. Y.; Tsung, C.-K.; Yamada, Y.; Yang, P.; Somorjai, G. A. Thermally Stable Pt/Mesoporous Silica Core–Shell Nanocatalysts for High-Temperature Reactions. *Nat. Mater.* **2009**, *8* (2), 126–131. <https://doi.org/10.1038/nmat2329>.
- (300) Wen, Y.-H.; Huang, R.; Li, C.; Zhu, Z.-Z.; Sun, S.-G. Enhanced Thermal Stability of Au@Pt Nanoparticles by Tuning Shell Thickness: Insights from Atomistic Simulations. *J. Mater. Chem.* **2012**, *22* (15), 7380–7386. <https://doi.org/10.1039/C2JM16187G>.
- (301) He, D. S.; Han, Y.; Fennell, J.; Horswell, S. L.; Li, Z. Y. Growth and Stability of Pt on Au Nanorods. *Appl. Phys. Lett.* **2012**, *101* (11), 113102. <https://doi.org/10.1063/1.4751288>.
- (302) Vara, M.; Wang, X.; Howe, J.; Chi, M.; Xia, Y. Understanding the Stability of Pt-Based Nanocages under Thermal Stress Using *In situ* Electron Microscopy. *ChemNanoMat* **2018**, *4* (1), 112–117. <https://doi.org/10.1002/cnma.201700298>.
- (303) Skorikov, A.; Albrecht, W.; Bladt, E.; Xie, X.; Van Der Hoeven, J. E. S.; Van Blaaderen, A.; Van Aert, S.; Bals, S. Quantitative 3D Characterization of Elemental Diffusion Dynamics in Individual Ag@Au Nanoparticles with Different Shapes. *ACS Nano* **2019**. <https://doi.org/10.1021/acsnano.9b06848>.
- (304) Albrecht, W.; Bladt, E.; Vanrompay, H.; Smith, J. D.; Skrabalak, S. E.; Bals, S. Thermal Stability of Gold/Palladium Octopods Studied *in situ* in 3D: Understanding Design Rules for Thermally Stable Metal Nanoparticles. *ACS Nano* **2019**, *13* (6), 6522–6530. <https://doi.org/10.1021/acsnano.9b00108>.
- (305) Bagiński, M.; Pedraza-Tardajos, A.; Altantzis, T.; Tupikowska, M.; Vetter, A.; Tomczyk, E.; Suryadharma, R. N. S.; Pawlak, M.; Andruszkiewicz, A.; Górecka, E.; Pocięcha, D.;

References

- Rockstuhl, C.; Bals, S.; Lewandowski, W. Understanding and Controlling the Crystallization Process in Reconfigurable Plasmonic Superlattices. *ACS Nano* **2021**. <https://doi.org/10.1021/acsnano.0c09746>.
- (306) Buffat, P.; Borel, J.-P. Size Effect on the Melting Temperature of Gold Particles. *Phys. Rev. A* **1976**, *13* (6), 2287–2298. <https://doi.org/10.1103/PhysRevA.13.2287>.
- (307) van Omme, J. T.; Zakhosheva, M.; Spruit, R. G.; Sholkina, M.; Pérez Garza, H. H. Advanced Microheater for *in situ* Transmission Electron Microscopy; Enabling Unexplored Analytical Studies and Extreme Spatial Stability. *Ultramicroscopy* **2018**, *192*, 14–20. <https://doi.org/https://doi.org/10.1016/j.ultramicro.2018.05.005>.
- (308) Skorikov, A.; Albrecht, W.; Bladt, E.; Xie, X.; Van Der Hoeven, J. E. S.; Van Blaaderen, A.; Van Aert, S.; Bals, S. Quantitative 3D Characterization of Elemental Diffusion Dynamics in Individual Ag@Au Nanoparticles with Different Shapes. *ACS Nano* **2019**, *13* (11), 13421–13429. <https://doi.org/10.1021/acsnano.9b06848>.
- (309) Carbó-Argibay, E.; Rodríguez-González, B.; Gómez-Graña, S.; Guerrero-Martínez, A.; Pastoriza-Santos, I.; Pérez-Juste, J.; Liz-Marzán, L. M. The Crystalline Structure of Gold Nanorods Revisited: Evidence for Higher-Index Lateral Facets. *Angew. Chemie Int. Ed.* **2010**, *49* (49), 9397–9400. <https://doi.org/10.1002/anie.201004910>.
- (310) Sheppard, D.; Terrell, R.; Henkelman, G. Optimization Methods for Finding Minimum Energy Paths. *J. Chem. Phys.* **2008**. <https://doi.org/10.1063/1.2841941>.
- (311) Kittel, C. Introduction to Solid State Physics, 8th Edition. *Wiley Sons, New York, NY* **2004**.
- (312) Eom, N.; Messing, M. E.; Johansson, J.; Deppert, K. General Trends in Core–Shell Preferences for Bimetallic Nanoparticles. *ACS Nano* **2021**. <https://doi.org/10.1021/acsnano.1c01500>.
- (313) Wang, L. L.; Johnson, D. D. Predicted Trends of Core-Shell Preferences for 132 Late Transition-Metal Binary-Alloy Nanoparticles. *J. Am. Chem. Soc.* **2009**. <https://doi.org/10.1021/ja903247x>.
- (314) Liu, H. B.; Pal, U.; Ascencio, J. A. Thermodynamic Stability and Melting Mechanism of Bimetallic Au-Pt Nanoparticles. *J. Phys. Chem. C* **2008**. <https://doi.org/10.1021/jp802804u>.
- (315) Ferrando, R.; Jellinek, J.; Johnston, R. L. Nanoalloys: From Theory to Applications of Alloy Clusters and Nanoparticles. *Chemical Reviews*. 2008. <https://doi.org/10.1021/cr040090g>.
- (316) Nilekar, A. U.; Ruban, A. V.; Mavrikakis, M. Surface Segregation Energies in Low-Index Open Surfaces of Bimetallic Transition Metal Alloys. *Surf. Sci.* **2009**. <https://doi.org/10.1016/j.susc.2008.10.029>.
- (317) Dreaden, E. C.; Alkilany, A. M.; Huang, X.; Murphy, C. J.; El-Sayed, M. A. The Golden Age: Gold Nanoparticles for Biomedicine. *Chem. Soc. Rev.* **2012**. <https://doi.org/10.1039/c1cs15237h>.
- (318) Lim, W. Q.; Gao, Z. Plasmonic Nanoparticles in Biomedicine. *Nano Today*. 2016. <https://doi.org/10.1016/j.nantod.2016.02.002>.
- (319) Brolo, A. G. Plasmonics for Future Biosensors. *Nature Photonics*. 2012. <https://doi.org/10.1038/nphoton.2012.266>.

References

- (320) Li, M.; Cushing, S. K.; Wu, N. Plasmon-Enhanced Optical Sensors: A Review. *Analyst*. 2015. <https://doi.org/10.1039/c4an01079e>.
- (321) Stockman, M. I. Nanoplasmonic Sensing and Detection. *Science (80-.)*. 2015. <https://doi.org/10.1126/science.aaa6805>.
- (322) Li, P.-C.; Huang, S.-W.; Wei, C.-W.; Chiou, Y.-C.; Chen, C.-D.; Wang, C.-R. C. Photoacoustic Flow Measurements by Use of Laser-Induced Shape Transitions of Gold Nanorods. *Opt. Lett.* 2005. <https://doi.org/10.1364/ol.30.003341>.
- (323) Li, P.-C.; Wang, C.-R. C.; Shieh, D.-B.; Wei, C.-W.; Liao, C.-K.; Poe, C.; Jhan, S.; Ding, A.-A.; Wu, Y.-N. In Vivo Photoacoustic Molecular Imaging with Simultaneous Multiple Selective Targeting Using Antibody-Conjugated Gold Nanorods. *Opt. Express* 2008. <https://doi.org/10.1364/oe.16.018605>.
- (324) Zijlstra, P.; Chon, J. W. M.; Gu, M. Five-Dimensional Optical Recording Mediated by Surface Plasmons in Gold Nanorods. *Nature* 2009. <https://doi.org/10.1038/nature08053>.
- (325) Taylor, A. B.; Kim, J.; Chon, J. W. M. Detuned Surface Plasmon Resonance Scattering of Gold Nanorods for Continuous Wave Multilayered Optical Recording and Readout. *Opt. Express* 2012. <https://doi.org/10.1364/oe.20.005069>.
- (326) Dai, Q.; Ouyang, M.; Yuan, W.; Li, J.; Guo, B.; Lan, S.; Liu, S.; Zhang, Q.; Lu, G.; Tie, S.; Deng, H.; Xu, Y.; Gu, M. Encoding Random Hot Spots of a Volume Gold Nanorod Assembly for Ultralow Energy Memory. *Adv. Mater.* 2017. <https://doi.org/10.1002/adma.201701918>.
- (327) Linic, S.; Aslam, U.; Boerigter, C.; Morabito, M. Photochemical Transformations on Plasmonic Metal Nanoparticles. *Nature Materials*. 2015. <https://doi.org/10.1038/nmat4281>.
- (328) Aslam, U.; Rao, V. G.; Chavez, S.; Linic, S. Catalytic Conversion of Solar to Chemical Energy on Plasmonic Metal Nanostructures. *Nature Catalysis*. 2018. <https://doi.org/10.1038/s41929-018-0138-x>.
- (329) Zhang, Z.; Zhang, C.; Zheng, H.; Xu, H. Plasmon-Driven Catalysis on Molecules and Nanomaterials. *Acc. Chem. Res.* 2019. <https://doi.org/10.1021/acs.accounts.9b00224>.
- (330) Link, S.; Burda, C.; Nikoobakht, B.; El-Sayed, M. A. Laser-Induced Shape Changes of Colloidal Gold Nanorods Using Femtosecond and Nanosecond Laser Pulses. *J. Phys. Chem. B* 2000. <https://doi.org/10.1021/jp000679t>.
- (331) Zijlstra, P.; Chon, J. W. M.; Gu, M. White Light Scattering Spectroscopy and Electron Microscopy of Laser Induced Melting in Single Gold Nanorods. *Phys. Chem. Chem. Phys.* 2009. <https://doi.org/10.1039/b905203h>.
- (332) Taylor, A. B.; Siddiquee, A. M.; Chon, J. W. M. Below Melting Point Photothermal Reshaping of Single Gold Nanorods Driven by Surface Diffusion. *ACS Nano* 2014. <https://doi.org/10.1021/nn5055283>.
- (333) Yan, J.; Zhu, D.; Xie, J.; Shao, Y.; Xiao, W. Light Tailoring of Internal Atomic Structure of Gold Nanorods. *Small* 2020. <https://doi.org/10.1002/sml.202001101>.
- (334) Link, S.; Burda, C.; Mohamed, M. B.; Nikoobakht, B.; El-Sayed, M. A. Laser Photothermal Melting and Fragmentation of Gold Nanorods: Energy and Laser Pulse-Width Dependence.

- Journal of Physical Chemistry A*. 1999. <https://doi.org/10.1021/jp983141k>.
- (335) Chen, Y.-S.; Frey, W.; Kim, S.; Homan, K.; Kruizinga, P.; Sokolov, K.; Emelianov, S. Enhanced Thermal Stability of Silica-Coated Gold Nanorods for Photoacoustic Imaging and Image-Guided Therapy. *Opt. Express* **2010**. <https://doi.org/10.1364/oe.18.008867>.
- (336) Zijlstra, P.; Chon, J. W. M.; Gu, M. Effect of Heat Accumulation on the Dynamic Range of a Gold Nanorod Doped Polymer Nanocomposite for Optical Laser Writing and Patterning. *Opt. Express* **2007**. <https://doi.org/10.1364/oe.15.012151>.
- (337) Horiguchi, Y.; Honda, K.; Kato, Y.; Nakashima, N.; Niidome, Y. Photothermal Reshaping of Gold Nanorods Depends on the Passivating Layers of the Nanorod Surfaces. *Langmuir* **2008**. <https://doi.org/10.1021/la800811j>.
- (338) Albrecht, W.; Deng, T. S.; Goris, B.; Van Huis, M. A.; Bals, S.; Van Blaaderen, A. Single Particle Deformation and Analysis of Silica-Coated Gold Nanorods before and after Femtosecond Laser Pulse Excitation. *Nano Lett.* **2016**. <https://doi.org/10.1021/acs.nanolett.5b04851>.
- (339) Nguyen, S. C.; Zhang, Q.; Manthiram, K.; Ye, X.; Lomont, J. P.; Harris, C. B.; Weller, H.; Alivisatos, A. P. Study of Heat Transfer Dynamics from Gold Nanorods to the Environment via Time-Resolved Infrared Spectroscopy. *ACS Nano* **2016**. <https://doi.org/10.1021/acsnano.5b06623>.
- (340) González-Rubio, G.; Díaz-Núñez, P.; Rivera, A.; Prada, A.; Tardajos, G.; González-Izquierdo, J.; Bañares, L.; Llombart, P.; Macdowell, L. G.; Palafox, M. A.; Liz-Marzán, L. M.; Peña-Rodríguez, O.; Guerrero-Martínez, A. Femtosecond Laser Reshaping Yields Gold Nanorods with Ultranarrow Surface Plasmon Resonances. *Science (80-.)*. **2017**. <https://doi.org/10.1126/science.aan8478>.
- (341) Della Picca, F.; Gutiérrez, M. V.; Bragas, A. V.; Scarpettini, A. F. Monitoring the Photothermal Reshaping of Individual Plasmonic Nanorods with Coherent Mechanical Oscillations. *J. Phys. Chem. C* **2018**. <https://doi.org/10.1021/acs.jpcc.8b09458>.
- (342) Graf, C.; Vossen, D. L. J.; Imhof, A.; Van Blaaderen, A. A General Method to Coat Colloidal Particles with Silica. *Langmuir* **2003**. <https://doi.org/10.1021/la0347859>.
- (343) Hanske, C.; Sanz-Ortiz, M. N.; Liz-Marzán, L. M. Silica-Coated Plasmonic Metal Nanoparticles in Action. *Advanced Materials*. **2018**. <https://doi.org/10.1002/adma.201707003>.
- (344) Zhang, Z.; Wang, L.; Wang, J.; Jiang, X.; Li, X.; Hu, Z.; Ji, Y.; Wu, X.; Chen, C. Mesoporous Silica-Coated Gold Nanorods as a Light-Mediated Multifunctional Theranostic Platform for Cancer Treatment. *Adv. Mater.* **2012**. <https://doi.org/10.1002/adma.201104714>.
- (345) Chen, Y. S.; Frey, W.; Kim, S.; Kruizinga, P.; Homan, K.; Emelianov, S. Silica-Coated Gold Nanorods as Photoacoustic Signal Nanoamplifiers. *Nano Lett.* **2011**. <https://doi.org/10.1021/nl1042006>.
- (346) Park, J. N.; Forman, A. J.; Tang, W.; Cheng, J.; Hu, Y. S.; Lin, H.; McFarland, E. W. Highly Active and Sinter-Resistant Pd-Nanoparticle Catalysts Encapsulated in Silica. *Small* **2008**. <https://doi.org/10.1002/smll.200800895>.
- (347) Link, S.; Wang, Z. L.; El-Sayed, M. A. How Does a Gold Nanorod Melt? *J. Phys. Chem. B*

References

- 2000**. <https://doi.org/10.1021/jp0011701>.
- (348) Sumimoto, N.; Nakao, K.; Yamamoto, T.; Yasuda, K.; Matsumura, S.; Niidome, Y. *In situ* Observation of Structural Transformation of Gold Nanorods under Pulsed Laser Irradiation in an HVEM. *Microscopy* **2014**. <https://doi.org/10.1093/jmicro/dfu012>.
- (349) Wang, Y.; Teitel, S.; Dellago, C. Surface-Driven Bulk Reorganization of Gold Nanorods. *Nano Lett.* **2005**. <https://doi.org/10.1021/nl051149h>.
- (350) Gan, Y.; Jiang, S. Ultrafast Laser-Induced Premelting and Structural Transformation of Gold Nanorod. *J. Appl. Phys.* **2013**. <https://doi.org/10.1063/1.4792659>.
- (351) Aso, K.; Shigematsu, K.; Yamamoto, T.; Matsumura, S. Sequential Transmission Electron Microscopy Observation of the Shape Change of Gold Nanorods under Pulsed Laser Light Irradiation. *Microscopy* **2019**. <https://doi.org/10.1093/jmicro/dfy136>.
- (352) Ye, X.; Zheng, C.; Chen, J.; Gao, Y.; Murray, C. B. Using Binary Surfactant Mixtures to Simultaneously Improve the Dimensional Tunability and Monodispersity in the Seeded Growth of Gold Nanorods. *Nano Lett.* **2013**. <https://doi.org/10.1021/nl304478h>.
- (353) González-Rubio, G.; González-Izquierdo, J.; Bañares, L.; Tardajos, G.; Rivera, A.; Altantzis, T.; Bals, S.; Peña-Rodríguez, O.; Guerrero-Martínez, A.; Liz-Marzán, L. M. Femtosecond Laser-Controlled Tip-to-Tip Assembly and Welding of Gold Nanorods. *Nano Lett.* **2015**. <https://doi.org/10.1021/acs.nanolett.5b03844>.
- (354) Petrova, H.; Juste, J. P.; Pastoriza-Santos, I.; Hartland, G. V.; Liz-Marzán, L. M.; Mulvaney, P. On the Temperature Stability of Gold Nanorods: Comparison between Thermal and Ultrafast Laser-Induced Heating. *Phys. Chem. Chem. Phys.* **2006**. <https://doi.org/10.1039/b514644e>.
- (355) Baffou, G. *Thermoplasmonics*; 2017. <https://doi.org/10.1017/9781108289801>.
- (356) Baffou, G.; Rigneault, H. Femtosecond-Pulsed Optical Heating of Gold Nanoparticles. *Phys. Rev. B - Condens. Matter Mater. Phys.* **2011**. <https://doi.org/10.1103/PhysRevB.84.035415>.
- (357) Taylor, A. B.; Siddiquee, A. M.; Chon, J. W. M. Below Melting Point Photothermal Reshaping of Single Gold Nanorods Driven by Surface Diffusion. *ACS Nano* **2014**. <https://doi.org/10.1021/nn5055283>.
- (358) Ekici, O.; Harrison, R. K.; Durr, N. J.; Eversole, D. S.; Lee, M.; Ben-Yakar, A. Thermal Analysis of Gold Nanorods Heated with Femtosecond Laser Pulses. *J. Phys. D: Appl. Phys.* **2008**. <https://doi.org/10.1088/0022-3727/41/18/185501>.
- (359) Incropera, F. P.; DeWitt, D. P.; Bergman, T. L.; Lavine, A. S. *Fundamentals of Heat and Mass Transfer in Fabrics*; 2007.
- (360) Inouye, H.; Tanaka, K.; Tanahashi, I. Ultrafast Dynamics of Nonequilibrium Electrons in a Gold Nanoparticle System. *Phys. Rev. B - Condens. Matter Mater. Phys.* **1998**. <https://doi.org/10.1103/PhysRevB.57.11334>.
- (361) Baffou, G.; Quidant, R. Thermo-Plasmonics: Using Metallic Nanostructures as Nano-Sources of Heat. *Laser and Photonics Reviews.* **2013**. <https://doi.org/10.1002/lpor.201200003>.

References

- (362) Hodak, J. H.; Henglein, A.; Hartland, G. V. Size Dependent Properties of Au Particles: Coherent Excitation and Dephasing of Acoustic Vibrational Modes. *J. Chem. Phys.* **1999**. <https://doi.org/10.1063/1.480202>.
- (363) Huang, W.; Qian, W.; El-Sayed, M. A.; Ding, Y.; Wang, Z. L. Effect of the Lattice Crystallinity on the Electron-Phonon Relaxation Rates in Gold Nanoparticles. *J. Phys. Chem. C* **2007**. <https://doi.org/10.1021/jp0738917>.
- (364) Hu, M.; Wang, X.; Hartland, G. V.; Salgueiriño-Maceira, V.; Liz-Marzán, L. M. Heat Dissipation in Gold-Silica Core-Shell Nanoparticles. *Chem. Phys. Lett.* **2003**. [https://doi.org/10.1016/S0009-2614\(03\)00506-2](https://doi.org/10.1016/S0009-2614(03)00506-2).
- (365) Patil, S. P.; Rege, A.; Sagardas; Itskov, M.; Markert, B. Mechanics of Nanostructured Porous Silica Aerogel Resulting from Molecular Dynamics Simulations. *J. Phys. Chem. B* **2017**. <https://doi.org/10.1021/acs.jpcc.7b03184>.
- (366) Kierys, A.; Buda, W.; Goworek, J. The Porosity and Morphology of Mesoporous Silica Agglomerates. *J. Porous Mater.* **2010**. <https://doi.org/10.1007/s10934-009-9337-9>.
- (367) Hsu, C. S.; Rahman, A. Interaction Potentials and Their Effect on Crystal Nucleation and Symmetry. *J. Chem. Phys.* **1979**. <https://doi.org/10.1063/1.438311>.
- (368) Li, J.; Shimizu, F. Least-Square Atomic Strain. *Report*, <http://164.107> **2005**.
- (369) Aso, K.; Shigematsu, K.; Yamamoto, T.; Matsumura, S. Detection of Picometer-Order Atomic Displacements in Drift-Compensated HAADF-STEM Images of Gold Nanorods. *Microscopy* **2016**. <https://doi.org/10.1093/jmicro/dfw018>.
- (370) Cho, H.; Shin, J. W.; Ryoo, R. Atomic Scale Mechanisms Underlying Thermal Reshaping of Anisotropic Gold Nanocrystals Revealed by *in situ* Electron Microscopy. *J. Phys. Chem. C* **2020**. <https://doi.org/10.1021/acs.jpcc.0c04281>.
- (371) Combe, N.; Jensen, P.; Pimpinelli, A. Changing Shapes in the Nanoworld. *Phys. Rev. Lett.* **2000**. <https://doi.org/10.1103/PhysRevLett.85.110>.
- (372) van der Hoeven, J. E. S.; Jelic, J.; Olthof, L. A.; Totarella, G.; van Dijk-Moes, R. J. A.; Krafft, J. M.; Louis, C.; Studt, F.; van Blaaderen, A.; de Jongh, P. E. Unlocking Synergy in Bimetallic Catalysts by Core-Shell Design. *Nat. Mater.* **2021**. <https://doi.org/10.1038/s41563-021-00996-3>.
- (373) Warriar, P.; Teja, A. Effect of Particle Size on the Thermal Conductivity of Nanofluids Containing Metallic Nanoparticles. *Nanoscale Research Letters*. **2011**. <https://doi.org/10.1186/1556-276X-6-247>.
- (374) Hohenester, U.; Trügler, A. MNPBEM - A Matlab Toolbox for the Simulation of Plasmonic Nanoparticles. *Comput. Phys. Commun.* **2012**. <https://doi.org/10.1016/j.cpc.2011.09.009>.
- (375) Yücelen, E.; Lazić, I.; Bosch, E. G. T. Phase Contrast Scanning Transmission Electron Microscopy Imaging of Light and Heavy Atoms at the Limit of Contrast and Resolution. *Sci. Rep.* **2018**. <https://doi.org/10.1038/s41598-018-20377-2>.
- (376) Lazić, I.; Bosch, E. G. T.; Lazar, S. Phase Contrast STEM for Thin Samples: Integrated Differential Phase Contrast. *Ultramicroscopy* **2016**. <https://doi.org/10.1016/j.ultramic.2015.10.011>.

References

- (377) Branicio, P. S.; Rino, J. P.; Gan, C. K.; Tsuzuki, H. Interaction Potential for Indium Phosphide: A Molecular Dynamics and First-Principles Study of the Elastic Constants, Generalized Stacking Fault and Surface Energies. *J. Phys. Condens. Matter* **2009**. <https://doi.org/10.1088/0953-8984/21/9/095002>.
- (378) Massidda, S.; Continenza, A.; Freeman, A. J.; De Pascale, T. M.; Meloni, F.; Serra, M. Structural and Electronic Properties of Narrow-Band-Gap Semiconductors: InP, InAs, and InSb. *Phys. Rev. B* **1990**. <https://doi.org/10.1103/PhysRevB.41.12079>.

List of scientific contributions

Peer-Reviewed Publications

- Pedraza-Tardajos, A., * Arslan Irmak, E., * Kumar, V., Sánchez-Iglesias, A., Chen, Q., Wirix, M., Freitag, B., Albrecht, W., Van Aert, S., Liz-Marzán, L. M., Bals, S. Thermal Activation of Gold Atom Diffusion in Au@Pt Nanorods. (*submitted*).
- Arslan Irmak, E., Liu, P., Bals, S., Van, S. 3D Atomic Structure of Supported Metallic Nanoparticles Estimated from 2D ADF STEM Images: A Combination of Atom-Counting and a Local Minima Search Algorithm. *Small Methods* 2021, 2101150. <https://doi.org/10.1002/smtd.202101150>.
- Albrecht, W., * Arslan Irmak, E., * Altantzis, T., Pedraza-Tardajos, A., Skorikov, A., Deng, T.-S., van der Hoeven, J. E. S., van Blaaderen, A., Van Aert, S., Bals, S. Three-Dimensional Atomic Scale Dynamics of Laser Light Induced Restructuring of Nanoparticles Unraveled by Electron Tomography. *Adv. Mater.* 2021, 33, 2100972. <https://doi.org/10.1002/adma.202100972>.
- Liu, P., * Arslan Irmak, E., * De Backer, A., De wael, A., Lobato, I., Béch e, A., Van Aert, S., Bals, S. Three-dimensional Atomic Structure of Supported Au Nanoparticles at High Temperature. *Nanoscale* 2021, 13, 1770. <https://doi.org/10.1039/D0NR08664A>.

(* Equal contribution to the published works)

Oral and Poster Presentations

- Arslan Irmak, E., Liu, P., Schrenker, N., Bals, S., Van Aert, S. Tomography-Free Atomic-Resolution 3D Imaging of Nanoparticles. Society for Industrial and Applied Mathematics Conference on Imaging Science (SIAM), online, March 21-25, 2022. (Talk)
- Arslan Irmak, E., Schrenker, N., Dümbgen, K., Zeger Hens, Van Aert, S., Bals, S. 3D modelling of InP nanoparticles from 2D STEM images. Quantum Dots for On Chip Luminescent Downconversion meeting (QDOCCO), online, January 1, 2022. (Talk)
- Arslan Irmak, E., Albrecht, W., Van Aert, S., Bals, S. Unraveling the structural transformation of gold nanorods upon femtosecond laser excitation with atomic resolution electron tomography and molecular dynamics simulations. Microscopy Conference (MC 2021), online, August 22-26, 2021. (Talk)
- Arslan Irmak, E., Liu, P., De Backer, A., De wael, A., Lobato, I., Bals, S., Van Aert, S. 3-D modeling of nanomaterials from 2-D STEM images acquired along a single viewing direction. Virtual Early Career European Microscopy Congress (emc2020), online, November 24-26, 2020. (Talk)
- Arslan Irmak, E., Pedraza-Tardajos, A., Kumar, V., Sánchez-Iglesias, A., Albrecht, W., Van Aert, S., Liz-Marzán, L. M., Bals, S. Thermal stability and three-dimensional structural evolution of Pt coated Au Nanorods. User Meeting of the European Soft Matter Imaging (EUSMI), online, November 19, 2020. (Poster, *Awarded with the second prize*)
- Arslan Irmak, E., Albrecht, W., Van Aert, S., Bals, S. Unravelling the laser induced structural evolution of coated and uncoated gold nanorods. Chemistry Conference for Young Scientists (ChemCYS), Blankenberge, Belgium, February 19-21, 2020. (Talk, *Awarded with the third prize*)
- Arslan Irmak, E., Lobato, I., De Backer, A., Van Aert, S., Bals, S. 3-D characterization of nanomaterials from a single 2-D scanning transmission electron microscopy image. Research Day of the Faculty of Science, Antwerp, Belgium, January 15, 2020. (Poster)
- Arslan Irmak, E., Lobato, I., De Backer, A., Van Aert, S., Bals, S. 3-D characterization of nanomaterials from a single 2-D STEM image. Royal Belgian Society for Microscopy (RBSM), Louvain-la-Neuve, Belgium, September 9, 2019. (Poster)

Summary

Nanomaterials are materials that have at least one dimension in the nanometer length scale, which corresponds to a billionth of a meter. When three dimensions are confined to the nanometer scale, these materials are referred to as nanoparticles. These materials are of great interest since they exhibit unique physical and chemical properties that cannot be observed for bulk systems. Due to their unique and often superior properties, nanomaterials have become central in the field of electronics, catalysis, and medicine. Moreover, they are expected to be one of the most promising systems to tackle many challenges that our society is facing, such as reducing the emission of greenhouse gases and finding effective treatments for cancer.

The unique properties of nanomaterials are linked to their size, shape, structure, and composition. If one is able to measure the positions of the atoms, their chemical nature, and the bonding between them, it becomes possible to predict the physicochemical properties of nanomaterials. In this manner, the development of novel nanostructures can be triggered. However, the morphology and structure of nanomaterials are highly sensitive to the conditions for relevant applications, such as elevated temperatures or intense light illumination. Furthermore, any small change in the local structure at higher temperatures or pressures may significantly modify their performance. Hence, three-dimensional (3D) characterization of nanomaterials under application-relevant conditions is important in designing them with desired functional properties for specific applications.

Among different structural characterization approaches, transmission electron microscopy (TEM) is one of the most efficient and versatile tools to investigate the structure and composition of nanomaterials since it can provide atomically resolved images, which are sensitive to the local 3D structure of the investigated sample. However, TEM only provides two-dimensional (2D) images of the 3D nanoparticle, which may lead to an incomplete understanding of their structure-property relationship. The most known and powerful technique for the 3D characterization of nanomaterials is electron tomography, where the images of a nanostructured material taken from different directions are mathematically combined to retrieve its 3D structure. Although these experiments are already state-of-the-art, 3D characterization by TEM is typically performed under ultra-high vacuum conditions and at room temperature. Such conditions are unfortunately not sufficient to understand transformations during synthesis or applications of nanomaterials. This limitation can be overcome by *in situ* TEM where external stimuli, such as heat, gas, and liquids, can be controllably introduced inside the TEM using specialized holders. However, there are some technical limitations to successfully perform 3D *in situ* electron tomography experiments. For example, the long acquisition time required to collect a tilt series limits this technique when one wants to observe 3D dynamic changes with atomic resolution.

A solution for this problem is the estimation of the 3D structure of nanomaterials from 2D projection images acquired along a single viewing direction. For this purpose, annular dark field scanning TEM (ADF STEM) imaging mode provides a valuable tool for quantitative structural investigation of nanomaterials from single 2D images due to its thickness and mass sensitivity. For quantitative analysis, an ADF STEM image is considered as a 2D array of pixels where relative

variation of pixel intensity values is proportional to the total number of atoms and the atomic number of the elements in the sample. By applying advanced statistical approaches to these images, structural information, such as the number or types of atoms, can be retrieved with high accuracy and precision. The outcome can then be used to build a 3D starting model for energy minimization by atomistic simulations, for example, molecular dynamics simulations or the Monte Carlo method. However, this methodology needs to be further evaluated for *in situ* experiments.

This thesis is devoted to presenting robust approaches to accurately define the 3D atomic structure of nanoparticles under application-relevant conditions and understand the mechanism behind the atomic-scale dynamics in nanoparticles in response to environmental stimuli. For this purpose, the thesis is organized as follows.

Chapter 1: Introduction

This chapter presents the background and the motivation for the research comprising this thesis. It starts with a short introduction to nanomaterials and relevance of TEM for their investigation. The chapter continues with the basic principles and different imaging modes of TEM. Moreover, developments in the 3D characterization of nanomaterials from 2D TEM images are given.

Chapter 2: Quantitative 3D characterization from 2D STEM images

In this chapter, the concepts of quantitative 3D characterization used and extended throughout this thesis are introduced. First, the physics behind image formation in ADF STEM is briefly explained from a theoretical point of view. In the second section, the basic principles of statistical parameter estimation theory, which is applied to extract structural information from single ADF STEM images, are given. In the last section, the atomistic simulations, such as the Monte Carlo approach and molecular dynamics simulations, are explained.

Chapter 3: Three-dimensional atomic structure of supported Au nanoparticles at high temperature

In this chapter, an atomic resolution 3D investigation of supported gold nanoparticles is performed from ADF STEM images acquired along a single viewing direction during *in situ* heating experiments. By combining atom counting and structural relaxation by molecular dynamics simulations, the 3D equilibrium structures of nanoparticles are investigated as a function of temperature and size, which is of importance to understand their behavior during catalytic reactions. In this manner, the surface dynamics and crystalline transformations at high temperature are also characterized.

Chapter 4: 3D atomic structure of supported metallic nanoparticles: a combination of atom counting and a local minima search algorithm

At high temperatures, it is very likely that the structure of a nanoparticle deviates from a ground state configuration, which is difficult to determine using purely computational energy minimization approaches. Therefore, this chapter presents a novel methodology to overcome the limitations of purely computational energy minimization approaches for accurate 3D structural characterization of supported nanoparticles at high temperatures. For this purpose, atom counting on ADF STEM

images acquired along a single viewing direction is combined with a local minima search algorithm by taking the particle-support interaction and temperature into account.

Chapter 5: Unravelling Pt-driven morphological transformations in Au@Pt nanorods upon heating

Understanding the thermal stability of bimetallic nanoparticles is of vital importance to preserve their functionalities during a variety of applications. This chapter investigates the thermal stability of Au@Pt bimetallic nanoparticles since these particles are important for photo- and electrocatalytic applications. 3D *in situ* investigations of heat-induced morphological and compositional changes of Au@Pt core-shell nanoparticles are performed using electron tomography. Due to some fundamental and technical limitations, these experiments are carried out in a stop-and-go manner. Thus, to understand the ongoing atomic scale transformations during the heating of Au@Pt nanoparticles, experimentally determined 3D reconstructions are used as realistic input models in molecular dynamics simulations. Combined results from both techniques enable to understand the atomistic mechanism behind the transformations and the influence of the detailed morphology of the Pt-shell on the thermal stability of Au@Pt nanoparticles.

Chapter 6: 3D atomic-scale dynamics of laser light induced restructuring of nanoparticles unraveled by electron tomography and molecular dynamics simulations

The investigation of nanoparticle transformations becomes even more challenging when the transformation triggers cannot be applied *in situ*. As an example, intriguing transformations have been observed upon laser excitation of nanoparticles, not achievable by simply heating the material. Understanding laser-induced changes in nanomaterials is crucial to control their structure and shape-dependent properties for optoelectronic, photonic and plasmonic applications. Due to the ultrafast time scales of pulsed laser excitation, these transformations cannot be monitored *in situ*. In this chapter, atomic-scale structural transformations of a mesoporous silica-coated Au nanoparticle upon femtosecond-laser excitation are investigated using the measured 3D atomic structure resulting from *ex situ* electron tomography as an input for molecular dynamics simulations. In this manner, the complex atomistic rearrangements, causing shape deformations and defect generation, are unraveled.

Finally, the last chapter draws a general conclusion of this thesis and presents several perspectives that can be further explored for this research.

Samenvatting

Nanomaterialen zijn materialen waarvan minstens één dimensie een afmeting heeft in de grootteorde van een nanometer, een miljardste van een meter. Als de drie dimensies beperkt zijn tot de grootteorde van een nanometer, spreken we van een nanodeeltje. Deze materialen zijn van groot belang, aangezien ze unieke fysische en chemische eigenschappen vertonen, die in bulk systemen niet voorkomen. Door hun unieke, vaak betere eigenschappen, zijn nanomaterialen ondertussen van centraal belang in de elektronica, katalyse en geneeskunde. Ze worden bovendien aanzien als de meest veelbelovende systemen om vele uitdagingen in onze maatschappij aan te pakken, zoals het verlagen van de uitstoot van broeikasgassen en de zoektocht naar een effectieve behandeling voor kanker.

De unieke eigenschappen van nanomaterialen worden bepaald door hun grootte, vorm, structuur en samenstelling. Als we de posities van de atomen kunnen meten, alsook het type atomen en de bindingen ertussen kennen, is het mogelijk om de fysische en chemische eigenschappen van de nanomaterialen te voorspellen. Op die manier wordt het gericht ontwikkelen van nieuwe nanostructuren mogelijk. De morfologie en structuur van de nanomaterialen zijn echter heel gevoelig aan de condities waarin ze hun toepassingen vinden, zoals hoge temperaturen of intense belichting. Bovendien kan elke kleine verandering in de lokale structuur bij hogere temperatuur of druk hun prestaties sterk beïnvloeden. Daarom is de driedimensionale (3D) karakterisering van nanomaterialen onder condities die relevant zijn voor hun toepassingen heel belangrijk om ze gericht te ontwikkelen met de gewenste functionele eigenschappen voor specifieke toepassingen.

Eén van de meest efficiënte en veelzijdige methoden voor structurele karakterisering is transmissie elektronenmicroscopie (TEM). Het is een uiterst geschikte methode om de structuur en compositie van nanomaterialen te onderzoeken, omdat het beelden met atomaire resolutie kan opleveren, die gevoelig zijn aan de lokale 3D structuur van het bestudeerde staal. TEM levert echter slechts tweedimensionale (2D) beelden op van het 3D nanomateriaal, waardoor het inzicht in de relatie tussen hun structuur en eigenschappen onvolledig is. De meest bekende en krachtige techniek om nanomaterialen in 3D te karakteriseren is elektronentomografie, waar de beelden van een nanomateriaal uit verschillende richtingen gecombineerd worden in een wiskundig algoritme om de 3D structuur te achterhalen. Hoewel deze experimenten reeds *state-of-the-art* zijn, wordt de 3D karakterisering met TEM typisch uitgevoerd onder ultrahoge vacuüm condities en bij kamertemperatuur. Zo'n condities volstaan niet om de transformaties die optreden tijdens synthese of toepassing van nanomaterialen te begrijpen. Daarvoor is *in situ* TEM nodig, waarbij externe factoren, zoals warmte, gas en vloeistoffen, gecontroleerd in de TEM gebracht kunnen worden, dankzij gespecialiseerde houders. Er zijn echter wel enkele technische beperkingen die beletten om succesvolle 3D *in situ* elektronentomografie experimenten uit te voeren. De lange opnametijd die nodig is om een tiltserie te verkrijgen, verhindert bijvoorbeeld om met deze techniek dynamische 3D veranderingen met atomaire resolutie te observeren.

Een oplossing voor dit probleem is om de 3D structuur van nanomaterialen te schatten op basis van 2D projectiebeelden opgenomen langs één kijkrichting. Daarvoor is ringvormige donkerveld raster

transmissie elektronenmicroscopie (ADF STEM) een waardevolle beeldvormingstechniek, die uitermate geschikt is voor kwantitatief structuuronderzoek van nanomaterialen op basis van een enkel 2D beeld, dankzij de gevoeligheid aan de dikte en het atoomnummer. Voor zo'n kwantitatieve analyse wordt een ADF STEM beeld beschouwd als een 2D set van pixels, waarbij de relatieve variatie in de pixelintensiteiten evenredig is aan het totaal aantal atomen in het materiaal en aan hun atoomnummer. Door geavanceerde statistische methoden toe te passen op deze beelden, kan structuurinformatie zoals het aantal of type atomen achterhaald worden met hoge accuraatheid en precisie. Het resultaat kan dan gebruikt worden om een 3D startmodel op te stellen voor een energiminimalisatie met behulp van atomistische simulaties, zoals moleculaire dynamica simulaties of de Monte Carlo methode. Deze methode moet echter verder bestudeerd worden voor *in situ* experimenten.

In deze thesis worden daarom robuuste methoden gepresenteerd om de 3D atomaire structuur van nanomaterialen accuraat te bepalen onder de relevante condities voor een specifieke toepassing. Dit laat toe om de mechanismen van de dynamica op atomaire schaal in de nanomaterialen als reactie op omgevingsfactoren te begrijpen. Om dit te bereiken, wordt de thesis als volgt georganiseerd.

Hoofdstuk 1: Inleiding

Dit hoofdstuk geeft een inleiding tot de achtergrond en motivatie voor het onderzoek in deze thesis. Het begint met een korte introductie over nanomaterialen en het belang van TEM om ze te bestuderen. Dan komen de basisprincipes en verschillende beeldvormingsmodes van TEM aan bod. Vervolgens worden de ontwikkelingen voor de 3D karakterisering van nanomaterialen uit 2D TEM beelden besproken.

Hoofdstuk 2: Kwantitatieve 3D karakterisering van 2D STEM beelden

In dit hoofdstuk worden de concepten geïntroduceerd die in de overige delen van deze thesis zullen worden gebruikt en uitgebreid. Eerst wordt de fysica achter ADF STEM kort uitgelegd vanuit een theoretisch standpunt. In het tweede deel worden de basisprincipes van statistische parameterschattingstheorie uitgelegd. Deze worden toegepast om structurele informatie uit afzonderlijke ADF STEM beelden te verkrijgen. In het laatste deel worden de basisprincipes van atomistische simulaties, waaronder de Monte Carlo methode en moleculaire dynamica simulaties, uitgelegd.

Hoofdstuk 3: Driedimensionale atomaire structuur van gedragen Au nanodeeltjes bij hoge temperatuur

Dit hoofdstuk beschrijft de studie van gedragen gouden nanodeeltjes in 3D met atomaire resolutie, op basis van ADF STEM beelden genomen vanuit één kijkrichting tijdens *in situ* verwarmingsexperimenten. Door atomen tellen te combineren met structurele relaxatie via moleculaire dynamica simulaties, wordt de 3D evenwichtsstructuur van de nanodeeltjes onderzocht in functie van temperatuur en grootte. Dit is belangrijk om hun gedrag tijdens katalytische reacties

te begrijpen. Op deze manier worden de oppervlaktedynamica en kristallijne transformaties bij hoge temperaturen gekarakteriseerd.

Hoofdstuk 4: 3D atomaire structuur van gedragen metalen nanodeeltjes: een combinatie van atomen tellen en een lokale minima zoekalgoritme

Bij hoge temperaturen is de kans groot dat de structuur van een nanodeeltje verschilt van de evenwichtstoestand. Dit is echter moeilijk aan te tonen met enkel computationele methodes gebaseerd op energiminimalisatie. Daarom wordt in dit hoofdstuk een nieuwe methodologie geïntroduceerd, die voorbij de beperkingen van een uitsluitend computationele energiminimalisatie gaat voor de nauwkeurige 3D karakterisering van de structuur van gedragen nanodeeltjes. Hiervoor wordt atomen tellen via ADF STEM beelden vanuit één kijkrichting gecombineerd met een lokale minima zoekalgoritme, door rekening te houden met de temperatuur en de interactie tussen het nanodeeltje en de drager.

Hoofdstuk 5: Pt-gedreven morfologische transformaties van Au@Pt nanostaafjes ontcijferen bij verhitting

Het begrijpen van de thermische stabiliteit van bimetallische nanodeeltjes is van groot belang om hun functionaliteiten te behouden voor verschillende toepassingen. In dit hoofdstuk wordt de thermische stabiliteit van Au@Pt bimetallische nanodeeltjes onderzocht. Dit type deeltjes zijn belangrijk in foto- en elektrokatalytische toepassingen. Met elektronentomografie worden veranderingen in compositie en morfologie van Au@Pt kern-schil nanodeeltjes in 3D *in situ* bestudeerd. Omwille van enkele fundamentele en technische beperkingen worden dit soort experimenten op een stop-en-go manier uitgevoerd. Om de transformaties op atomaire schaal tijdens de verhitting van Au@Pt nanodeeltjes te begrijpen worden experimentele 3D reconstructies gebruikt als realistische startmodellen voor de moleculaire dynamica simulaties. De gecombineerde resultaten van deze twee technieken maken het mogelijk om het atomair mechanisme van de transformaties en de invloed van de gedetailleerde morfologie van de Pt-schil op de thermische stabiliteit van Au@Pt nanodeeltjes te begrijpen.

Hoofdstuk 6: 3D dynamica op atomaire schaal van de herschikking van nanodeeltjes veroorzaakt door laserlicht ontcijferen met behulp van elektronentomografie en moleculaire dynamica simulaties

Het onderzoeken van transformaties van nanodeeltjes wordt nog uitdagender wanneer bepaalde triggers voor transformaties onmogelijk *in situ* kunnen worden verwezenlijkt. Een voorbeeld zijn de intrigerende transformaties die worden geobserveerd bij laserexcitatie van nanodeeltjes. Het is onmogelijk deze omstandigheden experimenteel na te bootsen door simpelweg het materiaal te verwarmen. Nochtans is het begrijpen van laser-geïnduceerde veranderingen in een nanomateriaal cruciaal om hun opto-elektronische, fotonische en plasmonische eigenschappen te kunnen controleren. Echter, gezien de ultra-snelle tijdsschaal van gepulste laserexcitatie, is het onmogelijk om deze *in situ* te volgen. Dit hoofdstuk behandelt de structurele transformaties in 3D, die een mesoporeus silica gecoat Au nanodeeltje op atomair niveau ondergaat na femtoseconde laser excitatie. Het resultaat van *ex situ* elektronentomografie wordt als input voor moleculaire dynamica

Samenvatting

simulaties gebruikt. Op deze manier worden de complexe atomaire herschikkingen die aanleiding geven tot vormveranderingen en defecten blootgelegd.

Tenslotte wordt in het laatste hoofdstuk een algemene conclusie voor deze thesis getrokken, en worden enkele toekomstperspectieven besproken die de moeite zijn om verder te onderzoeken.

Acknowledgements

Doing a PhD has been a special period in my professional and personal life. Although there have been many ups and downs, I am glad all of them turned into very nice studies that I am proud of and a unique experience in my life. Here, I would like to start by expressing my gratitude to my supervisors, Prof. Dr. Sandra Van Aert and Prof. Dr. Sara Bals, for giving me the opportunity of working in such a wonderful team and guiding me throughout my PhD. Your comments helped me a lot to improve my scientific work as well as my personal skills. I would also like to thank the members of my PhD committee for their valuable time and for all contributions to shape this thesis into its final form.

A special thanks go to all the colleagues I worked with on the projects presented in this thesis. Ivan, your passion and dedication to science have always inspired me. I am thankful for all our discussions and your help, especially for your friendship! Annick and Annelies, thank you so much for all your guidance on both work-related and non-related issues. Your help during my PhD and especially the preparation of my thesis and defense mean a lot to me. Many thanks Pei, for providing the wonderful STEM images, which became the central point of my thesis. Thank you Adrian, for a very nice collaboration which also resulted in the cover of my thesis. Your friendship and unique sense of humor always made my day ☺ I would like to thank Nadine for the collaboration during the last year of my PhD and for spending a great time together. It is great having you as a friend. Many thanks Kellie, for your kindness and always being understanding to me. I would particularly like to thank Wiebke. Having a chance to work with you was a great pleasure and an inspiring experience for me. I feel so lucky that you are always there whenever I have a problem or good news to share. Thank you Wiebke for being in my life!

A big thank you go to my friends at EMAT. Thomas and Chu-Ping thank you for the many enjoyable evenings and happy moments that we shared. Your valuable companionship made the last four years special to me. I would like to thank Zezhong, Andrey and Saeid for great organizations outside work and such a great trip to Madrid ☺ Gizem, Safiyye, Selma and Nesli thank you for being such good friends and making me always feel at home. Many thanks Alex, Noopur, Dani, Nathalie, Ajinkya, Misha, Saskia, Sven, Yansong, and Debora, for all the fruitful discussions during our meetings and for your valuable feedback. Furthermore, I would like to thank Lydia and Miek for their extensive administrative assistance. Also, thank you Armand, for sharing your technical knowledge without any hesitation and for tasteful wines ☺

Most importantly, I would like to thank my husband Erdem. The last couple of months were very difficult for me. I am so grateful that you always found a way to cheer me up and fill my happiness bar during these times. Thank you so much for all the support and encouragement you give me in every moment. I wouldn't get through this period without you. I love you!

Finally, I would like to thank my parents and brother from home. Anne, baba, ve abi, bu süreçte çoğu zaman yanınızda olamayışıma rağmen hiçbir zaman bu durumdan şikayet etmediğiniz, tersine her zaman destekleyici ve özverili olduğunuz için çok minnettarım. Sizleri çok seviyorum!